



HAL
open science

Characterization and modeling of multi-material assemblies under mixed quasi-static loadings for the design of automotive structures

Hugo Leonardo Alfonso Medina

► **To cite this version:**

Hugo Leonardo Alfonso Medina. Characterization and modeling of multi-material assemblies under mixed quasi-static loadings for the design of automotive structures. Mechanical engineering [physics.class-ph]. Université de Bretagne occidentale - Brest, 2016. English. NNT : 2016BRES0118 . tel-01453047v2

HAL Id: tel-01453047

<https://theses.hal.science/tel-01453047v2>

Submitted on 7 Jun 2017

HAL is a multi-disciplinary open access archive for the deposit and dissemination of scientific research documents, whether they are published or not. The documents may come from teaching and research institutions in France or abroad, or from public or private research centers.

L'archive ouverte pluridisciplinaire **HAL**, est destinée au dépôt et à la diffusion de documents scientifiques de niveau recherche, publiés ou non, émanant des établissements d'enseignement et de recherche français ou étrangers, des laboratoires publics ou privés.



université de bretagne
occidentale

UNIVERSITE
BRETAGNE
LOIRE

THÈSE / UNIVERSITÉ DE BRETAGNE OCCIDENTALE

sous le sceau de l'Université européenne de Bretagne-Loire

pour obtenir le titre de

DOCTEUR DE L'UNIVERSITÉ DE BRETAGNE OCCIDENTALE

Mention : Génie mécanique

École Doctorale des Sciences de la Mer

Présentée par

Hugo Leonardo ALFONSO

Préparée à

l'Institut de Recherche Dupuy de Lôme
(CNRS FRE 3744)

**Caractérisation et modélisation
d'assemblages multi-matériaux
sous sollicitations mixtes
quasi-statiques
pour la conception
de structures automobiles**

Thèse soutenue le 14 décembre 2016
devant le jury composé de :

Franck LAURO

Professeur des universités, UVHC / rapporteur

Frédéric LACHAUD

Professeur des universités, ISAE / rapporteur

Bruno CASTANIE

Professeur des universités, INSA / *examineur*

Frédéric LAURIN

Docteur-Ingénieur de recherche (HDR), ONERA / *examineur*

Sylvain CALLOCH

Professeur des Universités, ENSTA-Bretagne / *examineur*

Georgios STAMOULIS

Maître de Conférences, IUT / *examineur*

Laurent TOLLIER

Ingénieur, PSA / partenaire industriel

Claudiu BADULESCU

Maître de conférence, IRDL / *Co-encadrant*

Nicolas CARRERE

Docteur-Ingénieur (HDR), SAFRAN Tech / *Directeur de thèse*

A mes parents



Remerciements

Une étape de ma vie a pris fin aujourd'hui, beaucoup d'émotions et de sentiments rencontrés. Ce fut une période d'apprentissage mais aussi de professionnalisation qui m'a permis d'enrichir mon profil. Des moments agréables mais aussi d'autres, plus difficiles, se sont passés en compagnie d'une multitude de personnes qui ont su apporter leurs meilleures qualités et connaissances afin de mener à bon terme la thèse que je vous présente dans ce document. Il est donc temps de les remercier pour leurs efforts inconditionnels.

Commençons par le début, une personne qui m'a accompagné pendant ma formation d'ingénieur et qui a su me confier un projet d'une si grande complexité. Malgré ses deux genoux gravement endommagés à cause du taekwondo et sa passion pour la poésie, il a toujours eu le temps nécessaire pour guider mes travaux. A toi, mon leader et enseignant M. Nicolas CARRERE, je te remercie énormément d'avoir dirigé cette thèse et d'avoir su me prodiguer tes conseils que j'ai toujours bien reçus. Bonne continuation dans tes nouveaux projets.

Je voudrais ensuite remercier mon co-encadrant M. Claudiu BADULESCU de m'avoir transmis ses connaissances en conception, en instrumentation et en réalisation d'essais. Tu as été capable de me guider dans l'acquisition de compétences expérimentales afin d'assurer une bonne qualité des résultats (nonobstant ma maladresse).

Aux partenaires industriels du projet FASTLITE pour la qualité du travail en équipe réalisé et pour votre confiance tout au long de ce projet et plus particulièrement à M. Florent DECHALOTTE pour la direction de ce projet, je vous remercie.

Merci énormément à M. Georgios STAMOULIS pour toute l'aide que tu m'as apporté tant professionnelle que personnelle. Les discussions et échanges que nous avons eu m'ont permis de développer des compétences critiques et d'étoffer mes idées.

Je remercie également l'équipe de techniciens qui m'ont accompagné pendant les campagnes expérimentales et qui m'ont transmis leurs compétences en réalisation d'essais.

Je souhaite aussi remercier l'équipe de professeurs, enseignants et ingénieurs de l'Institut de Recherche Dupuy de Lôme pour leur grande maîtrise de la science des matériaux. Les discussions que nous avons eu m'ont permis de retrouver le chemin le plus adapté à mes problématiques.

Merci à vous, mes chers doctorants, d'avoir été là, présents et d'avoir apporté de la bonne humeur au laboratoire avec vos blagues et pour tous ces moments de détente notamment lors de nos pauses café ou au Foy'z le vendredi soir.

Enfin, gros merci à tous ceux qui ont été amenés à travailler avec moi. Grâce à vous et à votre esprit de camaraderie que j'ai beaucoup apprécié, ces trois dernières années sont passées très rapidement.

Caractérisation et modélisation d'assemblages multi-matériaux sous sollicitations mixtes quasi-statiques pour la conception de structures automobiles





Résumé général

En 2015, l'Agence De l'Environnement et de la Maîtrise de l'Énergie (ADEME) a publié un rapport montrant qu'une voiture neuve vendue en France émet en moyenne 111 grammes de CO₂/km (ADEME-Carlabelling, 2015). Les futures réglementations imposent que d'ici 2021, les nouveaux véhicules particuliers fabriqués devront émettre moins de 95 grammes de CO₂/km. Ces émissions correspondent à une consommation de 4,1 L/100 km pour un véhicule essence et de 3,6 L/100 km pour un véhicule diesel. Un axe essentiel d'amélioration en vue de respecter ces exigences est la réduction de la masse des véhicules grâce à l'utilisation de matériaux composites.

Les techniques d'assemblage utilisées classiquement telles que le rivetage, le boulonnage ou la soudure posent des problèmes de compatibilité avec l'utilisation de ces matériaux. Il est impératif avant de pouvoir les utiliser de mettre au point et de maîtriser de nouveaux procédés d'assemblages multi-matériaux métal-composite. Afin d'y parvenir, les fabricants automobiles français (Renault et PSA-groupe) et leurs partenaires industriels (Laser Cheval, ARaymond, Böllhoff, Plastic Omnium, Solvay, CETIM, ESI Group, Altair) se sont unis dans le projet « FASTLITE Assemblage » financé par l'ADEME. L'objectif global de ce projet est l'émergence de solutions d'assemblage mixte à des coûts compétitifs et compatibles avec les cadences de production de l'industrie automobile.

Dans le cadre du projet FASTLITE les assemblages multi-matériaux visés sont les matériaux métalliques (aluminium et acier), et composites (à fibres de verre ou de carbone et à matrices thermodurcissables ou thermoplastiques). Les travaux de thèse présentés dans ce document avaient deux objectifs principaux :

- La caractérisation de techniques d'assemblage multi-matériaux sous sollicitations quasi-statiques de traction-compression/cisaillement.
- La modélisation de la technique d'assemblage la plus prometteuse afin de réduire le temps de design des structures automobiles.

Afin de répondre à ces objectifs, une démarche séquentielle a été adoptée. Cette démarche est expliquée en plusieurs parties dans ce résumé. Une première partie (Chapter I du manuscrit de thèse) situe le contexte de l'étude et analyse les procédés d'assemblages multi-matériaux adaptés à l'industrie automobile. La deuxième présente la démarche expérimentale suivie dans cette étude (Chapter II). La troisième partie compare la résistance des assemblages multi-matériaux par goujon, rivetage, soudure laser et par collage (Chapter III et Chapter IV du manuscrit). Ces travaux permettent de sélectionner le collage comme système d'assemblage préférentiel dans le cadre des applications visées. Ainsi, dans la quatrième partie, la caractérisation du comportement mécanique de deux colles est présentée (Chapter V dans le manuscrit). Finalement, la sixième partie est consacrée à la présentation du modèle de comportement utilisé pour les deux colles ainsi que la méthode d'identification de leurs paramètres matériaux associés (Chapter VI).

Techniques d'assemblage (Chapter I)

Une première phase exploratoire a été consacrée à l'étude de la résistance de différentes techniques d'assemblage multi-matériaux. Les fabricants automobiles partenaires du projet ont donc sélectionné sept matériaux différents aux caractéristiques mécaniques, économiques et esthétiques diverses :

- Deux aciers (22MnB5 et DP600)
- Un alliage d'aluminium (AL5182)
- Quatre composites : un thermodurcissable à matrice vinyelester et fibres de verre coupées (SMC-Chopped), un tissu NCF thermodurcissable à matrice vinyelester (SMC-Fabric), un 5H satin à matrice époxy et fibres de carbone (Prepreg) et un 8H satin à matrice thermoplastique et fibres de verre (PA66).

Pour assembler ces différents matériaux, quatre techniques d'assemblage adaptées à l'industrie automobile ont été retenues (*cf.* Figure 1) :

- L'assemblage par goujon : Il s'agit de solidariser les deux parties de la structure grâce à un goujon en acier sur lequel une plaque métallique est vissée. La tête du goujon est ensuite collée sur la pièce composite. Quatre assemblages peuvent être formés par cette technique : DP600/SMC-Chopped, DP600/SMC-Fabric, DP600/Prepreg et DP600/PA66.
- La soudure laser : Un rayon laser est utilisé pour fondre localement la matrice du matériau thermoplastique utilisé. La matière transformée servira d'élément d'adhésion entre le thermoplastique et la plaque métallique. Seulement deux types d'assemblages incluant des composites thermoplastiques sont étudiés : DP600/PA66 et 22MnB5/PA66.
- L'assemblage par RivSet : Un rivet auto-perçant est utilisé pour assembler deux matériaux. Quatre types d'assemblages différents sont étudiés : AL5182/SMC-Chopped, AL5182/SMC-Fabric, AL5182/Prepreg et AL5182/PA66.

- Le collage : pour les assemblages par collage, deux colles (Betamate-1822 et Sikapower-498) ont été présélectionnées par les constructeurs automobiles partenaires pour leurs caractéristiques mécaniques. Afin de juger des performances des assemblages par collage, l'ensemble des couples métal/métal et métal/composite ont été testés.

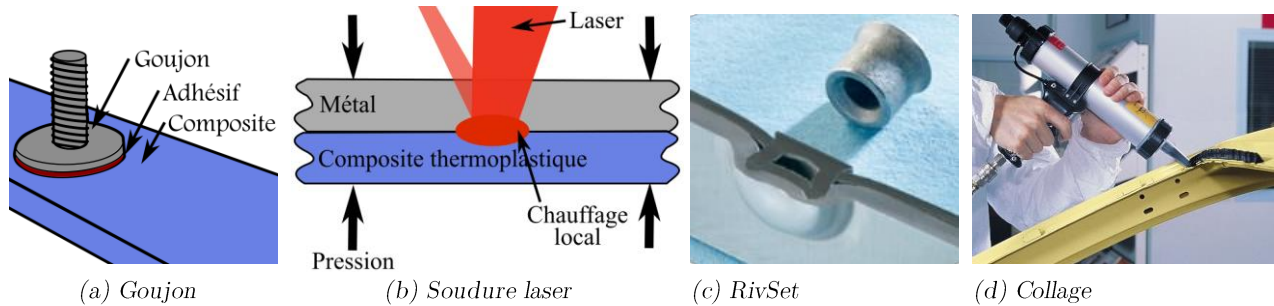


Figure 1 : Techniques d'assemblage présélectionnées.

Démarche expérimentale (Chapter II)

Le montage Arcan modifié a été sélectionné pour réaliser la majeure partie des essais. Seules les techniques d'assemblage par goujon et soudure laser ont été caractérisées avec des essais de « simple recouvrement » et de « traction sur éprouvette en croix ». Le choix d'utiliser majoritairement le montage Arcan est principalement fondé sur la possibilité de solliciter les éprouvettes avec différents ratios de traction-compression/cisaillement. En effet, la sollicitation appliquée par le montage Arcan est définie par l'angle γ entre la normale de la surface assemblée et l'axe de sollicitation de la machine d'essai. La Figure 2 montre le montage Arcan et les quatre configurations étudiées dans ce document : « traction » ($\gamma=0^\circ$), traction/cisaillement ($\gamma=45^\circ$), cisaillement ($\gamma=90^\circ$) et compression/cisaillement ($\gamma=135^\circ$). Par la suite, sur les courbes force-déplacement présentées, l'effort correspond à la valeur de la cellule de force de la machine d'essai utilisée. Le déplacement est lui obtenu grâce à un système de corrélation d'image 3D (GOM, 2011). Le déplacement est décomposé entre le déplacement relatif des substrats dans la direction tangentielle (TD) et celui dans la direction normale (ND) (cf. Figure 2-b). Le montage Arcan utilisé ayant initialement été développé pour l'étude des assemblages collés (Cognard *et al.*, 2005), de nouvelles géométries d'éprouvettes Arcan adaptées au RivSet ont dû être réalisées. La Figure 3 présente les trois types d'éprouvettes testées.

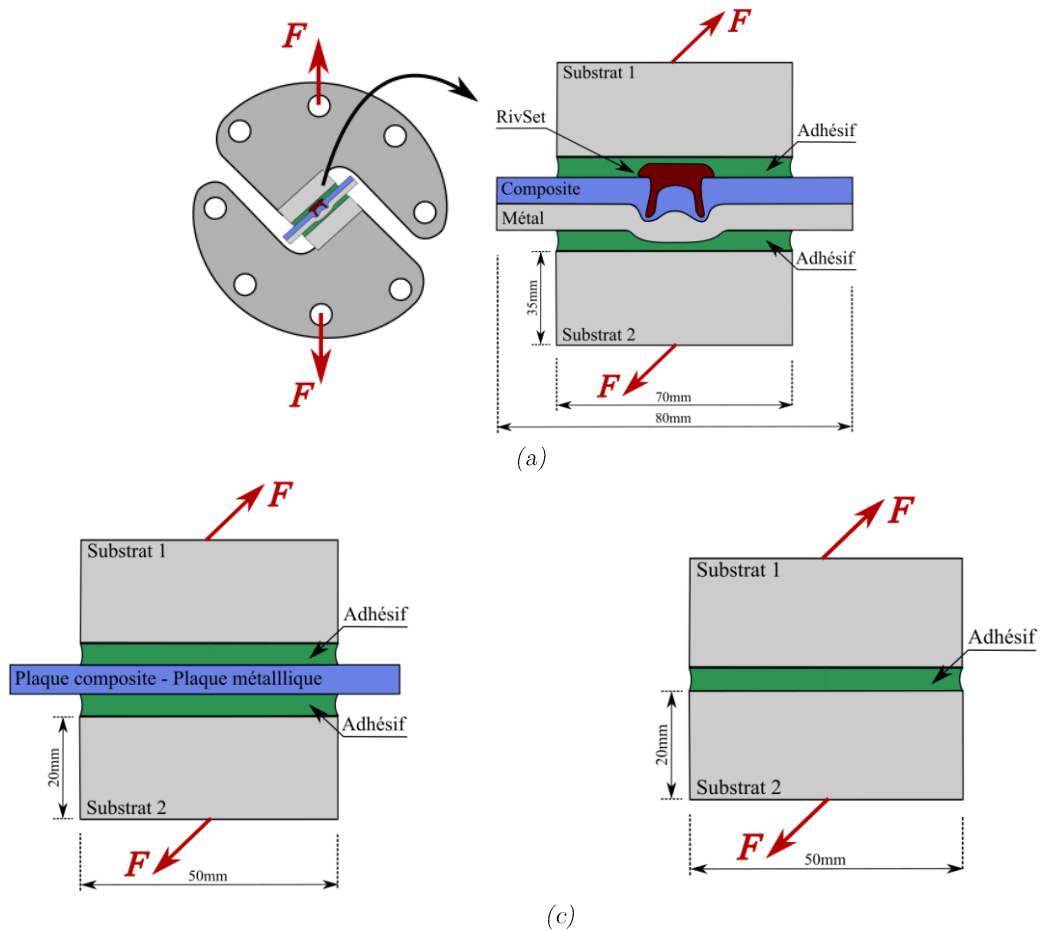
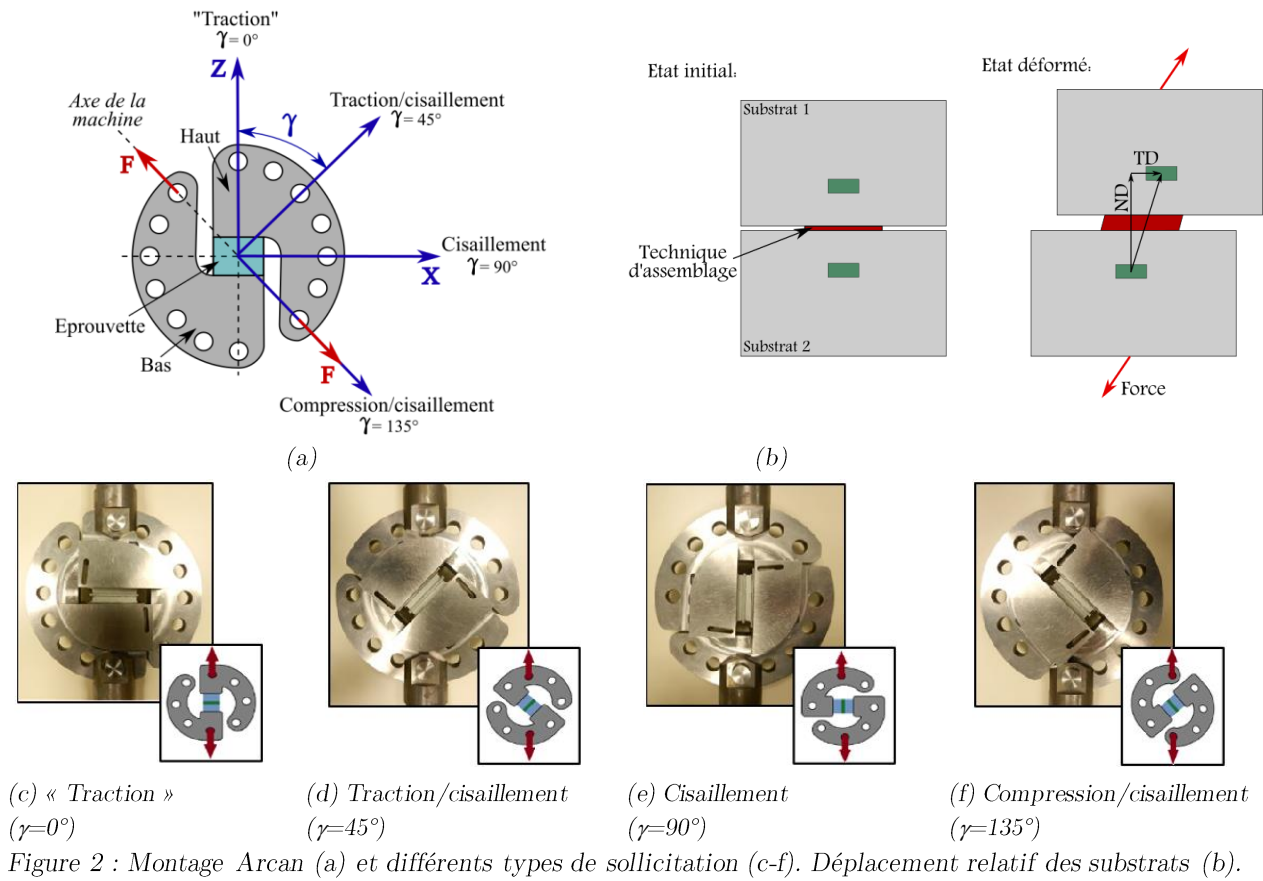


Figure 3 : Adaptation de l'éprouvette Arcan pour la caractérisation du RivSet (a), d'assemblages collés (b), ou de colles seules (c).

Caractérisation du comportement et de la résistance des techniques d'assemblage sélectionnées (Chapter III et Chapter IV)

La première campagne expérimentale réalisée a permis de déterminer la résistance mécanique des assemblages sous sollicitations monotones de type traction et cisaillement. Les Chapitres III et IV du manuscrit de thèse présentent plus en détail la campagne réalisée. Pour comparer les performances mécaniques des différentes techniques, l'indice de performance $I.P.$ a été défini comme

$$I.P. = \frac{F}{V * m}, \quad \text{Eq. 1}$$

avec,

- F = Force à rupture de l'assemblage ;
- V = Volume supplémentaire de la technique d'assemblage ;
- m = Masse supplémentaire de la technique d'assemblage.

Cet indice permet de comparer la performance mécanique tout en la relativisant par la masse et le volume additionnels induits par chaque technique utilisée. Cependant, il ne prend pas en compte les aspects économiques ni sa facilité de mise en œuvre (cf. Figures 4 et 5). De cette étude, le collage et la soudure laser ressortent comme les techniques d'assemblage les plus pertinentes du point de vue de la résistance mécanique. Cependant, le collage permet d'assembler une gamme plus large de couples matériaux.

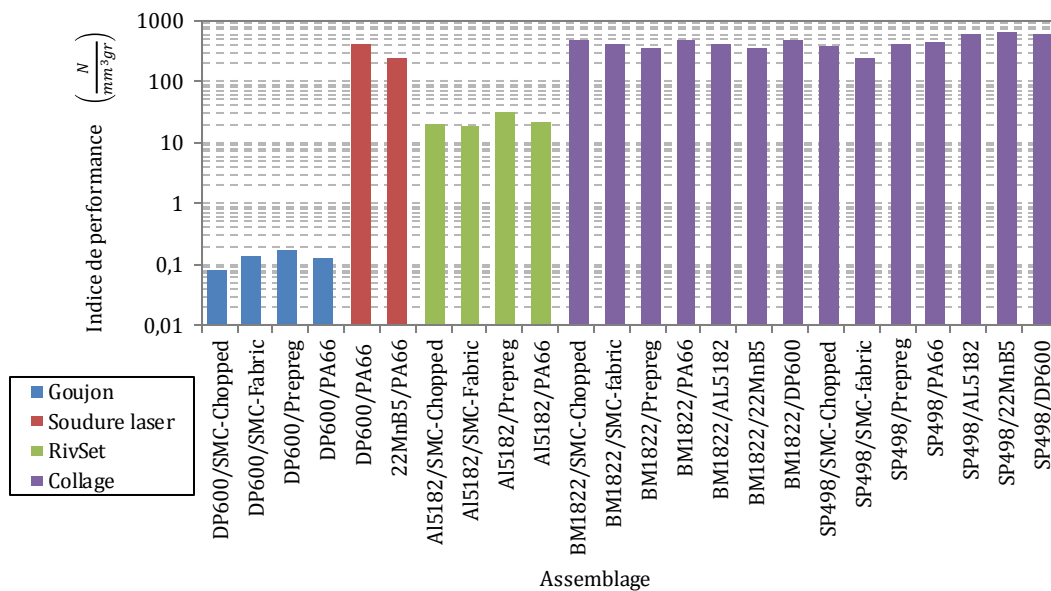


Figure 4 : Indice de performance des différents assemblages testés sous une charge de cisaillement.

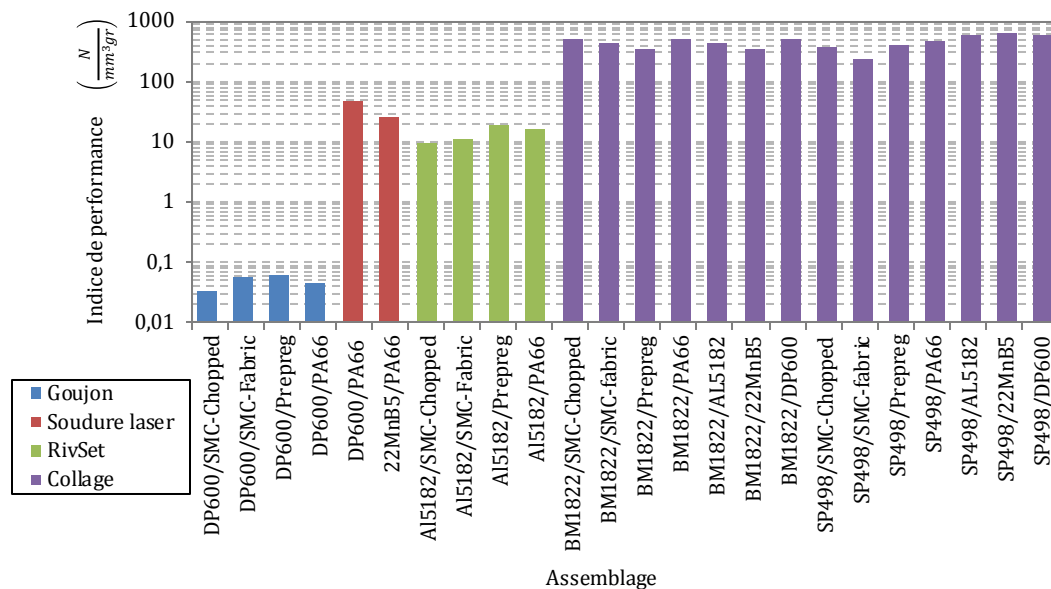


Figure 5 : Indice de performance des différents assemblages testés sous une charge de « traction ».

Afin de caractériser les propriétés des joints de colle, des résultats d'essais avec rupture cohésive de l'assemblage sont nécessaires. En effet, une rupture dite adhésive remet en cause la procédure de collage réalisée, et ne permet pas de juger la tenue mécanique du joint en lui-même. Une méthode d'assemblage par collage assurant des ruptures cohésives a donc été développée :

- (i) Préparation des substrats : Les surfaces de collage de chaque substrat sont poncées manuellement avec une taille de grain de 160 μm pour garantir une rugosité homogène. Ensuite, la surface est nettoyée à l'acétone. Finalement, les polluants et les résidus d'acétone sont évaporés par un courant d'air chaud.
- (ii) Pré-échauffement de la colle : Les cartouches de colles sont conservées sous vide à -18°C . Avant utilisation, la cartouche est portée à température ambiante afin de faciliter l'extraction de la quantité nécessaire aux éprouvettes. Le reste de la cartouche est stockée à nouveau tandis que la quantité prélevée est chauffée à 50°C dans le but de faciliter sa mise en œuvre sur les surfaces de collage.
- (iii) Collage de substrats : La colle est étalée le long des deux surfaces de collage grâce à une spatule. L'épaisseur de chaque joint de colle est de 0.2mm.
- (iv) Cycle de polymérisation : Le cycle de durcissement utilisé dans cette étude correspond à une montée jusqu'à 200°C en 25 minutes puis un maintien pendant 20 minutes. En plus d'être adapté à la chaîne de production automobile, ce cycle garantit une polymérisation complète des adhésives (selon les fiches techniques des produits).
- (v) Préparation finale de l'éprouvette : Une fois la colle polymérisée, un mouchetis est appliqué sur l'éprouvette afin de pouvoir utiliser la technique de corrélation d'images.

Malgré le suivi de cette procédure, des ruptures adhésives ont été observées dans le cadre des essais sur PA66. En conséquence, une étude sur l'influence de certains paramètres tels que l'orientation du tissage, l'état de la surface du composite et le taux d'humidité a été réalisée. Les résultats présentés sur la Figure 6, montrent peu d'influence de l'orientation du tissage tandis que l'état de la surface et l'humidité jouent un rôle très important.

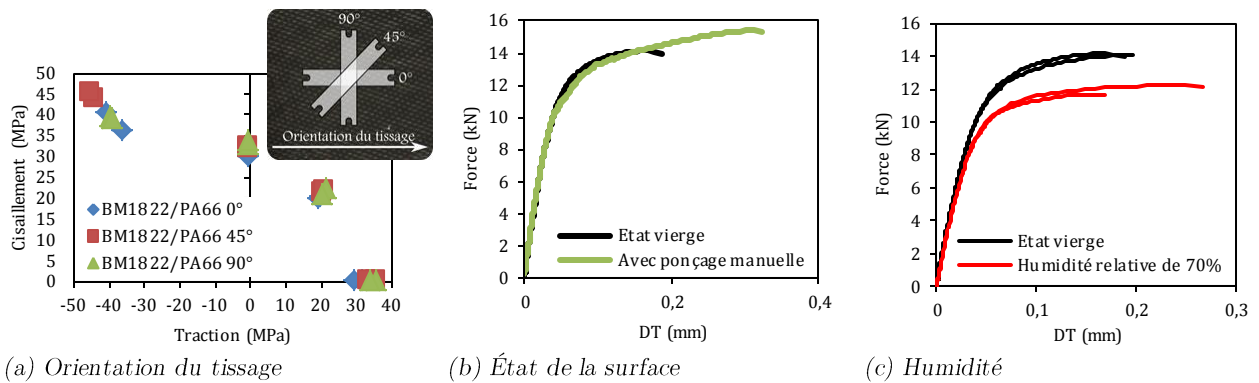


Figure 6 : Influence de certains paramètres sur le comportement des assemblages BM1822/PA66.

Caractérisation du comportement des colles (Chapter V):

Après avoir garanti un mode de rupture cohésif des assemblages, il a été décidé d'étudier le comportement des colles (présenté dans le Chapitre V du manuscrit). Trois types d'essais ont été sélectionnés pour caractériser le comportement mécanique des colles : (i) monotone à 0.2 kN/s et 2 kN/s, (ii) fluage multiple et (iii) traction incrémentale. Ces essais ont permis de mesurer le comportement fortement visqueux de deux colles (effets de vitesse et fluage) et de déterminer leurs propriétés à rupture.

Les enveloppes de rupture des adhésifs Betamate-1822 et Sikapower-498 à 0.2 kN/s sont tracées sur la Figure 7. La contrainte à rupture est définie comme la valeur de la force lors de la rupture divisée par la surface de collage ($S = 50 \times 9.5 \text{ mm}$).

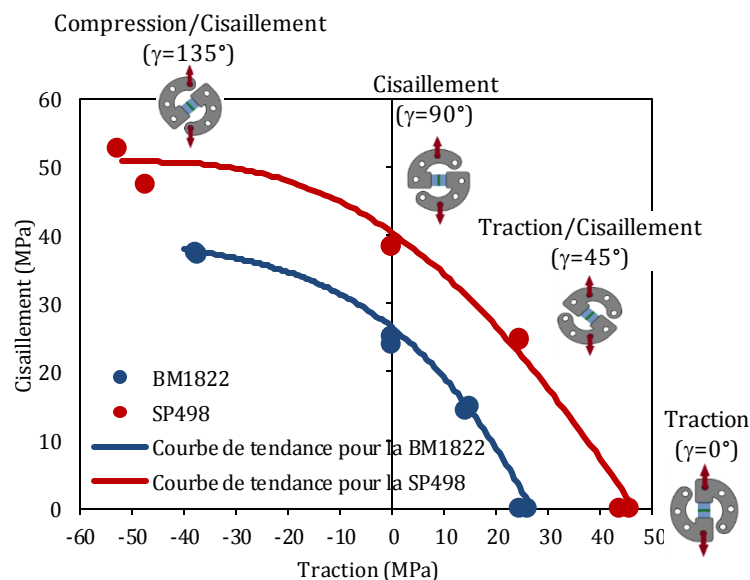
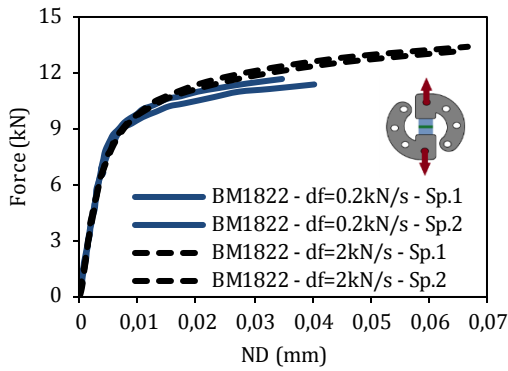
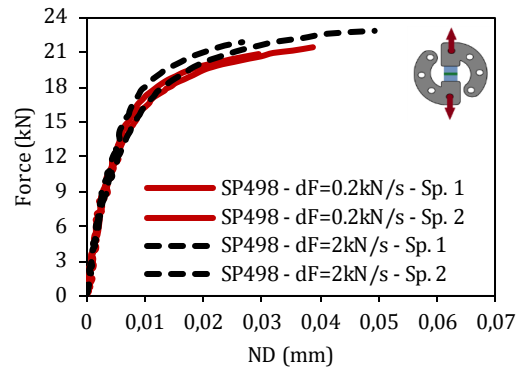


Figure 7 : Enveloppe de rupture des colles.

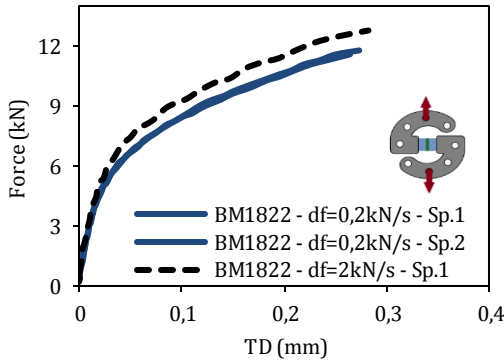
La Figure 8 présente les courbes force-déplacement des deux colles. Nous constatons que le comportement des adhésifs est sensiblement affecté par la vitesse de sollicitation. Une augmentation de la vitesse de sollicitation entraîne notamment une augmentation de la valeur de la force à rupture des deux adhésifs. Ces effets sont encore plus sensibles pour des sollicitations de cisaillement.



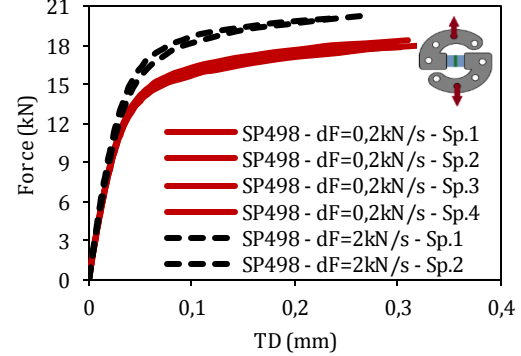
(a) Betamate-1822 en « traction »



(b) Sikapower-498 en « traction »



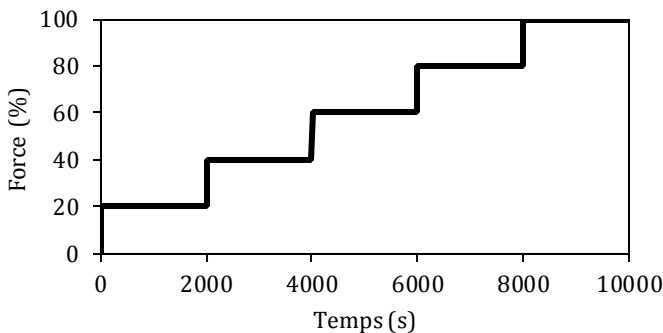
(c) Betamate-1822 en cisaillement



(d) Sikapower-498 en cisaillement

Figure 8 : Influence de la vitesse de sollicitation.

Des essais de fluage à paliers de chargement multiples ont été réalisés afin de caractériser le comportement visqueux des colles (cf. Figure 9). Trois rapports de charge ont été sélectionnés : « traction », traction/cisaillement et cisaillement. Chaque essai est composé de cinq paliers consécutifs de 2000 secondes à 20%, 40%, 60%, 80% et 100% de la force à rupture mesurée en chargement monotone. Comme visible sur la Figure 10, les deux colles présentent un comportement visqueux non-linéaire très important pour les trois types de sollicitations.



« Traction »

BM1822 : $F_{rupture}=12$ kN

SP498 : $F_{rupture}=21$ kN

Traction/cisaillement

BM1822 : $F_{rupture}=12$ kN

SP498 : $F_{rupture}=16$ kN

Cisaillement

BM1822 : $F_{rupture}=12$ kN

SP498 : $F_{rupture}=18$ kN

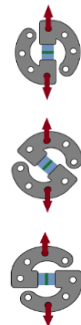


Figure 9 : Définition d'un essai de fluage multiple.

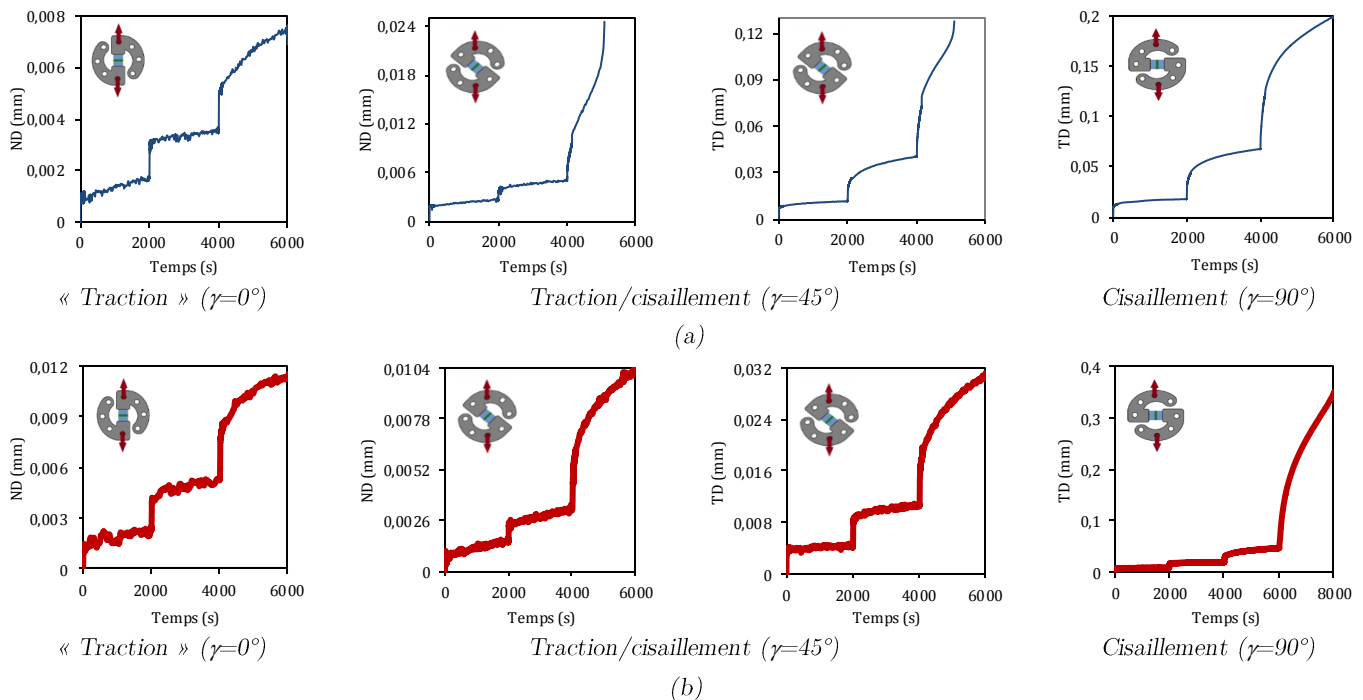


Figure 10 : Comportement en fluage des colles Betamate-1822 (a) et Sikapower-498 (b).

Modélisation du comportement des colles (Chapter VI):

La modélisation du comportement des colles est abordée dans le Chapitre VI du manuscrit. Le modèle proposé est défini comme

$$\underline{\sigma} = \underline{\underline{C}} : (\underline{\varepsilon} - \underline{\varepsilon}^{ve}), \quad \text{Eq. 2}$$

où $(\underline{\sigma})$ est le tenseur de contrainte, $(\underline{\underline{C}})$ le tenseur de rigidité élastique, $(\underline{\varepsilon})$ le tenseur de déformation totale, $(\underline{\varepsilon}^{ve})$ le tenseur de déformation viscoélastique. La déformation viscoélastique $(\underline{\varepsilon}^{ve})$ est considérée comme une somme de mécanismes viscoélastiques élémentaires $(\underline{\xi}_i)$ définies par,

$$\underline{\varepsilon}^{ve} = \sum_{i=1}^{n_t} \underline{\xi}_i \quad \text{avec,} \quad \underline{\xi}_i = \frac{1}{\tau_i} \left(\mu_i \underline{\underline{\sigma}}^R : \underline{\sigma} - \underline{\xi}_i \right). \quad \text{Eq. 3}$$

Les paramètres (τ_i) et (μ_i) représentent le temps de relaxation et le poids associé à chaque mécanisme. Une loi normale (*cf.* Figure 11) a été choisie afin de décrire la distribution de ces deux paramètres qui s'écrivent alors

$$\tau_i = \exp(n_i), \quad \mu_i = \frac{\mu_i}{\sum_{i=1}^{n_t} \mu_i}, \quad \text{Eq. 4}$$

avec,

$$\mu_i = \frac{1}{n_0 \sqrt{\pi}} \exp \left(- \left(\frac{n_i - n_c}{\sqrt{n_0}} \right)^2 \right).$$

Dans cette formulation, (n_c) correspond à la moyenne, $(n_0/\sqrt{2})$ est l'écart type, $(n_t = 20)$ est le nombre de mécanismes visqueux élémentaires utilisés pour décrire la viscosité. (n_i) est un entier qui varie entre deux limites : (n_1) et (n_2) . Ces limites ont été choisies pour éliminer les temps de relaxation trop rapides ou trop lents ($n_1 = -20$ et $n_2 = 30$).

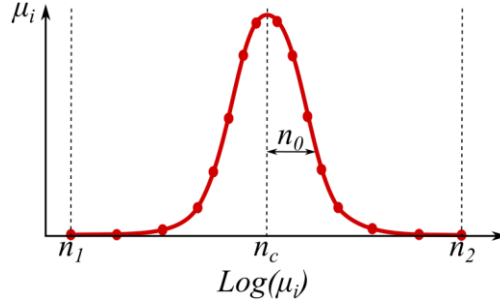


Figure 11 : Distribution normale du spectre de viscosité.

Afin de prendre en compte l'influence de la pression hydrostatique, le tenseur de souplesse ($\underline{\underline{S}}^R$) est divisé entre sa partie hydrostatique et sa partie déviatorique. Il s'écrit alors

$$\underline{\underline{S}}^R = \frac{1}{a(1-d^H)} \underline{\underline{P}}^H + \frac{1}{b(1-d^D)} \underline{\underline{P}}^D, \quad \text{Eq. 5}$$

avec,

$$\begin{aligned} \underline{\underline{P}}^H &= \underline{\underline{H}}^H = \frac{1}{3} \underline{\underline{I}} \otimes \underline{\underline{I}}, \\ \underline{\underline{P}}^D &= \underline{\underline{H}}^D = \underline{\underline{I}} - \underline{\underline{H}}^H, \end{aligned}$$

où (a) et (b) sont des paramètres matériaux à identifier. $(\underline{\underline{H}}^H)$ et $(\underline{\underline{H}}^D)$ correspondent respectivement aux projecteurs hydrostatique et déviatorique. La non-linéarité de la viscosité est décrite par deux variables d'assouplissement (d^H) et (d^D) . Ces variables suivent une évolution exponentielle telle que

$$\begin{aligned} d^H &= d_{max}^H \left(1 - e^{-\left(\frac{\langle Y - Y_0^H \rangle^+}{Y_c^H}\right)^{p^H}} \right) \\ d^D &= d_{max}^D \left(1 - e^{-\left(\frac{\langle Y - Y_0^D \rangle^+}{Y_c^D}\right)^{p^D}} \right), \end{aligned} \quad \text{Eq. 6}$$

où $(Y_0^H, Y_c^H, p^H, Y_0^D, Y_c^D, p^D)$ sont des paramètres du matériau à déterminer. Le cadre thermodynamique de la loi de comportement a été présenté dans les travaux de Schieffer (Schieffer, 2003). Il a été démontré que la construction d'un tel modèle permet de sortir du cadre standard pour définir la cinétique d'assouplissement tout en respectant les principes thermodynamiques. En effet, il a été montré que le second principe de la thermodynamique

est vérifié en s'assurant que ($\mathbf{d}^{H,D} \geq \mathbf{0}$) (Lévêque D. and Maire J.-F., Mavel A., Petipas C., Schieffer A., 2000). La force thermodynamique (Y) est ensuite définie par

$$Y = (\alpha(Y^H)^n + (Y^D)^n)^{1/n}, \quad \text{Eq. 7}$$

avec,

$$Y^H = \frac{1}{2a} (\underline{\underline{\sigma}} : \underline{\underline{H}}^H : \underline{\underline{\sigma}}),$$

$$Y^D = \frac{1}{2b} (\underline{\underline{\sigma}} : \underline{\underline{H}}^D : \underline{\underline{\sigma}}).$$

Finalement, la mixité des forces hydrostatique (Y^H) et déviatorique (Y^D) est régie par les paramètres (α) et (n). L'implémentation de la loi de comportement dans un code par éléments finis (Abaqus/standard) est faite grâce à une subroutine de type UMAT.

Identification de paramètres :

À cause de la distribution non-homogène des contraintes dans le joint de colle (Cognard *et al.*, 2008), il est nécessaire de réaliser une identification inverse pour revenir aux paramètres de la loi de comportement. Ce type de procédure demande l'utilisation d'un modèle par éléments finis afin de décrire la répartition des contraintes associées au chargement mécanique de l'éprouvette. Un modèle 3D, avec un seul élément dans la largeur de l'éprouvette (sous hypothèse de déformation plane), est utilisé pour décrire le comportement des éprouvettes Arcan. Ce modèle a été implémenté dans le logiciel Abaqus/standard (Dassault Systèmes, n.d.). La force machine est appliquée à un point de référence (RP), lié cinématiquement à la surface supérieure de l'éprouvette. Des conditions limites de symétries et d'antisymétries (Alfonso *et al.*, 2015) ont été implémentées. La Figure 12 montre le modèle par éléments finis et le maillage utilisés pour simuler le comportement des adhésifs.

Deux méthodologies ont été utilisées pour l'identification des paramètres :

- (i) Un balayage paramétrique : des simulations numériques sont réalisées en faisant varier la valeur de différents paramètres préalablement définis. À la fin de toutes les simulations, le choix du jeu de paramètres est réalisé comme étant celui minimisant la fonction erreur qui s'écrit

$$Error = \frac{1}{n} \sum_{i=1}^n \left(\frac{D^{exp} - D^{FE}}{D^{exp}} \right)_i^2, \quad \text{Eq. 8}$$

avec (n) le nombre de points expérimentaux, (D^{exp}) et (D^{FE}) les déplacements expérimentaux et numériques des essais de fluage multiple.

- (i) Une méthode d'optimisation : la recherche du bon jeu de paramètres est réalisée grâce à la fonction « *fminsearch* » de Matlab, cette fonction utilise la méthode de Nelder-Mead afin de minimiser l'erreur jusqu'à qu'elle soit inférieure à la tolérance. La recherche est terminée lorsque l'erreur atteint une tolérance.

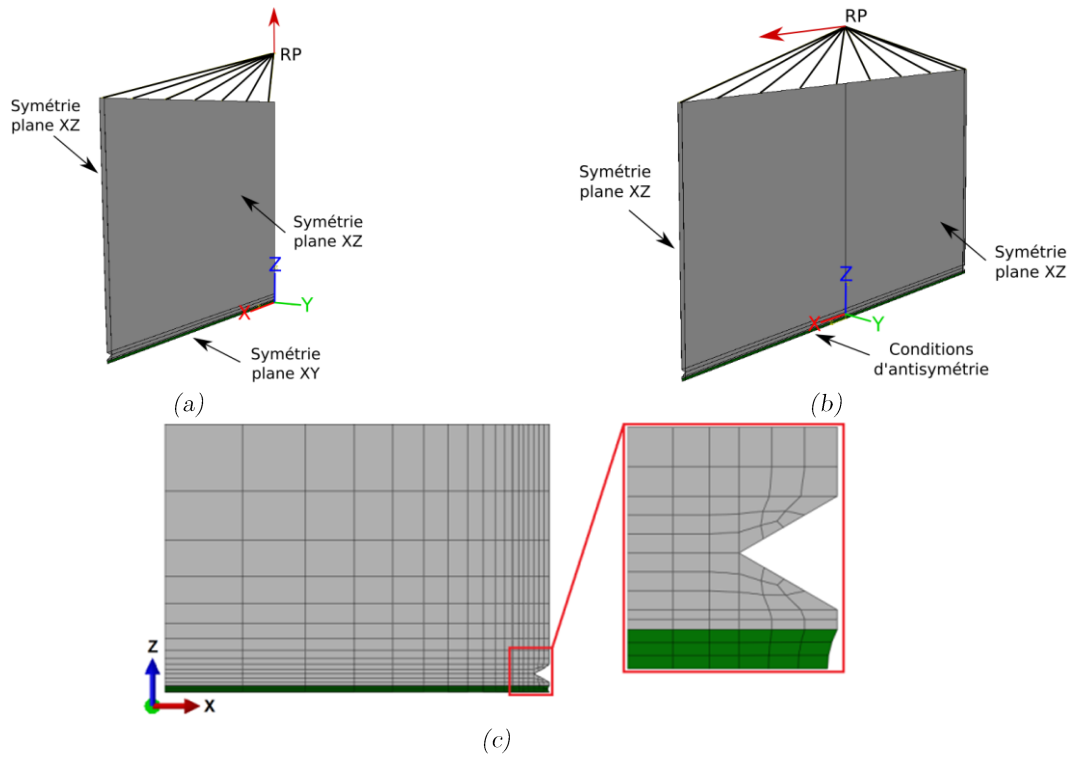


Figure 12 : Modèle 3D par éléments finis pour la simulation des sollicitations en traction (a), traction/cisaillement et cisaillement (b). Maillage du modèle par éléments finis pour la modélisation des sollicitations en « traction » (c).

Une procédure séquentielle est implémentée afin de déterminer les jeux de paramètres pour chacune des colles. Cette procédure est basée sur les essais de fluage multiple en traction, traction/cisaillement et cisaillement :

- 1) Paramètres élastiques (E, ν) : La rigidité expérimentale en « traction » et en cisaillement est déterminée grâce à la montée du premier palier des essais de fluage en « traction » et en cisaillement. Les paramètres élastiques ont été déterminés grâce à une comparaison entre les simulations numériques et la rigidité expérimentale. En effet, des simulations ont été réalisées en balayant le module de Young (E) entre 10 et 10000 MPa, et le coefficient de Poisson (ν) entre 0.2 et 0.49. Le couple (E, ν) permettant de retrouver en même temps une rigidité numérique à l'intérieur de l'intervalle de confiance de la rigidité expérimentale en « traction » et en cisaillement est retenu comme la valeur des paramètres élastiques.
- 2) Paramètres visqueux (n_0, n_c) : Les déplacements de chaque palier des essais de fluage multiple en traction, traction/cisaillement et cisaillement sont normalisés. Les déplacements des paliers normalisés sont ensuite comparés à des simulations numériques pour une liste de couples (n_0, n_c) variant entre 1 et 20.

- 3) Viscosité linéaire (\mathbf{a}, \mathbf{b}) : Les paramètres (\mathbf{a}) et (\mathbf{b}) sont identifiés sur le premier palier des essais de fluage respectivement en « traction » et en cisaillement. Le paramètre (\mathbf{b}) est identifié en premier sur les essais de cisaillement, puis le paramètre (\mathbf{a}) sur les essais de « traction », car la contrainte déviatorique n'est pas négligeable dans les essais de « traction ».
- 4) Seuil de viscosité linéaire (Y_0^H, Y_0^D) : Les paramètres (Y_0^H) et (Y_0^D) représentent le seuil de viscosité linéaire respectivement en « traction » et en cisaillement. Ces seuils correspondent à la valeur de la force thermodynamique (Y) lorsque la courbe numérique, obtenue sous hypothèse de viscosité linéaire, s'éloigne de la courbe expérimentale.
- 5) Évolution non-linéaire de la viscosité ($Y_c^H, \mathbf{p}^H, Y_c^D, \mathbf{p}^D$) : L'évolution non-linéaire de la viscosité est décrite par les variables d'assouplissement (\mathbf{d}^H) pour la partie hydrostatique et (\mathbf{d}^D) pour la partie déviatorique. Ces variables présentent une allure exponentielle définie par les paramètres (Y_c^H, \mathbf{p}^H) pour (\mathbf{d}^H) et (Y_c^D, \mathbf{p}^D) pour (\mathbf{d}^D). La procédure d'identification est basée sur les essais de fluage multiple respectivement en « traction » et en cisaillement. Comme pour les cas précédents, il est nécessaire de déterminer les paramètres en cisaillement (Y_c^D, \mathbf{p}^D), pour ensuite étudier le comportement en « traction » (Y_c^H, \mathbf{p}^H).
- 6) Mixité des modes (α, \mathbf{n}) : Les paramètres (α, \mathbf{n}) permettent de décrire le comportement des colles dans un chargement mixte traction/cisaillement. Ainsi, une optimisation sur les essais de fluage en « traction » et traction/cisaillement a été réalisée afin de déterminer ce jeu de paramètres.

La Figure 13 compare les simulations numériques avec les jeux de paramètres identifiés selon les résultats expérimentaux. Les valeurs des paramètres sont présentées dans le Tableau 1.

Paramètres	Phénomène associé	BM1822	SP498	Unité
E	Élasticité	1020	2300	MPa
ν		0.44	0.43	-
\mathbf{n}_0	Spectre visqueux	6	5	-
\mathbf{n}_c		9	11	-
\mathbf{a}	Viscosité linéaire	3500	1300	MPa
\mathbf{b}		170	900	MPa
Y_0^H	Seuil de non-linéarité	0.1797	0	MPa
Y_0^D		0.2	0	MPa
Y_c^H	Viscosité non-linéaire dans l'espace hydrostatique	0.021	0.4292	MPa
\mathbf{p}^H		0.41	1.5448	-
Y_c^D	Viscosité non-linéaire dans l'espace déviatorique	0.517	0.4292	MPa
\mathbf{p}^D		0.619	1.5448	-
α	Mixité des modes	1.33	0.5	-
\mathbf{n}		0.629	0.41	-

Tableau 1: Paramètres de la loi de comportement et leurs phénomènes associés.

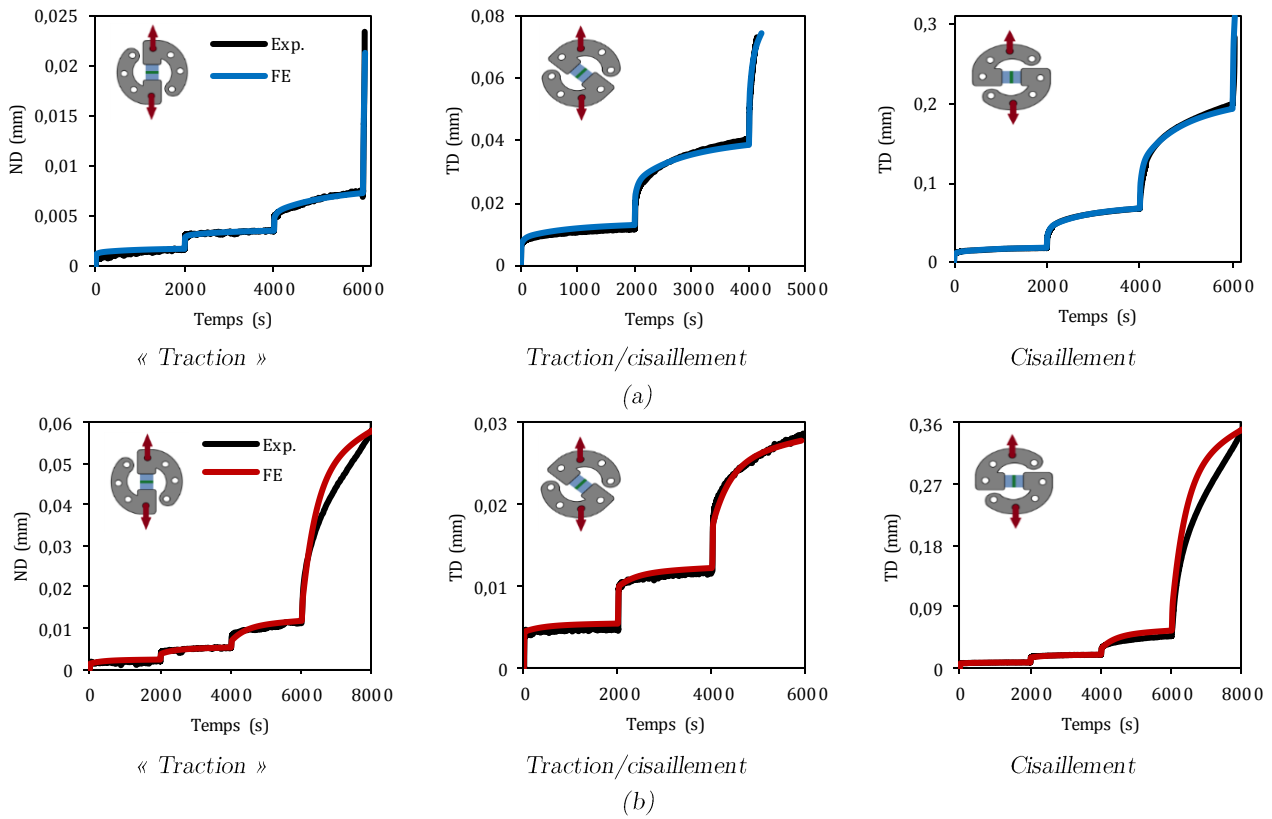


Figure 13 : Comparaison entre les simulations numériques (FE) et les courbes des essais de fluage multiple (Exp.) utilisées pour l'identification des paramètres des colles Betamate-1822 (a) et Sikapower-498 (b).

Afin de valider la loi de comportement, des simulations par éléments finis (FE) ont été réalisées sur différents types de chargement : essais Arcan monotones à différentes vitesses et essais Arcan de traction incrémentale (cf. Figure 14). Les Figures 15 et 16 montrent une bonne corrélation entre les prédictions numériques et les résultats expérimentaux des deux colles.

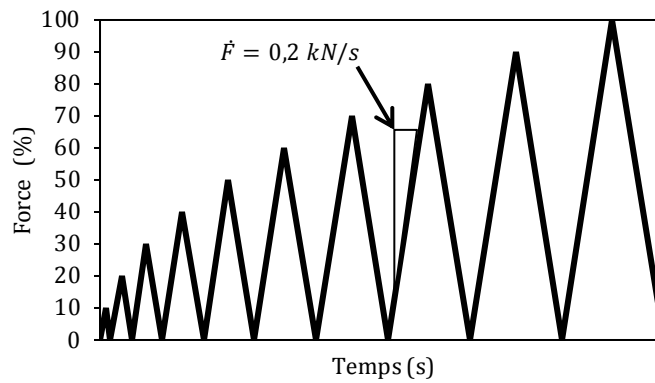


Figure 14 : Essai de traction incrémentale.

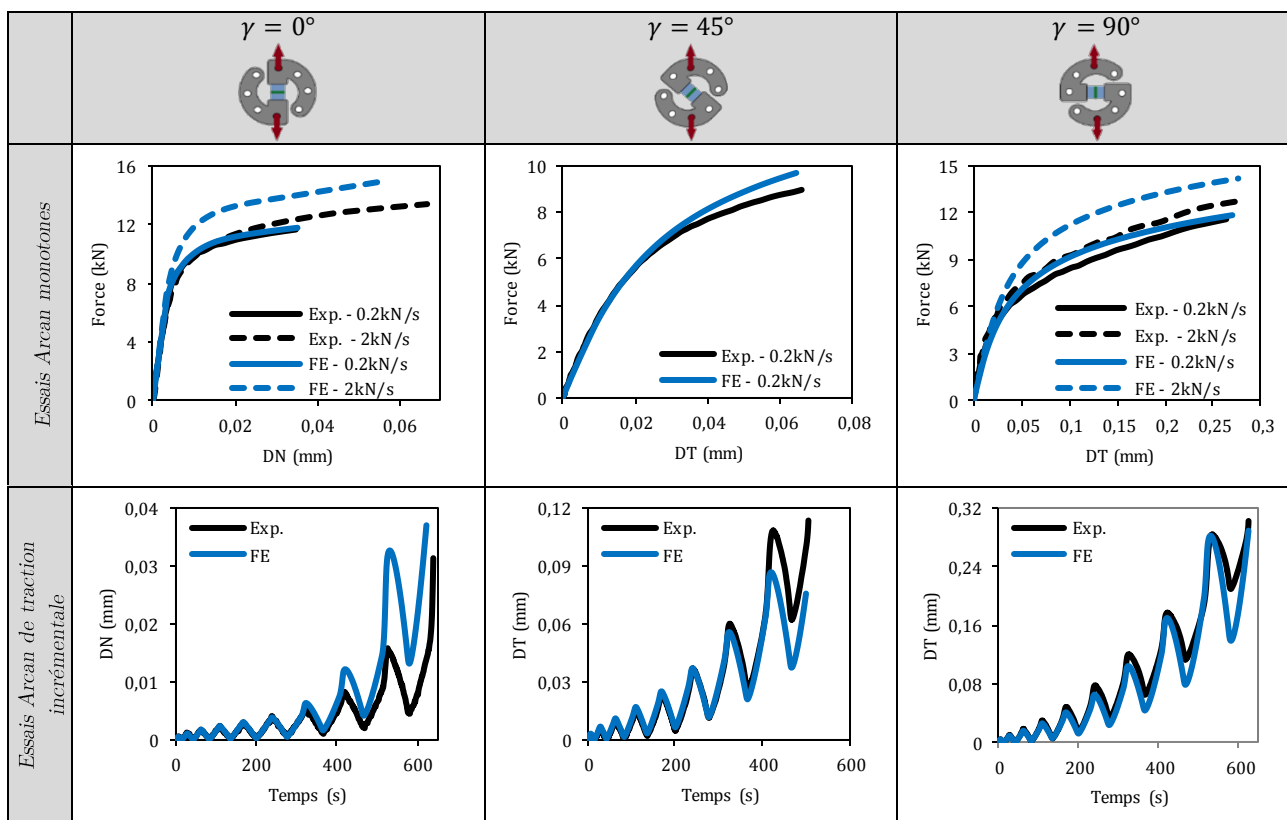


Figure 15 : Prédiction du modèle implémenté pour la colle Betamate-1822.

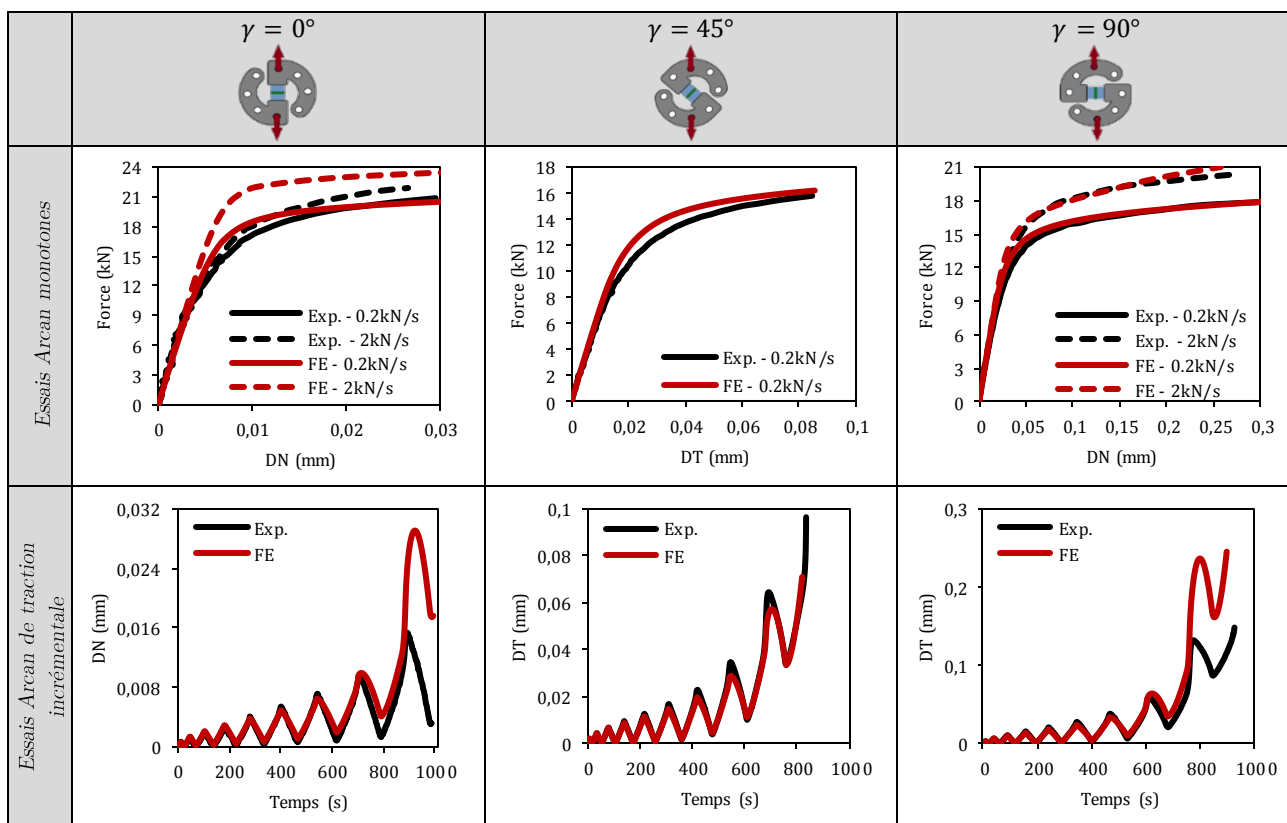


Figure 16 : Prédiction du modèle implémenté pour la colle Sikapower-498.

Des comparaisons avec des essais de simple recouvrement et Bulk ont également été réalisées. En ce qui concerne les essais Bulk, il est possible de constater une bonne prévision du comportement des adhésifs pour une vitesse de sollicitation de 1 mm/min (cf. Figure 17).

La comparaison des prévisions numériques entre les essais de simple recouvrement montre que ce type d'essai ne permet pas de valider la loi de comportement de l'adhésif, car la réponse macroscopique (déplacement relatif des substrats) est fortement influencée par la déformation des substrats. En effet, comme indiqué dans la Figure 18, les réponses obtenues en utilisant une loi linéaire élastique ou selon la loi de comportement développée sont similaires. Le comportement visqueux de l'adhésif n'a donc que peu d'influence sur la réponse macroscopique observée. Cependant, cette influence reste importante sur la distribution de contraintes dans le joint de colle (cf. Figure 18-b).

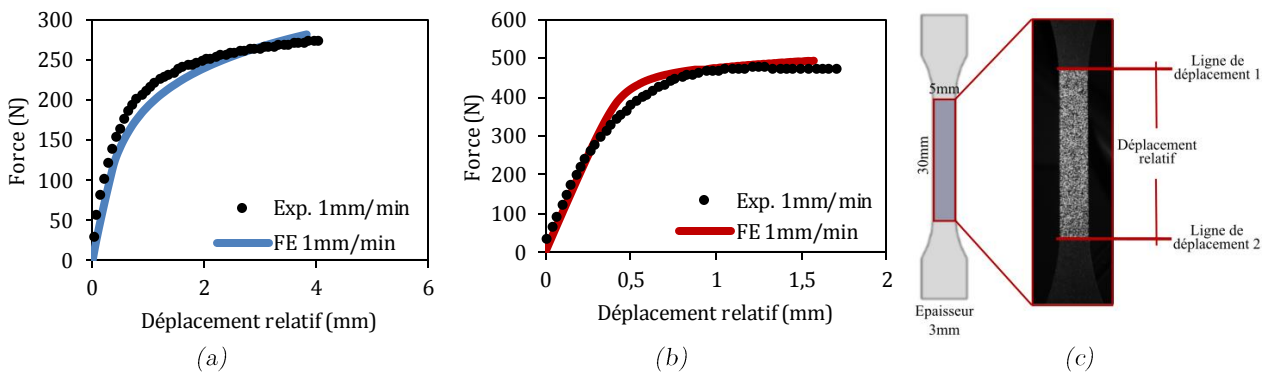


Figure 17 : Comparaison des courbes numériques et expérimentales, pour des essais Bulk, des colles Betamate-1822 (a) et Sikapower-498 (b). Éprouvette Bulk (c)

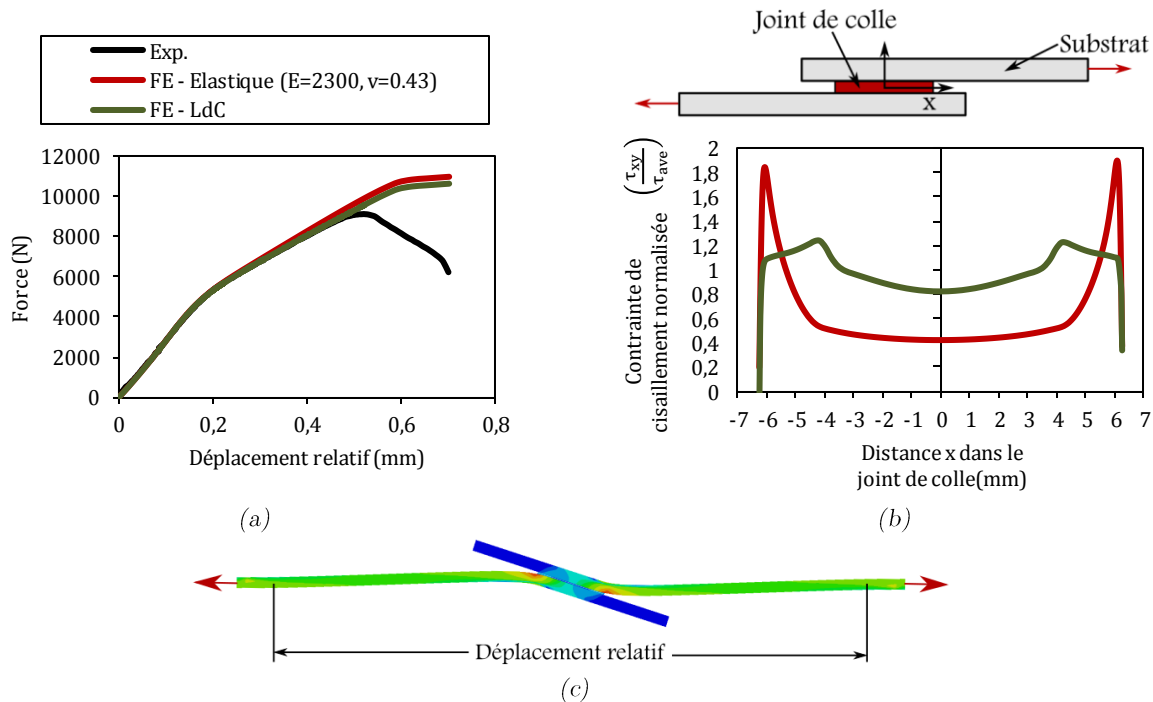


Figure 18 : Comparaison entre les courbes expérimentales et numériques avec différentes lois de comportement de la colle Sikapower-498 (a). Allure de la déformation d'un essai de simple recouvrement (b).

Conclusions et perspectives (Chapter VII)

Des campagnes expérimentales réalisées grâce au montage Arcan modifié ont permis de valider cette méthode expérimentale pour la caractérisation de différentes techniques d'assemblage sous sollicitations combinées de traction/cisaillement ou compression/cisaillement. Les techniques d'assemblage par RivSet et collage ont été caractérisées par cette méthode.

D'autre part, le comportement des colles a été décrit par un modèle viscoélastique spectral non-linéaire qui a été identifié grâce à des essais de fluage en « traction », traction/cisaillement et cisaillement. Les simulations numériques prévoient de manière correcte le comportement des colles dans différents cas de chargement.

Finalement, il sera important d'analyser d'autres aspects qui n'ont pas été traités dans cette étude. L'étape suivante pourra être la caractérisation et la modélisation des assemblages hybrides RivSet/collage. Le montage Arcan pourrait permettre d'atteindre cet objectif. En effet, cela permet l'identification rapide du comportement de ce type d'assemblage.

Enfin, il sera également nécessaire d'étudier l'évolution du comportement de l'adhésif en fonction de paramètres tels que la température, le vieillissement après polymérisation, l'humidité et la fatigue.

Characterization and modeling of multi-material assemblies under mixed quasi-static loadings for the design of automotive structures





Table of contents

Nomenclature	5
Abbreviations	7
Introduction	9
PART A: Context and methodology	11
Chapter I. Context	13
I.1. The automotive industry	15
I.2. The environmental problematic.....	15
I.3. The need for new materials and the lunch of the FASLITE project	17
I.4. Objectives of the current Ph.D. thesis.....	18
I.5. Materials of the study	18
I.5.1. Composite materials	18
I.5.1.1. Vinylester chopped glass fiber SMC	18
I.5.1.2. NCF vinylester glass fiber SMC.....	19
I.5.1.3. Epoxy carbon fiber prepreg	19
I.5.1.4. PA66 glass fiber consolidated.....	19
I.5.2. Metallic materials.....	19
I.5.2.1. 5182 Aluminum	19
I.5.2.2. 22MnB5 Steel.....	19
I.5.2.1. DP600 Steel	20
I.6. Background information on joining techniques of dissimilar materials	21
I.7. The selected joining techniques.....	23
I.7.1. Stud bonding.....	23
I.7.2. Laser welding.....	25
I.7.3. Self-pierce riveting (RivSet).....	25

I.7.4. Adhesive bonding.....	26
I.7.4.1. The selected adhesives.....	27
I.7.4.1.1. Betamate-1822.....	27
I.7.4.1.2. Sikapower-498.....	28
I.7.4.1. Curing cycle.....	28
I.7.4.1. Types of failure	29
I.8. Set of tested assemblies.....	30

Chapter II. Characterization test and methodology 33

II.1. Choice of the test.....	35
II.1.1. Summary of tests to characterize the strength of assemblies.....	35
II.1.1.1. Single lap joint test	35
II.1.1.2. Cross-tension test	35
II.1.1.3. Arcan test.....	35
II.1.2. Summary of tests to characterize the behavior of adhesives.....	36
II.1.2.1. Bulk tests	36
II.1.2.2. Bonded tests.....	37
II.1.2.2.1. Lap-shear test.....	38
II.1.2.2.2. Thick adherend shear test (TAST)	38
II.1.2.2.3. Butt joint test (tension-compression/torsion)	38
II.1.3. The Modified Arcan approach.....	39
II.1.3.1. The Arcan specimen.....	40
II.1.3.2. The bonding system	42
II.1.3.3. Post-processing	43
II.1.4. The selected characterization tests	44
II.2. Sequential solution methodology	44

PART B: Activities performed in this study 47

Chapter III. Characterization of stud bonded, laser welded and self-pierce riveted assemblies 49

III.1. Experimental campaign.....	51
III.1.1. Stud bonding and laser welding in a lap-shear test	52
III.1.2. Stud bonding and laser welding in a cross-tension test.....	54
III.1.3. RivSet assemblies in an Arcan test	57
III.2. Overview.....	64

Chapter IV. Characterization of adhesively bonded assemblies	65
IV.1. Experimental campaign.....	67
IV.1.1. Set-up.....	67
IV.1.2. Tested assemblies.....	67
IV.1.3. Specimen preparation	69
IV.2. Experimental results.....	71
IV.2.1. Composite assemblies.....	71
IV.2.1.1. Influence of the fabric orientation on the strength of bonded composite assemblies	73
IV.2.1.2. Influence of the surface state of the composite.....	74
IV.2.1.3. Influence of the humidity.	75
IV.2.2. Metal assemblies.....	76
IV.2.2.1. Influence of grease	77
IV.3. Adhesive bonding as the selected structural joining technique	79
IV.4. Overview	82
Chapter V. Characterization of adhesives in an assembly	83
V.1. Experimental campaign based on the modified Arcan device	85
V.1.1. Specimen preparation.....	85
V.2. Behavior of adhesives under monotonic loadings and the influence of the loading rate.....	86
V.2.1. “Tensile” loadings ($\gamma=0^\circ$).....	86
V.2.2. Shear loadings ($\gamma=90^\circ$).....	87
V.2.3. Mixed proportional loadings ($\gamma=45^\circ$ and $\gamma=135^\circ$)	88
V.2.4. Failure envelopes	89
V.2.5. Looking through the fracture mode	90
V.2.6. Influence of the loading rate.....	92
V.3. Multilevel creep tests and the non-linear evolution of the viscosity.....	94
V.3.1. Non-linear viscosity	98
V.4. Increasing cyclic test: toward the cyclic behavior	100
V.5. Overview	102
Chapter VI. Modeling of the behavior of adhesives	105
VI.1. Brief summary of the modeling of the adhesive behavior	107
VI.1.1. The Generalized Kelvin Model and the relaxation spectrum of viscosity	108
VI.1.1.1. Generalized Kelvin Model.....	109
VI.1.1.1. Relaxation spectrum	111

VI.2. The proposed behavior law	112
VI.3. Inverse identification methodology	115
VI.3.1. Modeling the Arcan test.....	118
VI.4. Parameters identification procedure	121
VI.4.1. Elastic parameters (E, ν)	122
VI.4.1.1. Calculating the experimental Arcan stiffness	122
VI.4.1.1. Determining the numerical elastic parameters	125
VI.4.2. Viscous spectrum (n_o, n_c).....	126
VI.4.3. Linear viscosity (a, b)	130
VI.4.4. Non-linear viscous parameters ($Y_o^H, Y_c^H, p^H, Y_o^D, Y_c^D, p^D$)	132
VI.4.5. Mixed mode (α, n).....	135
VI.4.6. Identified material parameters.....	137
VI.5. Validation of the behavior law	138
VI.5.1. Validation using Arcan tests.....	138
VI.5.2. Comparison with Bulk test	140
VI.5.3. Comparison with Lap-shear test.....	141
VI.6. Discussions and limitations of the model	143
VI.7. Overview.....	145

Chapter VII. Conclusions and prospects 147

VII.1. General conclusions.....	148
The Arcan device as an adapted tool for the characterization of joining techniques under mixed loadings	148
Characterization of adhesively bonded assemblies	148
Modeling the behavior of adhesives	149
Is it really necessary to model the behavior of the adhesive?	150
VII.2. Prospects.....	151
VII.2.1. Evolution of the adhesive behavior	151
VII.2.1.1. Aging of the component of the adhesive cartridge	151
VII.2.1.2. Aging of the adhesive after polymerization	152
VII.2.1.3. Influence of temperature	153
VII.2.2. Cyclic behavior	155
VII.2.3. Hybrid RivSet/adhesive joints	156
VII.2.4. “Cohesive” failures	157
VII.2.5. Some other parameters that should be taken into account	158

References 161

Nomenclature

Symbol	Explanation
γ	Angle between the axis of the tensile machine and the normal plane of the specimen in an Arcan test
Sp.	Specimen
F_{Load}	Failure load
S	Bonded surface
df ou \dot{F}	Loading rate
G_{IC}	Fracture toughness mode I
G_{IIC}	Fracture toughness mode II
$\underline{\underline{\sigma}}$	Stress tensor
$\underline{\underline{C}}$	Fourth-order elastic tensor
$\underline{\underline{S}}^R$	Fourth-order compliance tensor
$\underline{\underline{\epsilon}}$ and $\underline{\underline{\epsilon}}^{ve}$	Total strain tensor and the viscoelastic strain tensor
τ_i and μ_i	Relaxation time and weight
$\underline{\underline{H}}^H$	Hydrostatic direction tensor
$\underline{\underline{H}}^D$	Deviatoric direction tensor
D^{exp}	Experimental displacement
D^{FE}	Finite element displacement



Abbreviations

Abbreviation	Explanation
FEM	Finite element method
TAST	Thick adherent shear test
DMA	Dynamic mechanical analysis
UMAT	User material subroutine in Abaqus standard
NCF	Non-crimp fabric composite
PA66	Polyhexaméthylène adipamide
DIC	Digital Image Correlation method
ND	Normal displacement along the Z-axis in an Arcan specimen
TD	Tangential displacement along the X-axis in an Arcan specimen
BM1822	Betamate-1822 adhesive
SP498	Sikapower-498 adhesive
RH	Relative humidity
EEA	European Environment Agency
ADEME	French Environment and Energy Management Agency
CETIM	Technical Centre for Mechanical Industries
IRDL	Dupuy de Lôme Research Institute



Introduction

In order to respond to global warming and reduce the levels of air pollution caused by the use of the automobile, new regulations have been taken by governments around the world. In the European Union, these environmental laws impose that all new cars emit a maximum of 95 grams of CO₂ per kilometer by 2021, corresponding to an average consumption of 4.1 L/100km for petrol and 3.6 L/100km for diesel cars. A key point to achieve this target is the reduction of the car weight by using lighter materials such as aluminum and composite materials. However, these materials are not compatible with the classical joining techniques used by the automotive industry. Therefore, the research and modeling of joining techniques of dissimilar materials is a problem that must be solved in the next years.

For that purpose, the French automotive manufacturers (Renault and PSA-Group) and some other partners of the automotive industry have formed the FASTLITE project with the financial support of the French Environment and Energy Management Agency (ADEME). The goal of this project was the emergence of joining techniques of dissimilar materials at a competitive cost and adapted to industry requirements. Seven materials were preselected to form the assemblies: one aluminum alloy, two steels, and four composites with different morphologies (thermoplastic or thermosetting resin, glass or carbon fiber). Similarly, four joining techniques were selected in an exploratory phase as the most promising joining techniques: stud bonding, laser welding, self-pierce riveting and adhesive bonding (two crashes adhesives were selected: Betamate-1822 and Sikapower-498). The present Ph.D. study took then place in this project in order to collaborate with French industry. Two principal objectives were then fixed:

- Characterization of joining techniques of dissimilar materials under quasi-static mixed tensile-compression/shear loadings.
- Modeling of the most adapted joining technique in order to reduce the design time in automotive structures.

The Ph.D. study presented in this document is divided into seven chapters grouped together in two principal parts. Part A is composed of the first two chapters and is devoted to the presentation of the context, the automotive industry requirements, the materials of the study, the selected joining techniques, the characterization tests and the proposition of a solution methodology. Then, part B presents the activities performed for three years of the study.

Chapter III and Chapter IV present the experimental campaign performed in order to characterize the behavior of the selected joining techniques under quasi-static mixed loadings. Because of their high mechanical performance and great adaptability, adhesive bonding systems were selected as the structural joining technique. Therefore, the characterization of the adhesives of the study was an important aspect that was investigated in Chapter V. Thanks to the experimental data obtained by means of the modified Arcan device, a 3D spectral viscoelastic model was proposed in Chapter VI in order to describe the behavior of adhesives in an assembly. In this chapter, the behavior law and the identification procedure based on the multilevel creep test were presented. Similarly, a comparison with other types of test was performed in order to validate the proposed model.

The conclusions and prospects of the current work are presented in Chapter VII. A global review of the main conclusions is presented at the beginning of the chapter. Then some particular aspects that should be considered in future works are studied in the prospect section. The influence of temperature and aging on the behavior of adhesives and the behavior of hybrid rivet-bonded joints were briefly explored.

PART A: Context and methodology



Chapter I. Context

Introduction

This first chapter aims to give an introduction to the bases and the objectives of the study. The automotive industry, the environment problematic and the need to use composite materials and aluminum alloys on the body-shape of cars are exposed. An overview of the different joining techniques used to join dissimilar materials is also presented. Finally, the materials studied and the preselected joining techniques are presented at the end of the chapter.

Table of contents

I.1. The automotive industry	15
I.2. The environmental problematic	15
I.3. The need for new materials and the lunch of the FASLITE project	17
I.4. Objectives of the current Ph.D. thesis.....	18
I.5. Materials of the study	18
I.5.1. Composite materials	18
I.5.1.1. Vinylester chopped glass fiber SMC	18
I.5.1.2. NCF vinylester glass fiber SMC	19
I.5.1.3. Epoxy carbon fiber prepreg.....	19
I.5.1.4. PA66 glass fiber consolidated	19
I.5.2. Metallic materials	19
I.5.2.1. 5182 Aluminum	19
I.5.2.2. 22MnB5 Steel	19
I.5.2.1. DP600 Steel	20
I.6. Background information on joining techniques of dissimilar materials	21
I.7. The selected joining techniques.....	23
I.7.1. Stud bonding.....	23
I.7.2. Laser welding	25
I.7.3. Self-pierce riveting (RivSet).....	25
I.7.4. Adhesive bonding.....	26
I.7.4.1. The selected adhesives	27
I.7.4.1.1. Betamate-1822.....	27
I.7.4.1.2. Sikapower-498.....	28
I.7.4.1. Curing cycle.....	28
I.7.4.1. Types of failure	29

I.1. The automotive industry

There have been many changes since the first steam-powered automobile was built in 1768 by Nicolas-Joseph Cugnot; the type of propulsion, the number of wheels and the aspect are just a few examples of them. Nowadays, a large number of shapes can be found: sedan, convertible, hatchback, Sport Utility Vehicle, etc. These changes have consolidated a great industry with a market size of 620 billion euros in 2015 and about thirty manufacturers all around the world producing more than 65 million new passenger cars by year.

In order to remain competitive, manufacturers must offer attractive characteristics at affordable prices. Assembly lines have been then merged as the most popular production system in order to produce cars with high-speed production rates at significantly reduced costs. In the automotive production chain, the body-in-white which is basically a welded metal structure with the shape of the car, moves through different workstations. In each of these workstations, the parts are added in sequence until the final state of the car. It is worth noting that this process is usually semi or fully automated. The grade of coordination between pieces, tools, men and robots ensures an efficient assembly process without loss of time, energy or money.

New car models offer a wide range of possibilities over four principal items: comfort and luxe, security, connectivity and cost. A good balance between them ensures a large number of sales. However, as well as many other industries, automobiles are now in a time of change, and the objectives have changed dramatically over the last years. Good features can no longer be the only aspect of the car design, and the environmental impact must also be taken into account in the car conception.

I.2. The environmental problematic

Fossil fuels have permitted the human race to develop an industrialized society with advanced technologies in all fields. However, the continuous abuse of these resources in recent decades has contributed to a dramatic increase in air pollution, thereby increasing the risk of lasting health problems and accelerating global warming (See Figure I.1). These problems had been neglected by political leaders, but the social pressure in the last two decades has led governments around the world to implement a set of measures and regulatory constraints in order to reduce the emissions of CO₂.

Because road transport is responsible for about 17% of total CO₂ emissions, it is normal that some of these regulatory laws also involve the automotive industry. Indeed, the European regulation imposes that all new cars must respect a level of **95** grams of carbon dioxide per kilometer (g CO₂/km) by **2021** (corresponding to an average consumption of 4.1 L/100 km for petrol cars or 3.6 L/100 km for diesel cars). In order to respect these new environmental laws, various solutions can be studied, such as more efficient engines, the use of electronic or hybrid cars, bio-fuels, mass reduction and/or a better aerodynamic design. Indeed, significant advances have been made in all these fields by the automotive

manufacturers reducing the emissions of air pollutants. According to the European Environment Agency (EEA Technical report, 2014), vehicles sold in the European Union in 2014 had an average emission of 123.4 g CO₂/km, which is 2.5% more efficient than in 2013 and significantly below the 2015 target (130 g CO₂/km)(See Figure I.2).



Figure I.1: Environmental problematic due to the emission of CO₂.

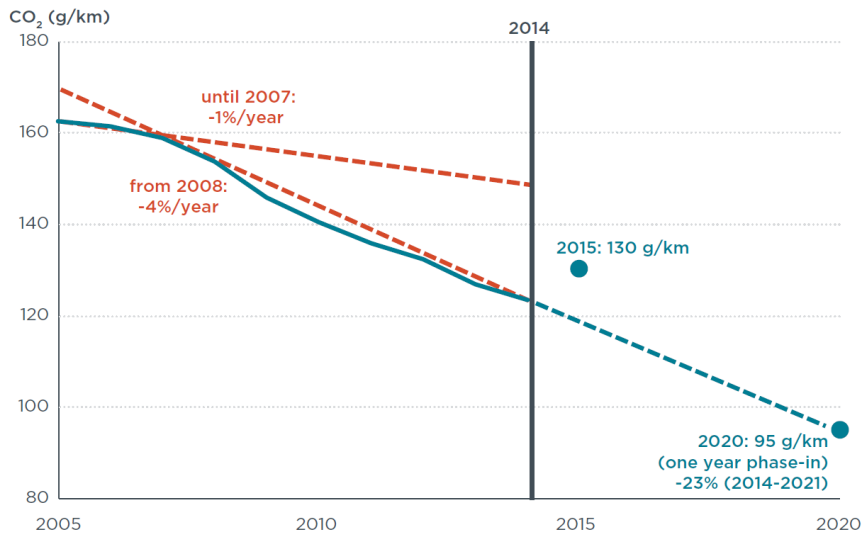


Figure I.2: Historical evolution and future targets for CO₂ emission levels of new passenger cars in the European Union. (Nikiforos Zacharof et al., 2015)

Even if French manufacturers (Renault, Citroen and Peugeot) produce most of the lowest-emitting cars (See Figure I.3), the final target (by 2021) has not been achieved and the global competition will get tougher in the next years. Therefore, it is necessary to continue developing and implementing new solutions.

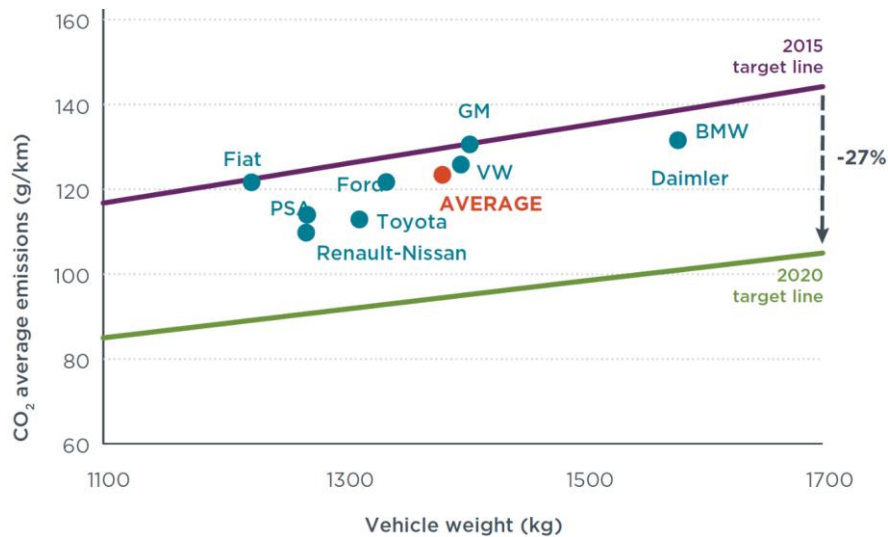


Figure I.3: Average CO₂ emissions in grams per kilometer of new passenger cars of the top-selling EU passenger car manufacturer groups in 2014. (Nikiforos Zacharof et al., 2015)

I.3. The need for new materials and the lunch of the FASLITE project

In order to achieve the targets and respect the regulatory constraints, the French manufacturers have focused on reducing the mass of cars. It is obvious that a lighter car will consume less fuel and in consequence pollute less. Indeed, a weight reduction of 100 kg represents a reduction of about 8 to 10g CO₂/km (ADEME-Carlabelling, 2015).

Nowadays, vehicles are made up of 75% metallic materials (50% ferrous materials) with good mechanical properties but with a high density. Therefore, weight reduction needs the progressive substitution of these classical heavy metal alloys by lighter materials. Composite materials and aluminum alloys seem to be a good option due to their high resistance/weight ratio (See Figure I.4). But, how can we assemble these new materials with all the other ones presented in a car body? Then, the problem becomes the research for a joining technique able to assemble dissimilar materials and, at the same time, adapted to the manufacturing process.

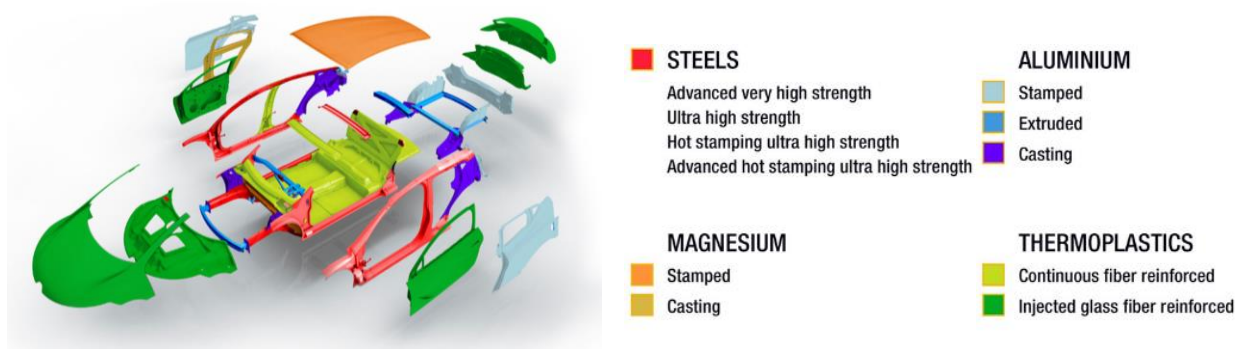


Figure I.4: Materials used in a future car. Renault Eolab concept car by 2020 with a total CO₂ emission lower than 22 g/km and a total weight down to 995 kg. (Groupe Renault, 2014)

It is worth noting the inclusion of composite materials and aluminum alloys must guarantee economic benefits. Hence, it is not only necessary to determine an adapted joining technique, but also be able to model it in order to reduce costs. It is clear that a good knowledge of materials and joining techniques increase the efficiency of the car design.

In order to obtain a response to the questions presented above, the French automotive industry has formed the FASTLITE project in 2013. This project has been financed by the ADEME agency and grouped the two main French manufacturers (Renault and PSA-Group), some industrial partners (Laser Cheval, ARaymond, Böllhoff, Plastic Omnium, Solvay, CETIM, ESI Group, Altair), and two laboratories (the Laboratory of Industrial and Human Automation, Mechanics and Computer Science “LAMIH”, and the Dupuy de Lôme Research Institute “IRDL”). Two Ph.D. studies were then born in the framework of this project: one focused on the dynamic aspect at the LAMIH laboratory and the other one focused on the static aspect at the IRDL institute.

I.4. Objectives of the current Ph.D. thesis

The Ph.D. thesis presented in this document was centered on the study of multi-material assemblies under mixed quasi-static loadings. The general objectives were then:

- (i) Characterization of joining techniques of dissimilar materials under quasi-static mixed tensile-compression/shear loadings.
- (ii) Modeling of the most adapted joining technique in order to reduce the design time of automotive structures.

I.5. Materials of the study

Four composite materials and three metallic materials were selected by the partners of the project as the materials to assemble. A brief description of the main properties of these materials is presented below.

I.5.1. Composite materials

I.5.1.1. Vinylester chopped glass fiber SMC

FE7520-26® is a sheet molding composite (SMC) based on thermosetting vinylester resin and reinforced with 50% of chopped glass fibers (25 mm). The composite is provided by Mixt Composites Recyclables® and manufactured by compression molding without flow at 145°C. It provides a very high volume production ability, excellent part reproducibility and low cost. The main characteristics of this material are presented in Table I-1.

I.5.1.2. NCF vinylester glass fiber SMC

NCF glass fiber vinylester SMC® is a non-crimp fabric (NCF) composite based on thermosetting vinylester resin and reinforced with 50% of glass fibers. This composite has similar properties than the previous composite and it's also manufactured by Mixt Composites Recyclables®. Table I-1 summarizes the main characteristics of this material.

I.5.1.3. Epoxy carbon fiber prepreg

This composite is a toughened 2x2 twill thermosetting epoxy composite with carbon fiber reinforcement and produced by Delta-Preg®. The composite sheets are autoclave cured at 6 bars pressure, with a caul plate. This type of procedure may lead to substantial delays in the automotive production chain. The mechanical properties are quite higher than the other composites as shown in Table I-1.

I.5.1.4. PA66 glass fiber consolidated

The last composite was an 8H satin thermoplastic polyamide resin (PA66) composite with glass fiber reinforcement. The material is manufactured by Solvay® by means of an injection molding process with controlled pressure and temperature. This process provides excellent mechanical properties. Main characteristics of this composite are listed in Table I-1.

I.5.2. Metallic materials

I.5.2.1. 5182 Aluminum

5182 aluminum is a lightweight and malleable aluminum alloy with good corrosion resistance. This material is principally used to mold complex geometries such as door inners. The material has been supplied by Constellium® and the principal mechanic properties are presented in Table I-2.

I.5.2.2. 22MnB5 Steel

22MnB5® steel is a cold-rolled or hot-rolled steel (for very thick sheets) manufactured by ArcelorMittal® and intended for hot-stamping automotive applications. The material presents a good hot formability allowing for complex geometries. The good mechanical properties of 22MnB5 pieces (fatigue strength and impact resistance) reduce both weight and cost substantially. These properties can only be obtained after quenching. Therefore, the pieces are hot-stamped and quenched in the same process. First, the 22MnB5 plates are coated with aluminum-silicon alloy (AlSi) to avoid surface-oxide formation during quenching. Then, the plates are heated at 900-950 °C and stamped with a cooled stamping

tool to start the quenching. The final pieces can be then painted directly without a cleaning operation such as shotblasting. The main mechanic properties of 22MnB5 steel are presented in Table I-2.

I.5.2.1. DP600 Steel

DP600 steel is a dual-phase steel developed for automotive applications and manufactured by ArcelorMittal®. The microstructure consists of a soft ferrite phase with dispersed islands of a hard martensite phase. The metal plates are electro-galvanized (zinc coating) and then manufactured by cold rolling, providing good strength, high strain energy absorption capabilities, excellent formability and corrosion resistance. Compared with 22MnB5, DP600 plates present a relative lower ultimate and yield strength as shown in Table I-2.

Property	Chopped glass fiber vinylester SMC	NCF glass fiber vinylester SMC	Epoxy carbon fiber prepreg	PA66 HF consolidated
Index	SMC-Chopped	SMC-Fabric	Prepreg	PA66
Morphology	Chopped fiber	2 layers, non-crimp fabric	Twill 2x2	5 layers, 8H Satin balanced
Fibers content (volume)	50% glass fiber	50% glass fiber	50% carbon fiber	50% glass fiber
Resins content	24%	48%	42 %	--
Fillers content	26%	2%	--	--
Glass transition temperature	145 °C	145 °C	115-120 °C after 90min	69 °C
Shaping process	Compression molding without flow under high temperature and pressure.	Compression molding without flow under high temperature and pressure.	Autoclave cured at 6 bars pressure	Injection molding under controlled pressure and temperature
Thickness sheet	2.2 (mm)	1.8 (mm)	2 (mm)	2 (mm)
Density	1.96 (g/cm ³)	1.61 (g/cm ³)	195 (g/m ²)	1.87 (g/cm ³)
<i>In-plane tensile test (warp 0°, if applied):</i>				
Ultimate strength	140 MPa	--	817 MPa	525 MPa
Elastic modulus	15 GPa	--	60 GPa	26 GPa
Axial elongation	1.8%	--		2.4%
<i>Flexural test (warp 0°, if applied):</i>				
Ultimate strength	430 MPa	--	966 MPa	766 MPa
Elastic modulus	17 GPa	--	53 Gpa	22 GPa
Axial elongation	3.3%	--		3.5%

Table I-1: Mechanical properties of the composite materials used in this study (according to the product datasheets)

Property	Aluminum 5182	Steel 22MnB5	Steel DP600
Index	AL5182	22MnB5	DP600
Chemical composition	Mg 4,74 %	C 0.25%	C 0.14%
	Mn 0.38%	Mn 1.4%	Mn 2.1%
	Fe 0.25%	Si 0.35%	Si 0.40%
	Si 0.10%		
Shaping process	--	Hot rolling + hot stamping	Cold rolling
Surface treatment	Not applied	Aluminized coating (AlSi)	Galvannealed
Density	2.65 g/cm ³	7.8 g/cm ³	7.8 g/cm ³
Thickness sheet	2 mm	2 mm	2 mm
Ultimate strength	400 MPa	1500 MPa	700
Yield strength (0.2%)	147 MPa	1100 MPa	300 MPa
Rigidity	E=70 GPa	E=210 GPa	E=210 GPa
	$\nu=0.33$	$\nu=0.3$	$\nu=0.3$
Elongation at break	>25%	6%	>21%
Fatigue limit	--	617 MPa (R = 0,1)	500 MPa (R = 0,1)
		305 MPa (R = -1)	250 MPa (R = -1)

Table I-2: Mechanical properties of the metallic materials used in this study after quenching (according to the product datasheets)

I.6. Background information on joining techniques of dissimilar materials

Industrialized mechanical products generally involve the joining of different parts that are usually manufactured at different times in different places and with different materials. The selection of a suitable joining technique by the technical designer is complex and depends on the final properties of the structure (mechanical strength), economic criteria (optics, repair possibilities) and production viability (*Handbook of industrial engineering: Technology and operations management*, 2001).

Classical joining processes are divided into fasteners¹, welding and adhesive bonding. A wide range of techniques has been developed in recent years for different materials; however, not all of them are adapted to composite/metal assemblies. In fact, the fiber damage due to mechanical and/or thermal stresses during the joining process may lead to an incorrect assembly when composite materials are used.

¹ A mechanical device that joins two or more objects together.

Figure I.5 presents some suitable techniques to join composite/metal assemblies. The first family is the *fasteners*, where rivets, snap fit and bolts are the most commonly used in the automotive industry (Barnes and Pashby, 2000). Their main advantages are high-speed of production, possible join of different thicknesses and not requiring heat. However, they usually need drilling and machining processes, which can induce water intrusion between the fastener and the composite, damage on the composite plate, delamination caused by stress concentrations (poor performance in tension), and overweight of the final assembly. In order to increase the performance of this kind of assembly, some studies have proposed certain design criteria to better distribute the load such as the minimum distance between fasteners and/or edges, the radius of the hole, the thicknesses of the composite and the head size of the fastener (R.T. Cole *et al.*, 1982).

Welding assemblies corresponds to the second family. In this technique, the composite matrix (or a filler material) is melted by heating. The matrix flows and solidifies between the surfaces of contact. Pressure is generally applied in order to ensure a good contact between the surfaces. The high-speed rate and the final appearance make it especially suitable for automotive industry uses. However, this technique generates local heat that may weaken the composite around the welded zone. Welding has proved to be especially effective to join thermoplastic composites in lap joint configurations (P A Hilton *et al.*, 2000).

The last joining technique is the *adhesive bonding*, in which an adhesive is placed between the materials to join. The structure will follow a bonding process, during which the adhesive will be polymerized² in order to consolidate the bonding joint. The polymerization process varies according to the adhesive. The most common harden (*i*) by mixing two or more components that chemically react, (*ii*) by drying the solvent component of the initial substance (mixture of polymers plus solvent), or (*iii*) via chemical reactions with an external energy source, such as radiation, heat, and moisture. Adhesive bonding systems offer a wide range of advantages such as high-speed production, low cost and low weight, and possible joining dissimilar materials. In addition, adhesives provide a relatively uniform stress distribution over the bonded surfaces and avoid the hole drilling issue. Thus, the automotive industry is increasingly focused on adhesive bonding, which implies that a big challenge around the bond reliability of adhesive joints must be faced. Hybrid joints (e.g. adhesive plus fasteners or adhesive plus laser welding) have emerged as an encouraging solution that may be used as reinforcement in many composite applications (Sadowski, T. *et al.*, 2014).

² The process of converting a monomer mixture of monomers into a polymer

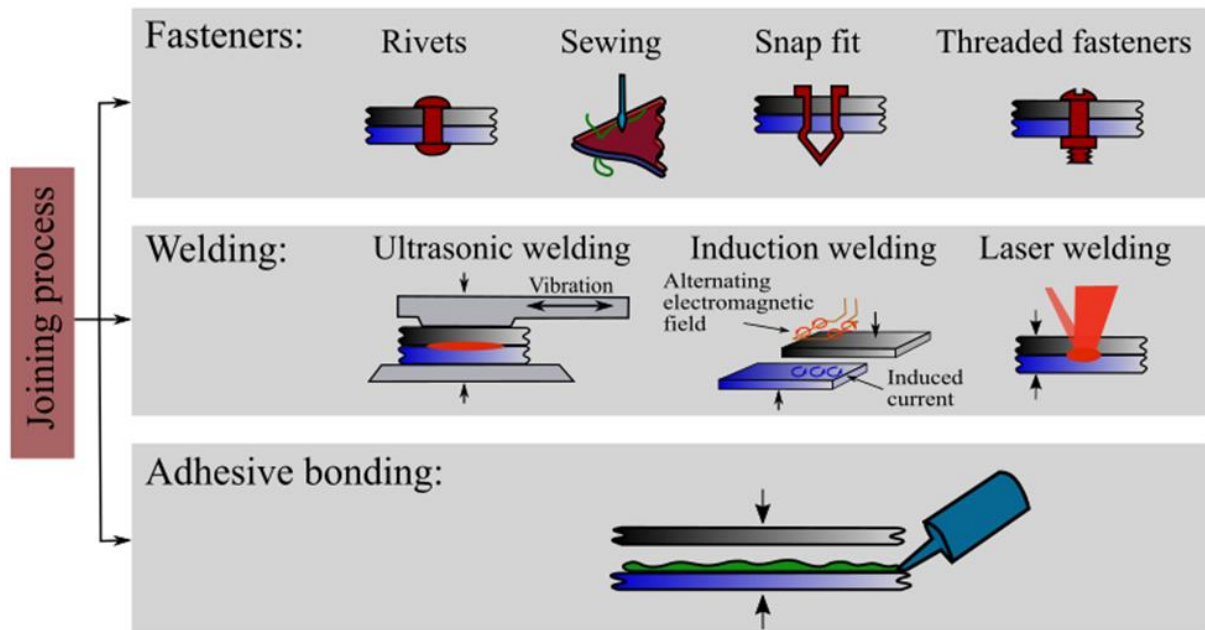


Figure I.5: Some classical joining techniques used to assemble dissimilar materials.

I.7. The selected joining techniques

The use of light materials as aluminum and composites in the body of automobiles involves the issue of joining dissimilar materials. The challenge for the automotive industry consists then in defining techniques able to join aluminum/metal, aluminum/composite, composite/metal and composite/composite assemblies.

In aluminum/metal assemblies, the problem has been solved by means of classical joining techniques as welding or fasteners (Chastel and Passemard, 2014). These techniques provide high mechanical performance and do not constitute a significant challenge. Therefore, aluminum/metal assemblies have not been investigated in this study.

In contrast, the research of joining techniques enabling the use of composite materials remains open to the industrial and scientific communities. Thus, a preliminary research was performed by the partners of the FASTLITE project in order to select the joining techniques able to join aluminum/composite, composite/metal and composite/composite assemblies. The criteria used in this preliminary research included the feasibility of assemblies, the additional weight, the total assembling price and the esthetic design. Four joining techniques were finally preselected: stud bonding, laser welding, self-pierce riveting and adhesive bonding.

I.7.1. Stud bonding

Stud bonding is a joining technique proposed by Raybond® (subsidiary company of the ARaymond network) for joining metal sheets to dissimilar materials such as laminated glass, tempered glass, plastics, glass and carbon fibers and many other composites. This technique consists of a threaded stud fastener over which the metal sheet is fixed with the

aid of a nut. The head of the fasteners is then adhesively bonded to the composite plate. The bonding process is based on the so-called “Pick & Bond” process, which follows the next steps (See Figure I.6):

- 1) Part heating: The fastener is pre-heated (hidden time)
- 2) “Pick”: the adhesive tablet, stored at room temperature, is picked up and sticks to the fastener by thermal conductivity (max. 10s)
- 3) “Bond”: the joint is then solidified while cooling (max. 5s).

The bonding process provides a wide range of advantages such as no drilling of composite materials, bonding facilitates since no adhesive residue needs to be removed from assembly equipment, removable and replaceable options, and immediate use (Up to 80% strength is achieved after 5 minutes). Additionally, the process can be completely automated and easily integrated into the automotive production line.

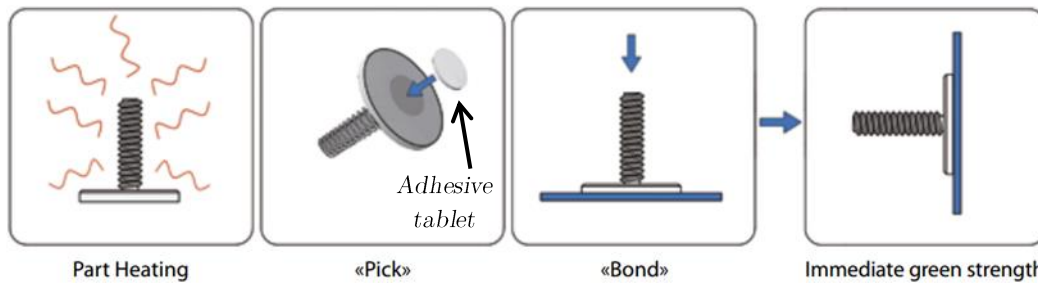


Figure I.6: Bonding process of the threaded stud fastener. Taken from (ARaymond Network and © Raygroup SASU, n.d.).

The adhesive used is one-component polyurethane adhesive that is pre-dosed and pre-shaped in order to ensure exact dosage. The stud fastener is a carbon steel with Zinc surface treatment by electro-galvanizing (cataphoresis). Some characteristics of the adhesive tablet and the stud fastener are presented in Table I-3.

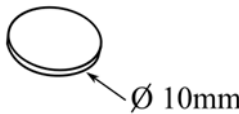
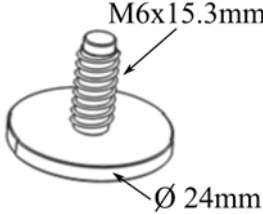
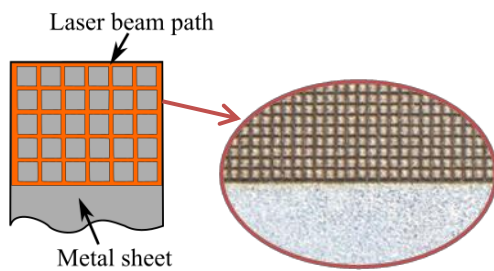
	Adhesive tablet	Stud fastener
Geometry	 Ø 10mm	 M6x15.3mm Ø 24mm
Weight	135 mg	<12g
Reference	Techbond® PUR2MAX	204.621.000

Table I-3: Basic information about the stud bonding system.

I.7.2. Laser welding

Using a laser beam to heat locally at melting temperatures of materials, laser welding creates excellent high-mechanical assemblies. The laser welding technique used in this study was developed by Laser Cheval® and it constitutes an ideal alternative to complex fiber-reinforced thermoplastic components, offering a solution for manufacturing clean, rapid and permanent fixed joints. Laser welding can also be automatized in the automotive production line.

1. Laser surface texturing:



2. Laser welding:

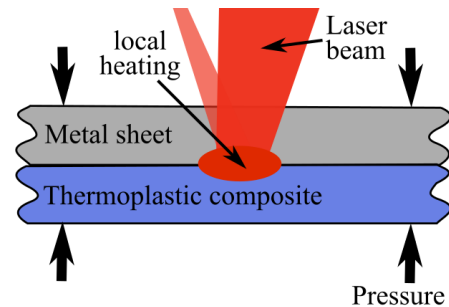


Figure I.7: Laser welding procedure to join the thermoplastic composite used in this study (PA66).

In metal/composite assemblies, the materials to join are overlapped. The top joining sheet (metallic materials) must be sufficiently transparent for the laser radiation to penetrate the weld zone without loss of intensity. The lower joining sheet (thermoplastic composite) must be strongly absorbing so that the incident radiation can be converted into heat near to the surface. Thus, the resin matrix flows and solidifies over the contact surfaces. Pressure may also be used in conjunction with heat to ensure a good final joint. Since the roughness of the metal substrate has a great influence overall the strength of the assembly, a laser surface texturing is usually applied over the surfaces of the metal sheets. This procedure creates channels through which the resin matrix flows. A better attachment is then ensured. Figure I.7 shows the laser welding procedure used in this study.

I.7.3. Self-pierce riveting (RivSet)

Self-pierce riveting is a simple and efficient process for a joining of similar or dissimilar sheet materials. This technique is especially adapted to high-speed production lines (as in the case of automotive) since no pre-drilling is needed. Additionally, it may be combined with other techniques (adhesive bonding) in order to create hybrid joints.

Böllhoff (partner of the FASTLITE project) proposes a semi-tubular self-pierce rivet called RivSet®, which is presented in Figure I.8-a. The Böllhoff system permits two or more sheets to be assembled by piercing a RivSet® fastener through the upper sheet of the workpiece and forming a locking head in the lower sheet (See Figure I.8-b). A wide range of RivSet® variations is proposed in order to fit the application in use. Thus, the RivSet® pieces may differ in material, shape, hardness, surface, head shape, shaft length and diameter (See Figure I.8-c).

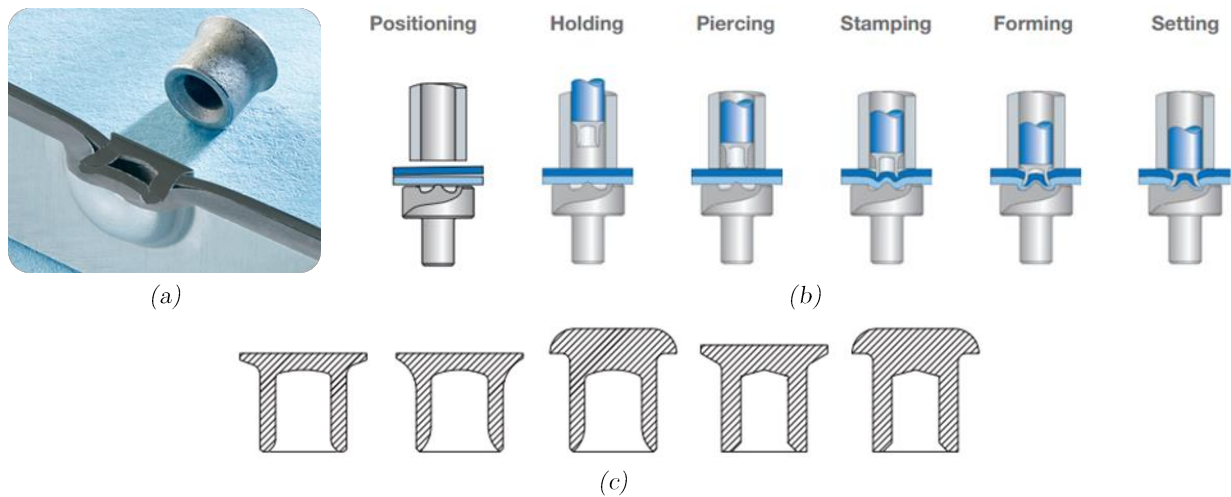


Figure I.8: RivSet® Self-pierce riveting system. Classical RivSet® fastener (a), joining procedure (b) and variants of the RivSet fastener (c). (Böllhoff group, n.d.).

I.7.4. Adhesive bonding

Adhesive bonding systems are possibly the most versatile technique for joining similar or dissimilar materials. Generally, adhesives provide more consistent and adapted results than other joining techniques. The wide variety of modern adhesives ensures that there is “always” an optimum adhesive bonding system for any application. However, a great number of variables must be considered when selecting adhesive bonding materials (Duncan, 2010), such as:

- Chemical compatibility with the materials being joined
- Flexibility/rigidity requirements
- Environmental and temperature requirements
- Desired method of adhesive application
- Storage conditions
- Economic and esthetic aspect

Adhesives can be organized by their chemical composition. Three families are then usually considered:

- (i) Reactive acrylic-based adhesives are able to bond a wide variety of substrates. They also have a fast bonding procedure; however, they are susceptible to the surface preparation as in toughened adhesives. The cyanoacrylate-based subfamily can produce quick bonds when exposed to damp air (usually they solidify in seconds); nevertheless, these adhesives can be brittle, which makes them useless for bending or crash applications. Besides, they are also susceptible to creep and high temperatures. Anaerobic acrylic adhesive is another subfamily of acrylate adhesives that cure when oxygen is excluded. This type of adhesive is usually used to secure, seal and retain metal structures to prevent loosening, leakage or corrosion.

- (ii) Polyurethane adhesives are chemically reactive formulation and may be found in single or two-component systems. They constitute the most versatile adhesive family and can be used in a wide variety of applications such as construction, sealants, crash, etc.
- (iii) Epoxy-based adhesives present excellent bond strength and durability for thermoplastic and thermosetting materials. They are also resistant to solvents, acids, bases and salts. Therefore, they are widely used in various applications. However, because of the price they are generally used in small quantities. Typical polymerization temperatures are between 20 and 200°C.

Careful preparation of adherend surfaces is essential to making a quality adhesive bond (Lucas F. M. da Silva *et al.*, 2011). Recommended preparation of adherends consists of a solvent wipe, to remove loose surface dirt and oil, and abrading operations. Surfaces can also be prepared chemically.

1.7.4.1. The selected adhesives

As explained before, a wide range of structural adhesives are provided by different suppliers; these adhesives are then usually adapted to specific applications such as aerospace (where high mechanical properties at high temperatures are pursued) or construction (where waterproof is a vital criterion). In automotive applications, the high accident rate and the long service life of cars impose the use of adhesives adapted to crash and cyclic loadings.

The CETIM institute has performed a preliminary experimental campaign in order to select the adhesives providing the highest mechanical properties and adaptability to the automotive industry (CETIM, 2013). The principal selection criteria were the strength, the compatibility with adherends, the possibility of a fully automatic application and an operating temperature between -20°C to +90°C. This campaign has concluded that at least two adhesives seem to be adapted: Betamate-1822 and Sikapower-498. These adhesives harden by heat and provide an excellent adhesion to coated steels, high-strength steel, aluminum and composites. Due to the oil consumption during heat curing, the selected adhesives provide a good tolerance to oil and dry-lubes. It is worth noting that they can also be used in combination with spot welding, riveting, clinching and other mechanical fastening techniques, forming hybrid joints with adapted solutions. The principal mechanical properties of adhesives are listed in Table I-4.

1.7.4.1.1. Betamate-1822

The first selected adhesive was the Betamate™ 1822® manufactured by Dow Automotive®. This one component epoxy-based adhesive has been developed to increase the operation durability, the crash performance and the stiffness of the body car. The principal difference respect to the other selected adhesive is its large deformation in Bulk tests.

I.7.4.1.2. Sikapower-498

Sikapower® 498 is a one component epoxy-based adhesive with high structural strength and adapted to impact applications. The SikaPower®-498 is produced by Sika Automotive®. This adhesive has a particularly high fracture toughness, ensuring a good integrity under crash loadings.

Property	Betamate-1822	Sikapower-498
Index	BM1822	SP498
Basis	Epoxy resin	Epoxy hybrid
Color	Green	Black
Density	1.38 Kg/l	1.3 Kg/l
Application temperature	40-50°C	50-60°C
Curing condition	> 140°C / 25 minutes	> 175°C / 20 minutes
Viscosity/Yield Point	40 Pas / 800 Pa	--
Glass transition temperature (T _g)	--	100°C
E-Modulus	approx. 500 MPa	--
Lap-Shear Strength	22 Mpa (Bonded area: 25mm x 10mm Adhesive layer thickness: 0.2mm)	30 Mpa (Bonded area: 25mm x 10mm Adhesive layer thickness: 0.3mm)
T-Peel	7.7 N/mm (Bonded area: 25mm x 100mm Adhesive layer thickness: 0.2mm)	10 N/mm (Bonded area: 25mm x 100mm Adhesive layer thickness: 0.3mm)
Tensile Strength	20 MPa (ISO 527-1:2012)	30 Mpa (ISO 527-1:2012)
Elongation at Break	approx. 25%	approx. 5%
Fracture toughness	--	G _{IC} =2.93±0.32 N/mm G _{IIC} =11.03 N/mm (calculated) (Stamoulis et al., 2014)

Table I-4: Mechanical properties of the Betamate-1822 and Sikapower-498 adhesives (according to the product datasheets)

I.7.4.1. Curing cycle

An efficient automobile assembly line can produce about 1500 cars per day for the most popular models. It represents a new car every minute, which implies the use of very fast assembly techniques. These high-speed rates are only possible with an adequate sequential organization of workers, tools, machines and pieces. Furthermore, in order to reduce the waiting time, some of the steps must be performed simultaneously. This is why the curing cycle of the adhesives must be compatible with the temperature cycle of the pre-gelling process (100°/120°C) and/or the paint shop processing of the car (150°/200°).

The curing cycle used in this study correspond to 25 minutes of controlled heat up to 200°C plus 20 minutes of stabilized temperature (No controlled cooling is needed). This cycle is not only adapted to the automotive production chain, but at the same time, it guarantees an 80% polymerization process, according to the product datasheets (See Table I-4).

It is important to say that even if the polymerization cycle has a great influence on the behavior of the adhesives, as suggested by Devaux (Devaux, 2015), this aspect was not taken into account in this study. Future works about this matter will be then carried out by the partners of the FASTLITE project during the third phase of the project: “Development of the assembly procedure”.

I.7.4.1. Types of failure

The characterization of adhesively bonded systems requires the definition of the failure mode of the assembly. In the case of assemblies involving composite materials, a large number of designation and classification may be found in the literature. The definitions of possible failure modes observed in this study is based on the ASTM D-5573 technical standard (ASTM 5573, 1999). This norm has been developed to classify, identify, and characterize the failure modes of adhesively bonded Fiber-Reinforced-Plastic (FRP) joints subjected in lap-shear test. Thus, the definition of the failure modes has been slightly adapted to the study (See Figure I.9):

- 1) Adhesive failure: The failure of the assembly occurs at the adhesive/composite interface. After failure, no evidence that any adhesive or composite, or both, have transferred to the other surface. In some cases, the adhesive surfaces may have a shiny appearance.
- 2) Cohesive failure: The fracture occurs within the adhesive layer. Two adhesive layers remain over the adherends with a relative similar thickness.
- 3) Thin-layer or interphase cohesive failure: It is a particular case of a cohesive failure where the failure is near the adhesive/adherend interface. Thus, a light dusting of adhesive is observed on one of the adherend and a thicker layer on the other.
- 4) Fiber-tear failure: The failure occurs exclusively within the composite plate, characterized by the presence of composite material on both ruptured surfaces.
- 5) Light-fiber-tear failure: The failure occurs within the composite plate near the adhesive/adherend interface. A thin layer of the resin matrix and some fibers may be transferred from the composite to the adhesive.
- 6) Mixed failure: Any combination of two or more of the failure modes presented above.

According to the interest of the project and in order to fully exploit the mechanical properties of the adhesives, it is necessary to ensure cohesive failures for all types of load. It is clear that when cohesive failure occurs, the adhesive has been subject to its maximum load capacity. Furthermore, with this type of failure, car manufacturers can ensure an optimal bonding process since the failure does not occur at the interfaces but within the adhesive joint. This last point is an important aspect in terms of quality processes and warranties.

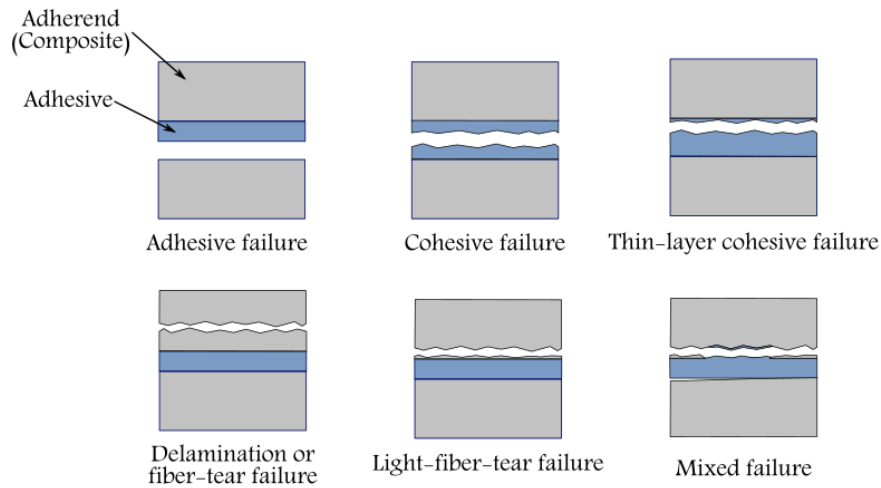


Figure I.9: Definition of the failure modes of adhesively bonded assemblies. Inspired from (ASTM 5573, 1999).

I.8. Set of tested assemblies

Even if the joining techniques detailed above have been developed to bond a large number of dissimilar materials, they are not adapted to the entire range of possible assemblies (four composites and three metallic materials combined with each other). Certain aspects such as the viability, the configuration of the joining procedure or the specimen size may limit the number of possible assemblies. Therefore, the final set of assemblies tested in this study was (See Figure I.10):

Stud bonding: Only composite/metal assemblies may be joined by means of stud bonding systems. Since the metal substrate has a minor influence on the macroscopic response of the assembly, it has been decided to use one single metal material (DP600) to validate the performance of this technique. Indeed, the key point of the assembly is the good adhesion between the fastener and the composite material. Thus, four assemblies have been tested with this technique: DP600/SMC-Chopped, DP600/SMC-Fabric, DP600/Prepreg and DP600/PA66.

Laser welding: Thermosetting composite take their final shape after the first chemical reaction (polymerization cycle). Thermoset materials are therefore not suitable for laser welding because they cannot merge or melt during welding. In contrast, thermoplastic composites can be deformed under the effect of heat, keeping the final shape when cooling. In consequence, the only adapted composite to this technique was the PA66 composite. Preliminary studies were carried out by Laser Cheval® in order to identify the laser configuration permitting aluminum/PA66 assemblies to be joined. However, no satisfactory results were obtained. In fact, during the assembly process, the laser was reflected almost in its entirety by the aluminum sheet; therefore, neither the aluminum nor the composite was heated at the contact surface. The only laser welded assemblies tested were: DP600/PA66 and 22MnB5/PA66.

RivSet: At the beginning of the present Ph.D. study, the unique metal substrate compatible with the RivSet technique and the selected composites was the 5182 aluminum alloy. Thus, the tests were performed over four different RivSet assemblies: AL5182/SMC-Chopped, AL5182/SMC-Fabric, AL5182/Prepreg and AL5182/PA66. It is worth mentioning that some parallel studies performed by Böllhoff® were carried out in order to establish a joining procedure permitting DP600 and 22MnB5 metal sheets to be used. These studies showed the feasibility of DP600/composite assemblies with 1.6mm-thick metal sheets. However, the studies also concluded that 22MnB5/composite assemblies could not be joined by the RivSet technique.

Adhesive bonding: Adhesive systems are the only joining technique allowing the entire range of materials to be joined: AL5182, DP600, 22MnB5, SMC-Chopped, SMC-Fabric, Prepreg and PA66. Therefore, a particular attention has been paid to the analysis of the experimental results. Chapter IV is devoted to the characterization of these bonded assemblies and the proposition of an adapted bonding procedure.

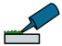
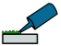
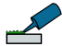
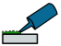























	SMC-Chopped	SMC-Fabric	Prepreg	PA66	AL5182	DP600	22MnB5
SMC-Chopped							
SMC-Fabric							
Prepreg							
PA66							
	 Stud bonding	 Laser welding		 RivSet	 Adhesive bonding		

Figure I.10: Set of “tested” assemblies and their corresponding joining technique.



Chapter II. Characterization test and methodology

Introduction

As discussed in the previous chapter, the automotive industry needs to characterize different joining techniques of dissimilar materials. To this end, the problematic was segmented into different sub-problems that have been solved step-by-step. This chapter presents then the characterization tests and the methodology followed in this study.

Since the characterization of joining techniques depends on the type of characterization test, a summary of traditional tests is presented at the beginning of the chapter. After analyzing the advantages and drawbacks of these tests, the modified Arcan approach proposed by the “Institut de Recherche Dupuy de Lôme” has been chosen. This test is of particular interest to the automotive industry because it allows the specimens to be subjected to compression-tensile/shear loadings.

Table of contents

II.1. Choice of the test.....	35
II.1.1. Summary of tests to characterize the strength of assemblies.....	35
II.1.1.1. Single lap joint test	35
II.1.1.2. Cross-tension test	35
II.1.1.3. Arcan test.....	35
II.1.2. Summary of tests to characterize the behavior of adhesives	36
II.1.2.1. Bulk tests	36
II.1.2.2. Bonded tests.....	37
II.1.2.2.1. Lap-shear test.....	38
II.1.2.2.2. Thick adherend shear test (TAST)	38
II.1.2.2.3. Butt joint test (tension-compression/torsion)	38
II.1.3. The Modified Arcan approach.....	39
II.1.3.1. The Arcan specimen.....	40
II.1.3.2. The bonding system	42
II.1.3.3. Post-processing	43
II.1.4. The selected characterization tests	44
II.2. Sequential solution methodology	44

II.1. Choice of the test

Several authors have proposed different devices, machines and configurations in order to subject assemblies under tensile, shear or compression stresses. A summary of the most commonly used tests is described below.

II.1.1. Summary of tests to characterize the strength of assemblies

In this section, some traditional tests used to determine the strength of assemblies are discussed. The main characteristics, the specimen configurations, the advantages and disadvantages are presented.

II.1.1.1. Single lap joint test

Lap-shear test is an industrialized test widely used to characterize the performance of an assembly under “shear” loadings. The strength, the type of failure, the surface preparation parameters and the environmental durability can easily be determined. In this test, two sheet samples are overlapped and joined at the center of the overlap region with the testing joining technique. The specimen is then pulled in tension (See Figure II.1-a). Since there is bending or even necking in the substrates during testing, the actual load is a combined shear/tensile load (Han *et al.*, 2010), which ratio is quite difficult to estimate. For the purpose of this study, we have neglected this particularity and considered that the lap-shear test results in a “pure” shear stress state in the joint.

II.1.1.2. Cross-tension test

In the cross-tension test, a quasi-tensile load is applied to the joining technique by means of a universal tensile machine. The specimens are made of two substrates positioned in (\times) configuration and joined at the center. The specimen is then gripped in the fixture system. When testing, one substrate is pulled upward and the other one remains static, generating a “tensile” load over the joint of the specimen (See Figure II.1-b).

II.1.1.3. Arcan test

The Arcan approach proposed by Arcan (Arcan *et al.*, 1978) has been modified in order to subject assemblies under mixed tensile/shear loadings. The experimental device consists of two half-moon shaped pieces (above and below) that grip the specimen by means of a fixture system (Figure II.1-c). The experimental device is then placed in a universal tensile machine. The type of load varies with the angle (γ), formed by the axis of the tensile machine (machine axis) and the normal plane of the specimen (Z -axis). In general, the specimen is composed of two metal U-shaped elements joined together in the central part by the testing joining technique. This type of test has been widely used in metal self-pierce

riveted assemblies (Porcaro *et al.*, 2004) and in adhesively bonded assemblies (Mahnken, 2012).

The “simplicity” of the specimen provides an easy way to test metal assemblies, but its geometry is not adapted to composite assemblies. Indeed, 90° radius profile presented in the U-shaped specimen are difficult to manufacture and may introduce stress singularities in the composite plate (See Figure II.1-c).

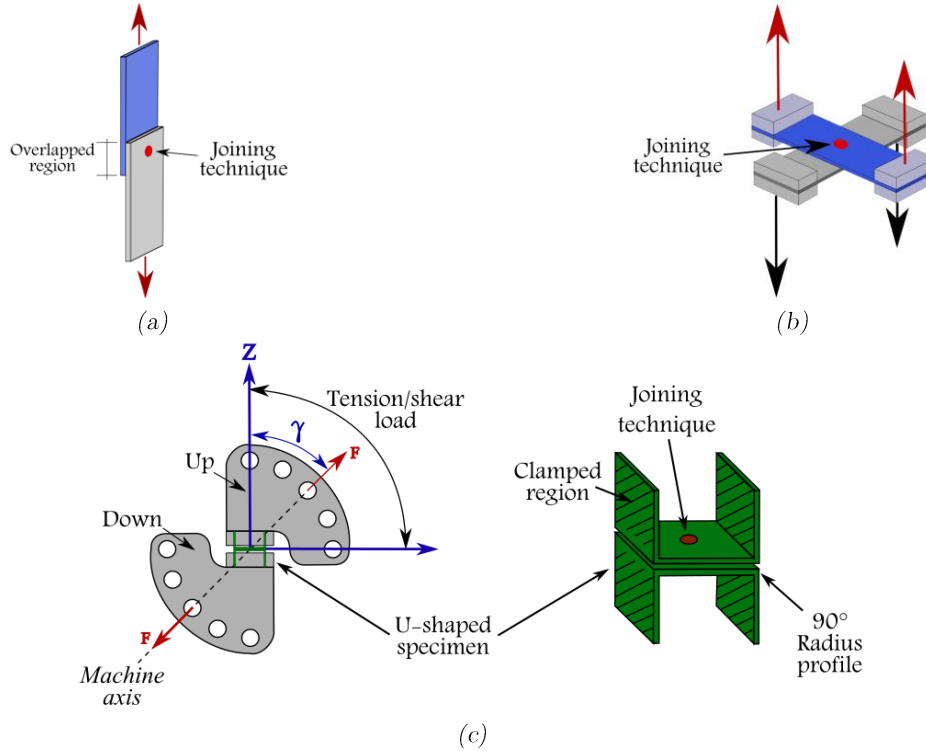


Figure II.1: Characterization test of assemblies. Lap-shear test (a), Cross-tension test (b) and Arcan test (c).

II.1.2. Summary of tests to characterize the behavior of adhesives

Divers experimental tests have been proposed in the literature to characterize the behavior of adhesives. These tests may be grouped according to their methodology of characterization in bulk tests or bonded tests:

II.1.2.1. Bulk tests

This family of tests uses bulk samples permitting massive adhesive specimens to be tested under different types of load. This approach considers the adhesion issue at the adhesive scale, focusing on the mechanical properties of the adhesive itself. It allows the behavior of the adhesive under cohesive assumptions to be modeled but neglects the role of the adherends and the interfaces on the global behavior of the assembly. The principal tests of the Bulk family may be defined as:

- a) Tensile test: a “dog-bone” specimen is subjected to uniaxial tensile loadings in order to determine the tensile mechanical properties of the adhesive.
- b) Compressive test: a cylindrical specimen is subjected to uniaxial compressive stresses in order to determine the compressive strength and the hydrostatic pressure dependence of the adhesive (Balieu *et al.*, 2013).
- c) Torsion test: solid or cylinder specimens are loaded in torsion in order to obtain the shear strength of the adhesive. It is worth noting that the round shape of the specimens is difficult to obtain (Chiminelli *et al.*, 2016).
- d) Iosipescu test: V-notched specimens are fixed in an asymmetric four-point bending device. When the specimen is loaded, shear stress is generated on the V-notched section (Iosipescu, N, 1967).
- e) Arcan test: V-notched specimens are fixed in an Arcan device in order to create different ratios of tensile/shear loadings. The test can thus provide information about the behavior of the adhesive varying from “tensile” to pure shear stresses (Arcan *et al.*, 1978).

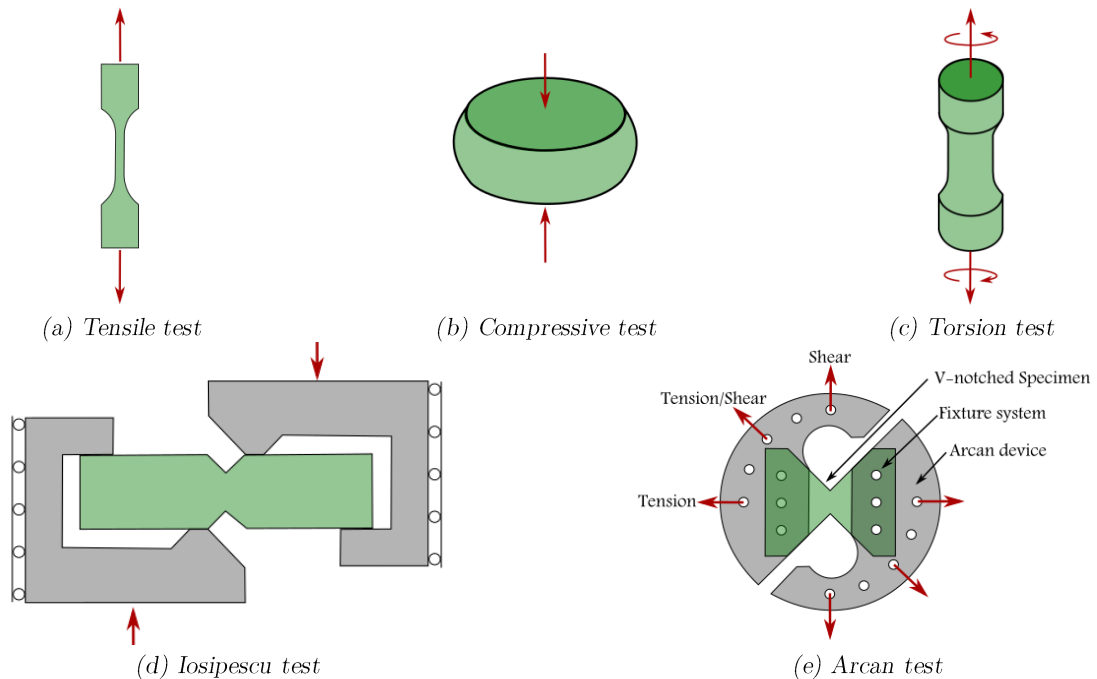


Figure II.2: Bulk tests used to characterize the behavior of adhesives.

II.1.2.2. Bonded tests

The second family considers the adhesion issue as a combination of the mechanical behavior of the adhesive (cohesive issue) and the role of the interfaces of the adherend (adhesive issue). This approach permits the global behavior of the assembly to be described accurately since the bonded joint is entirely tested. However, the analysis and modeling of the tests might be quite difficult to realize. This is because the global response of the specimen depends on the behavior of the substrates, the adhesive, the composite or metal plate (if applies) and the interfaces. In consequence, the global behavior of the assembly must take into account all these combined behaviors on the analysis of the experimental

results as suggested by Adams (R. D. Adams *et al.*, 1997). The most commonly used bonded configurations are presented below.

II.1.2.2.1. Lap-shear test

The analysis of the adhesive behavior under shear loadings in an assembly is commonly carried out by means of the single or double lap-shear tests. These types of test present an easy testing procedure which is beneficial to the automotive industry. At the same time, it permits thin adhesive joints to be tested at the real scale of applications. The use of standard procedures such as (ASTM D5868, 2014) has reduced the scattering due to the specimen preparation and the experimental procedure. However, such tests present considerable non-uniform stress distribution along the bonded surface with important edge effects, which might lead to premature fracture initiation at the interfaces (when adhesive is the weak link of the assembly) or to composite failure due to peel stresses peak at the edges of the overlap region (when the transverse tensile strength of the composite is lower than the adhesive strength). Some authors have proposed different geometries to avoid these problems and ensure a more uniform stress distribution (Cognard *et al.*, 2010). However, these solutions imply manufacturing issues and a rigorous analysis of the experimental results.

II.1.2.2.2. Thick adherend shear test (TAST)

The geometry of the adherends of the lap-shear test has been modified in order to overcome the inherent weaknesses of the specimen. Thus, thick rigid adherends with a short overlap length are used to subject the adhesive joint under shear stresses. Various thick adherend geometries have been suggested, including those specified in (ISO 11003-2, 2001) and (ASTM D5656-04, 2004). In principle, shear stress is the predominant stress along the overlap length; however, large peel stresses are also present at the corners of the overlap region, causing premature failure.

II.1.2.2.3. Butt joint test (tension-compression/torsion)

Some mechanical properties such as the elastic modulus, the Poisson's ratio and the average strength of thin bond-lines in tension, compression and shear may be determined by means of the butt joint tests. Cylindrical steel butt joints are the most common type of specimen; although, some other geometries have been included in the standards (ISO 6922, 1987). This type of test is difficult to perform due to the possible bending of substrates during curing and testing. Therefore, premature failures and great scattering are a common problem in this type of test. Furthermore, edge effects are observed at the interface of the adhesive joint. This is because the adhesive is restrained in the radial and circumferential directions by the adherends during testing, which induces radial and circumferential stresses at the edges of the bonded surface (ASM International, 1990). A specific device able to reduce the edge effects and the scattering of the results has been

proposed by Arnaud (Arnaud *et al.*, 2014); however, the machining of substrates and bonding system remains quite difficult.

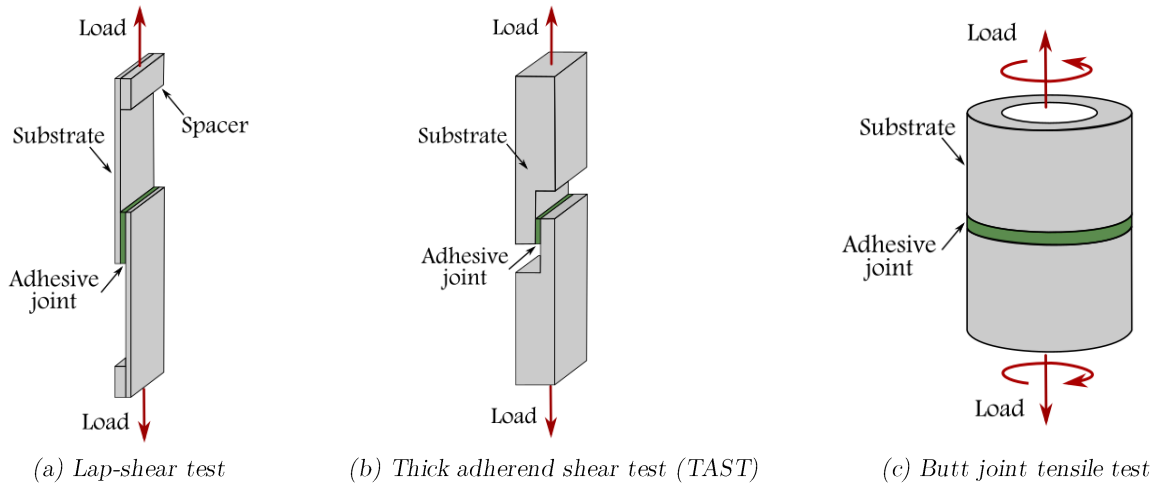


Figure II.3: Bonded tests used to characterize the behavior of adhesives.

II.1.3. The Modified Arcan approach

In order to analyze the behavior of adhesives under combined proportional compression-tensile/shear loadings, an improved Arcan test was developed by Cognard (Cognard *et al.*, 2005). Subsequent studies have shown the advantages of this experimental test and have consolidated a reliable method to characterize the behavior of adhesives and their assemblies (Thevenet *et al.*, 2013)(Sohier *et al.*, 2013)(Alfonso *et al.*, 2015).

The modified Arcan device is composed of two half-moon pieces made of high stiffness steel. It ensures an adequate load transmission from the tensile machine to the specimen. The specimen is gripped to the half-moon pieces by a fixture system. Then, the Arcan apparatus (the two half-moon shaped pieces and the specimen) is placed in the holding and static grips of the tensile machine by means of clevis pins (see Figure II.4-a). The type of load is defined by the angle γ between the axis of the tensile machine (v -axis) and the normal plane of the specimen (z -axis) (see Figure II.4-b). Thus, the specimen can be subjected to four different types of load according to the orientation of the specimen (see Figure II.4-c):

- **“Tensile”**: Where a quasi-tensile load is applied in the adhesive joint. The orientation of the Arcan apparatus is $\gamma=0^\circ$ (see Figure II.4-d).
- **Pure shear**: Where a shear load is applied in the adhesive joint. The orientation of the Arcan apparatus is $\gamma=90^\circ$ (see Figure II.4-e).
- **Tensile/shear**: Where a proportional mixed tensile/shear load is applied in the adhesive joint. The orientation of the Arcan apparatus is $0^\circ < \gamma < 90^\circ$ (see Figure II.4-f).
- **Compression/shear**: Where a proportional mixed compression/shear load is applied in the adhesive joint. The orientation of the Arcan apparatus is $90^\circ < \gamma < 135^\circ$ (see Figure II.4-g).

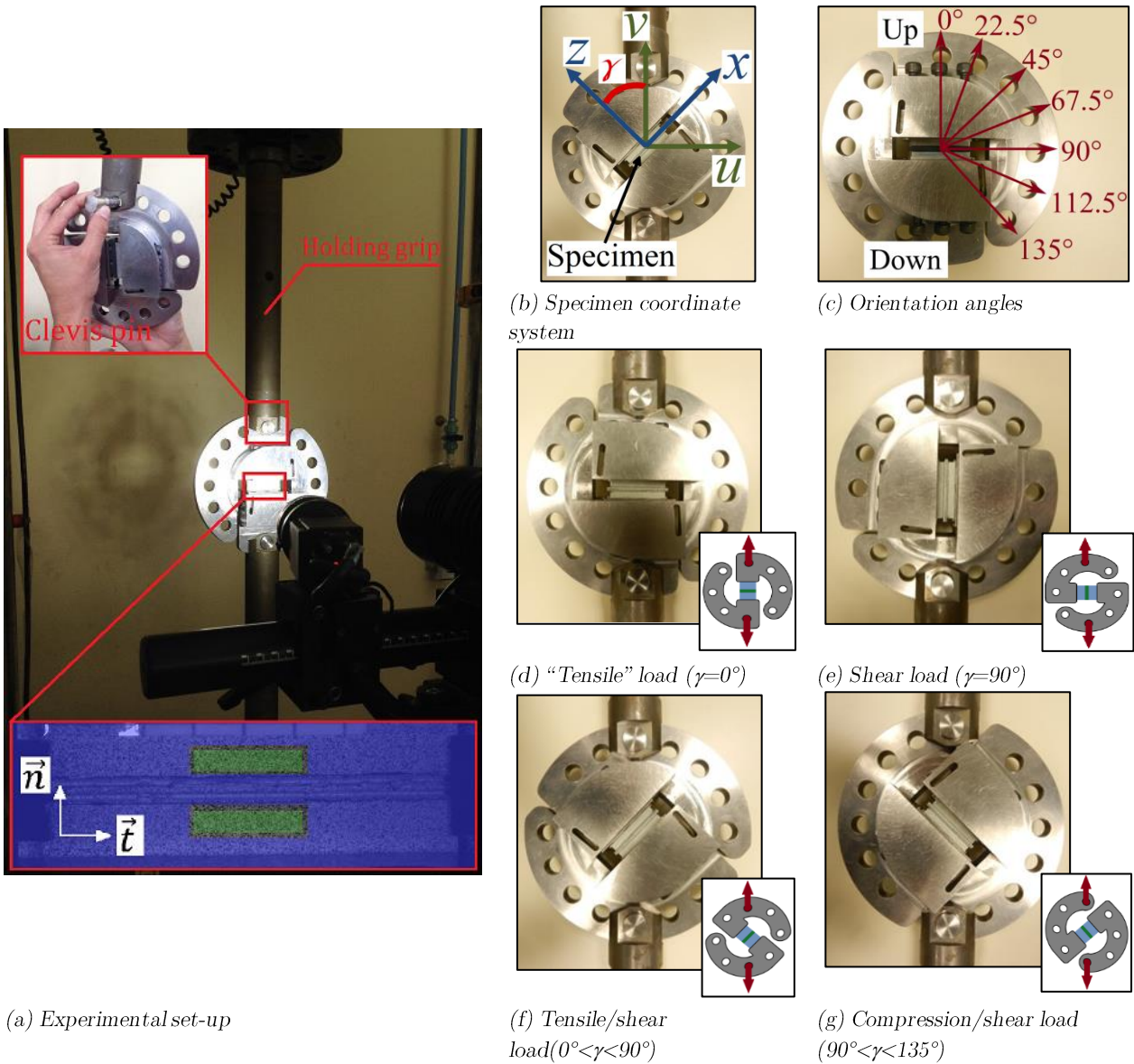


Figure II.4: Experimental set-up of the modified Arcan test and orientations of the Arcan device to generate the different mixed loadings.

II.1.3.1. The Arcan specimen

There are three Arcan specimen versions to analyze the behavior of adhesively bonded assemblies:

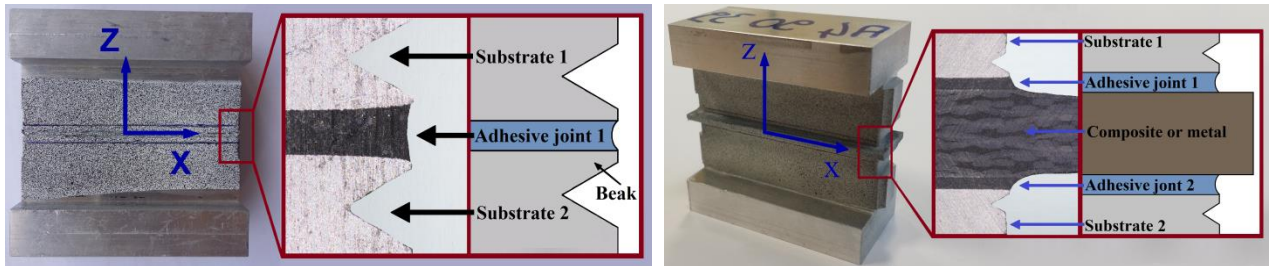
- (i) Adhesive specimen: the first specimen version is composed of two substrates bonded by an adhesive joint in the middle plane of the specimen (Figure II.5-a). This type of specimen allows the characterization of the adhesive depending on the type of fracture. Indeed, on the one hand, when a cohesive fracture is observed, the behavior and strength of the assembly correspond to the behavior and strength of the adhesive (assuming low or no plastic deformation of the substrates). This is because the adhesion strength at the substrate/adhesive interface is higher than the strength of the adhesive. On the other hand, if the failure occurs by adhesive fracture, the weak link of the assembly is the adhesive/substrate interface. In this case, it is recommended

performing a surface finishing process in order to improve the strength of the assembly.

- (ii) Metal/composite specimen: a thin composite plate is bonded to the two substrates in the middle plane of the specimen. Therefore, two adhesive layers are placed on each side of the composite plate (Figure II.5-b). Here, the behavior and the strength observed correspond to the overall behavior and strength of the assembly, which not only depends on the mechanical properties of the constituent materials (substrates, composite and adhesive) but also on the interfaces between themselves. In consequence, for some configurations, the fracture may occur by cohesive failure at the adhesive layer, by adhesive failure at the interfaces, by fiber-tear failure of the composite or by a combination of all of them. The geometry of the composite plate is shown in Figure II.7-d.
- (iii) Metal/metal specimen: the third version of the Arcan specimen interchanges the composite plate by a thin metal plate in order to analyze the behavior of metal bonded assemblies.

All the substrates used in this study were manufactured with an AW2022 aluminum-copper alloy (*Ultimate strength*=430MPa, *Yield strength*=270MPa, $E=72\text{GPa}$, $\nu=0.33$). This aluminum alloy is a commonly used in automotive applications due to its high manufacturability and relative good mechanical performance. Finally, the configurations of the Arcan specimens are:

- (i) aluminum/**adhesive**/aluminum assemblies
- (ii) aluminum/adhesive/**composite**/adhesive/aluminum assemblies
- (iii) aluminum/adhesive/**metal**/adhesive/aluminum assemblies



(a) Adhesive specimen

(b) Metal/composite specimen or Metal/Metal specimen

Figure II.5: Arcan specimen versions.

The influence of the edge effects has been overtaken thanks to the manufacturing of “beaks” all around the bonded surface of the substrates (See Figure II.5 and II.6-a) (Cognard *et al.*, 2008). These beaks considerably reduce the stress concentration on the edges of the bonded surface. Figure II.6 presents the stress distribution of the adhesive joint for different types of load obtained by FEM simulations under linear elasticity. As it can be seen, a non-homogeneous 3D stress distribution is created within the adhesive joint for all the types of load. In the case of “tensile” loadings, the out-of-plane tensile stress (σ_{zz}) is the principal stress with a regular value in the middle of the overlap length and a maximum value slightly higher near the edges. It is worth noting that (σ_{xx}) and (σ_{yy}) stresses are also

important, which implies that the “tensile” configuration of the Arcan test is far from pure tension load. This stress state is generated because the substrates of the specimen prevent free deformation of the adhesive joint in the (y) and (x) directions (which is representative of real adhesive bonding systems) (See Figure II.6-b). In shear loadings, a quasi-pure shear stress is observed on the adhesive joint with a parabolic shape distribution and a maximum value at the center of the bonding surface ($x = 0, y = 0, z = 0$) (See Figure II.6-d). Finally, the tensile/shear case is a superposition of the tensile and shear cases (See Figure II.6-c).

Even if the stress distribution of the adhesive joint without edge effects has been only presented for adhesive specimens, other studies have also confirmed the positive influence of the beaks in metal/composite assemblies (Alfonso *et al.*, 2015). Furthermore, other works have also shown that the stress distribution is maximal along the x -axis (path results in Figure II.6-a) and homogeneous over the thickness of the adhesive (Davies *et al.*, 2009).

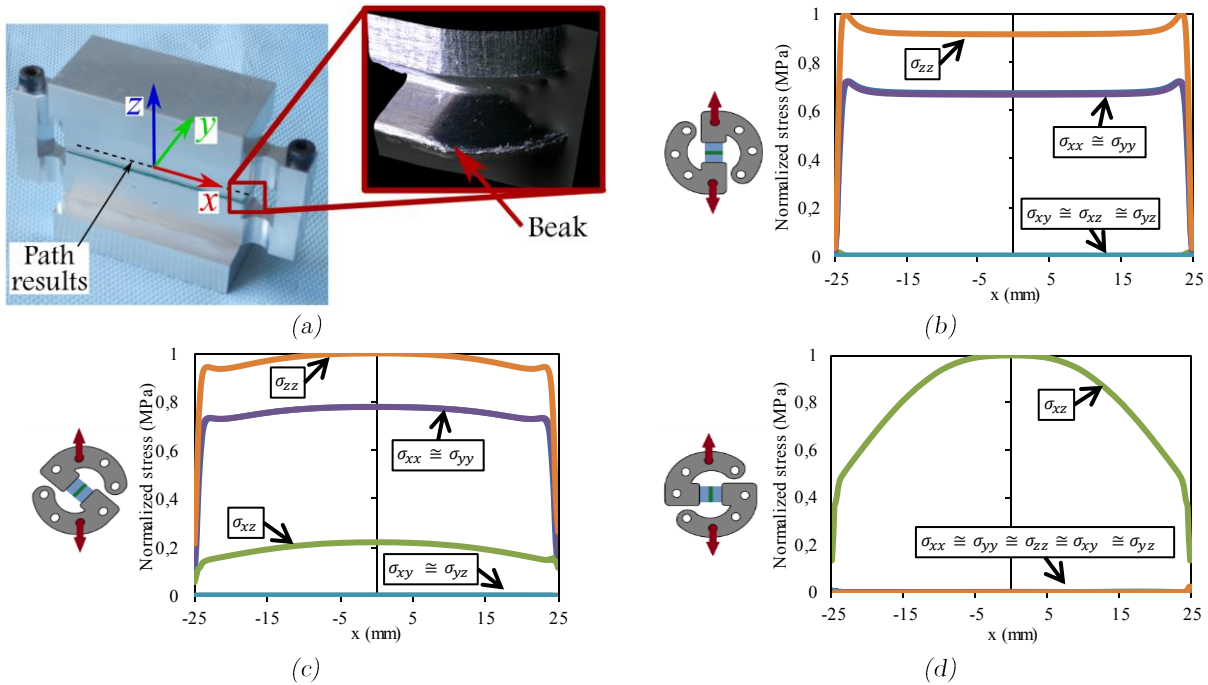


Figure II.6: Arcan specimen manufactured with “beaks” (a), stress distribution of the adhesive joint in “tensile” (b), tensile/shear (c) and shear loadings (d). The stresses are plotted along the x -axis ($y = 0, z = 0$) under linear elasticity.

II.1.3.2. The bonding system

After the adhesive is spread on the bonded surface of the substrates and of the composite or metal plate (if applies), the substrates are fixed by means of two screws as shown in Figure II.7-a. The specimen is maintained in this position during the curing cycle of the adhesive. The thickness of the adhesive is controlled by means of two spacers placed on each side of the substrates (Thevenet *et al.*, 2013). The contact surfaces between the spacers and the plate are parallel to the bonded surface and shifted 0.2mm to define the adhesive thickness as shown in Figure II.7-c. It is worth noting that there are two 0.2mm thickness adhesive joints when metal or composite plates are used, and one single 0.4mm thickness adhesive joint when no plate is used (in the case of adhesive specimens).

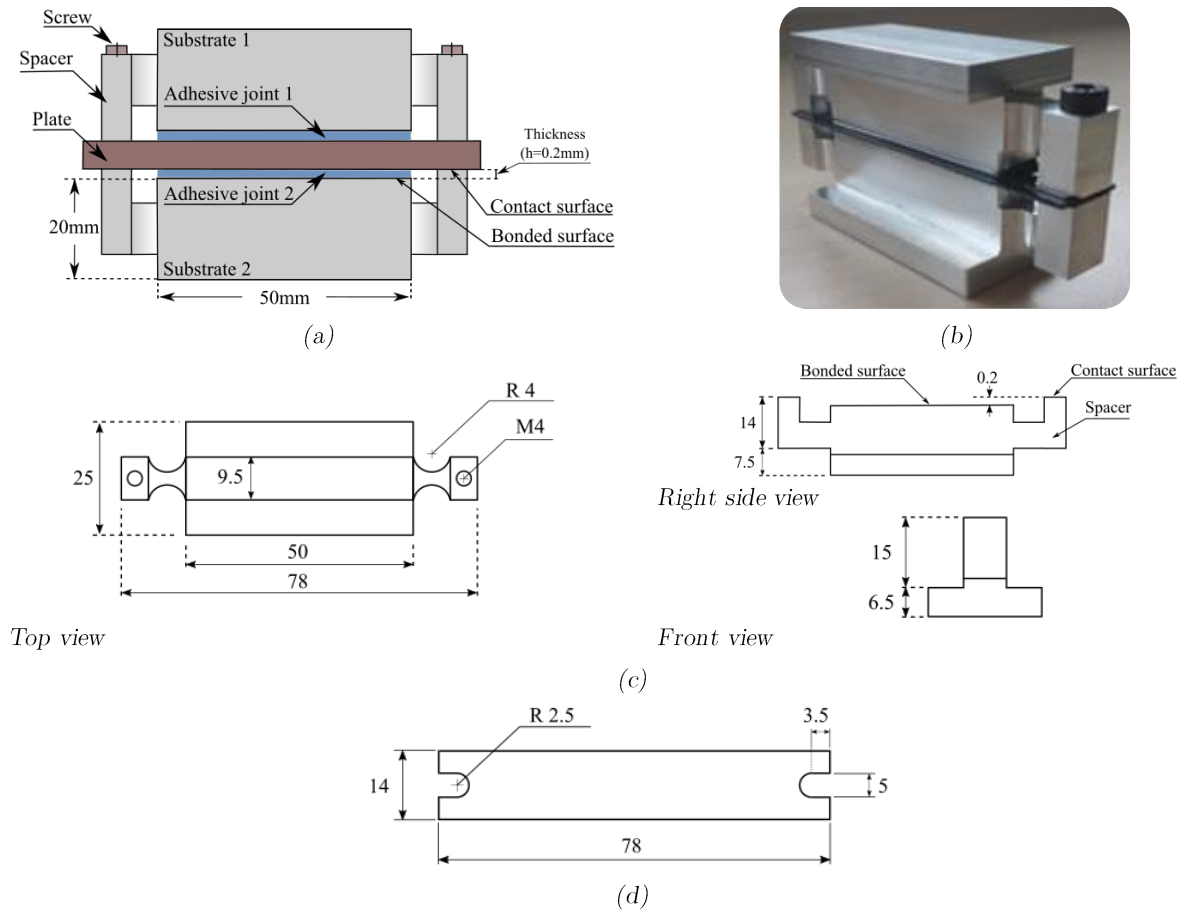


Figure II.7: Bonding system (a), photo of an Arcan specimen with a composite plate before polymerization (b), dimensions of the substrates (c) and the composite or metal plate in mm (d) (not to scale).

II.1.3.3. Post-processing

The post-processing technique used at the IRDL laboratory consists in the measurement of the relative displacement of the substrates using a Digital Image Correlation System (GOM, 2011). For that, a speckled pattern is applied over the substrates and the relative displacements is calculated between the two green regions presented in Figure II.4-a. These 10x3 mm regions are always at a distance of 2 mm from the bonded joint for all the specimens, guaranteeing a good comparison of the results. The load applied to the specimen is recorded by the machine load-cell. These data give us information about the behavior and the strength of the assembly. Note that the relative displacement of the substrates is composed of a normal displacement “ND” (which is the relative displacement along the \vec{n} direction) and a tangential displacement “TD” (which is the relative displacement along the \vec{t} direction) (See Figure II.4-a). In this manner, large normal displacements are observed in “tensile” loadings, and large tangential displacements are observed in shear loadings. Combined displacements are presented when mixed tensile-compression/shear loadings are applied.

Because of the nature of the Arcan test, the strain-stress curve (typically used in material science) is replaced by a load-displacement curve. Indeed, the stress in the adhesive is heterogeneous over the bonded surface (See Figure II.6), and therefore it is not possible to

extract the stress directly from the knowledge of the load. Some authors have determined a correction coefficient to estimate the real value of the stress on the adhesive joint under linear elasticity (Créac'hadeuc *et al.*, 2008).

II.1.4. The selected characterization tests

After comparing the advantages and drawbacks of the different tests proposed in the literature, it has been concluded that the most adapted test to characterize the joining techniques of this study is the Arcan test. This choice was made for two main reasons: *(i)* the Arcan test allows the characterization of joining techniques under different combinations of tensile-compression/shear loadings, and *(ii)* it possesses a well-known experimental procedure to analyze the behavior of adhesives in an assembly. Indeed, the modified Arcan methodology presented in section II.1.3 has been widely used to characterize the behavior of adhesives and their assemblies at the “Dupuy de Lôme Research Institute” (IRDL). Problems such as non-uniform stress distribution in the adhesive layer, scattering of the results and post-processing have been already solved. However, the use of the Arcan test on stud bonding systems, laser welded assemblies and RivSet joints has not been studied yet. Consequently, the experimental procedure has been slightly modified. Chapter III presents a modified Arcan specimen suitable to these joining techniques. Nevertheless, it is worth noting that stud bonded and laser welded assemblies were tested with traditional lap-shear and cross-tension tests instead of the modified Arcan device. This was because the specimens were manufactured before the beginning of the current Ph.D. study. Therefore, RivSet joints and bonding systems were the only techniques characterized by means of the Arcan device.

It is important to say that there is no technical impediment to characterize stud bonded and laser welded assemblies through Arcan tests. Indeed, the possibility of using the modified Arcan device to characterize different types of assemblies is open.

II.2. Sequential solution methodology

As described in Chapter I the automotive industry must solve the problem of joining dissimilar materials over the next years. This general problem may be segmented in various small problems that have been solved step-by-step during the current Ph.D. study. Thus, a sequential methodology was followed in order to achieve the objectives of the project:

First, the preselected joining techniques were tested under quasi-static mixed loadings in order to determine the strength of their assemblies. The objective was the quantitative and qualitative analysis of the experimental results in order to select the main joining technique providing the higher mechanical performance and good compatibility with the materials studied. Lap-shear, cross-tension and modified Arcan tests were used to subject the joining techniques under shear, “tensile”, tensile/shear and compression/shear loadings. A particular importance was given to adhesive bonding systems since they permit the whole set of materials of the study to be joined. Thus, the experimental results are presented

separately in Chapter III, where stud bonded joints, laser welded joints and RivSet joints are analyzed, and in Chapter IV, where adhesively bonded assemblies are studied.

After the analysis and comparison of the experimental results, the adhesive bonding system has emerged among all the other joining techniques as the structural solution allowing for the materials of the study to be assembled with great ease, high mechanical performance and good compatibility at relatively low cost. Therefore, the next step was the modeling of this technique. In order to achieve this objective, it was necessary the correct identification of the main phenomena present on the behavior of the adhesives of the study: Betamate-1822 and Sikapower-498. The next step was the characterization of these adhesives under mixed quasi-static loadings. Chapter V is then focused on this aspect. The adhesives were subjected to different ratios of compression-tensile/shear stresses under monotonic, creep and cyclic loadings.

Once the mechanical behavior of the adhesives has been identified, the modeling of the adhesives can be investigated. Chapter VI presents a non-linear viscoelastic model that describes the behavior of the adhesives of the study. This model is based on a spectral distribution of the viscosity and a softening law to describe the non-linear behavior of both adhesives. The identification procedure of the material parameters of the behavior law is based on the multilevel creep test. A good correlation between the numerical simulation and the experimental results validated the use of the proposed approach.

The use of adhesive bonding systems as the structural joining technique imposes a logistic problem due to the relative long polymerization process of the adhesive with regard to the automotive production rate. In order to reduce this loss of time, an additional attachment system must be used to fix the bonded parts during the curing cycle of the adhesives. Therefore, the “final” solution to assemble dissimilar materials corresponds to a hybrid joint where a fast attaching system will fix the parts during the hardening of the adhesive. Then, the polymerized adhesive will ensure the structural integrity of the assembly during the automobile service life.

RivSet joints were chosen by the partners of the project as the attachment system. Therefore, it was necessary to analyze the good compatibility and the mechanical performance of hybrid RivSet/adhesive joints. The characterization of the “final” solution under shear loadings is presented in Chapter VII as a prospect of the study. This chapter is also devoted to the conclusions of the current Ph.D. thesis and to the analysis of some aspects that should be considered in the use of adhesive bonding systems in order to accurately predict the behavior of the assemblies studied.

Figure II.8 represents the methodology followed in this study in order to solve the “automotive issue”.

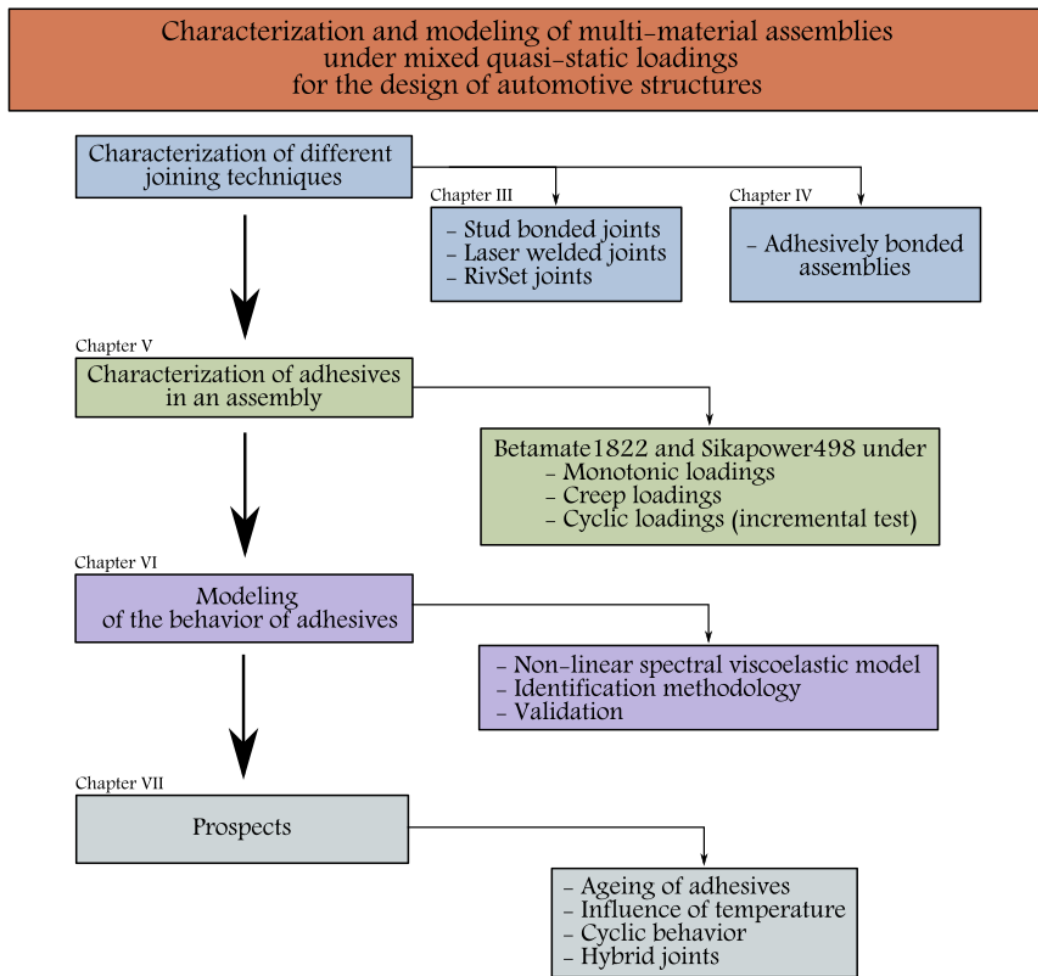



Figure II.8: Methodology followed in the current study.

**PART B: Activities performed in
this study**



Chapter III. Characterization of stud bonded, laser welded and self-pierce riveted assemblies

Introduction

The use of light materials such as aluminum and composites in the body structure of automobiles leads to the problem of joining dissimilar materials. A great number of techniques have been proposed to solve this issue and a wide range of possibilities can be found in the literature. Among all these possibilities, the partners of the FASTLITE project have selected four joining techniques able to join the materials studied in this study: stud bonding, laser welding, self-pierce riveting and adhesive bonding. This chapter is devoted to the characterization of the first three joining techniques and the analysis of their performance under monotonic tensile and shear loadings.

The experimental set-up and the specimens of each joining technique are presented at the beginning of the chapter. Then, the results of the tests are analyzed and compared.

Table of contents

III.1. Experimental campaign.....	51
III.1.1. Stud bonding and laser welding in a lap-shear test	52
III.1.2. Stud bonding and laser welding in a cross-tension test	54
III.1.3. RivSet assemblies in an Arcan test	57

III.1. Experimental campaign

From a mechanical point of view, the joint must ensure its correct structural integrity during service life. Structural integrity comprises thus three elements: *(i)* joint strength, *(ii)* material compatibility and *(iii)* durability. Joint strength is a measure of the ability of a joint to support internal forces (such as thermal stress) and external forces. Material compatibility is the degree to which the individual elements of a joint are able to function as a unit and resist the tendency to degrade one another (as corrosion in the case of metal joints). Durability is the ability of a joint to retain its strength and serve its intended purpose over an extended period of time.

This chapter is principally devoted to *(i)* the joint strength and *(ii)* the material compatibility of the joining techniques presented in Table III-1. Hence, the stiffness, the failure load and the failure mode of such specimens need to be determined.

Two types of tests are typically used to assess the strength of assemblies. One is called the lap-shear test and the other is the cross-tension test (Yuh J. Chao, 2003). These tests permit the specimens to be tested under “shear” and “tensile” loadings respectively. The stud bonding and the laser welding techniques were then studied with this type of test. On the other hand, in order to propose a new test able to subject the joining technique to a wide range of combined tensile/shear loadings, a modified Arcan test (Cognard *et al.*, 2005) have been adapted to the RivSet technique.

The load was generated by means of a universal tensile machine with a maximum load of 100kN. The experiments were performed under displacement control at a rate of 10 mm/min in the case of stud bonding and laser welding, and 1 mm/min in the case of RivSet assemblies. All tests were carried out under standard laboratory conditions (around 40% air humidity and 25°C).

The relative displacements of the substrates were measured by means of an optical tracking system based on a Digital Image Correlation method (DIC system). The device employed to record the real-time images of the specimens was a single 1.3-megapixel camera with a 60Hz acquisition frequency. The post-processing of images was made using the Aramis® software version 6.3.1. (GOM, 2011). This procedure requires a speckled pattern applied on each substrate in order to track the displacements of the substrates during testing. The relative displacement between them was measured at two regions defined on the upper and lower substrates. These regions were always at the same position and at the same size for all specimens. This allowed a correct comparison between the results. The load applied to the specimen is recorded thanks to the machine load-cell.

Joining technique	Substrate 1		Substrate 2		Index
	Material	Thickness (mm)	Material	Thickness (mm)	
Stud bonding	DP600	1	SMC-Chopped	2.2	DP600/SMC-Chopped
	DP600	1	SMC-Fabric	2.2	DP600/SMC-Fabric
	DP600	1	Prepreg	2	DP600/Prepreg
	DP600	1	PA66	2	DP600/PA66
Laser welding	DP600	1	PA66	2	DP600/PA66
	22MnB5	1.5	PA66	2	22MnB5/PA66
RivSet	AL5182	2	SMC-Chopped	2.2	AL5182/SMC-Chopped
	AL5182	2	SMC-Fabric	2.2	AL5182/SMC-Fabric
	AL5182	2	Prepreg	2	AL5182/Prepreg
	AL5182	2	PA66	2	AL5182/PA66

Table III-1: Set of “tested” assemblies and their corresponding feasible joining technique.

III.1.1. Stud bonding and laser welding in a lap-shear test

Lap-shear tests have been performed in order to determine the shear strength of stud bonded and laser welded assemblies (See Table III-1). The specimens used to test the joining techniques are presented in Figure III.1. The specimens were composed of a metal substrate and a composite substrate measuring 125 mm long \times 38 mm wide. The overlap region was approximately 35 mm. Two spacers were bonded at the ends of the specimen in order to ensure a unidirectional load and avoid a parasitic torque. Thus, the measures (e_c), (e_{c1}) and (e_{c2}) are all equal (See Figure III.1-b). The green regions on each substrate represent the zones used to determine the relative displacement.

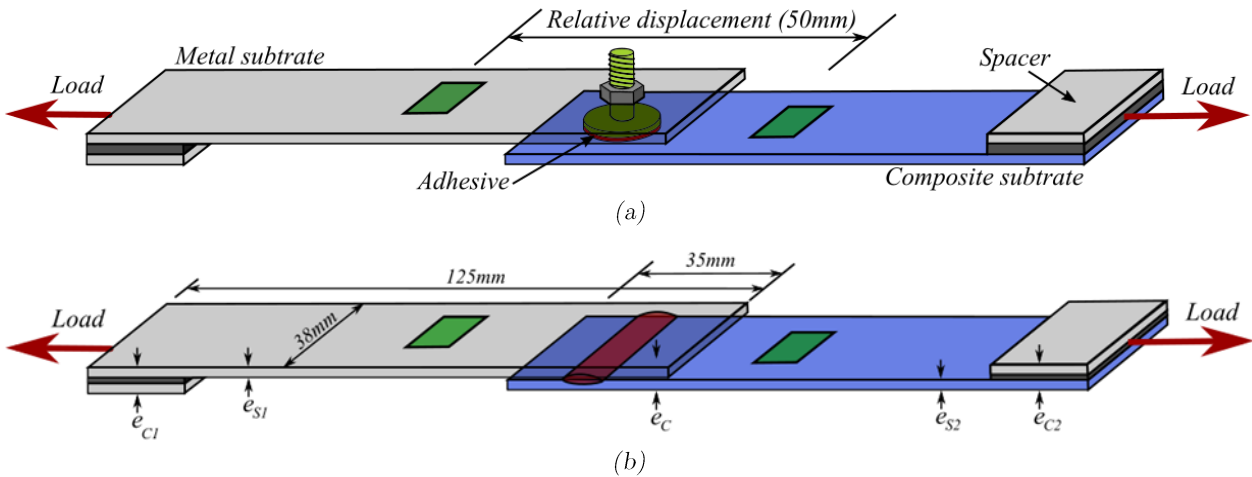


Figure III.1: Lap-shear specimens in the case of stud bonding (a) and laser welding (b) (Not to scale).

The experimental set-up of the tests is shown in Figure III.2. The DIC system and a real-time image of the specimen during testing can be seen. Six specimens for every assembly were tested in order to estimate the scattering.

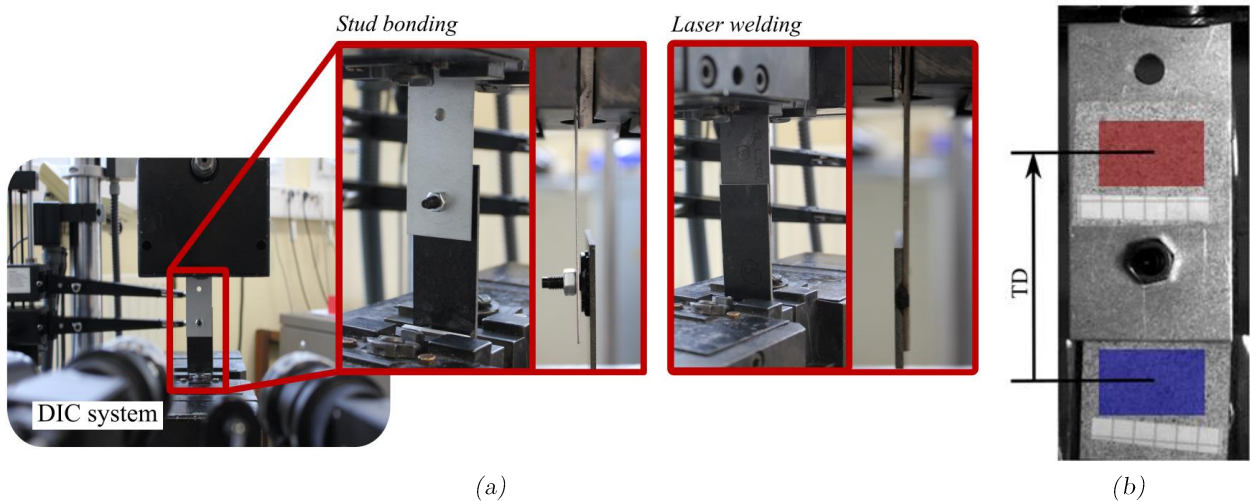


Figure III.2: Experimental set-up of the lap-shear test (a), real-time DIC system view of the specimen to measure the relative displacements of the substrates in the shear direction “TD” (b).

Figure III.3 summarizes the most relevant information about the mechanical strength of the assemblies in lap-shear test. As it can be seen, all stud bonded assemblies had a failure load between 2kN and 4kN. The failure of DP600/SMC assemblies always occurred by fiber-tear failure in the composite. DP600/Prepreg and DP600/PA66 assemblies exhibit an interphase cohesive failure mode. This type of failure corresponds to a cohesive failure where the fracture occurs near the adhesive-substrate interface. Thus, a thin layer of adhesive is observed on the composite surface and a thick layer of adhesive is left on the stud. The denomination of adhesive failure modes is based on the ASTM D-5573 technical standard (ASTM 5573, 1999).

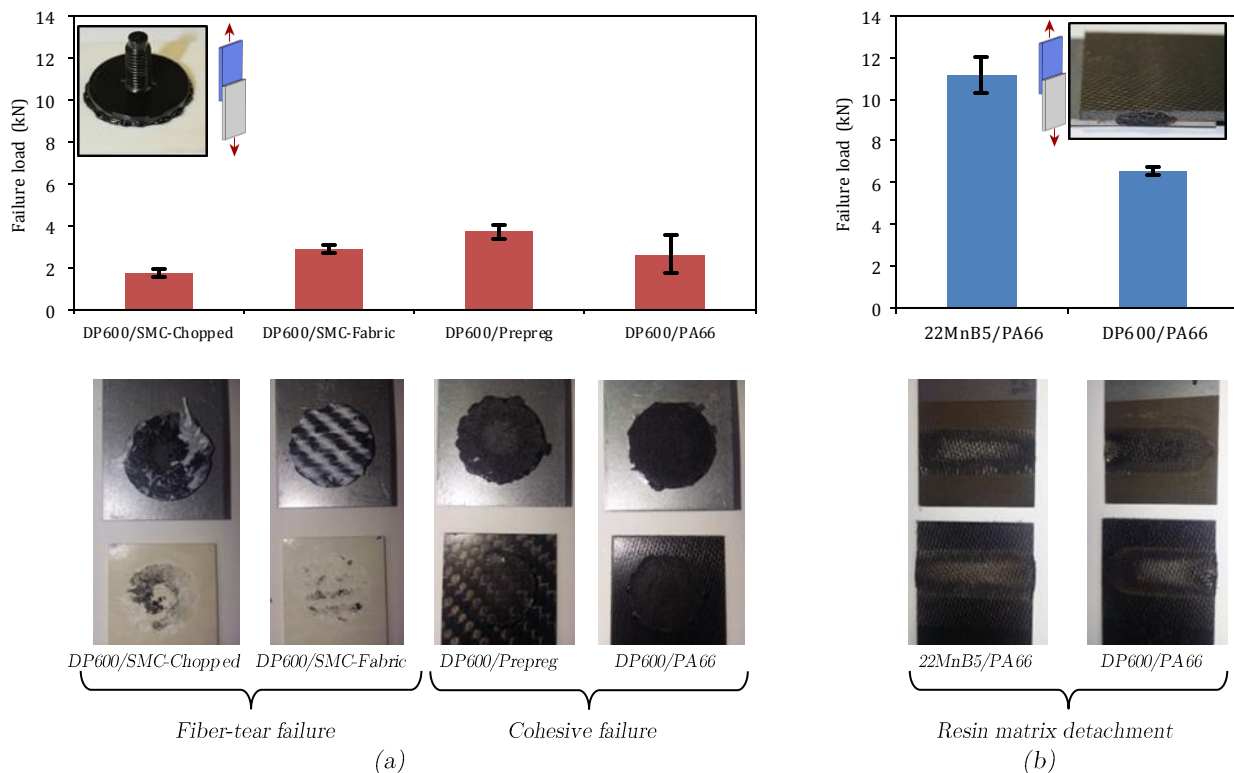


Figure III.3: Failure load and failure modes of stud bonding specimens (a) and laser welding specimens (b) in lap-shear test.

In laser welded assemblies, the failure load of the specimens was considerably large. Indeed, the 22MnB5/PA66 assemblies presented a failure load at 11kN, which is relatively high in comparison with some other classic joining techniques. The fracture of the welding specimens was always by a detachment of the resin matrix. A thin-layer of resin remains on the metal substrate with few or no glass fibers transferred from the composite substrate to the metal substrate; thus, a region with fiber exposure can be seen on the composite surface.

Figure III.4 plots the load-displacement curves of the assemblies tested in lap-shear test. All assemblies present a brittle behavior without any “non-linear” regime. Stud bonded assemblies describe a very similar behavior with a different value of the failure load. This aspect suggests that the adherend has no influence on the behavior of the assembly but a great impact on the failure load. Laser welded assemblies present quite a different behavior; indeed, the macroscopic response is characterized by a considerably larger failure load and a very low relative displacement. It is worth noting that a huge dispersion is observed in 22MnB5/PA66 assemblies.

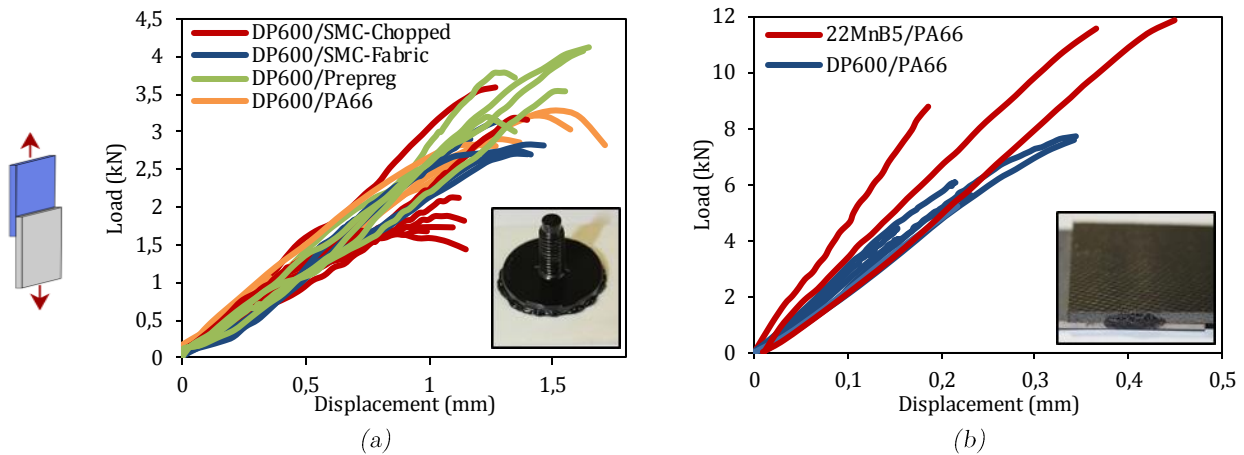


Figure III.4: Load-displacement curves of stud bonded assemblies (a) and laser welded assemblies (b) in lap-shear test.

III.1.2. Stud bonding and laser welding in a cross-tension test

A “tensile” load is applied to the joining technique by means of a universal tensile machine. The specimens are made of two substrates measuring 125 mm long \times 38 mm wide positioned in a (\times) configuration and joined at their center. Figure III.5-a shows the experimental set-up and the fixture system used to grip the specimens to the cross-tension device. As in the previous test, a DIC system was also used in order to track the displacements of the substrates. A speckled pattern was applied over the red and blue regions over the cross-tension device (See Figure III.5-b). Thus, the normal displacement of the substrate has been measured.

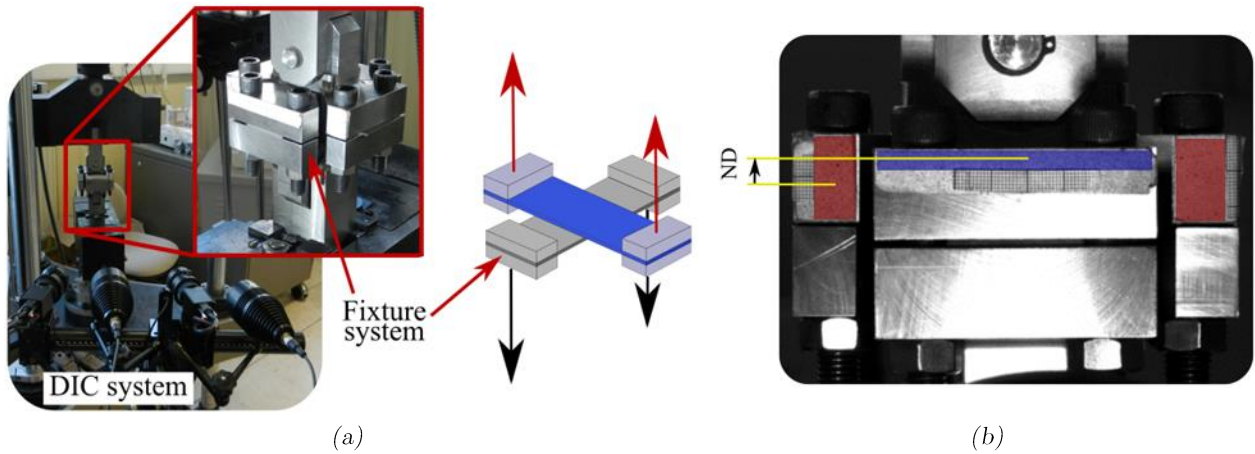


Figure III.5: Experimental set-up of the cross-tension test with a zoom at the fixture system that holds the cross-tension specimens during the test. Three of the four holding points that clamp the specimen are visible in the picture (a). Real-time DIC system view of the specimen to measure relative displacements of the substrates in the normal direction “ND” (b).

Three specimen configurations were tested (See Figure III.6):

- (i) Stud bonding specimens
- (ii) Laser welding specimens with the welding path parallel to the fabric orientation of the PA66 composite (referenced as longitudinal specimens)
- (iii) Laser welding specimens with the welding path perpendicular to the fabric orientation of the PA66 composite (referenced as transverse specimens)

The purpose of the last two specimens was the determination of the influence of the welding direction over the failure of laser welded assemblies.

The deformation pattern and the failure process of the specimens are presented in Figure III.7. As the specimen is loaded, a permanent bending deformation might occur in metal substrates. This aspect was principally observed in stud bonding specimens subjected to high tensile loadings. This is because of the stress concentration at the hole of the metal plate. Eventually, the substrates are completely separated when the fracture occurs.

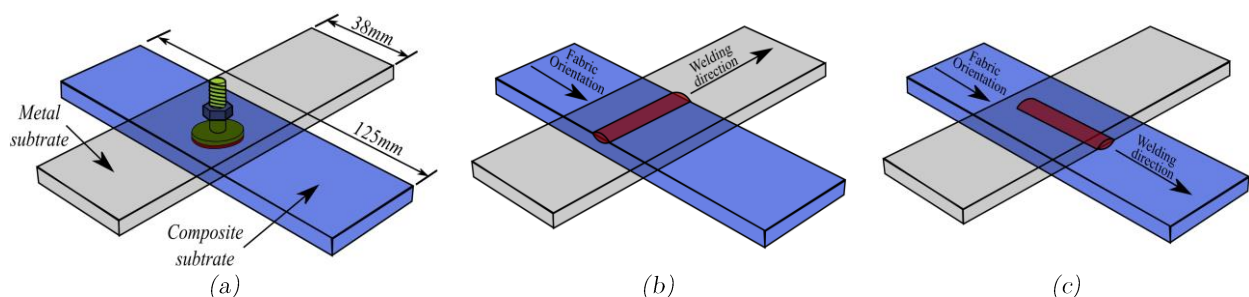


Figure III.6: Cross-tension specimens: stud bonding (a), longitudinal laser welding (b) and transverse laser welding specimens (c).

Figure III.8 compares the failure load and the failure mode of the assemblies in the study in cross-tension test. The standard deviation of the failure load of each assembly has

also been plotted. A very low failure load can be observed in all the tested assemblies (lower than 1.4kN) with similar failure modes to those obtained in lap-shear tests. In stud bonding, DP600/SMC assemblies has failed by fiber-tear failure in the composite; whereas DP600/Prepreg and DP600/PA66 assemblies failed by interphase cohesive failure. In laser welding, the failure mode was resin matrix detachment with exposition of the composite fibers.

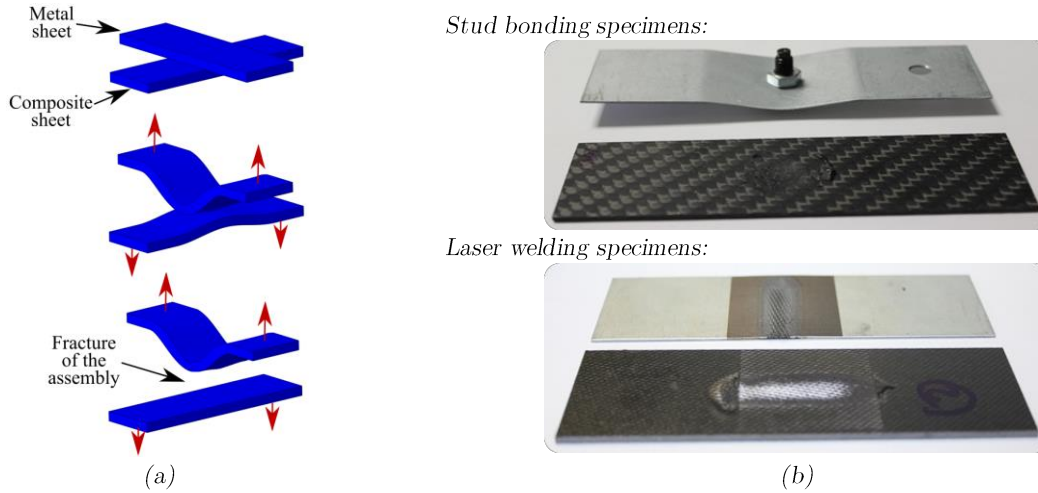


Figure III.7: Global deformation pattern of cross-tension specimens (a) and common final shape of the specimens after failure (c).

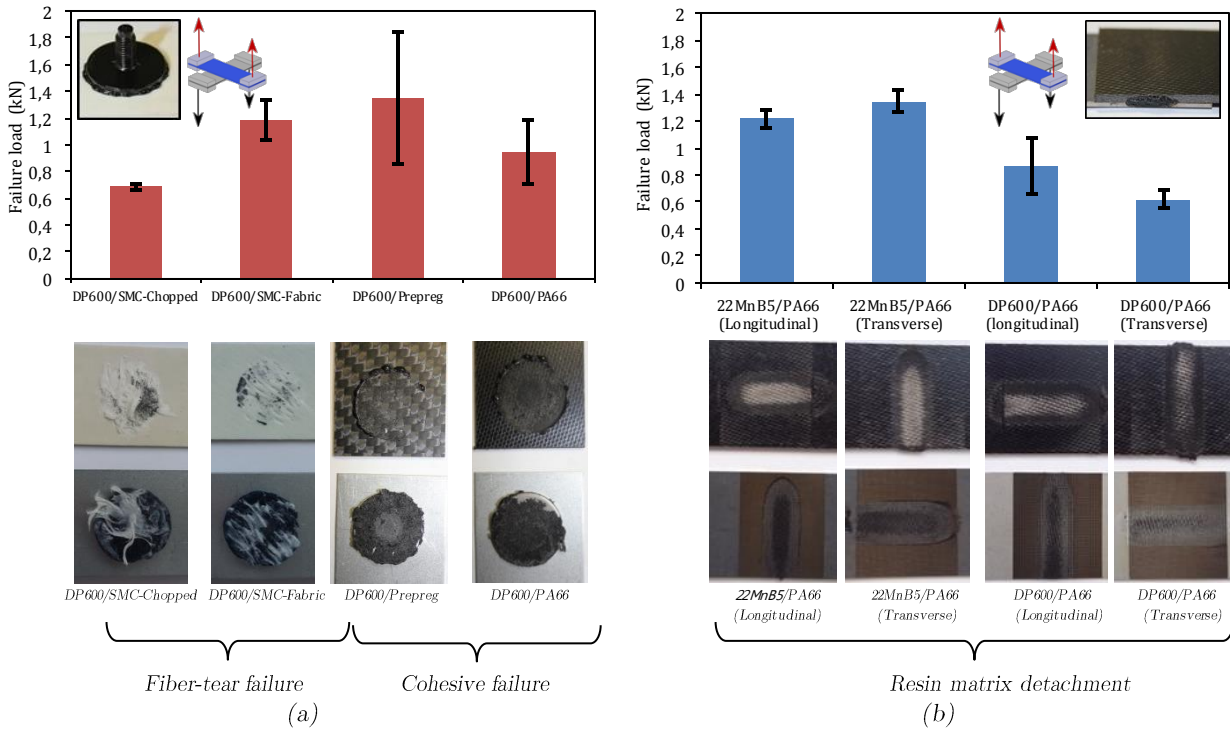


Figure III.8: Failure load and failure modes of stud bonding specimens (a) and laser welding specimens (b) in cross-tension test.

On the subject of the influence of the welding direction on the strength of laser welded assemblies, it is not possible to conclude a clear tendency from the results. Indeed, as shown in Figure III.9, the DP600/PA66 and 22MnB5/PA66 assemblies have a contradictory conclusion about the influence of the welding direction. In DP600/PA66 assemblies, the

longitudinal direction presents a higher rigidity and a higher failure load than the transverse direction. However, in 22MnB5/PA66 assemblies, this observation cannot be confirmed. Indeed, the longitudinal and transverse specimens present a very similar behavior. Furthermore, the failure load of the transverse specimens is slightly higher than the longitudinal specimens.

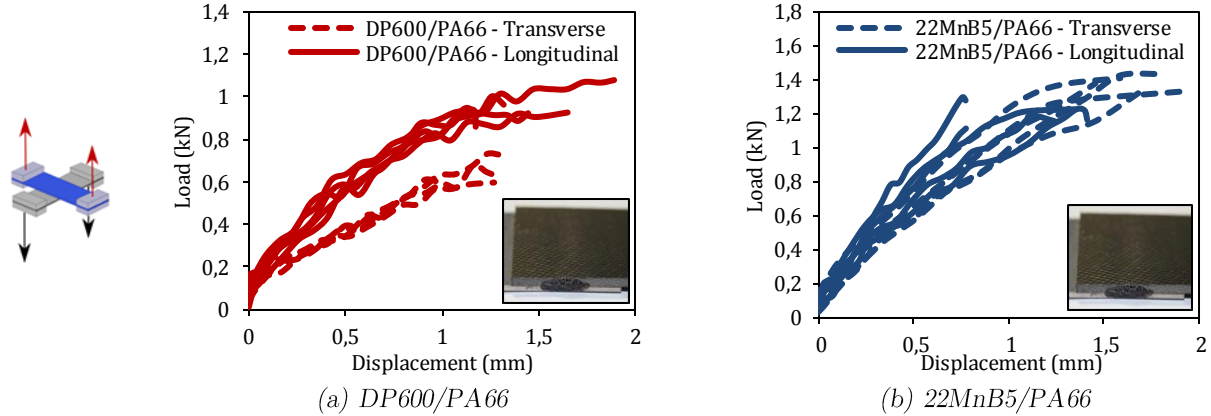


Figure III.9: Load-displacement curves of laser welded assemblies in cross-tension test.

The load-displacement curves of stud bonded assemblies are plotted in Figure III.10. The results show a really similar behavior for all assemblies and a slight non-linear regime that may be due to the plasticity of the metal substrates during testing.

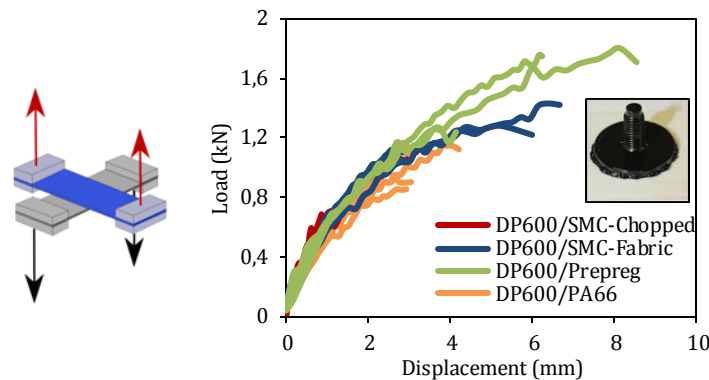


Figure III.10: Load-displacement curves of stud bonded assemblies in cross-tension test.

III.1.3. RivSet assemblies in an Arcan test

In order to propose an alternative to traditional tests (Han *et al.*, 2010) and be able to subject the specimen to combined tensile/shear and compression/shear loadings, a modified Arcan device (Cognard *et al.*, 2005) has been adapted to the RivSet assemblies (See Figure III.11). For the needs of the study, four different types of load were tested:

- Tensile load when $\gamma=0^\circ$
- Shear load when $\gamma=90^\circ$
- Proportional tensile/shear load when $\gamma=45^\circ$
- Proportional compression/shear load when $\gamma=135^\circ$

The RivSet assemblies (AL5182/composite) were fixed to the Arcan substrates by means of an adhesive. It allows an easy manufacturing process of the specimens and avoids stress concentrations on the composite plate. Therefore, the RivSet specimen is composed of a RivSet assembly bonded to two aluminum substrates. The specimen can be then gripped to the Arcan device when testing (See Figure III.12).

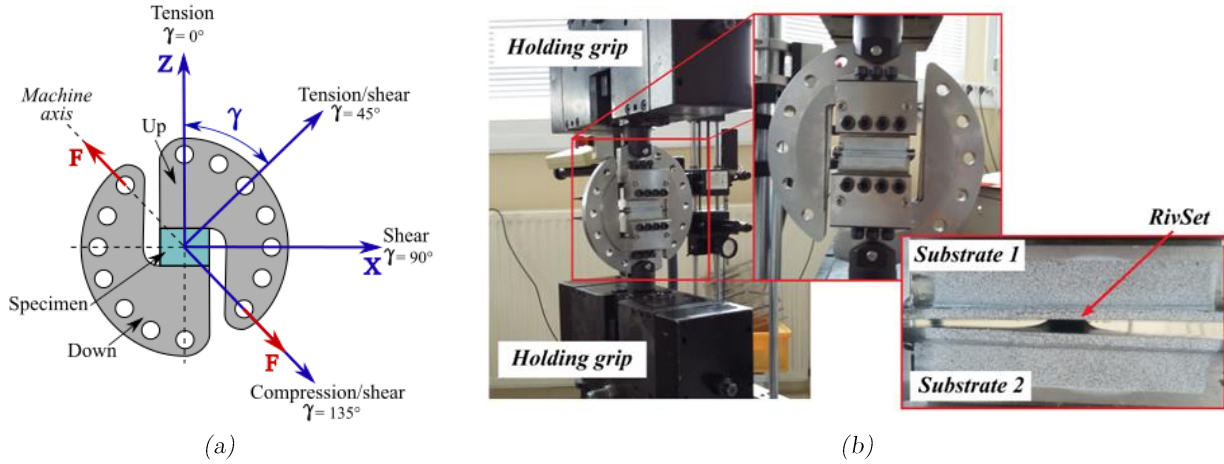


Figure III.11: Modified Arcan device (a), the type of load is defined by the angle (γ). Experimental set-up of the modified Arcan test with a RivSet specimen in “tensile” load (b).

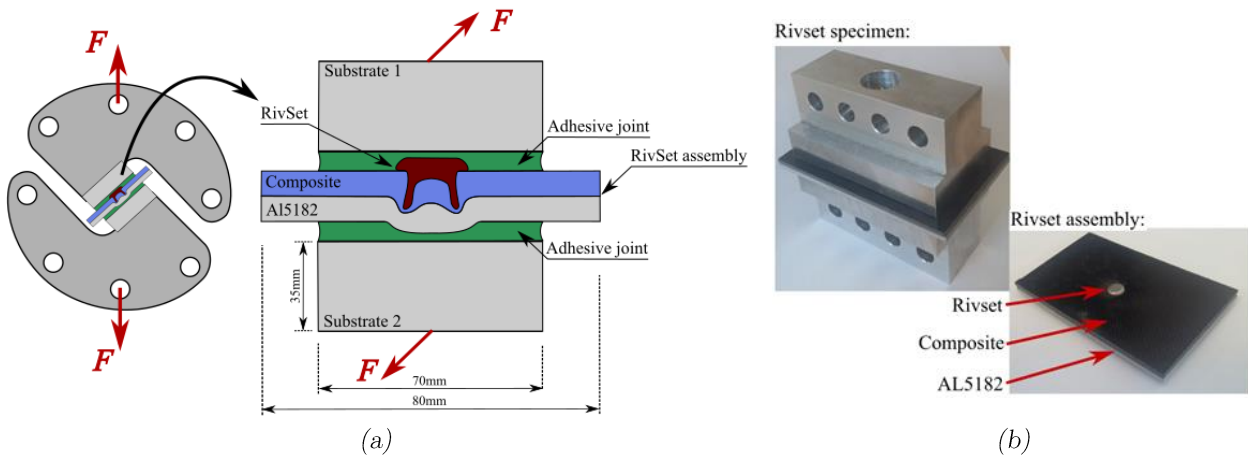


Figure III.12: RivSet specimen in a modified Arcan test (not to scale) (a). Picture of a RivSet specimen (b).

The hardening of the adhesive layers is carried out by means of the fixture system presented in Figure III.13. It permits the substrates to be fixed to the RivSet assembly through screws during the polymerization of the adhesive. The thickness of the adhesive layers is equal to 0.5mm, but the relative uniformity of the thickness overall the bonded surface is not ensured ($\pm 0.3\text{mm}$). This aspect has a minor influence on the purpose of this study since only the failure load of the RivSet joint is needed. However, it must be ensured that the fracture always takes place in the RivSet joint and not at the adhesive joints. Consequently, the adhesive chosen to bond the specimens was the Sikapower-498, which has a high relative Young modulus, yield strength and ultimate strength as compared with some other traditional adhesives (See Table I-4). Additionally, the bonded surface (approx. $40 \times 70 \text{ mm}^2$) has been defined in order to ensure that the adhesive remains elastic (See Figure III.14). The curing cycle of the Sikapower-498 adhesive corresponds to one hour

at 180°C. This thermal-cure process is advised by Syka® on the datasheet of the adhesive and should not have any influence on the used composite materials as marked on the datasheet of these materials (See Table I-1).

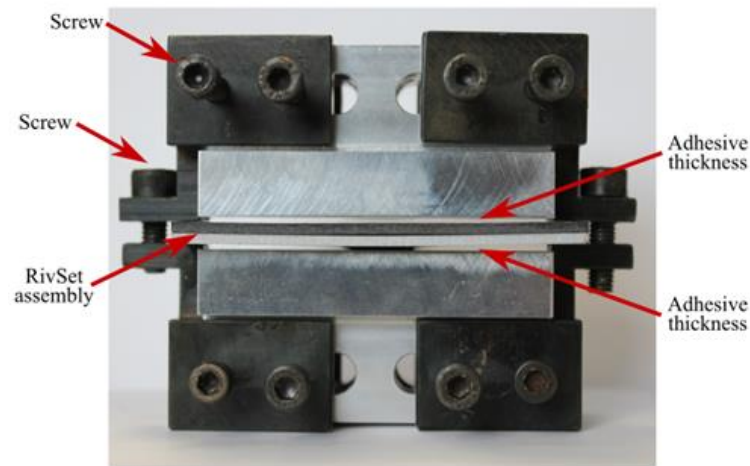


Figure III.13: Fixture system of the RivSet specimens during the polymerization of the adhesive layers.

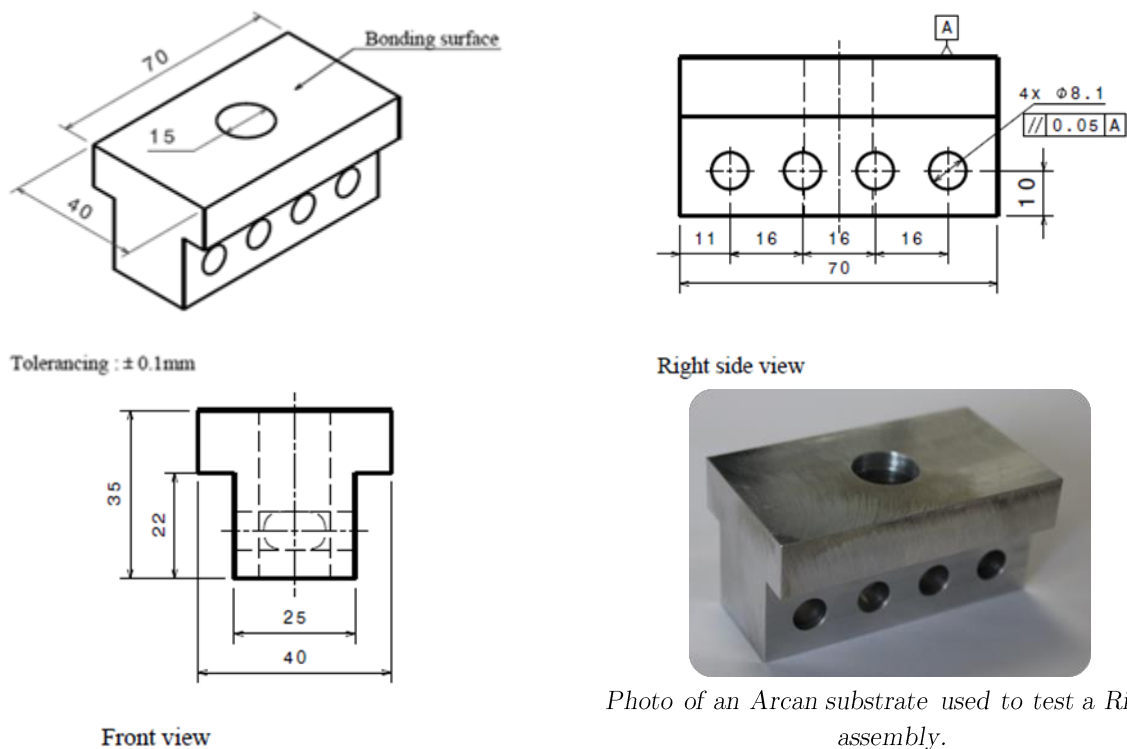


Figure III.14: Main dimensions of the RivSet substrate (mm).

The RivSet assemblies presented in Table III-1 have then been tested under four types of load: “tensile” ($\gamma=0^\circ$), tensile/shear ($\gamma=45^\circ$), shear ($\gamma=90^\circ$) and compression/shear ($\gamma=135^\circ$). Two tests per configuration (type of load and assembly) were performed and a low dispersion of the macroscopic response is observed. Figure III.15 presents the typical load-displacement curves obtained for the tested RivSet assemblies under different ratios of tensile/shear loadings. The shape of the curves is typically observed in metal self-pierce riveted assemblies tested in lap-shear test (He *et al.*, 2015). All curves are characterized by three different phases. The first phase corresponds to the “elastic” macroscopic response,

where a very small displacement proportional to the applied load is observed. During the second phase, the slope of the curve decreases and bigger displacements are observed. The load achieves its maximum value at the end of this phase. In the third phase, the load-displacement curve declines progressively. The assembly is completely separated at the end of the test.

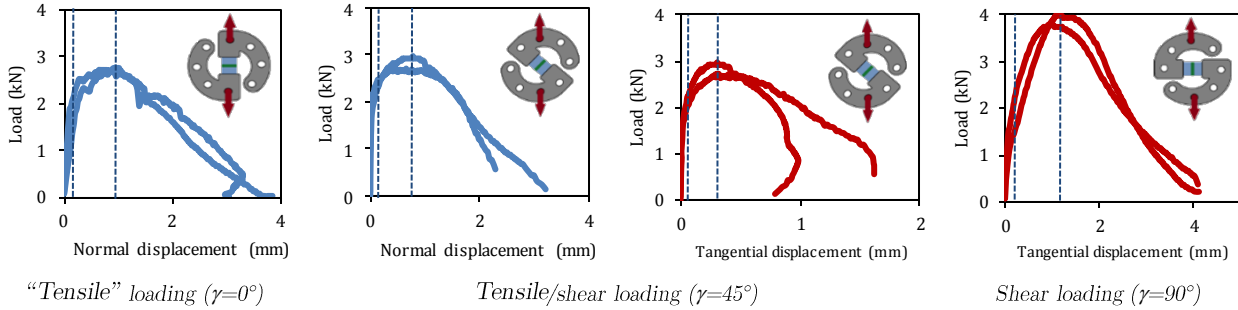


Figure III.15: Typical load-displacement of RivSet assemblies under different ratios of tensile/shear loadings. The plotted experimental data correspond to the AL5182/PA66 assembly.

Figure III.16 shows the average failure load of the RivSet assemblies in “tensile”, tensile/shear and shear Arcan tests. AL5182/Prepreg assemblies and AL5182/PA66 assemblies present the higher failure load for the three types of load.

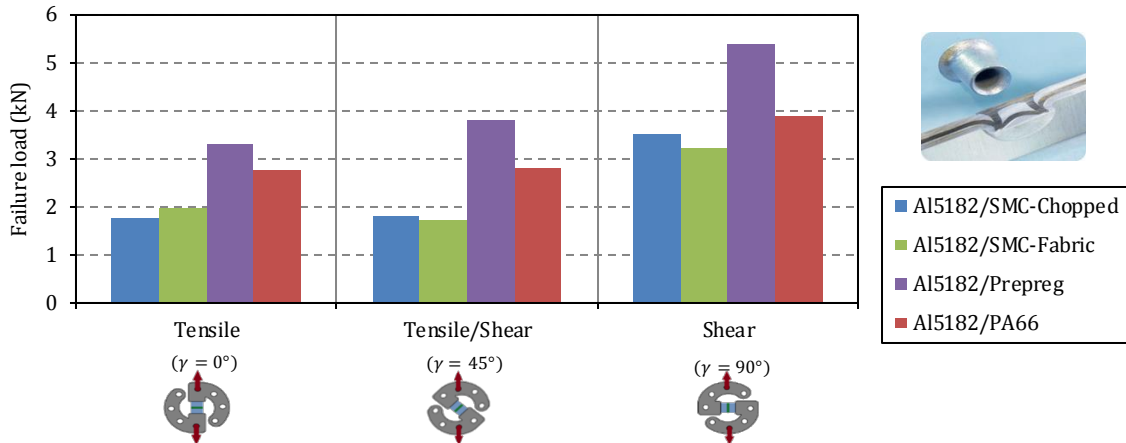


Figure III.16: Failure load of RivSet specimens in “tensile”, tensile/shear and shear Arcan tests.

The failure envelopes of the RivSet specimens are shown in Figure III.17. Some additional points corresponding to the failure load of AL5182/PA66 assemblies in lap-shear and in cross-tension tests found in the literature have also been plotted (Gay *et al.*, 2016)(Bollhoff, 2013). The failure loads determined by lap-shear tests and cross-tension tests are lower than the failure load obtained by Arcan tests. This aspect is more appreciated in cross-tension tests, where the tensile failure load obtained is about 40% lower than in Arcan tests. These differences can be explained by the different type of load generated by the tests. Indeed, during testing, the Arcan specimen is loaded uniformly over a large surface close to the RivSet joint, which reduces significantly the bending deformation of the substrates observed in cross-tension test and lap-shear test (Han *et al.*, 2010) (See Figure III.18 and Figure III.19).

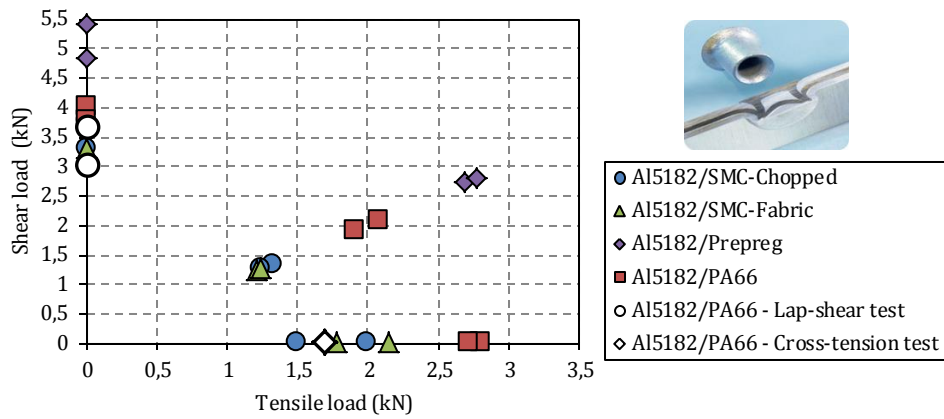


Figure III.17: Failure envelopes of the RivSet assemblies under tensile, tensile/shear and shear loadings.

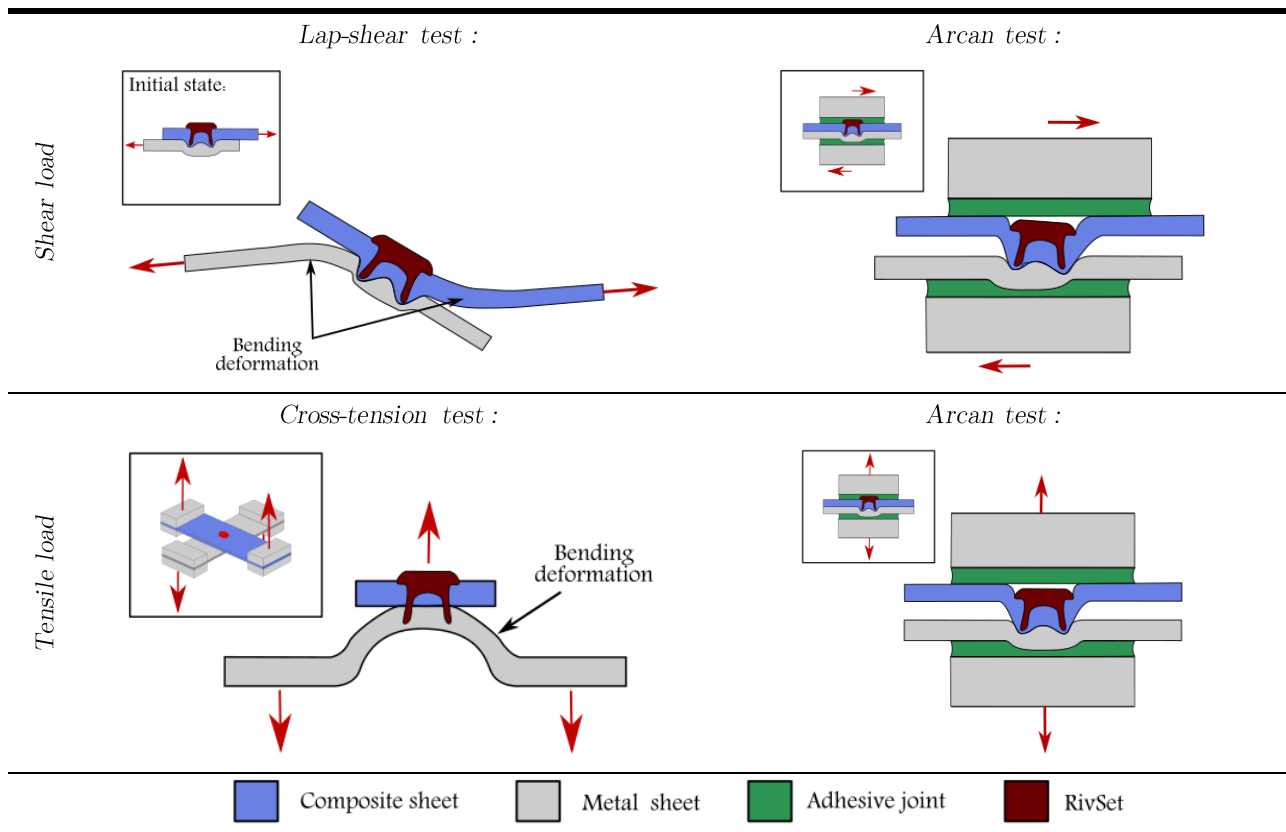


Figure III.18: Comparison of the global deformation pattern in lap-shear, cross-tension and Arcan test.

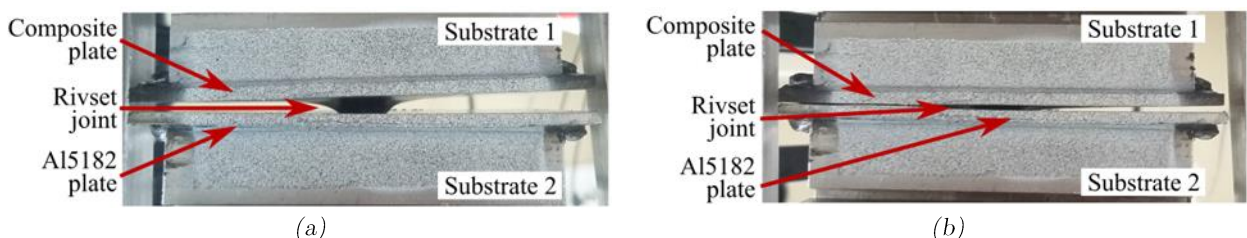


Figure III.19: Typical deformation of the RivSet specimen before failure in a “tensile” Arcan test (a) and in a shear Arcan test (b).

The failure modes of the RivSet specimens studied in this chapter are given in Figure III.20. These failure modes are typically observed in metal self-pierce riveted assemblies

tested by means of U-shape specimens (Porcaro *et al.*, 2006). They can be grouped into four different types:

- Fiber-tear failure: The failure occurs within the composite plate. Only one single SMC-Chopped specimen has failed by this mode.
- Pull-over failure : The RivSet goes through the composite plate, dragging the material under the RivSet head.
- Tilting and pull-out of the fastener : The RivSet rotates generating yield and fiber-tear inside the composite plate while it is sliding out from the aluminum plate. It was the predominant failure mode.
- Adhesive failure : The failure of the specimen occurs at the composite/adhesive interface. This type of failure does not permit the analysis of the failure of the RivSet assembly. AL5182/Prepreg in tensile loadings was the only assembly affected by this failure mode.

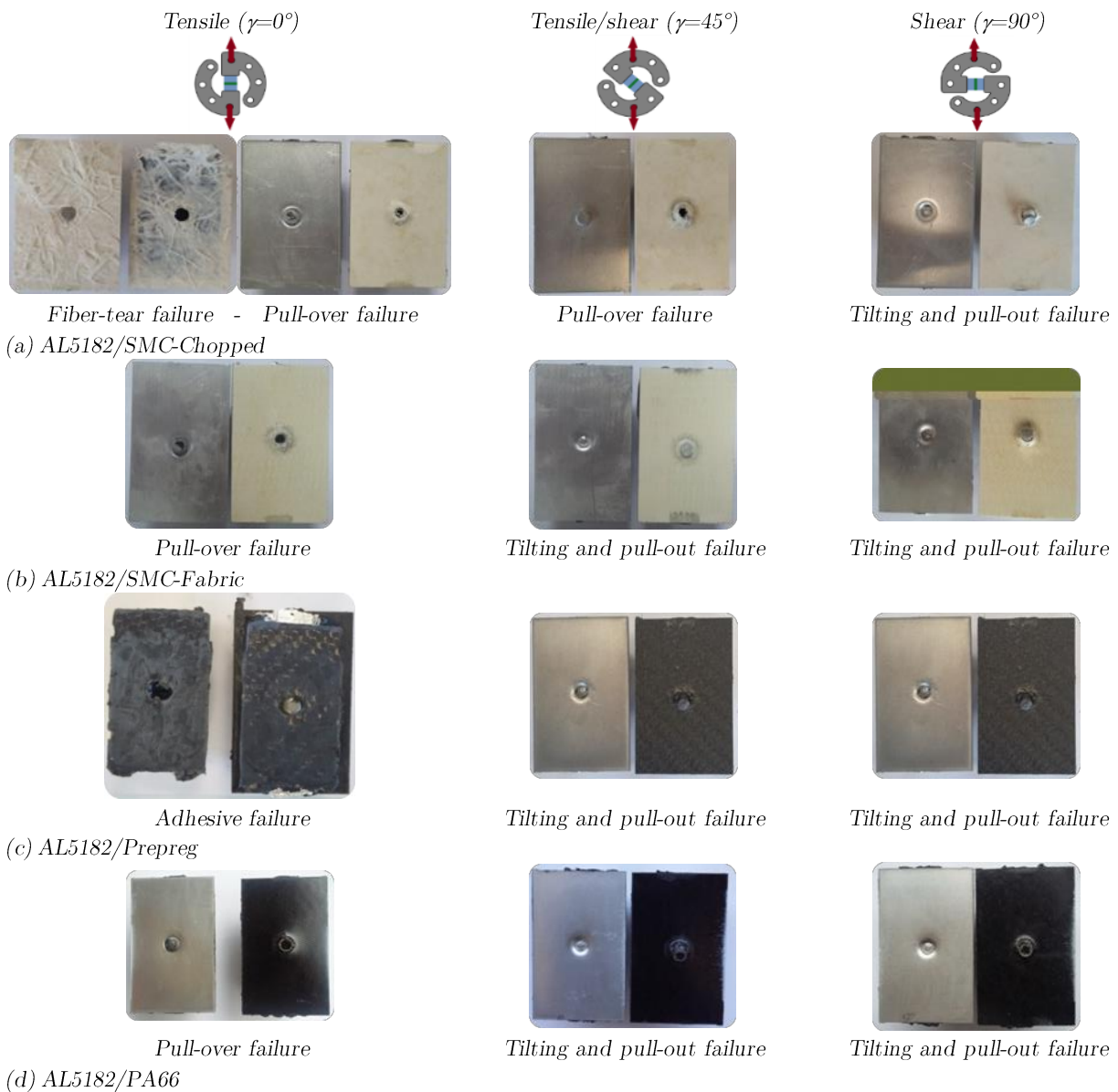


Figure III.20: Failure modes of the RivSet assemblies in “tensile”, tensile/shear and shear loadings.

Figure III.21 presents a typical load-displacement curve of a RivSet specimen in a compression/shear Arcan test. It can be seen that the macroscopic response of the assembly is composed of two different phases:

- (i) An initial phase where the specimen is progressively loaded until the failure of the RivSet joint. In this phase, the RivSet rotates generating fiber-tear inside the composite plate and deforming the aluminum sheet. The failure of the RivSet joint occurs when the RivSet is completely detached from the two adherends.
- (ii) Then, the detached RivSet remains stuck between the composite and the aluminum plates due to the compression stress. Even if the integrity of the assembly is no longer ensured, the failure of the specimen does not occur and the applied load continues to increase. This is because of the flattening of the detached RivSet, which retards the final failure of the assembly.

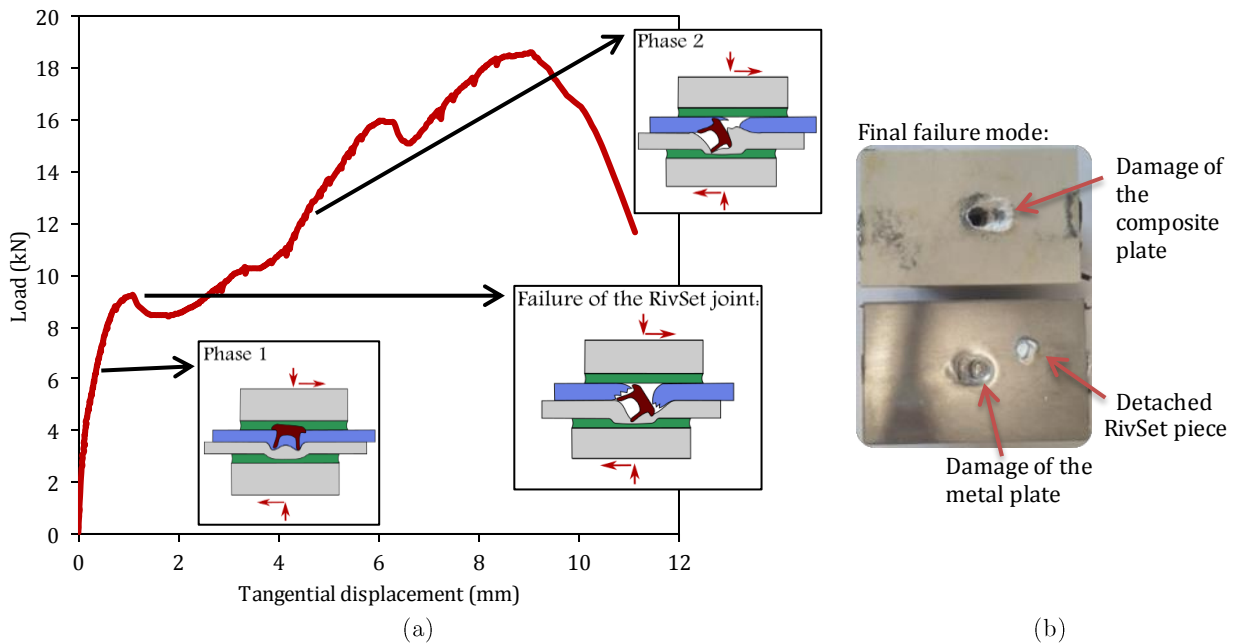


Figure III.21: Typical load-displacement curve (a) and failure modes of RivSet specimens (b) in compression/shear tests.

Since the adherends are no longer joined by the RivSet during the second phase, the failure load of the assembly has been considered as the maximum local value of the load before the first decreasing load. This value has been considered as the moment when the RivSet joint is completely detached from the adherends. Figure III.22 shows the failure load of the RivSet assemblies tested under compression/shear loading. It can be seen that failure loads under compression/shear loadings for all assemblies are higher than the failure load under tensile/shear loadings. This aspect highlights the positive influence of compression stresses on the shear strength of these assemblies. Hence, it's clear that the critical loading condition will be a combined tensile/shear load.

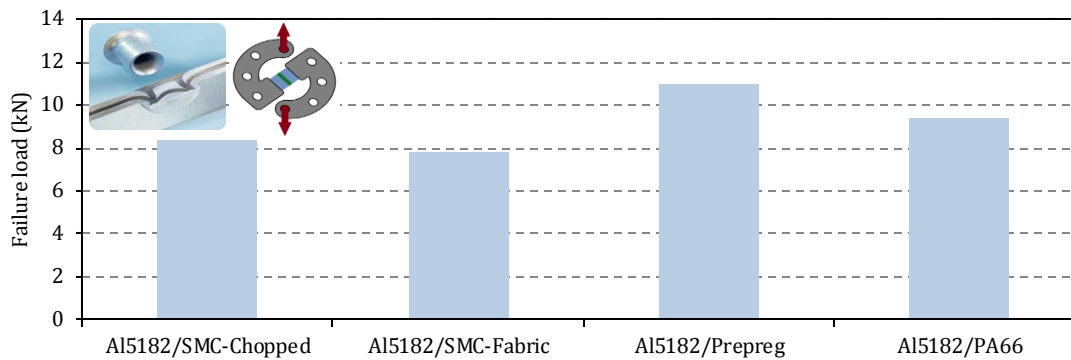



Figure III.22: Failure load of the RivSet specimens in compression/shear Arcan tests.

III.2. Overview

A previous study performed by the members of the FASTLITE project has preselected four joining techniques among all possible techniques to assemble dissimilar materials. The first three techniques were then investigated under “tensile” and shear loadings in this chapter: stud bonding, laser welding and RivSet joints. Therefore, the geometry of the specimens, the experimental tests and the analysis of results were discussed.

Classical lap-shear tests and cross-tension tests were used to subject the stud bonded and laser welded specimens under shear and tensile loadings, respectively. One additional test was proposed in order to subject the specimens under mixed tensile/shear loadings. This test was based on the Arcan device and was used to characterize RivSet assemblies.

The last technique corresponding to the bonding system will be studied in the next chapter.



Chapter IV. Characterization of adhesively bonded assemblies

Introduction

Four joining techniques were preselected among the different systems to assemble dissimilar materials. These techniques seem to be adapted to the automotive industry and their mechanical performances under quasi-static loadings need to be determined. The previous section was devoted to the analysis of the first three techniques: *(i)* stud bonded, *(ii)* laser welded and *(iii)* RivSet joints. This chapter is then dedicated to the strength and the behavior of the last joining technique under monotonic loadings: *(iv)* adhesive bonding. The bonded assemblies were composed of four composites with different natures (one carbon-thermoplastic composite, one carbon-epoxy prepreg composite and two glass-epoxy composites), two steels (22MnB5 and DP600), one aluminum alloy (AL5182) and two mono-compound crash adhesives (Sikapower-498 and Betamate-1822).

As it permits composite/metal assemblies to be subjected to combined tensile/shear and compression/shear loadings, and takes into account the influence of adherends and interfaces on the global behavior of the assembly, the Arcan device was chosen as the characterization test of adhesively bonded assemblies.

The bonding process and the experimental method are presented in this chapter. A comparative study of the strength properties under different combinations of tensile-compression/shear loadings has been performed; the failure envelopes of all assemblies have been then determined. Simultaneously, the influence of some crucial parameters such as air humidity, the presence of grease and the surface preparation on the strength of the assemblies has been analyzed.

Table of contents

IV.1. Experimental campaign.....	67
IV.1.1. Set-up.....	67
IV.1.2. Tested assemblies.....	67
IV.1.3. Specimen preparation	69
IV.2. Experimental results.....	71
IV.2.1. Composite assemblies	71
IV.2.1.1. Influence of the fabric orientation on the strength of bonded composite assemblies	73
IV.2.1.2. Influence of the surface state of the composite.	74
IV.2.1.3. Influence of the humidity.	75
IV.2.2. Metal assemblies	76
IV.2.2.1. Influence of grease	77
IV.3. Adhesive bonding as the selected structural joining technique	79
IV.4. Overview.....	82

IV.1. Experimental campaign

As explained in section I.7.4, it is essential for the automotive industry to avoid adhesive failures in any of the bonded assemblies during the automobile service life. Thus, the purpose of the experimental campaign presented in this chapter is to determine a bonding procedure that ensures cohesive failures under mixed tensile-compression/shear loadings. It is worth noting that fiber-tear failures will not be investigated. This is because the failure of the composite does not indicate an assembling problem but a poor material strength.

The modified Arcan approach has been selected to characterize the automotive assemblies under monotonic loadings. Thus, the assemblies were tested under “tensile” ($\gamma=0^\circ$), shear ($\gamma=90^\circ$), tensile/shear ($\gamma=45^\circ$) and compression/shear ($\gamma=135^\circ$) loadings.

IV.1.1. Set-up

All tests were performed under controlling displacement rate (1 mm/min) by means of a hydraulic tensile machine with a maximum load of 100kN. The temperature and humidity were not controlled (about 25° Celsius and 40% air humidity). The load applied to the specimen was recorded by the machine load-cell. As presented in section II.1.3.3, the relative displacements of the substrates were measured by means of a DIC system. Note that the relative displacement of the substrates is composed of the normal displacement “ND” and the tangential displacement “TD”.

IV.1.2. Tested assemblies

Adhesive bonding is the only joining technique able to join the full range of dissimilar assemblies required by the automotive industry. Thus, forty-two adherend/adhesive/adherend assemblies must be tested (two adhesives, four composites and three metallic materials combined with each other). In order to reduce the number of tests, we have decided to study separately the good compatibility of the adhesives with each of the adherends. It is clear that the adhesive/adherend combination with the lowest failure load will be the weak point in an adherend/adhesive/adherend assembly. Therefore, the whole set of possible combinations was reduced to fourteen adhesive/adherend combinations. These combinations were tested by means of the Arcan specimen shown in Figure IV.1. Table IV-1 shows the specimen configuration of the tested combinations.

In order to validate the methodology presented above, it must be ensured that failure never occurs at the substrate/adhesive interface. Some precautions have therefore been taken during the bonding procedure such as a good cleaning of the bonded surface of the substrates.

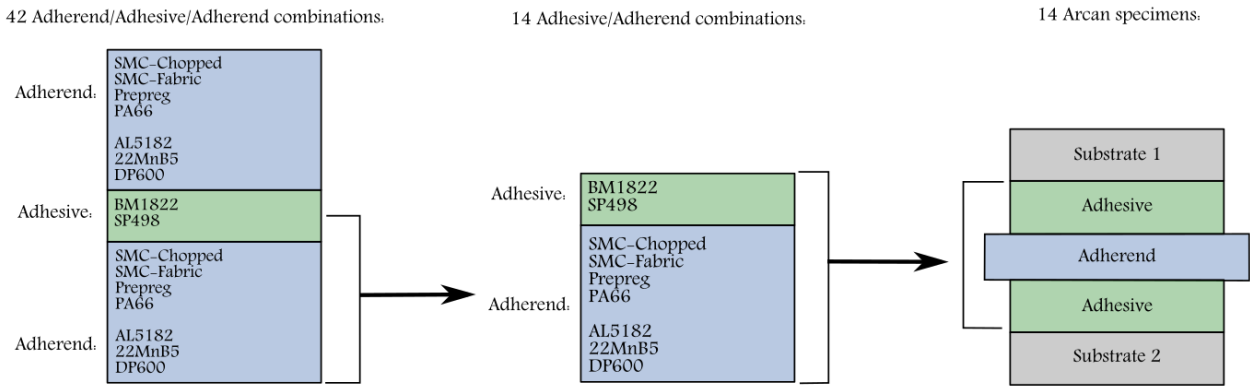


Figure IV.1: Reduction of the total number of tests.

Index	Substrate	Adhesive joint	Plate	Adhesive joint	Substrate
<i>Composite assemblies:</i>					
BM1822 / PA66	AL2022	BM1822	PA66	BM1822	AL2022
BM1822 / Prepreg	AL2022	BM1822	Prepreg	BM1822	AL2022
BM1822 / SMC-Chopped	AL2022	BM1822	SMC-Chopped	BM1822	AL2022
BM1822 / SMC-fabric	AL2022	BM1822	SMC-fabric	BM1822	AL2022
SP498 / PA66	AL2022	SP498	PA66	SP498	AL2022
SP498 / Prepreg	AL2022	SP498	Prepreg	SP498	AL2022
SP498 / SMC-Chopped	AL2022	SP498	SMC-Chopped	SP498	AL2022
SP498 / SMC-fabric	AL2022	SP498	SMC-fabric	SP498	AL2022
<i>Metal assemblies:</i>					
BM1822 / AL5182	AL2022	BM1822	AL5182	BM1822	AL2022
BM1822 / 22MnB5	AL2022	BM1822	Steel 22MnB5	BM1822	AL2022
BM1822 / DP600	AL2022	BM1822	Steel DP600	BM1822	AL2022
SP498 / AL5182	AL2022	SP498	Aluminum 5182	SP498	AL2022
SP498 / 22MnB5	AL2022	SP498	Steel 22MnB5	SP498	AL2022
SP498 / DP600	AL2022	SP498	Steel DP600	SP498	AL2022

Table IV-1: Specimen configurations of the adhesively bonded assemblies tested in the experimental campaign.

For the sake of simplicity, the specimens are referenced as indicated in Eq. IV-1:

$$\text{Adhesive/Adherend} = \text{Substrate/Adhesive/Adherend/Adhesive/Substrate} \quad \text{Eq. IV-1}$$

Where,

Adhesive=Betamate-1822 or Sikapower-498

Adherend=SMC-Chopped, SMC-Fabric, Prepreg, PA66, AL5182, 22MnB5, DP600

Thus, for example, a specimen noted as BM1822/PA66 corresponds to a substrate/Betamate-1822/PA66/Betamate-1822/substrate assembly.

IV.1.3. Specimen preparation

In order to ensure the same experimental condition for every specimen to reduce the scattering of the results due to the specimen preparation, a bonding procedure has been defined and respected as much as possible. However, it is worth noting that this procedure is not exempt from possible inherent problems such as material and machining defects. The preparation of the Arcan specimens can be listed as follows:

- (i) First, the bonded surfaces of the substrates were sandpapered manually to guarantee a homogeneous roughness. The grain sandpaper was 160 μm of average particular grain.
- (ii) Next, the surfaces of the substrates and of the plate (composite or metal) were wiped with a cloth moistened with acetone to degrease and remove all pollutants from the surface. Then, the surfaces were blow-dried for five minutes in order to evaporate the acetone applied in the previous step. The adhesive was applied over the surfaces with a maximum timeout of five minutes.

Because of technical and human limitations, it was not possible to characterize the entire set of bonded assemblies in one single experimental campaign. Therefore, the same adhesive cartridge was reused to bond different specimens at different dates. This choice ensures the same chemical composition of the adhesive for all the specimens (few cartridges were used), but induces some other problems such as stockade conditions and aging of the adhesive components after opening (Cognard *et al.*, 2006). For this reason, a rigorous procedure was implemented in order to ensure the same chemical conditions for all the experimental campaigns:

- (iii) The adequate quantity of adhesive needed for the current campaign was extracted from the adhesive cartridge. The adhesive cartridge was warmed up to room temperature to facilitate the extraction of adhesive. Next, the adhesive portion was preheated to 50° Celsius with the purpose of facilitating the adhesive spread over the bonded surfaces. Meanwhile, the remainder of the adhesive cartridge was stored in a vacuum bag at -18°C. Additionally and following the guidelines of the technical datasheet of both adhesives, the substrates to bond are also stored at around 20° C.
- (iv) The adhesive spread was carried out by means of an acetone-degreased spatula, trying to have a homogeneous adhesive layer and avoiding the formation of air pockets or the inclusion of pollutants (visual verification). Once the bonded surfaces of both substrates and the plate (metal or composite) were covered with adhesive, the specimen was screwed with a torque of 2.5Nm. It is worth noting that there are two 0.2mm-thick adhesive joints in the specimens.
- (v) Next, the surplus adhesive was removed in order to clean the edges. This cleaning was necessary to ensure a low influence of the edge effects on the adhesive behavior (Cognard, 2008).
- (vi) The curing cycle used in this study corresponds to 25 minutes of controlled heating up to 200°C, followed by 20 minutes of stabilized temperature. This cycle is not only

adapted to the automotive production chain, but at the same time, it guarantees a complete polymerization process according to the product datasheets (See Table I-4).

- (vii) After polymerization, the spacers were removed from the specimens by means of a Discotom cut-off machine.
- (viii) Finally, a speckled pattern was applied on the surfaces of the substrates.

Figure IV.2 represents the specimen procedure applied to the Arcan specimens in the case of adhesively bonded assemblies.

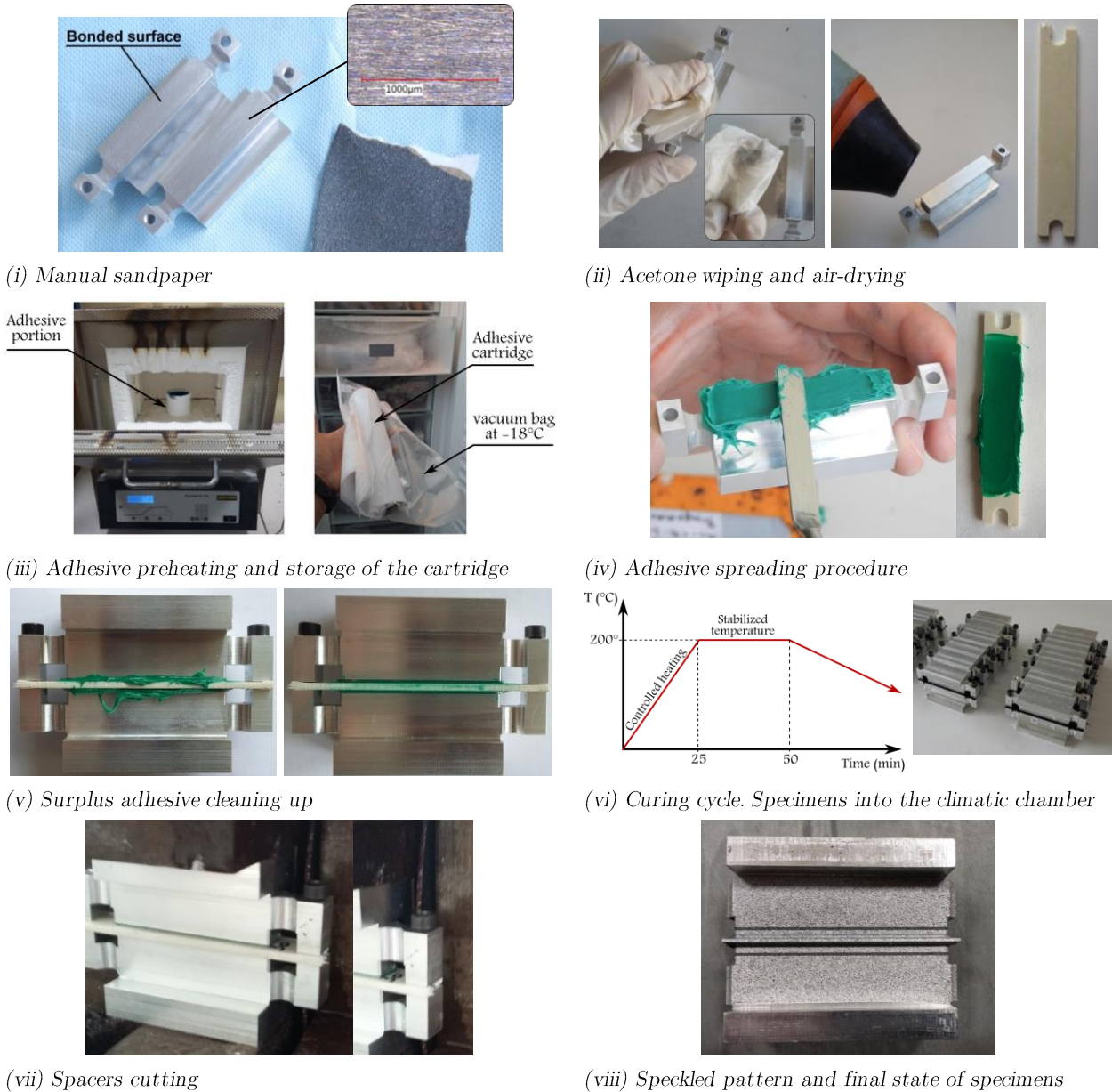


Figure IV.2: Specimen preparation in the case of adhesively bonded assemblies.

IV.2. Experimental results

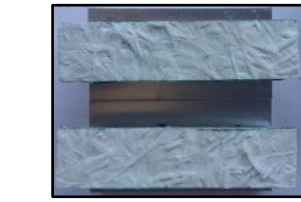
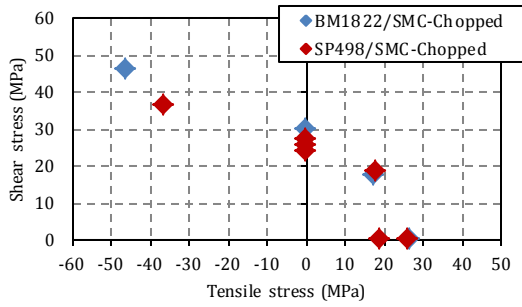
IV.2.1. Composite assemblies

As a first step, all the composite assemblies presented in Table IV-1 were bonded with the procedure detailed above and tested in monotonic Arcan tests. Figure IV.3 presents the failure envelopes and the failure modes of the tested assemblies. Here, the ultimate strength stress has been considered as the load applied by the tensile machine before failure divided by the bonded area ($S=50 \times 9.5 \text{mm}$). This hypothesis is not completely true because it supposes that the stress distribution within the adhesive joint is totally homogeneous (Cognard, 2008). However, it is acceptable for the purposes of this section that is aimed at determining an estimation of the mechanical properties of the assemblies. It is worth noting that for all assemblies, the nature of the adhesive (BM1822 or SP498) seems to have a minor influence on the failure load since the failure envelopes have almost the same values.

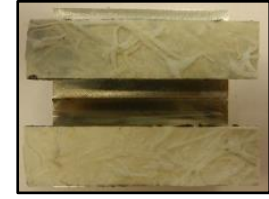
In the case of assemblies with SMC-Chopped and SMC-Fabric composite plates, fiber-tear failures were always observed (see Figure IV.3-a-b). Therefore, the out-of-plane strength of the SMC composites determines the strength of the assembly.

When BM1822/Prepreg and SP498/Prepreg assemblies are subjected to tensile/shear, shear and compression/shear loadings, cohesive failures occurred near to the adhesive/composite interface, with a light dusting of adhesive on the composite and a thicker layer of adhesive on the substrate (see Figure IV.3-c). In contrast, in “tensile” loadings, Prepreg assemblies exhibit fiber-tear failures. Indeed, BM1822/Prepreg assemblies present mixed failures, characterized by a zone of fiber-tear and a large zone of cohesive failure. A complete fiber-tear failure of the composite is observed in SP498/Prepreg. These aspects suggest that under “tensile” loadings, the Prepreg composite is the weak link of the assembly.

Adhesive failures were observed in BM1822/PA66 and SP498/PA66 assemblies for all types of load, which indicates a poor adhesive compatibility between the polyamide 6/6 thermoplastic resin (composite) and both adhesives.



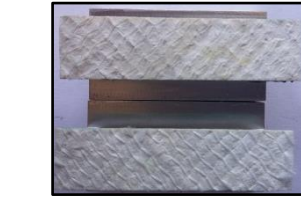
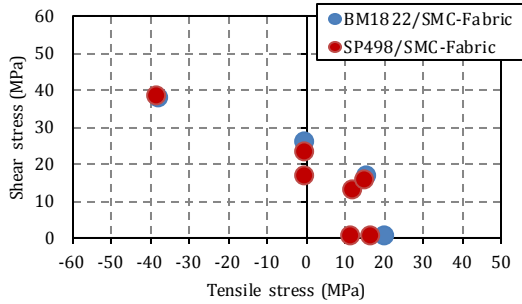
BM1822/SMC-Chopped fracture



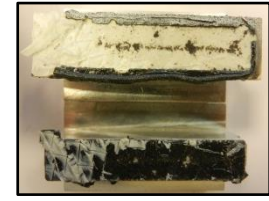
SP498/SMC-Chopped fracture

Failure envelope

(a) SMC-Chopped assemblies



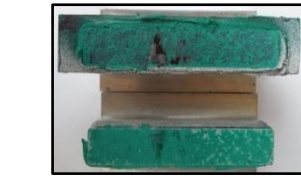
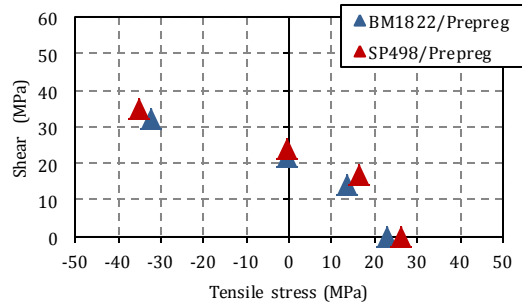
BM1822/SMC-Fabric fracture



SP498/SMC-Fabric fracture

Failure envelope

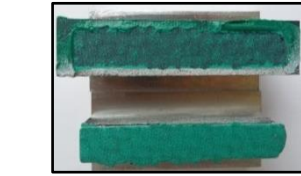
(b) SMC-Fabric assemblies



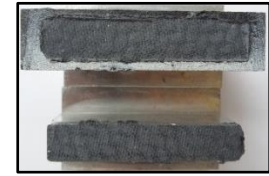
BM1822/Prepreg fracture for $\gamma=0^\circ$



SP498/Prepreg fracture for $\gamma=0^\circ$



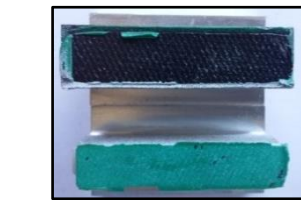
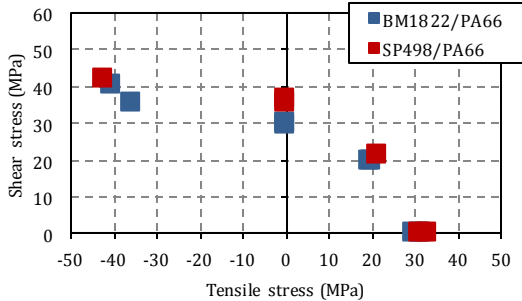
BM1822/Prepreg fracture for $\gamma=45^\circ; \gamma=90^\circ$ and $\gamma=135^\circ$



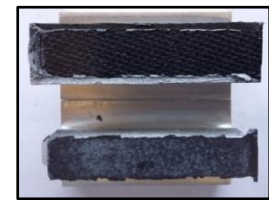
SP498/Prepreg fracture for $\gamma=45^\circ; \gamma=90^\circ$ and $\gamma=135^\circ$

Failure envelope

(c) Prepreg assemblies



BM1822/PA66 fracture



SP498/PA66 fracture

Failure envelope

(d) PA66 assemblies

Figure IV.3: Failure envelopes and failure modes for the adhesively bonded composite assemblies. Assemblies subjected to four types of load: tensile, shear/tensile, shear and compression/shear.

IV.2.1.1. Influence of the fabric orientation on the strength of bonded composite assemblies

In order to determine the influence of the fabric orientation on the strength of adhesively bonded composite assemblies, a second campaign was performed. The assemblies analyzed were the SP498/PA66 and the BM1822/PA66; the orientations of the outer ply were 0° , 45° and 90° (See Figure IV.4-a). Two tests per configuration (orientation and assembly) were carried out. Figure IV.4 presents the failure envelopes of the tested assemblies. We can notice for both of them that the fabric orientation has a minor effect on the overall response of the assembly (very low discrepancy).

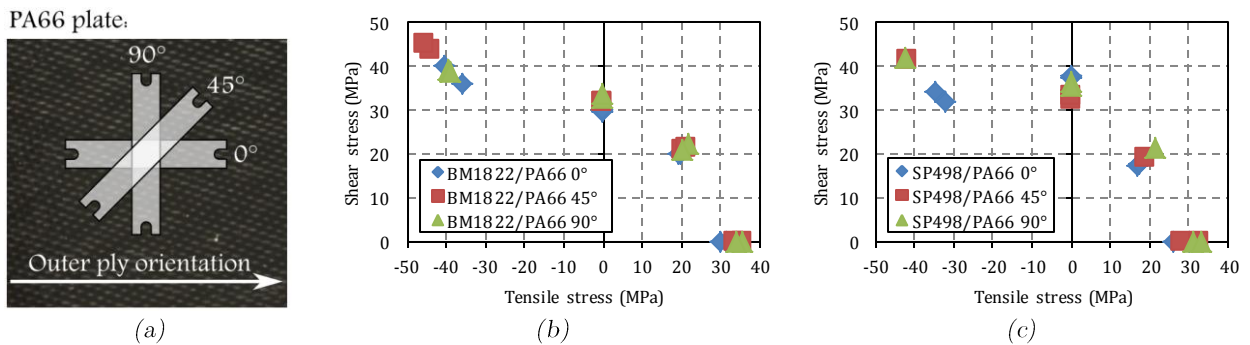


Figure IV.4: Fabric orientation of the composite samples (a) and failure envelopes of the BM1822/PA66 (b) and SP498/PA66 assemblies (c) depending on the fabric orientation.

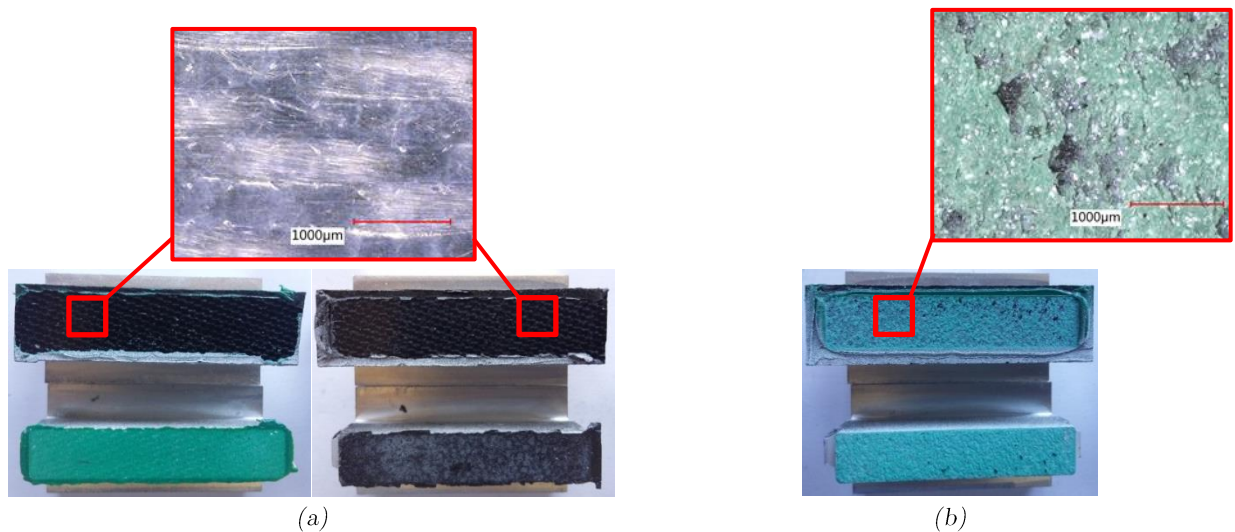


Figure IV.5: Type of fracture observed depending on the fabric orientation. Adhesive failure in BM1822/PA66 assemblies (left) and in SP498/PA66 assemblies (right) (a). Partial cohesive failure for BM1822/PA66 assemblies with a fabric orientation of 45° and subjected to tensile/shear loadings (b).

Adhesive fractures were observed in all configurations and for both adhesives (See Figure IV.5-a). However, a particular case exhibits a cohesive failure when the BM1822/PA66 assembly with a fabric orientation of 45° is subjected to tensile/shear loadings ($\gamma=45^\circ$) (see Figure IV.5-b). It means that, at this phase angle, an interaction between the cohesive failure mode and the adhesive failure mode takes place. Furthermore, it is also obvious that, due to the morphology of the composite (8H satin), the behavior of

the assembly is orthotropic. Therefore, the stiffness of the composite plate is different at a 45° orientation as compared to 0° or 90° orientations. These aspects and the surface roughness of the outer weave of the composite may explain the difference of the failure mode. However, as the failure load of both modes remains close, no further studies were performed on this matter.

IV.2.1.2. Influence of the surface state of the composite.

PA66 assemblies bonded with the basic procedure presented in section IV.1.3 failed by adhesive failures (See Figure IV.5). In order to ensure cohesive fractures with higher failure loads for these composite assemblies, a manual sanding process has been applied over the composite surfaces. Four progressive levels of manual sanding have been performed (see Figure IV.6-a):

- P1. Virgin state without sanding*: The composite surface was only cleaned up with acetone.
- P2. Soft manual sanding*: The objective was to homogenize the surface of the composite. The sandpaper used had a granulation size of 120 μ m.
- P3. Intermediate manual sanding*: The fibers were exposed and the resin was removed. The sandpaper used had a granulation size of 530 μ m. Under this configuration, the adhesive would stick directly over the fibers.
- P4. Aggressive manual sanding*: The outer weaves of the composite were strongly sanded and no piece of resin was observed. The sandpaper used had a granulation size of 530 μ m.

The specimens were subjected to shear loadings using the Arcan device. Figure IV.6-b shows the registered load-displacement curves of the four surface states for a BM1822/PA66 assembly. All states presented a pretty close behavior. However, P3 and P4 levels exhibited a larger non-linear regime and higher failure loads (about 10%). It is worth mentioning that the strength of the P4 state was slightly lower than the P3 state. These results conclude that exposing the fiber of the composite improved the adhesion with the adhesive. However, an aggressive sanding could have led to a weakening of the in-plane mechanical properties of the composite because the outer fibers were cut, and consequently, the strength of the outer weave was reduced. The failure mode was also affected by the surface state of the composite. P1 and P2 levels presented an adhesive fracture, while P3 and P4 levels exhibited a partially cohesive fracture. This means that the ultimate strength of the adhesive was achieved, generating a failure of the assembly by a fracture in the adhesive layer.

A similar campaign of manual sanding was performed on BM1822/Prepreg and SP498/Prepreg assemblies. In this case, only P1 and P3 levels were applied over the surface of the composite. The results also showed an improvement of the mechanical properties of the assemblies with a higher failure load and a greater non-linear regimen (see Figure IV.6-c-d). This aspect was more noticeable for SP498/Prepreg assemblies. Similarly, the failure

modes changed from thin-layer cohesive fracture to classical cohesive fracture at the center of the adhesive thickness. It is worth noting that the assemblies with SMC composites were not tested since the failure in a virgin state (P1) always occurred by fiber-tear failure inside the composite plate (See Figure IV.3-a-b).

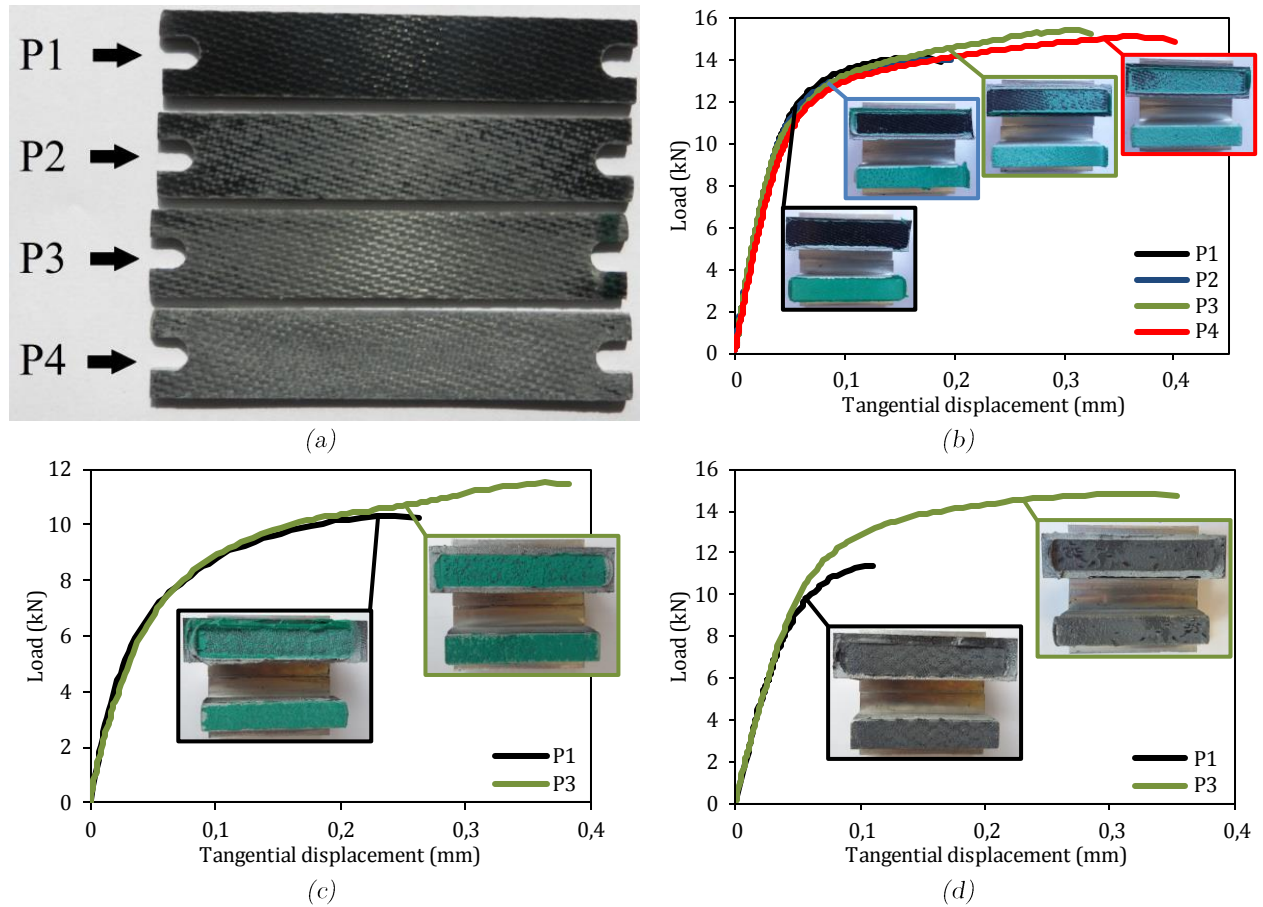


Figure IV.6: Influence of manual sanding on the failure load and the failure mode. Different levels of manual sanding tested (a). Load-displacement curves of shear Arcan test of BM1822/PA66 assemblies (b), BM1822/Prepreg assemblies (c) and SP498/Prepreg assemblies (c).

IV.2.1.3. Influence of the humidity.

It is well known that the mechanical properties of thermoplastic composites and adhesives can be greatly affected by the absorption of humidity (Chaichanawong *et al.*, 2016). Indeed, humidity might lead to premature failures in bonded thermoplastic assemblies. Therefore, in order to identify the susceptibility of PA66 assemblies to humid environments representative of the service life of the car, shear Arcan tests were performed using BM1822/PA66 specimens conditioned at two different humidity levels: two specimens without humidity (RH0) and two others with 70% air humidity (RH70). The objective was to determine which element of the assembly (composite, adhesive or interface) was mainly affected by humidity.

In order to ensure a virgin state, the tests without humidity were performed just after curing. The two other specimens were conditioned for fifteen days at 70% of relative humidity and at 60° Celsius. This process was based on the work of (Broudin *et al.*, 2015)

that it predicted a complete saturation of 70% humidity in the composite plate under the conditions established. However, it is important to say that this conditioning does not ensure 70% RH saturation either of the adhesive joint or the interface.

Figure IV.7 presents the experimental results for the two types of specimens described before. As it can be noticed, the presence of humidity leads to an early non-linear threshold and, in consequence, to a lower failure load (about -15% as compared with the virgin state). It is worth noting that the curves are superposed at the linear part at the beginning of the test. For assemblies with 0% humidity (RH0), the fracture is adhesive. In contrast, assemblies with 70% humidity (RH70) present a mixed adhesive/cohesive failure. This phenomenon suggests that the strength of the adhesive is severely affected by the presence of humidity, and not the composite, or the interface.

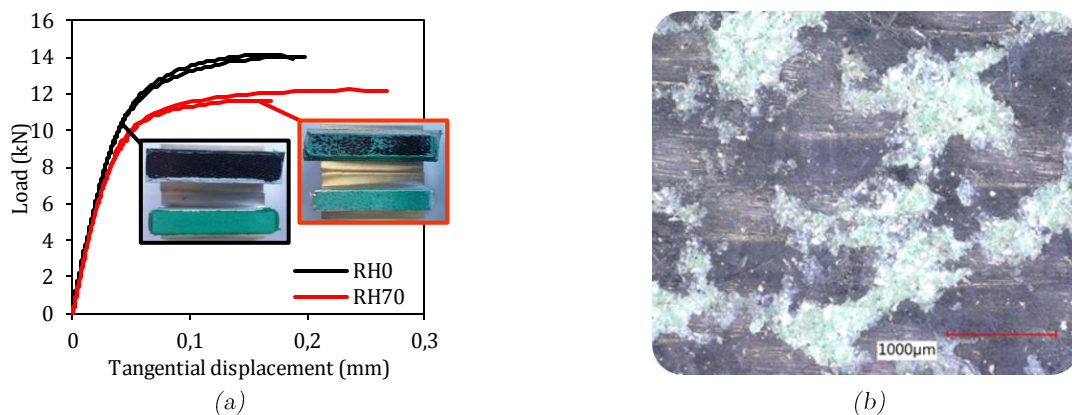


Figure IV.7: Influence of the humidity on the BM1822/PA66 assemblies under shear monotonic Arcan test. (a) Load-displacement response of RH0 and RH70 specimens and (b) Keyence digital microscopic image of the fracture surface of the RH70 specimens.

IV.2.2. Metal assemblies

This section has been consecrated to the study of the good adhesion between the adhesives and the metallic materials of the study. In the first case, the metal plates followed a degreasing procedure in order to remove all possible pollutants and ensure optimal adhesion:

Process for degreasing:

- (i) First, the metal plates are wiped with a cloth moistened with heptane in order to pre-degrease and remove solid pollutants.
- (ii) Then, the plates are immersed in a 98% heptane container for 10 minutes.
- (iii) The metal plates were removed from the container and dried with absorbent paper until the surface was dulled and no residual traces were observed.

However, according to industry requirements, metallic materials are usually exposed to greasy environments, it was then necessary the study of the influence of the presence of

grease on the strength of metal bonded assemblies. Consequently, some metal plates followed an additional re-greasing process employed in the automotive industry:

Process for re-greasing:

- (i) The metal plates were immersed in a greasing solution for 2 minutes.
- (ii) Then, the plates were removed and drained for 30 minutes, resting vertically on absorbent paper in order to absorb the excess greasing solution accumulated on the bottom edge of the plate.

The two types of specimens (greasy and non-greasy) have then followed the same bonding procedure presented in section IV.1.3. It is worth mentioning that the spreading procedure of the adhesives was quite difficult in presence of grease.

IV.2.2.1. Influence of grease

Figure IV.8 shows the comparison between the failure envelopes for greasy and non-greasy assemblies. The failure modes are also given. The results seem to show that the SP498/22MnB5 specimens were strongly affected by the presence of grease over the bonded surface. Indeed, mixed adhesive/cohesive failures were observed with a 25% lower failure load. However, since the failure occurred at the substrate/adhesive interface, it cannot be possible to conclude if the SP498/22MnB5 assembly was affected, or not, by the presence of grease. For all the other greased assemblies, the failure was always cohesive and the failure load was very similar to the virgin state, ensuring a good adhesion between the adhesives and the tested metal plates without any influence of the presence of grease.

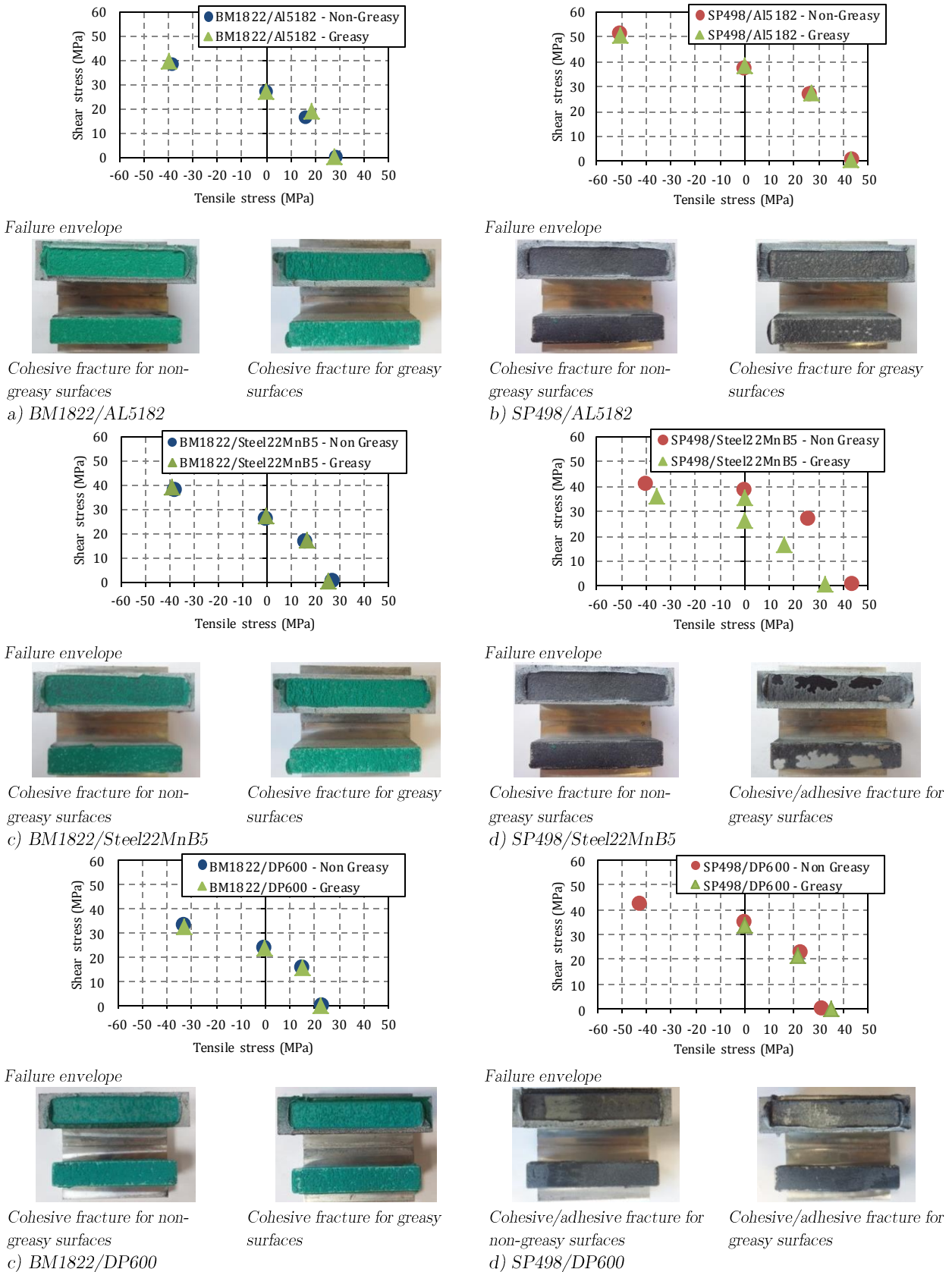


Figure IV.8: Failure envelope for adhesively bonded metal assemblies and influence of greasy surfaces.

IV.3. Adhesive bonding as the selected structural joining technique

As stated in the objectives of the study, it is necessary to select and model the most adapted joining technique in order to reduce the design time in automotive structures. However, the methodology to compare and select different joining techniques remains a subject vaguely studied. This is mainly because the selection process is highly dependent on diverse items such as work environment, materials, feasibility, time and economic costs. Therefore, the selection criteria vary strongly from one application to another (Lovatt and Shercliff, 1998). Here, we have considered three main criteria to compare the four joining techniques studied in this study:

- 1) The failure load, which is an item to maximize.
- 2) The additional volume of the joining technique. The volume is an important item to take into account in order to facilitate the design of the final shape of the car. This is why the volume has been considered as a selection criterion.
- 3) The additional mass of the joining technique³. A joining technique limiting the weight of the car will be preferred.

These criteria were grouped in a performance index as follows:

$$P.I. = \frac{F}{V * m} \quad \text{Eq. IV.1}$$

With,

$$\begin{aligned} F &= \text{Failure load} \\ V &= \text{Affected volume} \\ m &= \text{Affected mass} \end{aligned}$$

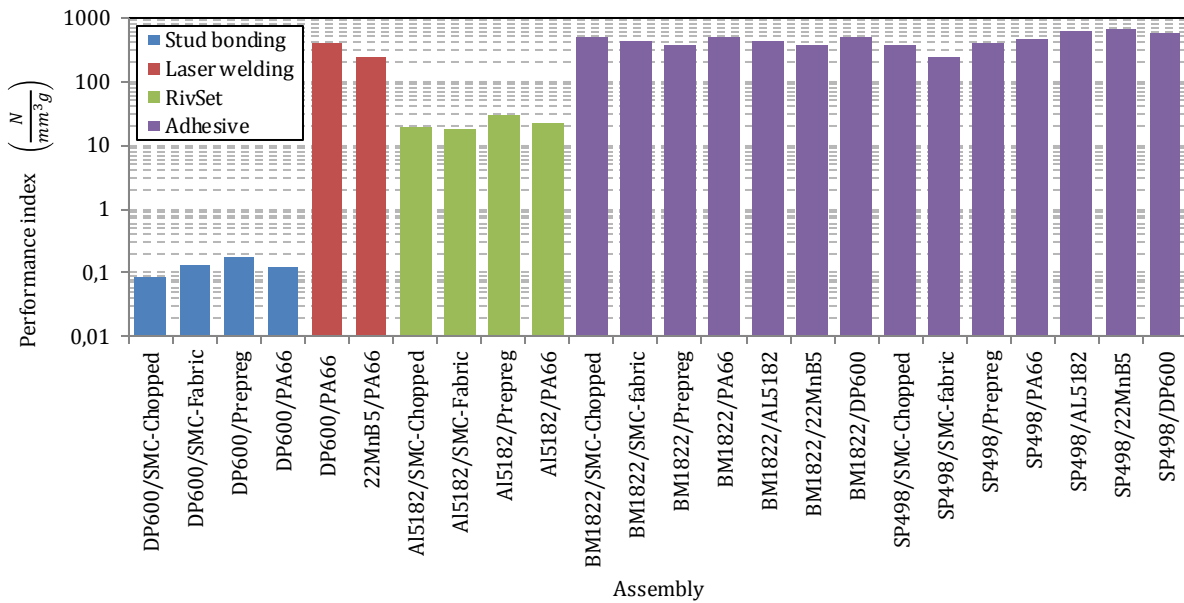
This index does not constitute a rigorous selection process since it does not take into account a large list of selection items as proposed by LeBacq (LeBacq *et al.*, 2002); however, it constitutes an easy way to compare the joining techniques as shown in Figure IV.8.

Due to their high performance and the possibility of joining the entire set of materials, adhesive joints seem to be an adapted solution to the automotive industry. Nevertheless, this technique requires an important wait time due to the polymerization cycle of the adhesive. In order to be able to use adhesives without negatively affecting the automotive production chain, it has been decided to combine bonding systems with another technique

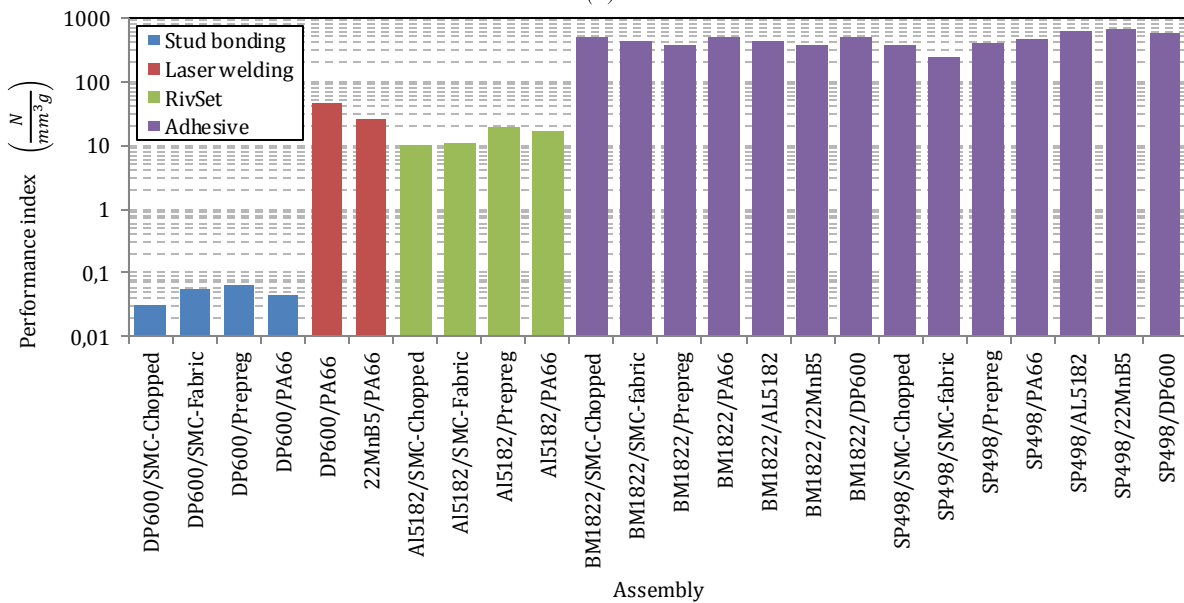
³ In the case of laser welding, the additional volume and mass were considered as the volume and mass of the composite affected during the welding procedure.

allowing for the assembly of the materials during curing. RivSet joints have been selected as the second joining technique because of their high relative mechanical properties, their high joining rate and their compatibility with adhesives. Therefore, the “final solution” to join the entire set of assemblies corresponds to hybrid RivSet/adhesive joints. It is important to say that laser welded assemblies also presented a high performance index; however, they are strongly limited to the use of thermoplastic materials.

Since the key point in hybrid RivSet/adhesive joints is the adhesive layer, it has been decided to characterize and model carefully the behavior of the adhesives of the study. The next chapter is devoted to these aspects. Finally, the analysis of the behavior of hybrid joints is briefly discussed in the prospects of the study (Section VII.2.3).



(a)



(b)

Figure IV.9: Performance index of the whole range of assemblies tested in shear (a) and “tensile” loadings (b).

Figure IV.10 compares the assemblies tested as a function of the failure load and the additional mass of the joining technique. The results are quite similar to those obtained by using the performance index presented in Eq. IV.1.

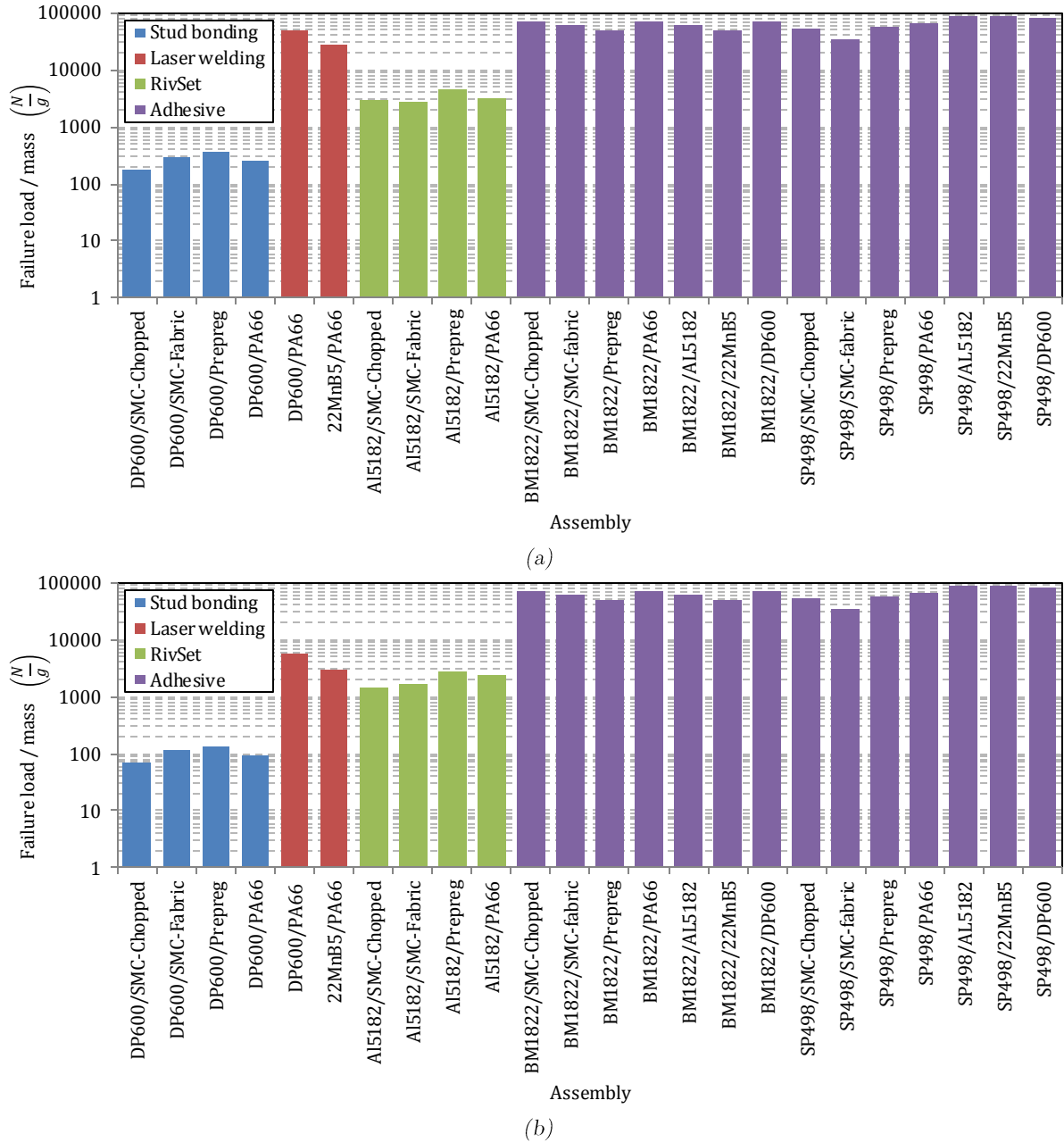


Figure IV.10: Comparison of the joining techniques as a function of the failure load and the additional mass in shear (a) and “tensile” loadings (b).


IV.4. Overview

The methodology followed in this study based on the Arcan approach, permitted the characterization of adhesively bonded assemblies under mixed tensile-compression/shear loadings. A wide range of different assemblies have been evaluated and, some of their advantages/drawbacks have been exposed.

The study was principally focused on the strength of the assemblies considered in the analysis. However, the influence of some parameters on the behavior of these assemblies was also investigated.

As cohesive failures were observed in almost all of the combinations of adhesive/adherend tested, it is possible to assume that the use of Betamate-1822 and Sikapower-498 to join the whole range of possible assemblies has been validated. However, some particular aspects such as the surface state and the presence of greasy need special attention when PA66 and 22MnB5 plates are used.

Adhesive Bonding systems have been selected as the most suitable solution to the objectives of the FASTLITE project. Since the weak link in a bonding joint corresponds to the adhesive, it is necessary to characterize and model the behavior of the adhesives of the study. The next chapters will expose the methodology followed and the most important contributions of the current Ph.D thesis concerning these issues.



Chapter V. Characterization of adhesives in an assembly

Introduction

This chapter contains the experimental campaign performed in order to characterize the behavior of the Betamate-1822 and Sikapower-498 adhesives. The aim of this campaign was to highlight the most relevant phenomena presented on the behavior of these adhesives under mixed quasi-static loadings. Consequently, the experimental campaign was performed by means of the modified Arcan device presented in section II.1.3. This type of test allows thin adhesive joints to be tested under mixed tensile-compression/shear loadings, representing as real as possible, the behavior of an adhesive in an assembly. Additionally, it avoids the influence of edge effects, which can lead to an early failure of the specimen.

The specimen preparation was respected as much as possible in order to ensure cohesive fractures and low scattering of the results. Three types of tests have been chosen to characterize the adhesives: monotonic, multilevel creep and increasing cyclic tests. These tests showed a strong viscous character in both adhesives. The failure envelopes of the adhesives are also exposed.

Table of contents

V.1. Experimental campaign based on the modified Arcan device	85
V.1.1. Specimen preparation.....	85
V.2. Behavior of adhesives under monotonic loadings and the influence of the loading rate	86
V.2.1. “Tensile” loadings ($\gamma=0^\circ$)	86
V.2.2. Shear loadings ($\gamma=90^\circ$).....	87
V.2.3. Mixed proportional loadings ($\gamma=45^\circ$ and $\gamma=135^\circ$)	88
V.2.4. Failure envelopes.....	89
V.2.5. Looking through the fracture mode	90
V.2.6. Influence of the loading rate.....	92
V.3. Multilevel creep tests and the non-linear evolution of the viscosity	94
V.3.1. Non-linear viscosity	98
V.4. Increasing cyclic test: toward the cyclic behavior	100
V.5. Overview	102

V.1. Experimental campaign based on the modified Arcan device

As stated in section II.1.3, the possibility of subject adhesives under mixed tensile-compression/shear loadings and the reduction of the edge effects on the adhesive joint, make the modified Arcan test an adapted solution to the characterization of adhesives in an assembly. Adhesive specimens with a 0.4mm-thick adhesive joint were then used (See Figure V.1). The specimens bonded with Betamate-1822 adhesive will be referenced as BM1822 and the specimens bonded with Sikapower-498 will be noted as SP498.

The tests were performed under controlling loading rate ($dF=0.2\text{kN/s}$) and standard laboratory conditions (around 40% air humidity and 25°C). A 3D DIC system was used in order to track the relative displacement of the substrates (See section II.1.3.3). The specimens were tested under four types of load: “tensile” ($\gamma=0^\circ$), shear ($\gamma=90^\circ$), tensile/shear ($\gamma=45^\circ$) and compression/shear ($\gamma=135^\circ$). Two tests per type of load were performed and a very low dispersion in the load-displacement curves was observed.

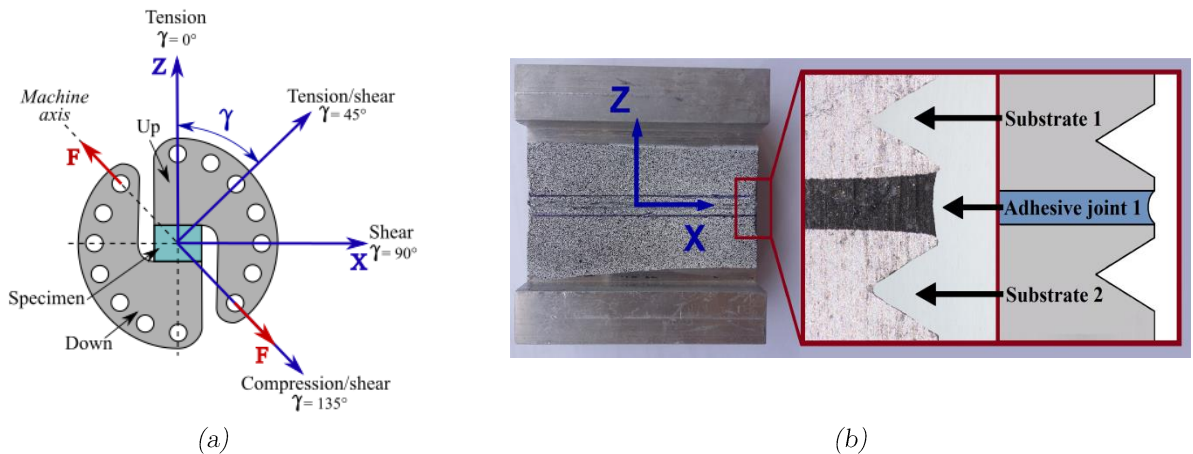


Figure V.1: Modified Arcan device (a) and Arcan specimen used to characterize the adhesive behavior in an assembly (b).

V.1.1. Specimen preparation

The bonding procedure presented in section IV.1.3 was followed step by step, except that in this case, there is no composite or metal plate. Thus, the preparation of the Arcan specimens may be summarized as follows:

- (i) The surfaces of the substrates are sandpapered manually to guarantee a homogeneous roughness.
- (ii) Then, all remaining dust are removed from the substrate surfaces by means of 99% pure acetone and air-drying.
- (iii) The adequate quantity of adhesive needed for the current campaign is extracted from the adhesive cartridge and preheated at 50° Celsius.
- (iv) The adhesive is then immediately applied over the bonded surface of the adhesives.

- (v) The surplus adhesive is removed in order to clean the edges and the specimen is placed into the thermal chamber.
- (vi) The curing cycle was 25 minutes of controlled heating up to 200°C, followed by 20 minutes of stabilized temperature.
- (vii) After polymerization, the spacers are removed from the specimens by means of a Discotom cut-off machine.
- (viii) A speckled pattern is applied on the substrate surfaces.

V.2. Behavior of adhesives under monotonic loadings and the influence of the loading rate

Monotonic loadings constitute a traditional form to characterize the behavior of materials under static and dynamic loadings. The most important experimental data given by this type of test is the stress-strain curve, which allows the identification of some mechanical properties such as Young's modulus, ultimate strength, yield strength and failure mode. However, due to the characteristics of the Arcan test, the stress-strain curve must be replaced by the load-displacement curve and the mechanical properties cannot be directly determined. Therefore, a detailed analysis of the behavior and the strength of the adhesives has been performed:

V.2.1. “Tensile” loadings ($\gamma=0^\circ$)

The behavior of the adhesives under “tensile” loadings are presented in the Figure V.2. The principal observations are listed below:

- Since the type of failure of both assemblies is cohesive, it is possible to assume that the load-displacement curve is quite representative of the behavior of the adhesives. It is worth noting that finite element simulations have been performed in order to ensure an elastic behavior of the substrates and to validate the previous hypothesis.
- The strength of the SP498 adhesive is greater than the strength of the BM1822 adhesive. Indeed, the failure load of the SP498 specimens is about 55% bigger than the BM1822.
- For both adhesives, an “elastic” regime followed by a large non-linear regime can be seen. This reveals a great ductility for both adhesives, which is an important aspect in crash applications.
- The “pseudo-elastic limit” of the BM1822 adhesive may be estimated at 7.5 kN, while for the SP498 it is hardly identified (approximately 11 kN). The reader can note that the “elastic limit” in the case of adhesives, which are essentially polymer materials, is not accurately defined. This is because adhesives exhibit non-elastic strains even for low levels of loading (see section V.3). Therefore, we call “pseudo-elastic limit” the loss of linearity observed in the load-displacement curve.
- A very low scattering is observed in the behavior of the adhesives. The scattering of the failure load in an Arcan test was just about 5%.

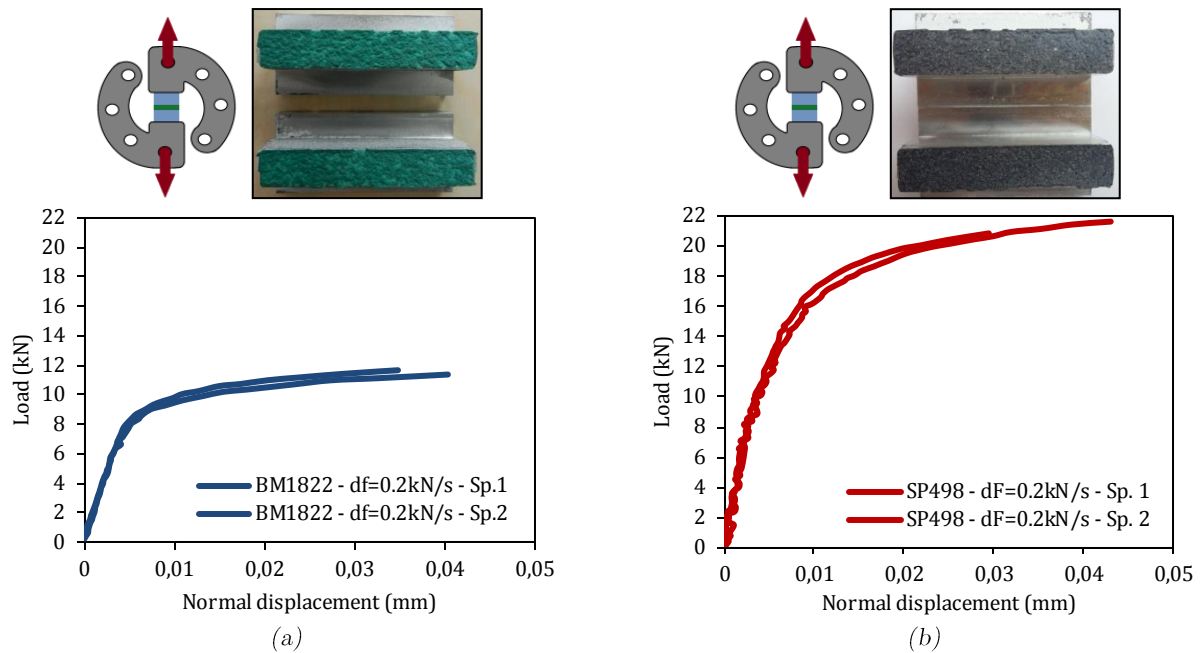


Figure V.2: Failure modes and load-displacement curves of the Betamate-1822 (a) and Sikapower-498 (b) adhesives.

V.2.2. Shear loadings ($\gamma=90^\circ$)

The behavior of the adhesives under shear loadings is presented in Figure V.3; the most important conclusions are listed below:

- Once again, the fracture of both adhesives is cohesive.
- The strength of the BM1822 adhesive under shear loadings remains at the same failure load than under “tensile” loadings (12 kN). In contrast, in the case of SP498 specimens, the shear failure load is lower (18kN) than the tensile failure load (21 kN).
- The “pseudo-elastic limit” is estimated at 12 kN for the SP498 and 4kN for the BM1822. It can be noticed that the BM1822 exhibits a non-linear behavior even for very low stresses, which makes it difficult to estimate the “pseudo-elastic limit”.
- The order of magnitude of the tangential displacement in shear tests is about 10 times larger than the normal displacement in “tensile” tests.
- The scattering observed in the load-displacement curves of the adhesives is significantly low. Indeed, the results overlap each other overall the curve. This aspect is a really important advantage of the modified Arcan test in comparison to classical lap-shear tests.

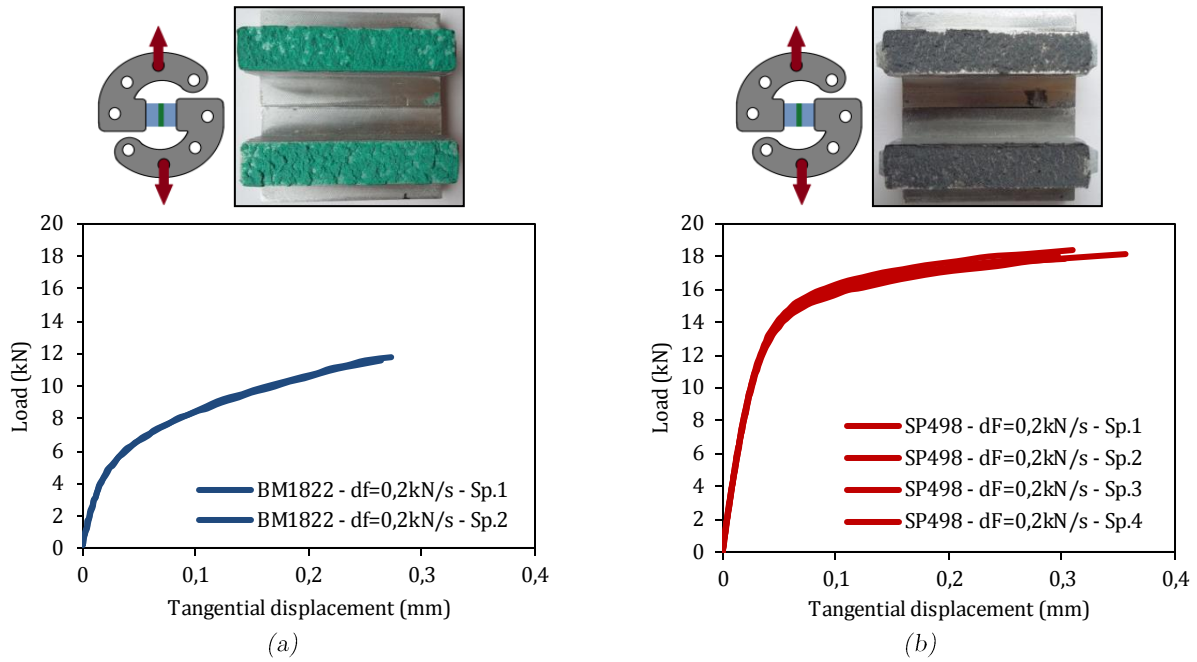
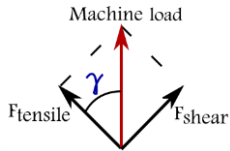


Figure V.3: Load-displacement curves of the Betamate-1822 (a) and Sikapower-498 (b) adhesives.

V.2.3. Mixed proportional loadings ($\gamma=45^\circ$ and $\gamma=135^\circ$)

The adhesives were also tested under mixed tensile-compression/shear loadings. In this type of test, the applied machine load corresponds to the superposition of a tensile load (F_{tensile}) and a shear load (F_{shear}):



$$\begin{aligned} F_{\text{tensile}} &= F_{\text{machine}} \times \cos \gamma^\circ \\ F_{\text{shear}} &= F_{\text{machine}} \times \sin \gamma^\circ \end{aligned} \quad \text{Eq. V.1}$$

Figures V.4 and V.5 present the load-displacement curves and the cohesive failure modes observed in both adhesives. In tensile/shear loadings, the tangential displacement (TD) and the normal displacement (ND) present the same order of magnitude (Figure V.4). Additionally, the strength of both adhesives has decreased as compared with “tensile” or shear tests.

In compression/shear loadings, the assemblies present higher failure loads and larger tangential displacements (See Figure V.5). Note that in this case, the normal displacement remains near zero. This aspect is totally normal because of the very slight normal deformation of the adhesive in compression loadings. In the case of SP498, the scattering observed is larger than the other types of load. This scattering starts after the “pseudo-elastic limit” and increases during the non-linear regime. It is worth saying that the definition of the failure load under combined compression/shear loadings is quite complicated. Indeed, cracks may be generated within the adhesive layer without a significant reduction of the load (due to the high friction forces involved), which can be the explanation of the scattering observed. Nevertheless, the compression/shear state generated

by the Arcan test allows the estimation of the failure load in compression loads. Finally, it is worth noting the positive influence of compression stresses on the shear behavior of the adhesive.

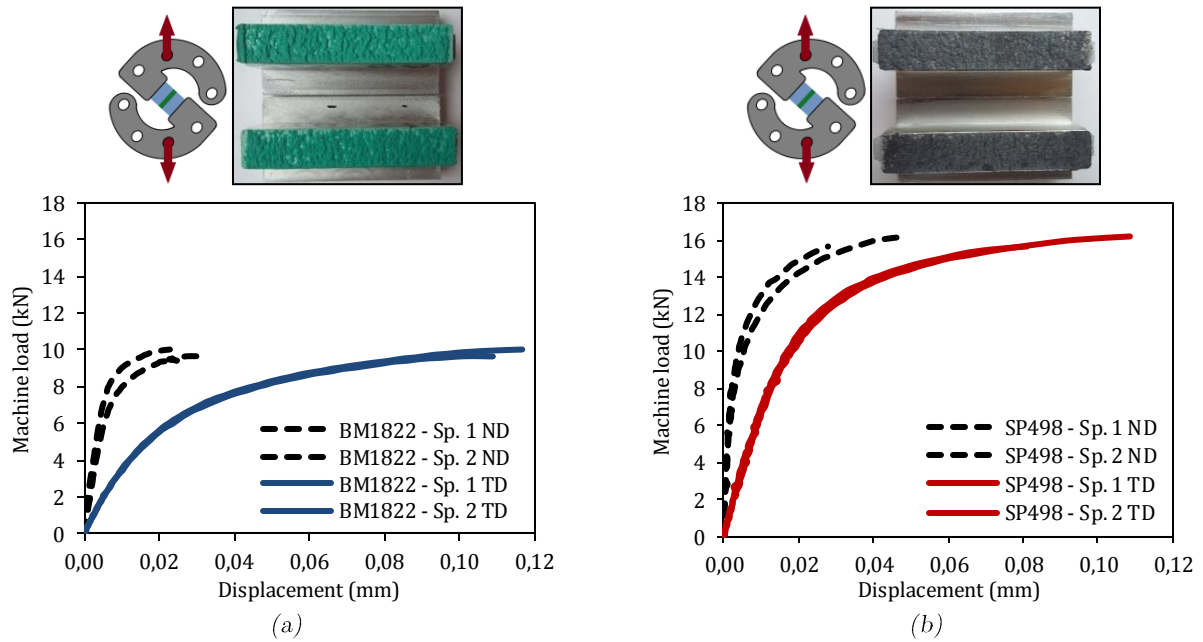


Figure V.4: Load-displacement curves in tensile/shear test of the Betamate-1822 (a) and Sikapower-498 (b). ND is the normal displacement and TD is the tangential displacement.

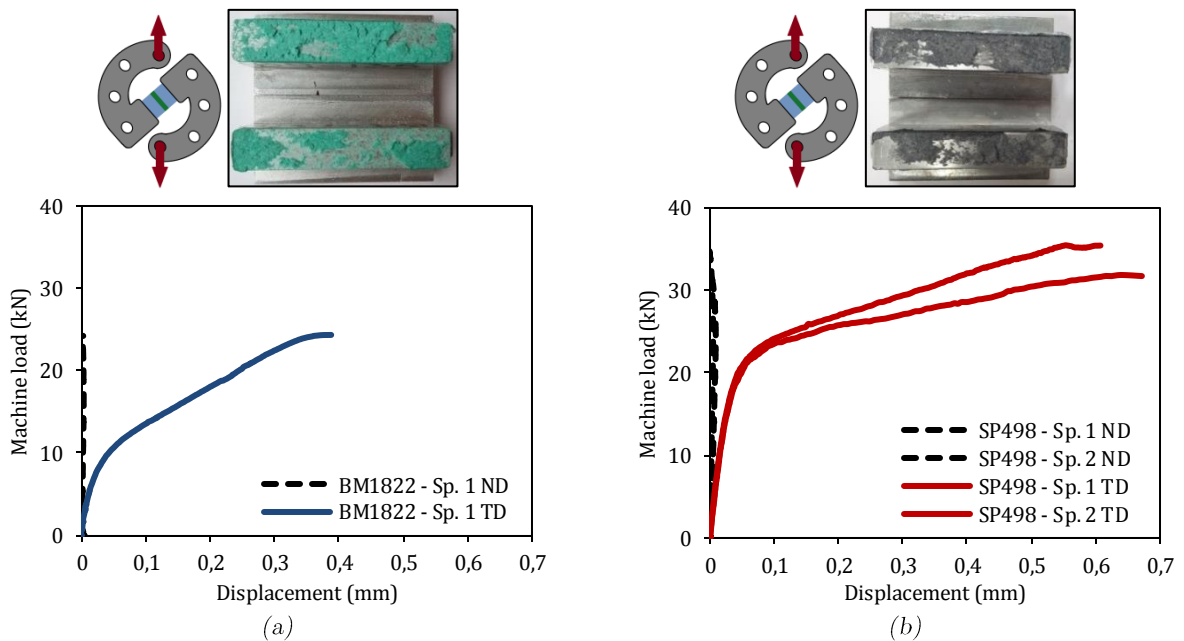


Figure V.5: Load-displacement curves in compression/shear test of the Betamate-1822 (a) and Sikapower-498 (b). ND is the normal displacement and TD is the tangential displacement.

V.2.4. Failure envelopes

Once the experimental campaign of the adhesives under static loadings (0.2kN/s) has been performed, the failure envelopes of the BM1822 and SP498 adhesives may be determined. The ultimate strength stress has been considered as the load applied by the

tensile machine before failure divided by the bonded area ($S=50 \times 9.5 \text{ mm}$). Figure V.6 shows the failure envelopes of the adhesives under the four types of load: “tensile” ($\gamma=0^\circ$), shear/tensile ($\gamma=45^\circ$), shear ($\gamma=90^\circ$) and compression/shear ($\gamma=135^\circ$). Two continuous lines have been plotted as trend lines as a guide in the analysis of results. The SP498 adhesive presents a considerably high failure envelope. Indeed, for every type of load, the SP498 failure load is about 40% higher than the BM1822. The figure also shows a low scattering of the failure load of both adhesives.

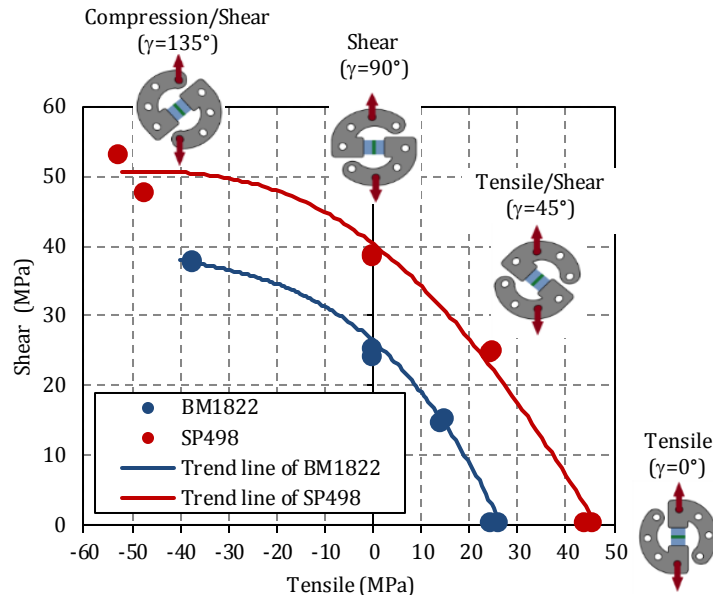


Figure V.6: Failure envelopes of the Betamate-1822 and Sikapower-498 adhesives. Specimens with a 0.4mm-thick adhesive joint subjected to a constant loading rate of 0.2kN/s.

The envelopes also show the influence of tensile-compression stresses on the apparent shear strength. Indeed, the apparent shear strength decreases in presence of tensile stresses (weakening) and increases in presence of compressive stress (reinforcement).

V.2.5. Looking through the fracture mode

Cohesive failures have been observed for every type of loads. However, these fractures present a different shape depending on the type of load. Thus, for example, “tensile” fractures present a homogeneous surface with a “uniform roughness”, while shear fractures present a kind of “sharp ridges” with an irregular overlapping rows distribution and a preferential direction towards the shear loading plane. For a compression/shear loading, the fracture arrives with a highly stored energy (the cracking sound when failure was significantly loud), leading to an irregular pattern with some of the “sharp ridges” observed for shear loadings and with some areas with adhesive failure (See Figure V.7).

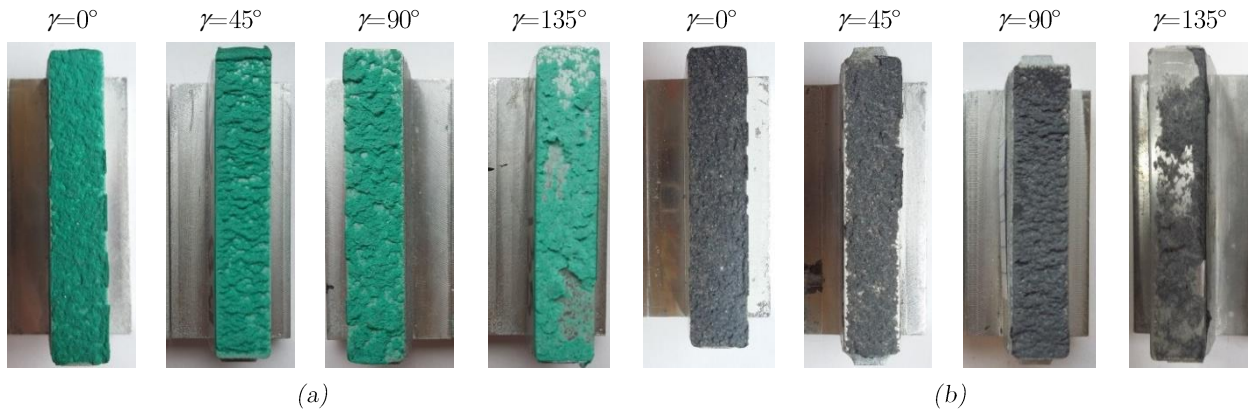


Figure V.7: Cohesive failure modes of the Betamate-1822 (a) and Sikapower-498 (b) adhesives.

The molecular structure of an epoxy adhesive (as many thermoset polymers) is a cross-linked lattice upon curing with an amorphous pattern (See Figure V.8). This arrangement promotes a non-uniform stress distribution during loading, which leads to local stress concentrations in the shortest linked bonds. If the stress is large enough, several bonds will be progressively broken, leading to void formation (dimple). Fracture finally takes place when the micro-voids coalesce (T.L., 2005).

In tensile loadings, the dimples are perpendicular to the maximum normal stress. Because of the presence of additives in the adhesive formulation, the dimples may present an amorphous form with a size of a few micrometers. Note that several coplanar dimples can be presented during loading. Finally, the failure arrives with a single macro-crack in the middle plane of the adhesive joint (See Figure V.9-a). In contrast, in the presence of shear loadings, the dimples are elongated along the planes of maximum shear stress. Several macro-cracks can take place slipping in the same direction of the dimples and creating the sharp ridges observed on the fracture surface. In thin adhesive layers, the failure arrives when the macro-cracks coalesce in the final crack in the middle of the adhesive thickness (See Figure V.9-b). In thick adhesive layers, a single macro-crack might propagate until the adhesive/substrate interfaces and then induces an adhesive failure (Bidaud, 2014).

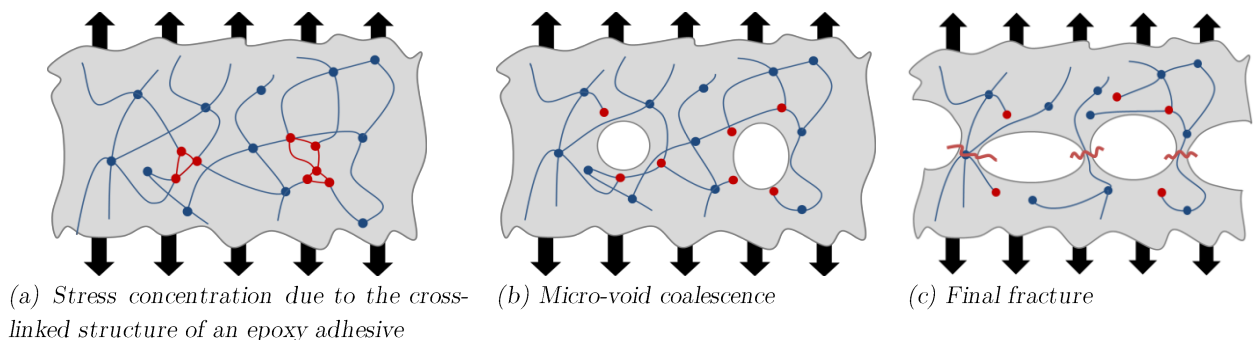


Figure V.8: Fracture mechanisms in the adhesive joint.

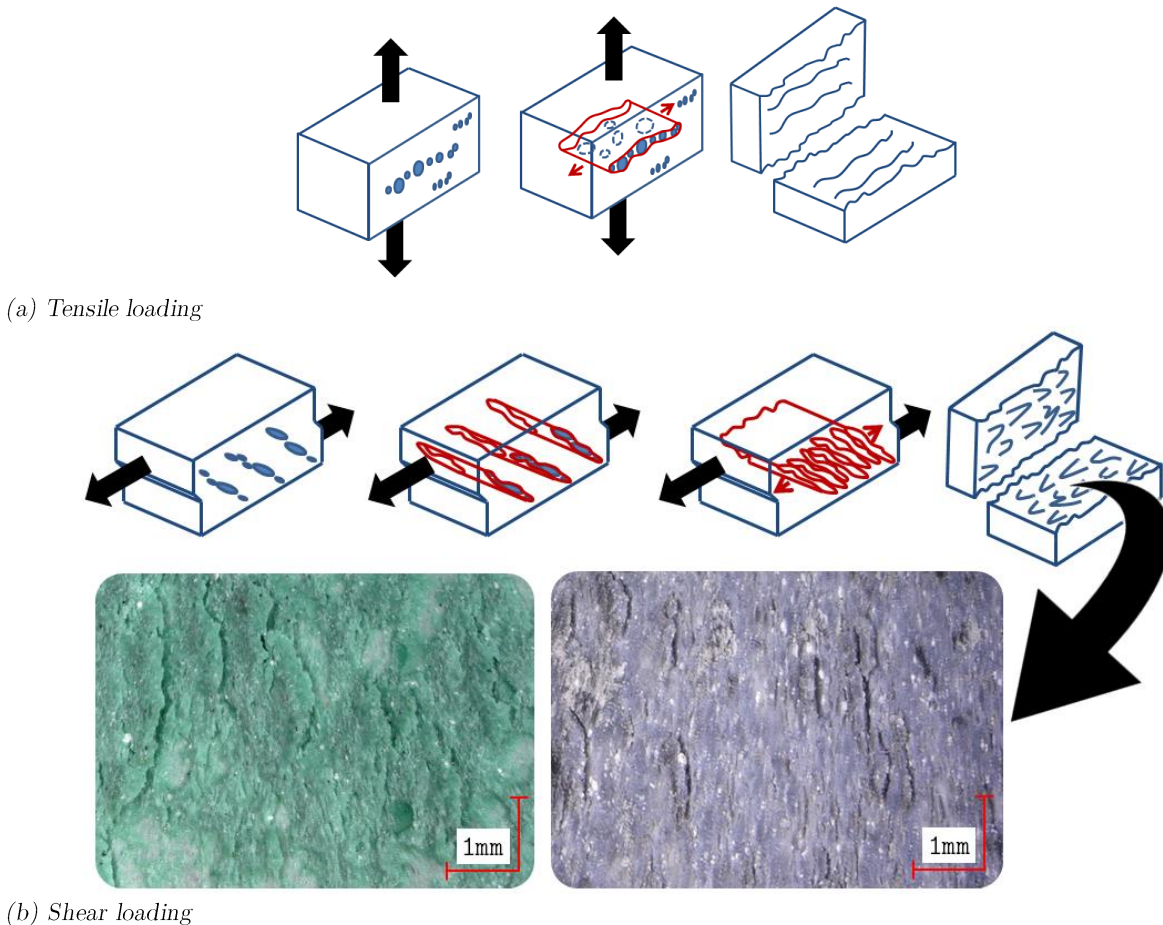


Figure V.9: Schema of the evolution of the fracture depending on the type of load in tensile tests (a) and in shear tests (b). Keyence digital microscopic images of the fracture surface in shear tests. Inspired from (ASM International, Metals Park, 1994).

V.2.6. Influence of the loading rate

This section is devoted to the influence of the loading rate on the behavior of the adhesives of the study. For that purpose, the adhesives have been tested under monotonic “tensile” and shear tests with a loading rate of 2 kN/s (ten times faster than the previous cases). Figure V.10 compares the load-displacement curves of the adhesives tested under two different loading rates.

The most important conclusion is that the behavior of both adhesives is substantially affected by the loading rate; it can clearly be seen that a faster loading rate increases the failure load. Indeed, at low loading rates (0.2kN/s), the adhesives are compliant since the molecular chains have sufficient time to move. In contrast, at higher loadings rates (2 kN/s), the motion of the molecular chains produces friction, and a higher stress is required to deform the adhesives. This aspect is more appreciated for shear loadings than for “tensile” loadings, which once again underlines the dissimilar behavior under “tensile” and shear loadings.

As regards the rigidity of the adhesives, it appears that the loading rate has a minor influence on the elastic slope. From a macroscopic point of view, this particularity can be explained because the instantaneous-elastic response will govern the behavior of the adhesives for the very low loadings (lower than 4kN); progressively, the viscous character of the adhesives will be activated as a function of the stress rate, leading to different slopes of the load-displacement curves for higher loadings.

Another important aspect is that the adhesives are not affected in the same way by the loading rate. Indeed, the load-displacement curves show that the SP498 is strongly affected by this aspect, while the behavior of the BM1822 is slightly modified. Finally, it is worth noting that this influence does not affect either the cohesive failure mode or the great non-linear regime of both adhesives.

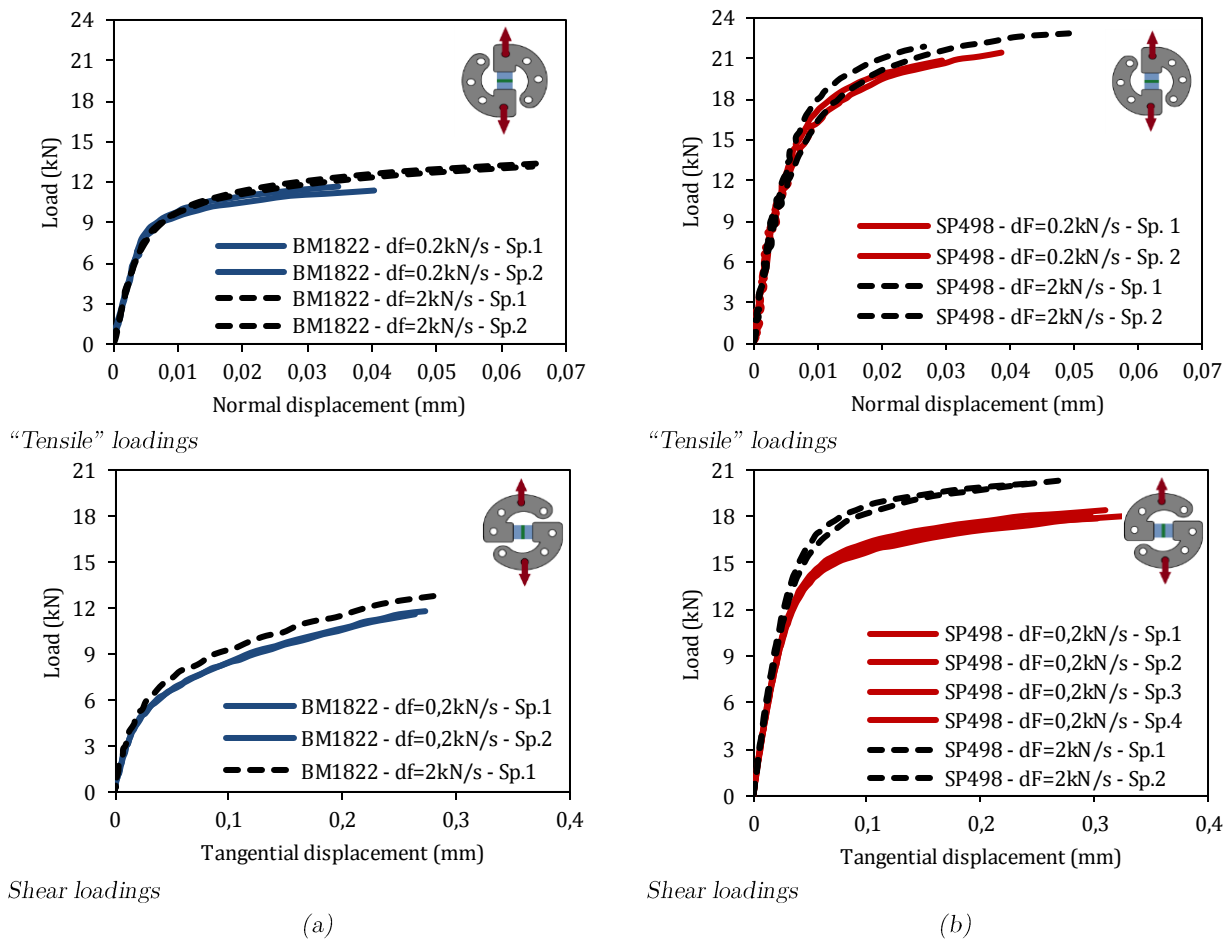


Figure V.10: Influence of the loading rate on the Betamate-1822 (a) and Sikapower-498 adhesives (b). Load-displacement curves under different loading rates in "tensile" and shear Arcan tests.

V.3. Multilevel creep tests and the non-linear evolution of the viscosity

Creep is defined as the deformation of a material as a result of long-term exposure to constant stress. This deformation can be large enough to lead to the failure of the structure and this is why it constitutes a crucial aspect of the design of pieces and the choice of materials.

In the case of adhesives, it is well known that the behavior under creep loadings can present a very large deformation, which must be taken into account to characterize the strength of the assembly. Consequently, in order to characterize the creep behavior of the BM1822 and SP498 adhesives, multilevel creep tests have been performed under “tensile”, tensile/shear and shear loadings. Here, the multilevel creep test is composed of five consecutive stepped creeps of 2000 seconds at 20%, 40%, 60%, 80% and 100% of the failure load obtained by the monotonic test (F_{load}) (See Figure V.11). This type of test allows the study of the evolution of the viscosity for different levels of stress and for different ratios of tensile/shear loadings.

The loading rate in the uploading/unloading slopes was 0.5kN/s, this value was fixed in order to be fast enough to reduce the activation of viscous-mechanisms before the creep levels, while ensuring a low overshoot of the applied load⁴. Consequently, the PID controller of the tensile machine has been adapted to the test requirements.

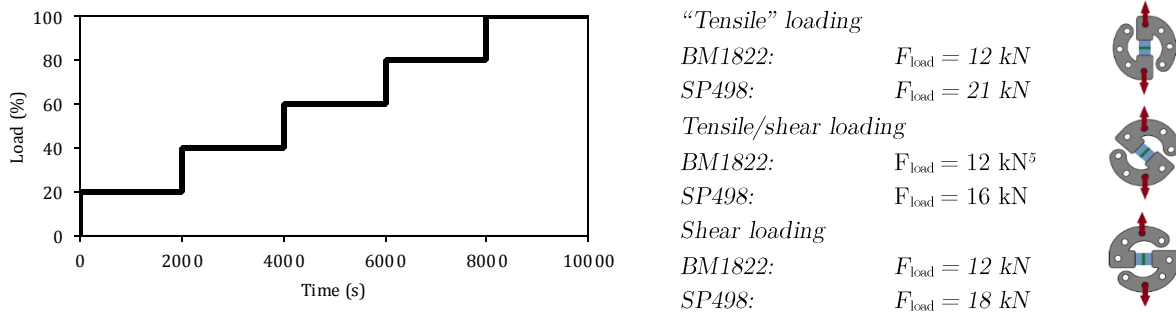


Figure V.11: Multilevel creep test for different types of load.

Figure V.12 shows the machine load applied to the adhesives during the multilevel creep tests. Most of the tests were performed at least twice; however, only one test was performed using BM1822 adhesive under “tensile” and tensile/shear loadings. Note that failure always occurred at a lower load than the failure load registered in monotonic tests. Additionally, the failure load in the multilevel creep tests is highly scattered, which is common in this kind of test.

⁴ At the beginning of a creep step, the load applied over the specimen might present an overshoot with respect to the desired load. This is due to the mechanical inertia of the tensile machine.

⁵ The value of the ultimate monotonic loading of the BM1822 under tensile/shear loadings used in multilevel creep tests was 12kN (instead of 10 kN).

The relative displacement of the specimens under multilevel creep loadings is shown in figures V.13 and V.14. The existence of these displacements during the creep levels highlights the strong viscous behavior of the adhesives. It is remarkable that the displacements are presented even below the “pseudo-elastic” limit of the adhesives.

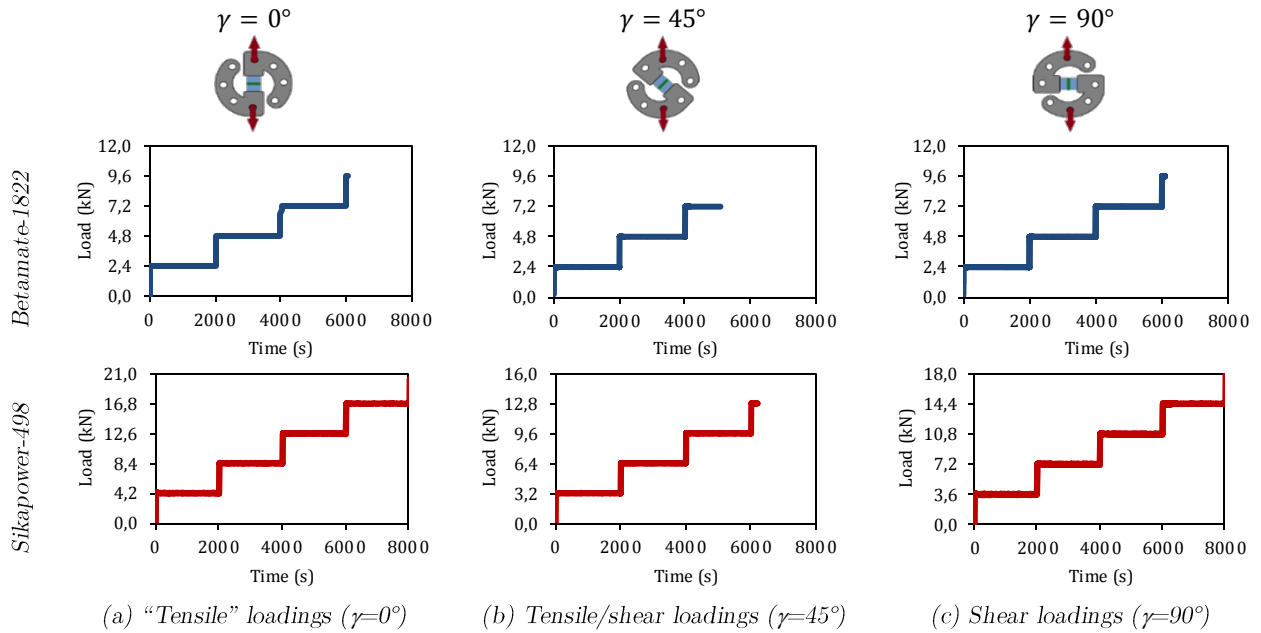


Figure V.12: Imposed load in multilevel creep tests.

On the subject of the evolution of the creep displacement of the adhesives as a function of the type of load, it can be seen that the SP498 adhesive has a similar evolution of the creep displacement under “tensile” and shear loadings. In contrast, the BM1822 adhesive has a very small creep displacement under “tensile” loadings in comparison to the creep displacement observed under shear loadings. It means that the BM1822 adhesive exhibits a slight or a large creep deformation depending on the type of load applied: “tensile” or shear.

The behavior of the adhesives under tensile/shear multilevel creep loadings is also presented in figures V.13 and V.14. As in the case of monotonic loads, the tangential displacement is bigger than the normal displacement. It can also be seen that the BM1822 adhesive presents a greater creep deformation than the SP498 adhesive. This larger deformation leads to an early fracture during the third creep level (for all other cases the failure always occurs during the fourth creep level).

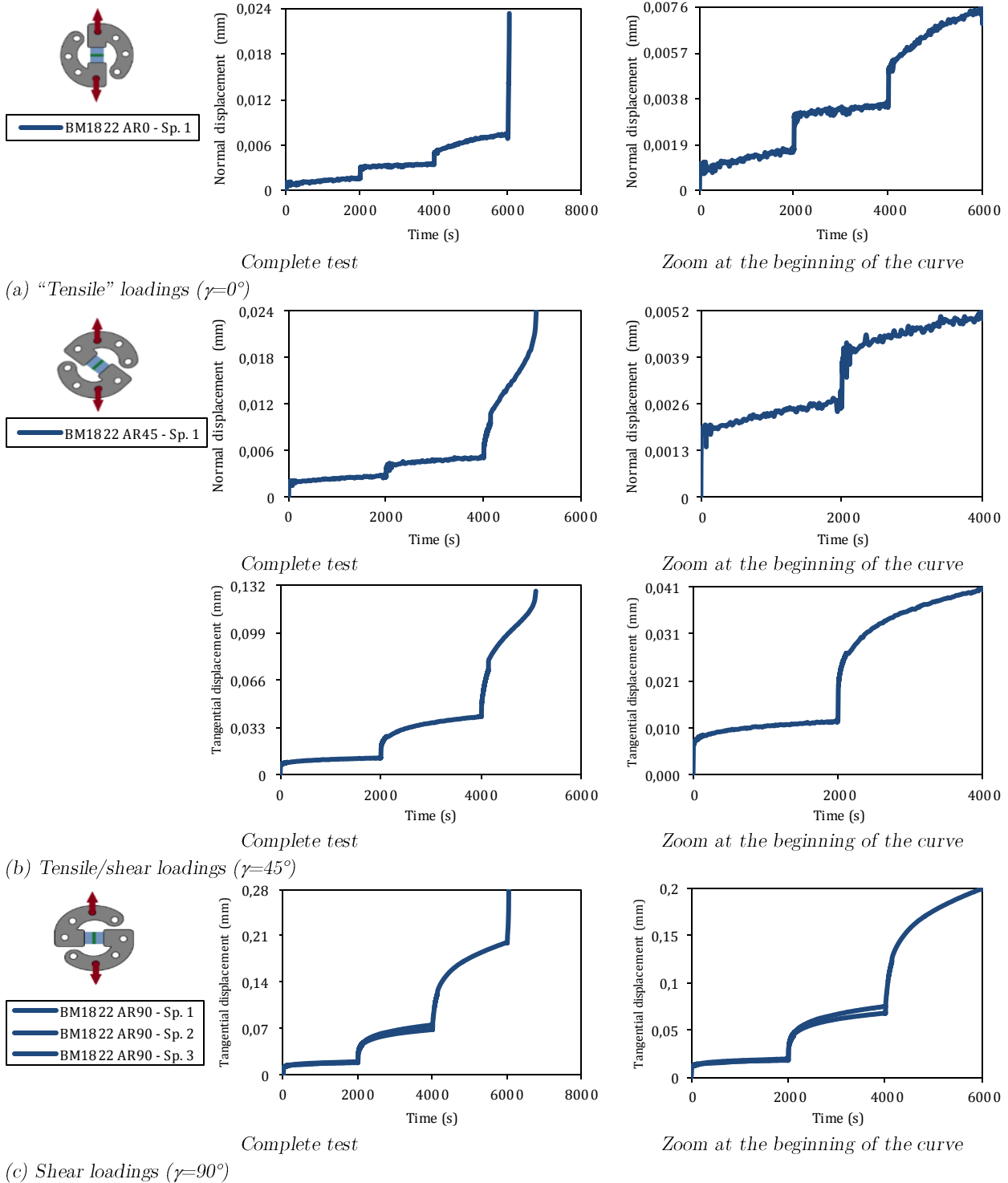


Figure V.13: Relative displacements of the Betamate-1822 adhesive under multilevel creep tests.

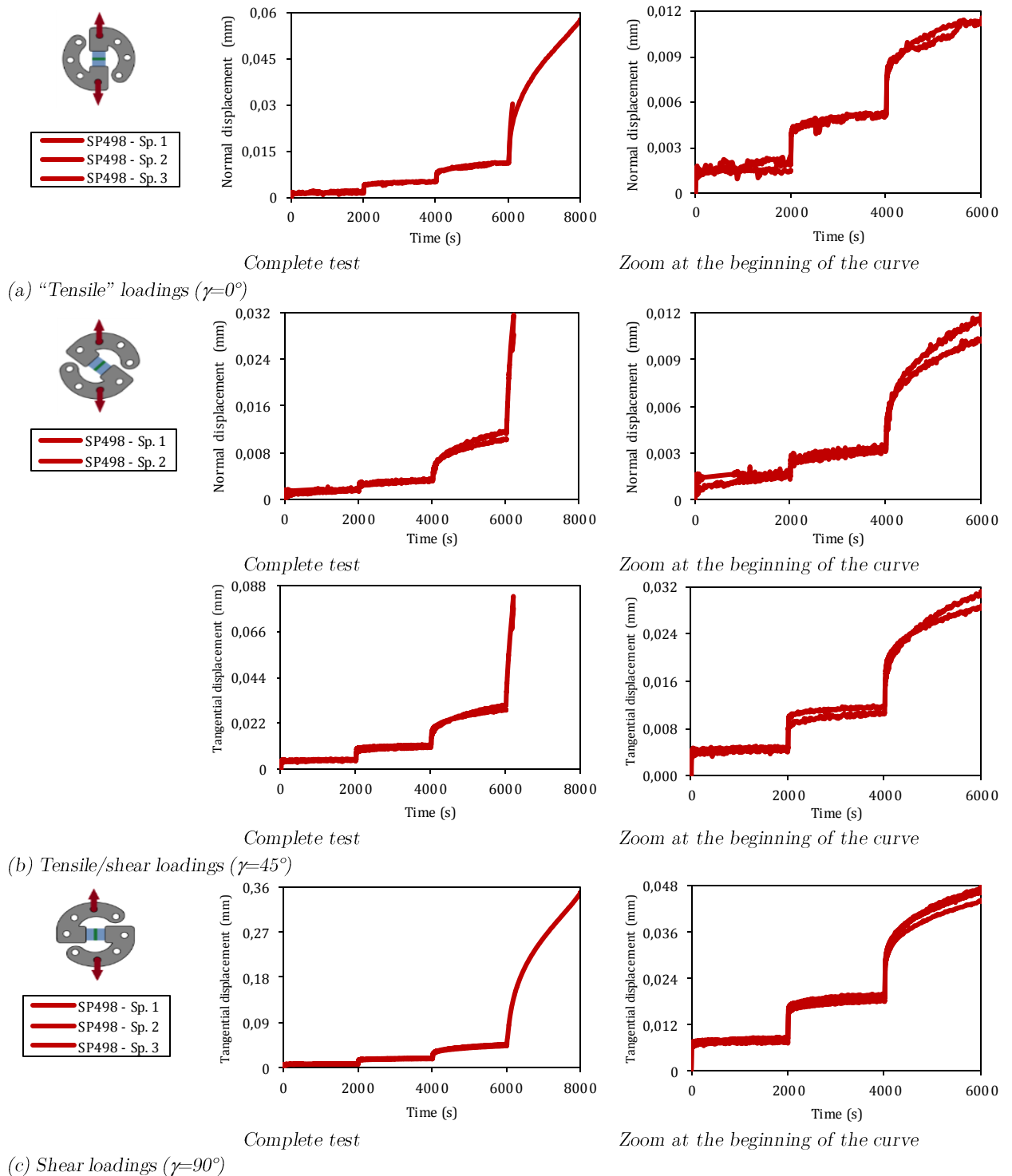


Figure V.14: Relative displacements of the Sikapower-498 adhesive under multilevel creep tests.

V.3.1. Non-linear viscosity

Another remarkable aspect observed in the creep tests is that the creep displacement under different stress levels appears to increase as a non-linear function of the load. It can be seen that for all types of load, the displacement at the last creep level is considerably bigger than the displacement at the first level. This suggests a non-linear character of the viscosity of both adhesives; otherwise, the displacements at the end of every creep level would be proportional to the applied load (e.g. the displacement at the end of the third level would be three times the displacement at the end of the first level).

In order to investigate the evolution of the viscosity of the adhesives, some variables have been defined through the displacement-time curve of the creep tests (See Figure V.15). In this manner, the elastic displacement of the i creep level (D_e^i) is defined as the displacement at the beginning of the i creep level (it is not a rigorous definition of the elastic displacement but it is sufficient for the discussion). Similarly, the viscous displacement of the i creep level (D_v^i) is defined as the displacement at the end of the i creep level minus the displacement at the beginning of the i creep level:

$$D_e^i = D_{initial}^i$$

$$D_v^i = D_{final}^i - D_{initial}^i = D_{final}^i - D_e^i \quad \text{Eq. V.2}$$

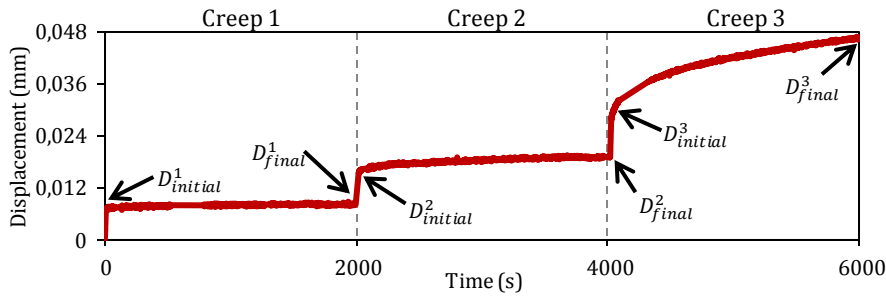


Figure V.15: Initial and final displacements defined for every creep level in a multilevel creep test.

Plotting the elastic and viscous displacements of the adhesives for the three types of load (See Figure V.16), a non-linear evolution of the viscous displacements can clearly be seen, which highlights, the fact that the viscosity is a non-linear function of the current value of the stress. In contrast, the elastic displacement presents more or less a linear behavior proportional to the applied load, which means that the instantaneous Young's modulus seems to have a slight influence on the viscosity of the adhesives.

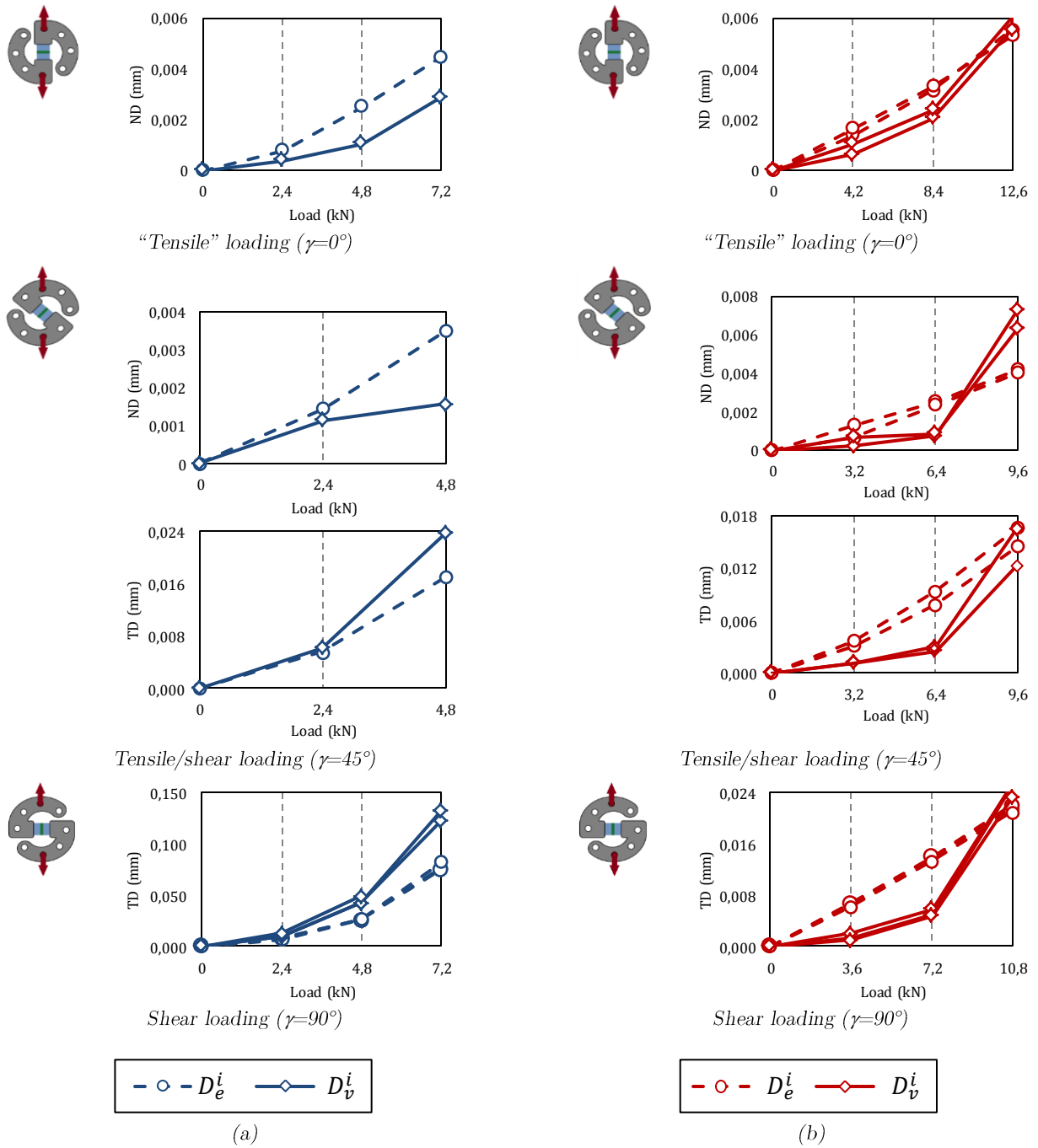


Figure V.16: Elastic and viscous displacement of the Betamate-1822 (a) and Sikapower-498 adhesives (b) at the end of every creep level of multilevel creep tests.

V.4. Increasing cyclic test: toward the cyclic behavior

Even if the objectives of the current study are not the analysis of the behavior of adhesives under cyclic loadings, this is relatively important to the partners of the FASTLITE project. Therefore, this section constitutes a preliminary study to analyze the behavior of the adhesives of the study under very short cyclic loadings.

Increasing cyclic tests have been chosen to test the adhesives under ten repetitive uploading/unloading steps at 10%, 20%, 30%, 40%, 50%, 60%, 70%, 80%, 90% and 100% of the failure load (F_{load}) obtained by the monotonic tests (See Figure V.17). The uploading and unloading rate was 0.2kN/s.

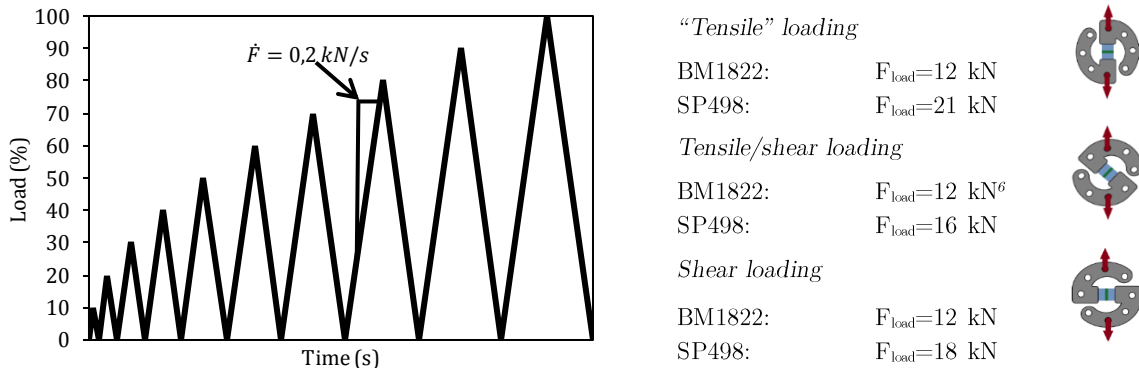


Figure V.17: Increasing cyclic test for different types of load.

Figure V.18 presents the experimental results of both adhesives under “tensile”, tensile/shear and shear increasing cyclic tests. Additionally, the monotonic response at the same loading rate (0.2kN/s) is also plotted in order to compare it with the cyclic response. Discarding the hysteresis of the unloading/loading loop, it is remarkable that the cyclic behavior follows in every case the corresponding monotonic curve.

For all cases, both the hysteresis and the accumulative deformation increase as loading increases. Finally, the cyclic specimens have failed by cohesive fractures at a similar monotonic failure load.

⁶ The value of the ultimate monotonic loading of the BM1822 under tensile/shear loadings was 12 kN (instead of 10 kN).

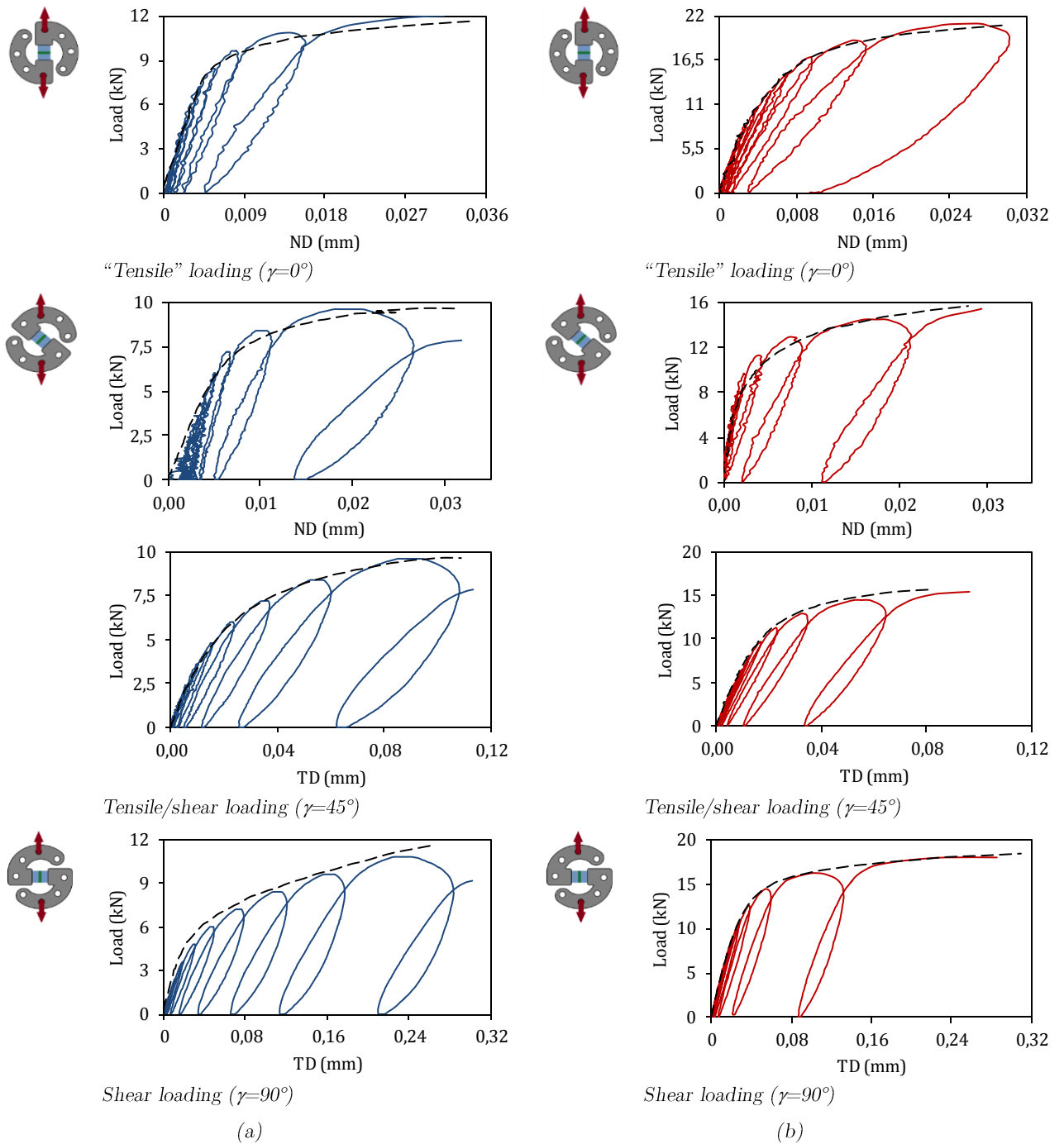


Figure V.18: Betamate-1822 (a) and Sikapower-498 (b) response under increasing cyclic test. The dotted line represents the monotonic response of the corresponding adhesive.

V.5. Overview

The experimental campaign presented in this chapter exposes the principal characteristics of the behavior of the adhesives under static loadings. Three main phenomena have been observed: (i) the influence of the loading rate, (ii) the non-linear evolution of the viscosity and (iii) the hydrostatic pressure dependence. These phenomena are inherent to the behavior of the adhesive and a good modeling of these will permit the correct prediction of the mechanical response of adhesively bonded assemblies.

First, the adhesives were tested under different combinations of tensile/shear monotonic loadings at a loading rate of 0.2kN/s. Figure V.19 shows the load-displacement curves for three types of load ($\gamma=0^\circ$, 45° , 90°). The behavior of the adhesives under “tensile” loading and shear loading at 2kN/s is also plotted with dashed lines in order to highlight the influence of the loading rate.

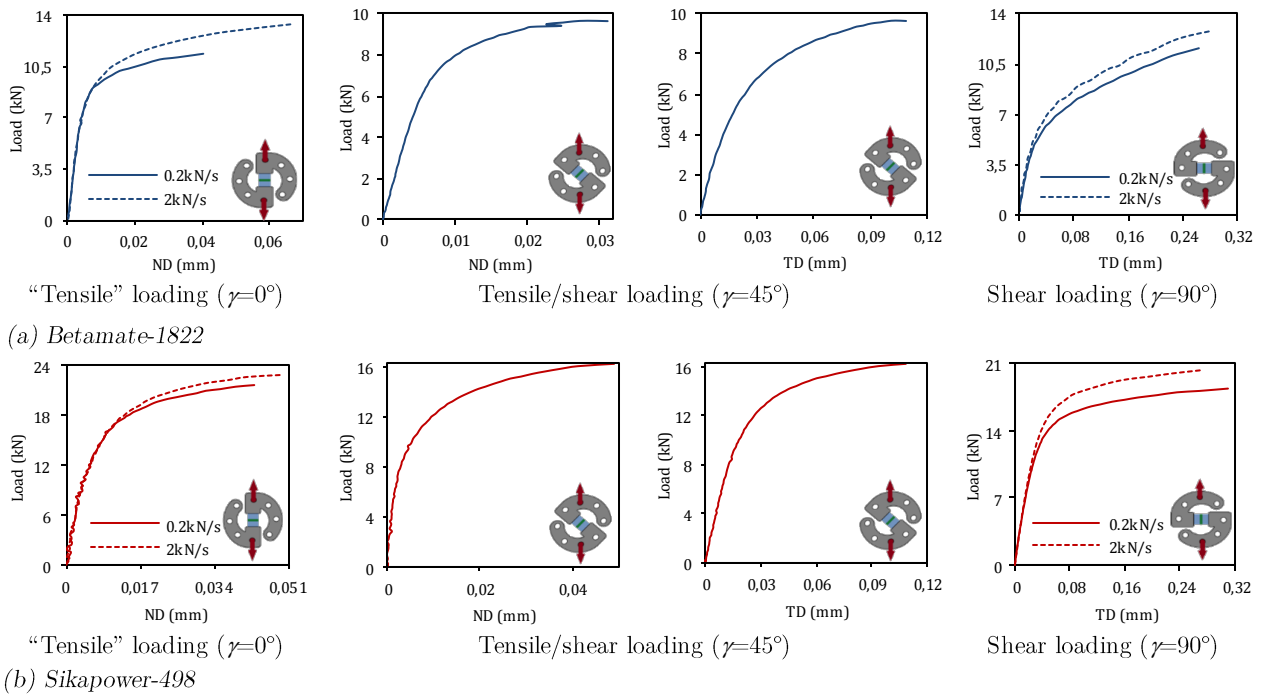


Figure V.19: Overview of the behavior of the adhesives in monotonic tests at 0.2kN/s. Only one single specimen has been plotted for each case. Curves with dashed lines represent the behavior of the adhesives at 2kN/s.

Multilevel creep tests composed of five consecutive stepped creeps of 2000 seconds at 20%, 40%, 60%, 80% and 100% of the failure load have been performed in order to characterize the viscous behavior of the adhesives. The results are presented in Figure V.20. For every type of load ($\gamma=0^\circ$, 45° , 90°), a creep deformation even below the “pseudo-elastic” limit of the adhesives can be seen. The creep displacements under shear loadings are significantly higher than under “tensile” loadings. A non-linear evolution of the viscosity is also observed for both adhesives.

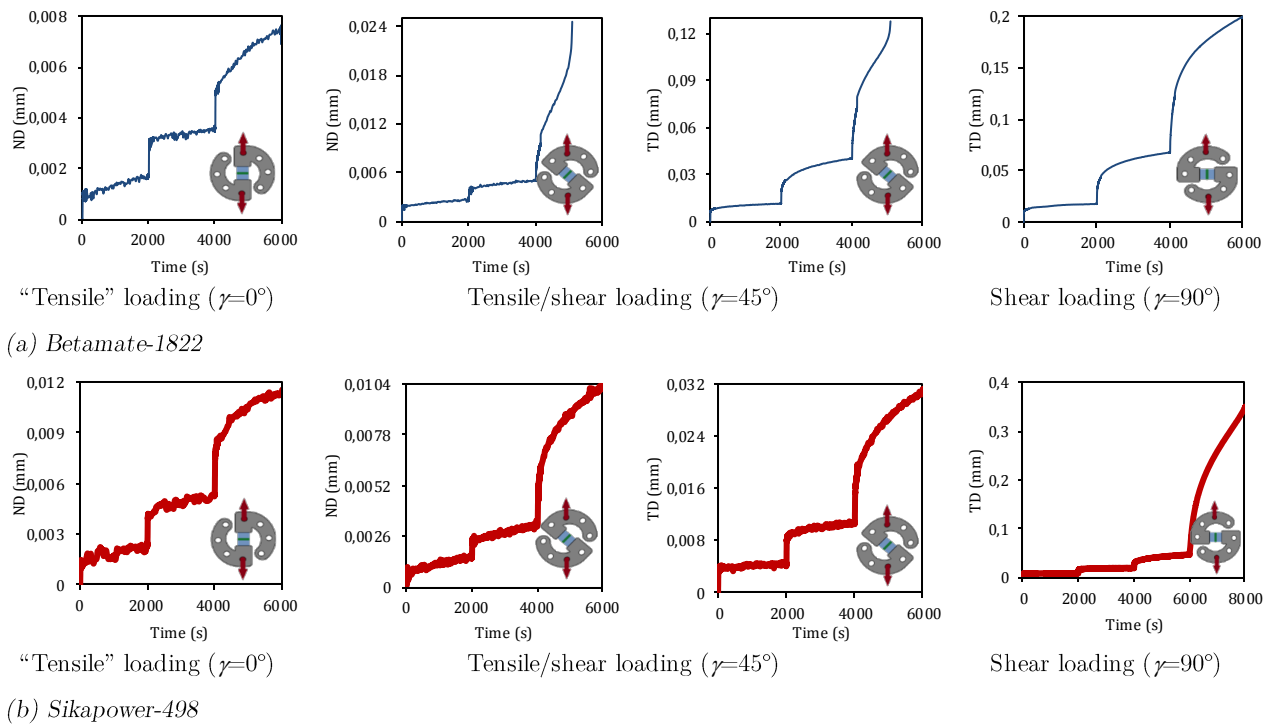
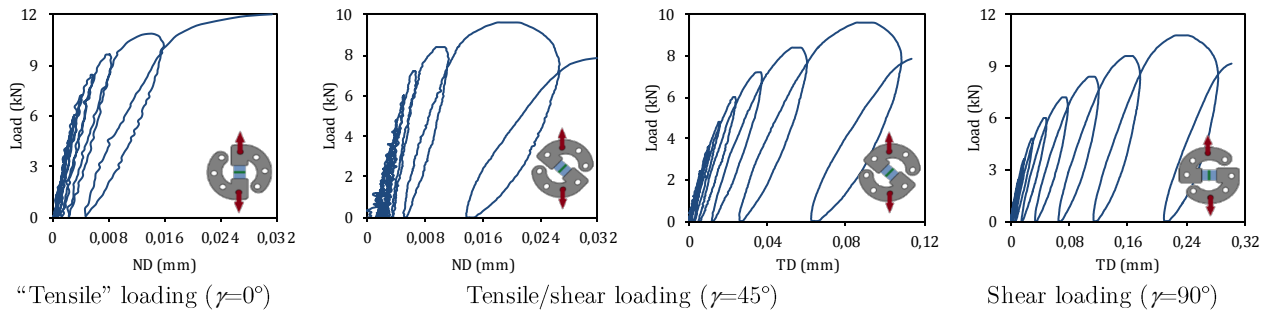


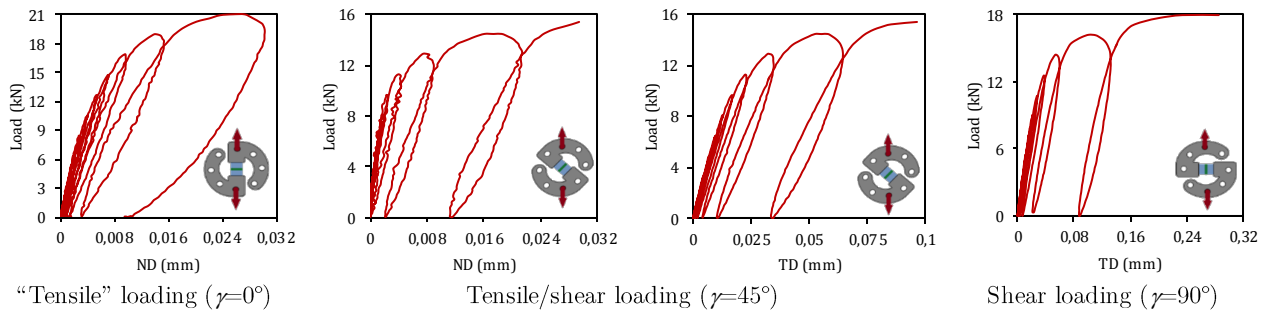
Figure V.20: Overview of the behavior of the adhesives in multilevel creep tests. Only one single specimen has been plotted for each case.

In order to explore the behavior of the adhesives under short cyclic loadings, increasing cyclic tests have been performed with ten repetitive uploading/unloading steps at 10%, 20%, 30%, 40%, 50%, 60%, 70%, 80%, 90% and 100% of the failure load. Figure V.21 presents the displacement of each adhesive under three types of load ($\gamma=0^\circ$, 45° , 90°). For each configuration, a big hysteresis cycle which is associated with the viscous behavior of the adhesives can be seen. This type of behavior confirms the viscous observations previously discussed in monotonic and creep tests.

Finally, the cohesive failures were observed for both adhesives under different combinations of tensile-compression/shear loadings. Furthermore, the scattering on the load-displacement curves was significantly low. These observations allow us to considerate the experimental results obtained by the Arcan test as an accurate representation of the behavior of the adhesives in an assembly.



(a) *Betamate-1822*



(b) *Sikapower-498*

Figure V.21: Overview of the behavior of the adhesives in increasing cyclic tests. Only one single specimen has been plotted for each case.



Chapter VI. Modeling of the behavior of adhesives

Introduction

The previous chapter studied the mechanical behavior of the Betamate-1822 and Sikapower-498 adhesives in an assembly under quasi-static mixed loadings. Hydrostatic sensibility, time dependence and a non-linear evolution of the viscosity were observed in both adhesives. Several models have proposed different alternatives to predict these aspects. Some of them use a viscoelastic law to describe the time-dependence and an elastoplastic law to define the evolution of the accumulative deformation.

This chapter presents a viscoelastic model based on a spectral distribution of the viscosity to describe the time-dependence effects, and a softening law to represent the non-linear evolution of viscosity. In order to take into account the influence of the hydrostatic pressure, the viscoelastic compliance tensor has been separately defined in the hydrostatic and deviatoric space.

The identification of the material parameters is based on an inverse identification of “tensile”, tensile/shear and shear multilevel creep tests. Therefore, FE models have been implemented in order to simulate as close as possible the behavior of the adhesive joint in an Arcan specimen.

At the end of this chapter, the numerical predictions are compared with some experimental curves obtained from different tests. A close macroscopic response is observed in all cases.

Table of contents

VI.1. Brief summary of the modeling of the adhesive behavior	107
VI.1.1. The Generalized Kelvin Model and the relaxation spectrum of viscosity.....	108
VI.1.1.1. Generalized Kelvin Model	109
VI.1.1.1. Relaxation spectrum	111
VI.2. The proposed behavior law	112
VI.3. Inverse identification methodology	115
VI.3.1. Modeling the Arcan test.....	118
VI.4. Parameters identification procedure	121
VI.4.1. Elastic parameters (E, ν)	122
VI.4.1.1. Calculating the experimental Arcan stiffness	122
VI.4.1.1. Determining the numerical elastic parameters	125
VI.4.2. Viscous spectrum (n_o, n_c)	126
VI.4.3. Linear viscosity (a, b)	130
VI.4.4. Non-linear viscous parameters $(Y_o^H, Y_c^H, p^H, Y_o^D, Y_c^D, p^D)$	132
VI.4.5. Mixed mode (α, n)	135
VI.4.6. Identified material parameters.....	137
VI.5. Validation of the behavior law	138
VI.5.1. Validation using Arcan tests.....	138
VI.5.2. Comparison with Bulk test	140
VI.5.3. Comparison with Lap-shear test.....	141
VI.6. Discussions and limitations of the model	143
VI.7. Overview.....	145

VI.1. Brief summary of the modeling of the adhesive behavior

The experimental campaign presented in the previous section has exposed crucial aspects of the behavior of the two adhesives of the study:

- Strong time-dependence effect. This aspect is more noticeable under shear loadings.
- Presence of creep strain for loadings far away from the “pseudo-elastic limit”.
- Non-linear evolution of the viscosity of both adhesives.
- Influence of the hydrostatic pressure on the viscosity. It has been observed a different behavior of the adhesives under “tensile” or shear loading.

These aspects need to be modeled not only with accuracy but with relative ease. Indeed, it is important to the partners of the project that the time calculus and the complexity of the model remain affordable.

The time-dependence aspect and the existence of creep responses under the “pseudo-elastic limit” of the adhesives are evidence of a very important viscous behavior. A great number of models describing the viscoelastic behavior of different materials can be found in the literature; the classic ones assume a rheological model with a linear evolution of the viscosity such as the linear Maxwell model, the linear Kelvin–Voigt model, the Standard Linear Solid (SLS) model or the Wiechert model (Gallegos, 2010). The reader is invited to consult the works of (López-Guerra and Solares, 2014), where a brief comparison of these models is presented. The principal assumption is that the response of the adhesives to constant stress is independent of the loading history (Boltzmann’s superposition principle) and directly proportional to the applied stress. However, the experimental tests discussed in Chapter V showed a non-linear behavior of the viscosity of the adhesives, which implies that the Boltzmann’s superposition principle cannot be assumed.

Other models are based on a meso-scale constitutive model with a non-linear evolution of the viscosity as a function of the stress state and the loading rate (Majda and Skrodzewicz, 2009). These models are more accurate, but their implementation into a 3D finite element modeling often requires a certain degree of complexity. Finally, the most complex models describe the behavior of the adhesive by using a viscoplastic law as in (Mahnken, 2005) or a viscoelastic-viscoplastic law as in (Groth, 1990). These models are adapted for applications with very large deformations where the permanent strain must be taking into account. However, the adhesives of the study will be mainly subjected to low stresses during their service life (less than 50% of their maximum strengths); for these levels, the behavior of the adhesive is principally controlled by a viscoelastic regime. Additionally, the identification of the material parameters of a plastic law usually needs a large number of experimental tests. We conclude then, that a non-linear viscoelastic law may be preferable to describe the behavior of the adhesives.

Another important aspect to take into account in the modeling of the adhesives is the influence of the hydrostatic pressure. As suggested by M. Zgoul in

(Zgoul and Crocombe, 2004), a material model that takes into account the hydrostatic pressure dependence as well as the loading rate effects should be more appropriate in predicting the behavior of the adhesives under mixed loadings.

An encouraging model proposed by Maire (Maire, 1992) in order to describe the non-linear behavior of polymer matrix composite seems to be easily adapted to the objective of this study. This model assumes that the viscosity can be described with a spectral distribution, which permits a wide range of relaxation times to be taken into account in order to better predict multiple relaxation times. This model has recently been implemented to accurately describe the behavior of adhesives under monotonic and creep shear loadings in (Badulescu *et al.*, 2015). However, the non-linear evolution of the viscosity has been described as a function of the current stress state, which implies that the hysteresis loops observed in the increasing cyclic tests cannot be predicted. Additionally, the non-linear behavior under “tensile” and shear loadings has been described by the same law, which contradicts the experimental results observed in the current study in multilevel creep tests under “tensile” and shear loadings (see section III.2).

VI.1.1. The Generalized Kelvin Model and the relaxation spectrum of viscosity

Kelvin–Voight and Maxwell models can be connected with springs and dashpots in order to construct more complex viscoelastic models, such as the Standard Linear Solid Model (SLS). As illustrated in Figure VI.1, the SLS model consists of a spring (E_{el}), which is connected in series with a Kelvin–Voight model represented by a spring (E_1) and a dashpot (η_1). This allows the spring (E_{el}) to be activated instantaneously during loading and unloading accompanied by a time-dependent response of spring (E_1) due to the load transfer through the spring-dashpot Kelvin-Voigt element.

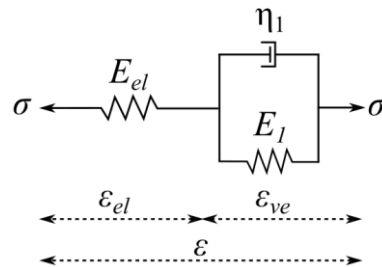


Figure VI.1: Standard linear solid model.

When stress (σ) is applied, the stress-strain equations can be defined as follows:

$$\begin{aligned}\sigma &= \sigma_{el} = \sigma_{ve} \\ \epsilon &= \epsilon_{el} + \epsilon_{ve} \\ \dot{\epsilon} &= \dot{\epsilon}_{el} + \dot{\epsilon}_{ve}\end{aligned}\tag{Eq. VI.1}$$

The stress applied produces strain in spring (E_{el}) described by:

$$\sigma_{el} = E_{el} \varepsilon_{el} \quad \text{Eq. VI.2}$$

This applied stress is also distributed in the Kelvin-Voigt element such that:

$$\sigma = \sigma_{E_1} + \sigma_{\eta_1} \quad \text{Eq. VI.3}$$

Where,

$$\begin{aligned} \sigma_{E_1} &= E_1 \varepsilon_{ve} \\ \sigma_{\eta_1} &= \eta \dot{\varepsilon}_{ve} \end{aligned}$$

Thus, the viscoelastic strain rate can be written as:

$$\dot{\varepsilon}_{ve} = \frac{\sigma}{\eta_1} - \frac{E_1}{\eta_1} \varepsilon_{ve} \quad \text{Eq. VI.4}$$

By making substitutions, appropriate for each individual element, we may deduce from Eq. VI.1 the following first-order non-linear differential equation:

$$\dot{\varepsilon} + \frac{E_1}{\eta_1} \varepsilon = \frac{1}{E_{el}} \dot{\sigma} + \left(\frac{E_{el} + E_1}{\eta_1 E_{el}} \right) \sigma \quad \text{Eq. VI.5}$$

If a constant stress (σ_0) is applied instantaneously at the time $t=0$, the strain state is given by:

$$\varepsilon(t) = \frac{\sigma_0}{E_{el}} + \frac{\sigma_0}{E_1} \left(1 - \exp^{-\left(\frac{E_1}{\eta_1}\right)t} \right) \quad \text{Eq. VI.6}$$

If a constant strain (ε_0) is applied instantaneously at the time $t=0$, the stress response is:

$$\sigma(t) = \varepsilon_0 \left(\frac{E_{el}^2}{E_{el} + E_1} \exp^{-\left(\frac{E_{el} + E_1}{\eta_1}\right)t} + \frac{E_{el} E_1}{E_{el} + E_1} \right) \quad \text{Eq. VI.7}$$

VI.1.1.1. Generalized Kelvin Model

The generalized Kelvin model (also known as the generalized Kelvin-Voigt Standard Linear Solid model) is a linear model where several Kelvin-Voigt elements are connected in series with an equilibrium spring, which represents the elastic response (See Figure VI.2-a). Under constant stress, the material presents several molecular segments with different lengths, which will not be subjected at the same time, inducing multiple relaxation times. The generalized Kelvin model represents this by having as many spring-dashpot elements as are necessary to accurately describe the real distribution (Findley *et al.*, 1989). Once the

load is removed, the material attempts to return to its initial state, but molecular entanglements prevent instantaneous elastic recovery. Besides, if the load is large enough, a permanent strain may take place, this due to chain scission and crazing. Figure VI.2 presents the generalized Kelvin-Voight model and the mechanical response in creep and relaxation tests.

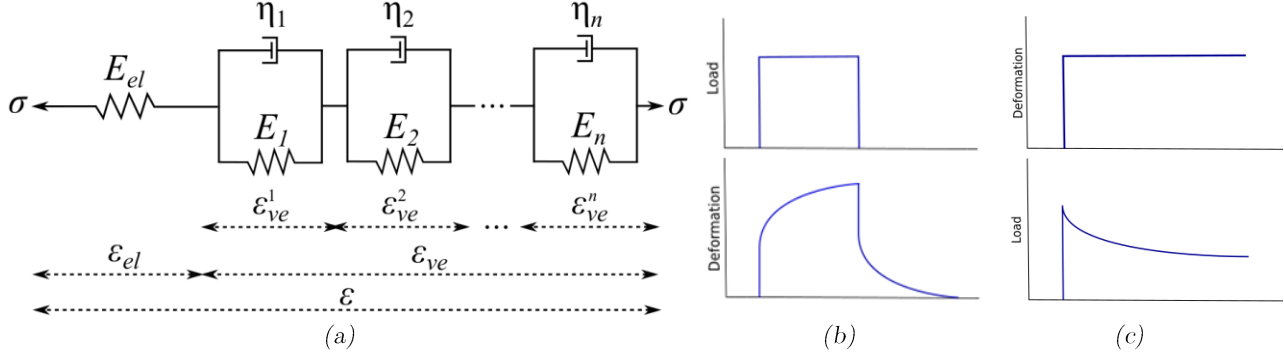


Figure VI.2: Generalized Kelvin model (a). Response of the generalized Kelvin model in a creep and recovery test (b) and in a stress relaxation test (c).

The viscoelastic strain in a generalized Kelvin model can be considered as the sum of the strains of every spring–dashpot Kelvin element. Therefore, the stress-strain equations are defined as follows (See Figure VI.2):

$$\begin{aligned}\sigma &= \sigma_{el} = \sigma_{ve}^1 = \sigma_{ve}^2 = \dots = \sigma_{ve}^n \\ \varepsilon &= \varepsilon_{el} + \varepsilon_{ve}\end{aligned}\quad \text{Eq. VI.8}$$

Where,

$$\begin{aligned}\varepsilon_{el} &= \frac{\sigma_{el}}{E_{el}} \\ \varepsilon_{ve} &= \sum_{i=1}^n \varepsilon_{ve}^i\end{aligned}$$

Thus, the viscoelastic strain rate can be easily defined by:

$$\dot{\varepsilon}_{ve} = \sum_{i=1}^n \frac{\sigma}{\eta_i} - \frac{E_i}{\eta_i} \varepsilon_{ve}^i \quad \text{Eq. VI.9}$$

Or,

$$\dot{\varepsilon}_{ve} = \sum_{i=1}^n \frac{1}{\tau_i} (\mu_i \sigma - \varepsilon_{ve}^i)$$

Where $(\mu_i = \frac{1}{E_i})$ is the compliance modulus (or weight), $(\tau_i = \frac{\eta_i}{E_i})$ is the relaxation time, and (ε_{ve}^i) is the elementary strain of the i -Kelvin-Voight element.

Finally, the creep strain of the generalized Kelvin model under constant stress (σ_0) has the following form:

$$\varepsilon(t) = \frac{\sigma_0}{E_{el}} + \sigma_0 \sum_{i=1}^n \frac{1}{E_i} \left(1 - \exp^{-\left(\frac{E_i}{\eta_i}\right)t} \right) \quad \text{Eq. VI.10}$$

VI.1.1.1. Relaxation spectrum

Other models based on a discrete definition of the viscosity propose a distribution function to model multiple relaxation times. These models are commonly called spectral models and can be seen as a generalized Kelvin model where the compliance modulus (μ_i) and the relaxation times (τ_i) are defined by a distribution function. Therefore, every spring-dashpot Kelvin element is replaced by an elementary viscous mechanism (ξ_i), which represents the viscoelastic strain of the i -Kelvin element (See Eq. VI.11). Figure VI.3 illustrates the concept of spectral models.

$$\varepsilon_{ve} = \sum_{i=1}^{n_t} \xi_i \quad \text{Eq. VI.11}$$

With,

$$\xi_i = f(\tau_i, \mu_i)$$

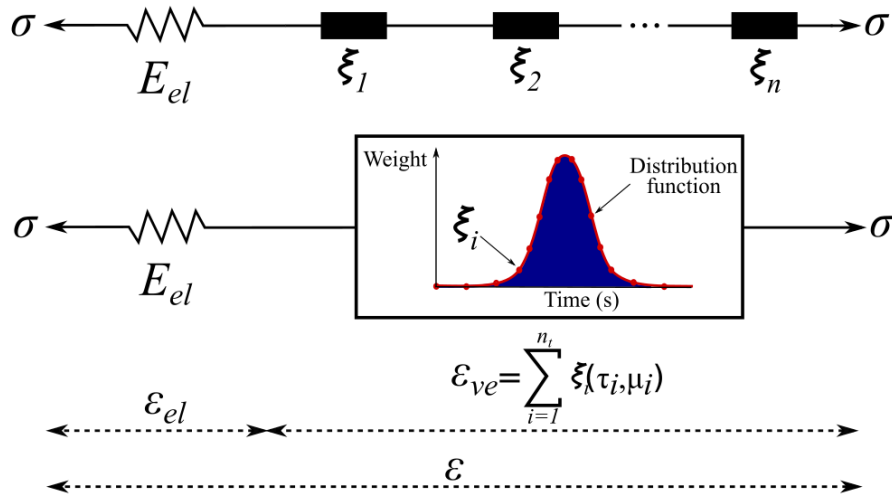


Figure VI.3: Representation of a spectral model.

VI.2. The proposed behavior law

In order to be able to describe as close as possible the experimental results, the model proposed in this study is defined as follows:

$$\underline{\underline{\sigma}} = \underline{\underline{C}} : (\underline{\underline{\varepsilon}} - \underline{\underline{\varepsilon}}^{ve}) \quad \text{Eq. VI.12}$$

Where $(\underline{\underline{\sigma}})$ is the stress tensor, $(\underline{\underline{C}})$ the fourth-order elastic tensor, $(\underline{\underline{\varepsilon}})$ the total strain tensor and $(\underline{\underline{\varepsilon}}^{ve})$ the viscoelastic strain tensor. The viscoelastic strain $(\underline{\underline{\varepsilon}}^{ve})$ is considered as a summation of elementary viscous mechanisms $(\underline{\underline{\xi}}_i)$ which have a specific relaxation time (τ_i) and weight (μ_i) .

$$\underline{\underline{\varepsilon}}^{ve} = \sum_{i=1}^{n_t} \underline{\underline{\xi}}_i \quad \text{Eq. VI.13}$$

With,

$$\underline{\underline{\xi}}_i = \frac{1}{\tau_i} \left(\mu_i \underline{\underline{S}}^R : \underline{\underline{\sigma}} - \underline{\underline{\xi}}_i \right) \quad \text{Eq. VI.14}$$

The reader can see the similar form of equations Eq. VI.4, Eq. VI.9 and Eq. VI.14. The set of all couples (τ_i, μ_i) defines the spectrum of relaxation times (viscous spectrum) that is supposed to have a Gaussian form:

$$\begin{aligned} \tau_i &= \exp(n_i) \\ \mu_i &= \frac{\bar{\mu}_i}{\sum_{i=1}^{n_t} \bar{\mu}_i} \end{aligned} \quad \text{Eq. VI.15}$$

With,

$$\bar{\mu}_i = \frac{1}{n_0 \sqrt{\pi}} \exp\left(-\left(\frac{n_i - n_c}{n_0}\right)^2\right)$$

Where (n_c) is the mean and (n_0) can be considered as the standard deviation⁷. The number of mechanisms used to describe the spectrum of the viscosity (n_t) , is a user parameter that must be chosen carefully. Here, we have considered twenty elemental viscous mechanisms to ensure a good representation of the viscoelastic strain (Badulescu *et al.*, 2015). The value (n_i) is an integer number comprised between two limits: $(n_1 = -20)$ and $(n_2 = 30)$. These values permit the too low or too high relaxation times to be eliminated (see Figure VI.4):

$$\tau_i \in [\exp(n_1) : \exp(n_2)] = [2.0612e^{-9} : 1.0686e^{13}] \quad \text{Eq. VI.16}$$

⁷ The actual value of the standard deviation corresponds to $S_d = n_0/\sqrt{2}$.

It is worth noting that this viscoelastic spectral model cannot model permanent strain. Nevertheless, since very long relaxation times have been considered, it is possible to predict “pseudo” permanent strain in recovery tests.

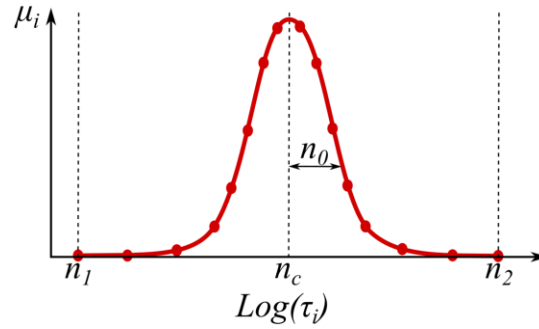


Figure VI.4: Definition of the Gaussian form of the viscous spectrum.

As stated in the experimental campaign, the adhesives present a different behavior under “tensile” and shear loadings due to the strong influence of the hydrostatic. In order to considerate this particularity in the modeling of the viscosity, the “softened” viscoelastic compliance tensor ($\underline{\underline{S}}^R$) presented in Eq. VI.14 is separated in two parties: the hydrostatic part and the deviatoric part. The hydrostatic direction tensor ($\underline{\underline{H}}^H$) and the deviatoric direction tensor ($\underline{\underline{H}}^D$) are used in order to define the viscoelastic flow direction. Additionally, two material parameters: (a) for hydrostatic loadings and (b) for deviatoric loadings will define the linear evolution of the viscosity. Finally, the non-linear character of the viscosity is modeled by two softening variables (d^H) and (d^D), which describe, respectively, the hydrostatic and deviatoric non-linear evolution:

$$\underline{\underline{S}}^R = \frac{1}{a(1-d^H)} \underline{\underline{P}}^H + \frac{1}{b(1-d^D)} \underline{\underline{P}}^D \quad \text{Eq. VI.17}$$

Where,

$$\underline{\underline{P}}^H = \underline{\underline{H}}^H = \frac{1}{3} \underline{\underline{I}} \otimes \underline{\underline{I}} = \frac{1}{3} \begin{bmatrix} 1 & 1 & 1 & 0 & 0 & 0 \\ 1 & 1 & 1 & 0 & 0 & 0 \\ 1 & 1 & 1 & 0 & 0 & 0 \\ 0 & 0 & 0 & 0 & 0 & 0 \\ 0 & 0 & 0 & 0 & 0 & 0 \\ 0 & 0 & 0 & 0 & 0 & 0 \end{bmatrix}$$

$$\underline{\underline{P}}^D = \underline{\underline{H}}^D = \underline{\underline{I}} - \underline{\underline{H}}^H = \begin{bmatrix} \frac{2}{3} & -\frac{1}{3} & -\frac{1}{3} & 0 & 0 & 0 \\ -\frac{1}{3} & \frac{2}{3} & -\frac{1}{3} & 0 & 0 & 0 \\ -\frac{1}{3} & -\frac{1}{3} & \frac{2}{3} & 0 & 0 & 0 \\ 0 & 0 & 0 & 1 & 0 & 0 \\ 0 & 0 & 0 & 0 & 1 & 0 \\ 0 & 0 & 0 & 0 & 0 & 1 \end{bmatrix}$$

It is worth mentioning that every elementary viscous mechanism ($\underline{\xi}_i$) have the same compliance tensor ($\underline{\underline{S}}^R$) and they only differ in their relaxation times (τ_i) and weights (μ_i).

The softening variables (d^H, d^D) follow an exponential form characterized by the material parameters (Y_c^H, p^H) and (Y_c^D, p^D). The threshold of non-linearity is defined by the parameters (Y_0^H) for hydrostatic loadings and (Y_0^D) for deviatoric loadings:

$$\begin{aligned} d^H &= d_{max} \left(1 - e^{-\left(\frac{\langle Y - Y_0^H \rangle^+}{Y_c^H}\right)^{p^H}} \right) \\ d^D &= d_{max} \left(1 - e^{-\left(\frac{\langle Y - Y_0^D \rangle^+}{Y_c^D}\right)^{p^D}} \right) \end{aligned} \quad \text{Eq. VI.18}$$

With,

$$\begin{aligned} \dot{d}^H &\geq 0 \\ \dot{d}^D &\geq 0 \end{aligned}$$

In order to respect the second law of thermodynamics, the softening variables must always be monotonically increasing, this is why ($\dot{d}^{H,D} \geq 0$) (Lévêque D. *et al.*, 2000). The reader can find more information about the thermodynamic analysis of this type of postulate in (Maire, 1992), (Maire J.F. *et al.*, 1996) and (Schieffer, 2003).

The thermomechanical potential (Y) presented in Eq. VI.18 is a coupled potential of mode I (hydrostatic sensibility) and mode II (deviatoric sensibility). This potential only depends on the current stress state ($\underline{\sigma}$):

$$Y = (\alpha(Y^H)^n + \beta(Y^D)^n)^{1/n} \quad \text{Eq. VI.19}$$

Where,

$$\begin{aligned} Y^H &= \frac{1}{2a} (\underline{\sigma} : \underline{\underline{H}}^H : \underline{\sigma}) \\ Y^D &= \frac{1}{2b} (\underline{\sigma} : \underline{\underline{H}}^D : \underline{\sigma}) \end{aligned}$$

The mixed mode kinetic is assumed by the parameters (α, β, n). For simplicity in the identification procedure, we have chosen $\beta = 1$.

Finally, fourteen material parameters are used to characterize the behavior of the adhesive (See Table VI-1).

Modeling relevance	Material parameter	Symbol	Unit
Elasticity	Young modulus	E	MPa
	Poisson's ratio	ν	-
Viscous spectrum	“Standard” deviation	n_0	-
	Mean	n_c	-
Linear viscosity	Hydrostatic sensibility	a	MPa
	Deviatoric sensibility	b	MPa
Linear viscoelastic threshold	Hydrostatic linear viscoelastic threshold	Y_0^H	MPa
	Deviatoric linear viscoelastic threshold	Y_0^D	MPa
Non-linear viscosity	Seed of the softening law in hydrostatic loadings	Y_c^H	MPa
	Shape of the softening law in hydrostatic loadings	p^H	-
	Seed of the softening law in deviatoric loadings	Y_c^D	MPa
	Shape of the softening law in deviatoric loadings	p^D	-
Mixed mode	Mode I sensibility	α	-
	Mode coupling	n	-

Table VI-1: Material parameters to identify.

VI.3. Inverse identification methodology

Due to the non-uniform stress distribution overall the adhesive joint during an Arcan test (See Section II.1.3.1), the strain-stress curve typically used in material science to determine the material parameters of the behavior law cannot be easily defined. Therefore, the identification of the material parameters must be based on a comparison of the experimental results and the numerical predictions of a Finite Element Modeling (FEM) of the Arcan test (Cognard, 2008). This type of approach is commonly named “inverse identification” since the material parameters of the behavior law are determined by a trial-and-error method. This section illustrates the numerical methodology and the FEM used in this study.

In general, the inverse identification procedure determines the inputs of a system based on the given responses, the boundary conditions and a system model. This procedure supposes accurate knowledge of the boundary conditions and a well-defined system model in order to ensure a correct identification of the inputs. In materials science, several authors have already used this technique to determine the material parameters of a behavior law (Oliveira *et al.*, 2015). It has the advantage of taking into account the non-homogeneous stress distribution of the adhesive joint (Cognard *et al.*, 2008) and the elastic strains of the substrates during loading, as suggested by Adams (R. D. Adams *et al.*, 1997). However, the accuracy of the identification is strongly linked to the accurate representation of the tests by the FE model (the boundary conditions, the mesh convergence, the consistent tangent matrix and the time increment, etc.), the initial set of parameters and the search algorithm. We have considered that the FE models presented in this section are able to describe the “real” behavior of the adhesive joint in an Arcan specimen. Consequently, at the end of the identification procedure, a good concordance between the experimental results and the numerical predictions was expected. The finite element code used was Abaqus/standard version 6.12 (Dassault Systèmes Simulia, 2012).

The inverse identification technique needs the definition of an objective function (error) that must be minimized:

$$Error = \frac{1}{n} \sum_{i=1}^n \left(\frac{D^{exp} - D^{FE}}{D^{exp}} \right)_i^2 \quad Eq. VI.20$$

Where (n) , (D^{exp}) and (D^{FE}) are, respectively, the number of experimental data, the numerical displacement and the experimental displacement of the tests performed for both adhesives. It is worth noting that the displacements are compared at the same time interval (t^{exp}) .

In this work, two procedures have been performed in order to identify the material parameters of the behavior law:

- (i) Iterative procedure: This technique allows a general analyze of the influence of the researched parameters. However, it requires a good initial estimation of their possible correct values. The procedure is controlled by a Matlab function, which receives the experimental data and the full sets of material parameters to test (See Figure VI.5). The numerical simulations start with the first set of parameters and the Abaqus calculus. Then, the numerical prediction (which is recovered by a Python script) is compared with the experimental response. The error of the current set of parameters is calculated and stored in a vector type variable. The next numerical simulation is started with a new set of parameters. The iterative loop is ended when all possible sets have been tested. At the end of the iterative process, a vector type variable containing the objective function of each set of parameters is stored; the lower value is then chosen as the correct set of parameters.
- (ii) Optimization procedure: This technique is generally used when the values of the material parameters are particularly hard to estimate. Once again, a Matlab function is used in order to control the procedure (See Figure VI.6). The initial parameters and the experimental data are received as input arguments. The numerical simulations are performed with the initial set of parameters and the macroscopic response is recovered by a Python script. Then, the objective function is evaluated and the error is compared with a termination tolerance. If the error is bigger than the tolerance, the *fminsearch* function of Matlab generates a new set of parameters and the cycle starts all over again. The calculus ends when the current value of the function error is lower than the tolerance. The algorithm used by the *fminsearch* function is a “Nelder-mead simplex method” descent algorithm described in (Jeffrey c. Lagarias *et al.*, 1998).

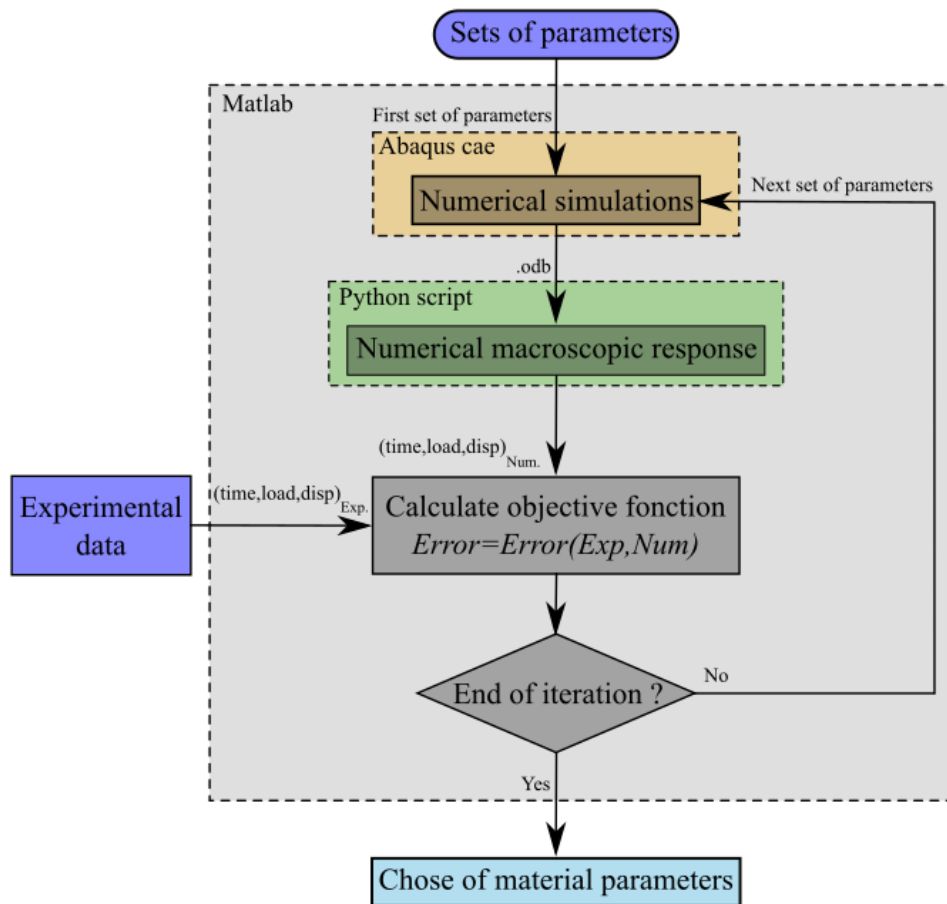


Figure VI.5: Inverse identification in an iterative procedure.

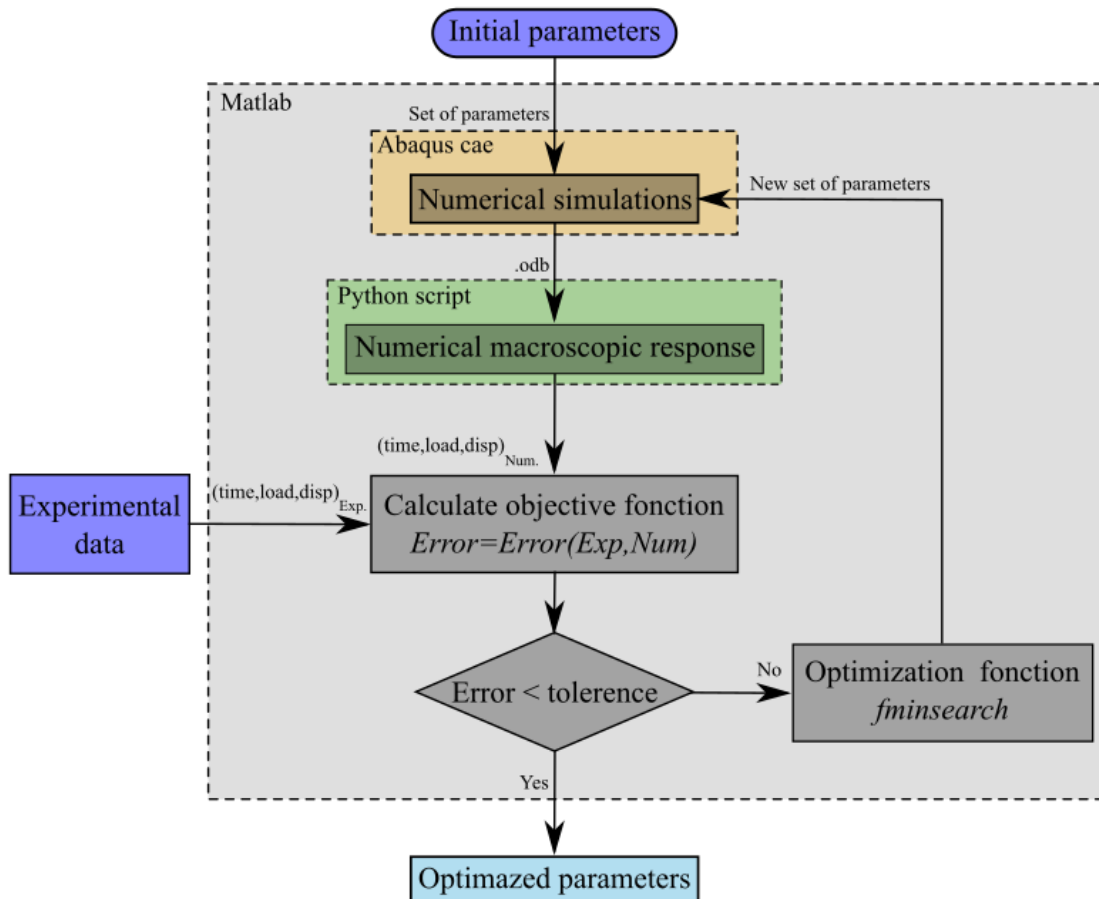


Figure VI.6: Inverse identification in an optimization procedure.

VI.3.1. Modeling the Arcan test

A fine model of the Arcan test should consider the deformation of the holding grip plus the Arcan device plus the specimen. However, this kind of approach is expensive in terms of computing time and machine requirements due to the interactions between the pieces (contact forces) and the geometrical complexity (mesh and stress concentrations). In order to simplify the modeling, it has been assumed that the machine load is perfectly transferred from the tensile machine to the specimen (See Figure VI.7-a). In consequence, the FEM of the Arcan test only includes the modeling of the Arcan specimen. Additionally, the computing time can be reduced by using the planes of symmetry of the Arcan specimen. Indeed, in the case of “tensile” loadings ($\gamma=0^\circ$), the planes $(\mathbf{O}, \vec{x}, \vec{y})$, $(\mathbf{O}, \vec{x}, \vec{z})$ and $(\mathbf{O}, \vec{y}, \vec{z})$ are used as planes of symmetry, reducing the FEM at one eighth of the specimen size (See Figure VI.7-b). On the other hand, when tensile/shear or shear loadings are applied ($\gamma=45^\circ, 90^\circ$), only the plane $(\mathbf{O}, \vec{y}, \vec{z})$ can be considered as a plane of symmetry. In this case, node-by-node antisymmetric boundary conditions are implemented over the middle plane of the adhesive joint (noted as the bottom surface) as proposed in (Alfonso *et al.*, 2015). It reduces the Arcan model at half of the Arcan specimen (See Figure VI.7-b). Finally, the load applied to the specimen may be modeled by a reference points (RP-1) linked to the top surface of the substrate by kinematic coupling. The type of element mesh used is 8-node linear brick elements with reduced integration and hourglass control (C3D8R).

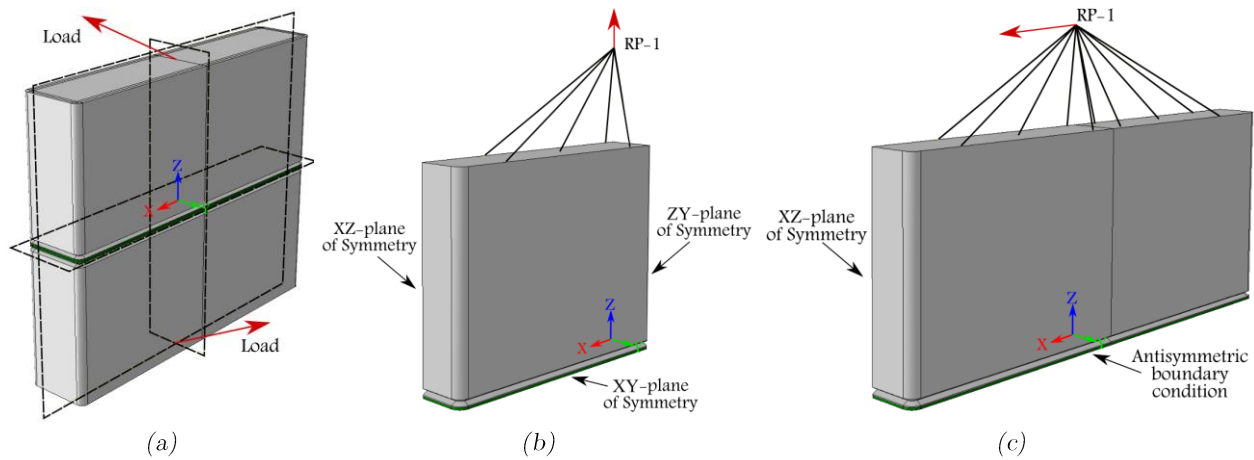


Figure VI.7: 3D finite element model of the whole Arcan specimen (a). FEM used in the case of a “tensile” loading (b) and a shear loading (c).

The node-by-node antisymmetric boundary conditions link the displacements of the left nodes ($x > 0$) with the right nodes ($x < 0$) of the bottom surface by linear constraint equations:

$$\begin{cases} U_x^{i,j,l} = -U_x^{i,j,r} \\ U_y^{i,j,l} = U_y^{i,j,r} \\ U_z^{i,j,l} = -U_z^{i,j,r} \end{cases} \quad \text{Eq. VI.21}$$

Where (x, y, z) represent the three principal directions in the coordinate system, (l) and (r) the left and right side of the bottom surface, and (i, j) the position of the node. Thus, for example, the displacement along the (\vec{x}) direction of the node (i, j) on the left side ($U_x^{i,j,l}$) is inversely proportional to the displacement along the (\vec{x}) direction of the node (i, j) on the right side ($U_x^{i,j,r}$) (See Figure VI.8). The node-by-node definition of the antisymmetric equations requires a symmetric mesh in order to properly link the associated nodes. The equations have been implemented in Abaqus by a Python script. Finally, we considered that there was no displacement of the central line nodes along the (\vec{x}) and (\vec{z}) directions.

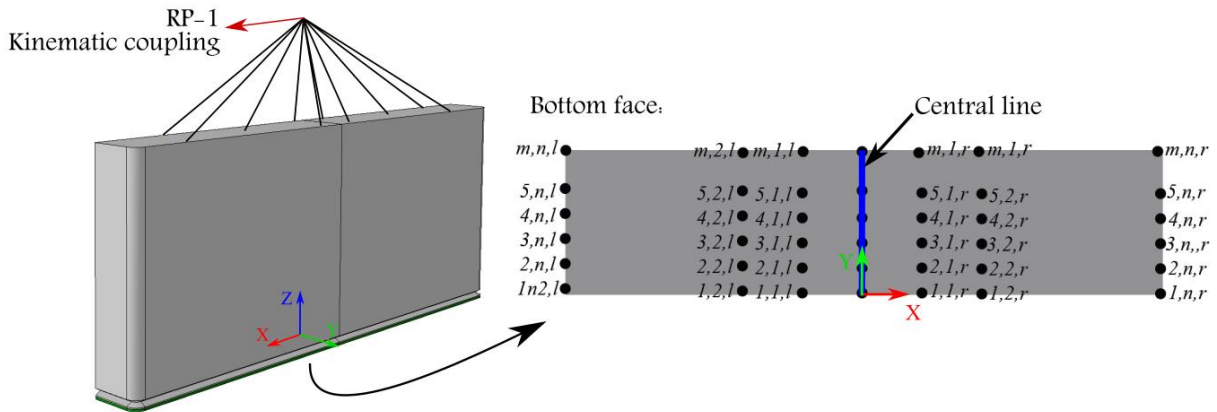


Figure VI.8: Definition of the node-by-node antisymmetric boundary conditions.

The 3D models presented in Figure VI.7 have been used to identify the elastic parameters of the behavior law by an iterative procedure (See section VI.4.1). However, for all other parameters, the implementation of these models in an iterative process leads to very long computing times. In order to overtake this problem, reduced 3D models with one element in the thickness direction were implemented (plane strain assumption) have been implemented. The reduced 3D model and the boundary conditions for “tensile” and shear loadings are presented in Figure VI.9. It is worth noting that the applied load is adapted to the top surface area modeled by each model (3D model or reduced 3D model).

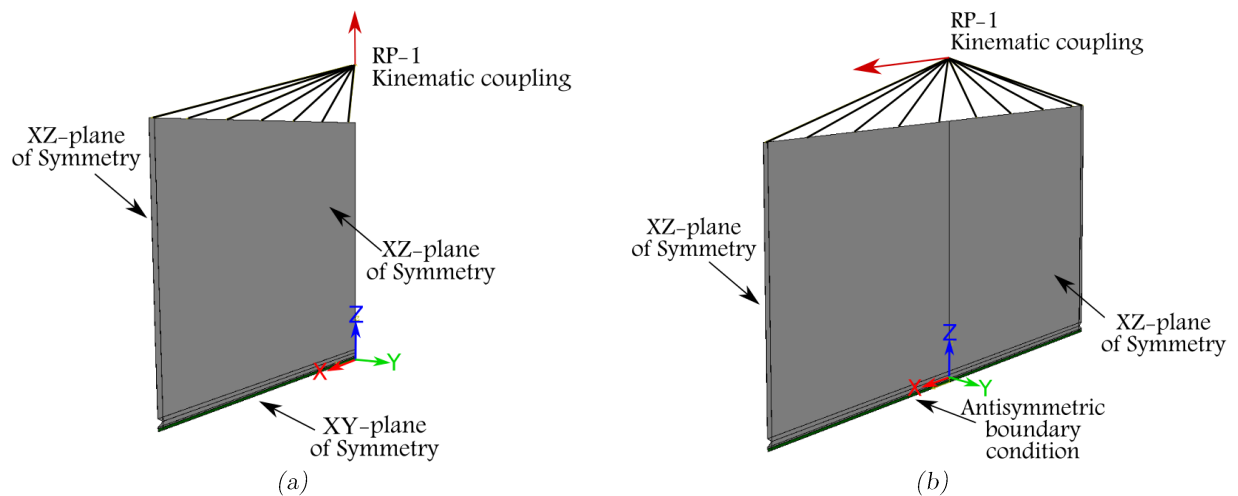


Figure VI.9: Reduced 3D finite element model of the Arcan specimen under “tensile” loadings (a) and shear loadings (b).

Due to the stress concentration presented near the edges at the adhesive/substrate interface, a progressively refined mesh is required in these zones. Additionally, a parametric study performed in (Badulescu *et al.*, 2015) has shown that an enlarged mesh with five elements in the thickness of the adhesive (element size around $80\mu\text{m}$) is sufficient to obtain a convergent macroscopic load-displacement curve with a non-linear viscoelastic model. Thus, the size of the elements is minimum (around $100\mu\text{m}$) near the edges and increases gradually by bias techniques along the (\vec{x}) , (\vec{y}) and (\vec{z}) axes. A typical mesh for the 3D model and the reduced 3D model is shown in Figure VI.10. The element type used was an 8-node linear brick (C3D8) meshed with the sweep medial axis technique.

The substrates of the Arcan specimen are made of aluminum; and typical linear isotropic parameters are assumed (*Young modulus* $E_{al}=73\text{GPa}$, *Poisson's ratio* $\nu_{al}=0.3$). The behavior of the adhesives is modeled by a non-linear spectral viscoelastic model presented in section VI.2. This model has been implemented by means of a UMAT user subroutine with a classical implicit iterative procedure. The state variables are overloaded at the end of every time increment $[t_0 : t_1]$. The user subroutine calculates the consistent tangent matrix and the residual nodal vector by the Newton-Rapshon method. Details about the numerical implementation of constitutive models can be found in books specialty devoted to the FE method (Jean-Louis Batoz, 1995).

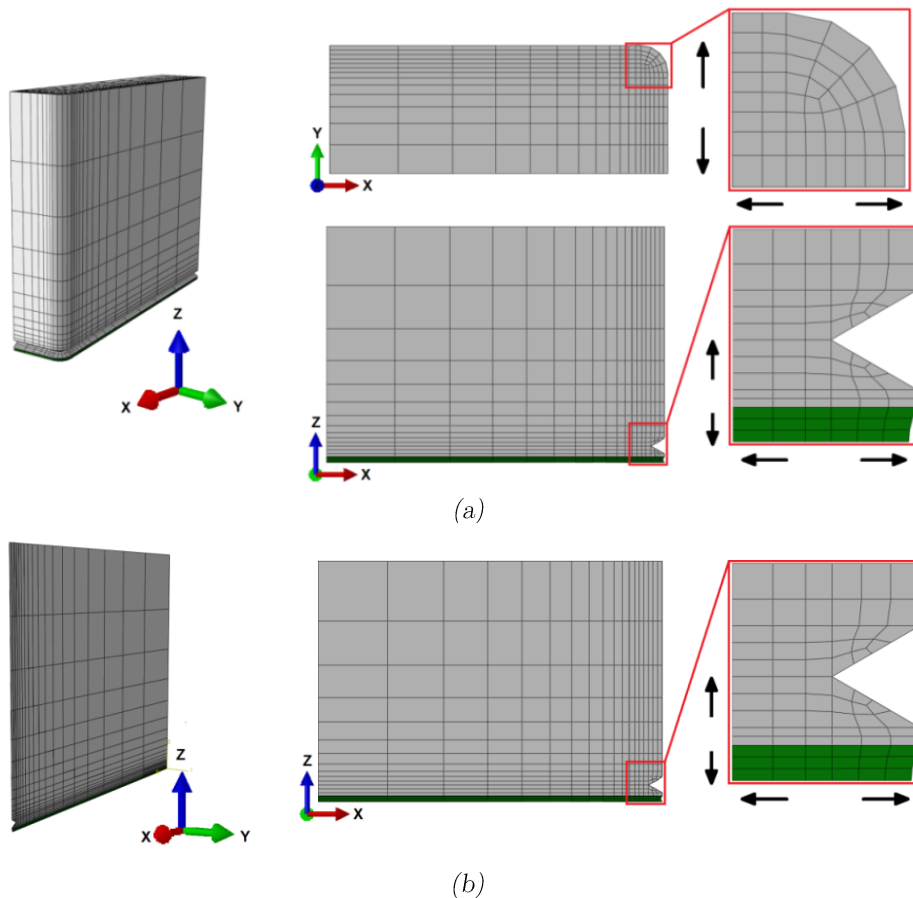


Figure VI.10: Typical mesh used in the FEM of the Arcan test for the 3D model (a) and the reduced 3D model (b).

In order to validate the use of a reduced model, numerical predictions of the 3D model and the reduced 3D model were compared. As shown in Figure VI.11, both models predict a similar numerical response, nevertheless, the use of a reduced model decreases the computing time by about 80%. The hypothetical test case presented in Figure VI.11 was a monotonic tensile/shear Arcan test at a loading rate of 2kN/s; the relative displacements were obtained at the same region for both models.

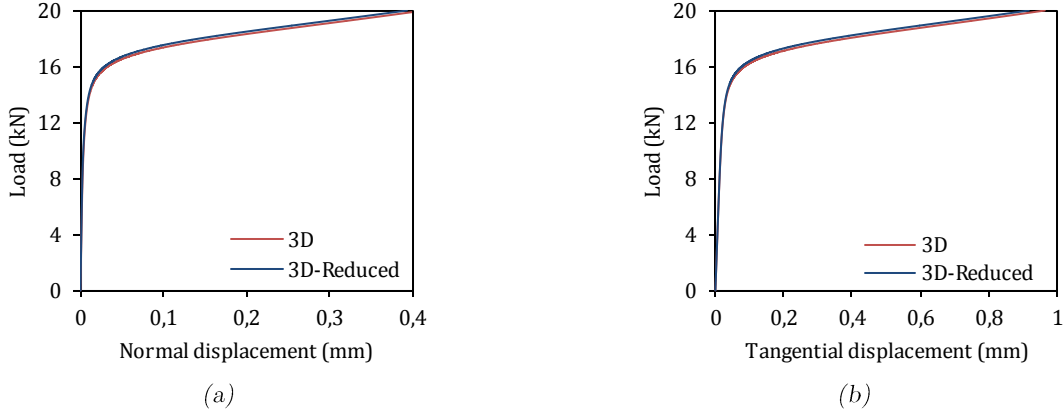


Figure VI.11: Comparison of the numerical prediction of 3D and reduced 3D models. Normal displacement (a) and tangential displacement (b) of a monotonic tensile/shear Arcan test.

VI.4. Parameters identification procedure

The material parameters of the proposed behavior law can be grouped as a function of their modeling feature. This permits the developing of a sequential identification procedure, starting with the elastic behavior, then the viscous spectrum, the linear viscosity, the non-linear evolution of viscosity and finally the mixed mode as shown in Figure VI.12.

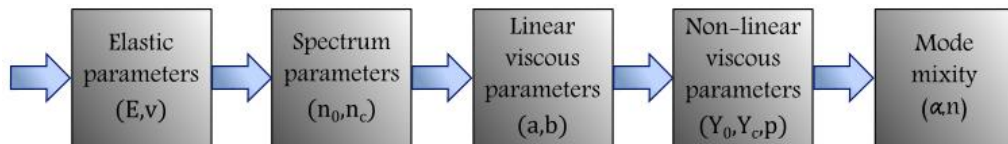


Figure VI.12: Sequential identification procedure.

One of the aims of this study is the rapid and easy identification of the material parameters of the adhesives. Consequently, in order to reduce the number of tests and the time spent in the experimental campaign, we have based the identification procedure on the multilevel creep test presented in section V.3. Three types of load are needed to completely identify the behavior law: “tensile”, tensile/shear and shear loadings. This choice reduces the experimental campaign to one single working day (three tests, each one of two hours and thirty minutes).

Finally, even if a low scattering was observed, all the experimental curves obtained from the characterization campaign have been considered in the identification procedure in order to take into account the possible discrepancies in the results.

VI.4.1. Elastic parameters (E, ν)

The identification of the elastic parameters has been widely investigated and debated over the last centuries. Several authors consider the interpretation of static and dynamic tensile stress-strain curves as a good technique to estimate the Young's modulus; some others prefer the use of DMA tests (Dynamic mechanical analysis), which have proven accurate results for the calculus of the Young's modulus as a function of frequency and temperature. The reader may consult (Lemaitre and Chaboche, 1994) in chapter 4 for additional information about the elastic parameters identification. Here, we have proposed a new technique based on the different behavior of adhesives for different orientations of the Arcan device. The idea is to estimate by numerical simulations the Young's modulus and the Poisson's ratio that represent simultaneously the stiffness observed in "tensile" and shear Arcan tests.

VI.4.1.1. Calculating the experimental Arcan stiffness

First, in order to consider the noise measurement due to the sampling rate (2 images by second), a bootstrapping technique has been implemented. This technique determines a confidence interval of the "tensile" and shear experimental stiffnesses of the adhesives. The procedure is described as follows:

- 1) Selection of the experimental data: It has been assumed that adhesives present a "perfect" elastic regime (i.e. without the influence of viscosity) for loadings lower than 20% of their failure load. Therefore, the experimental data used to determine the elastic parameters correspond to the unloading part of the first creep level of the "tensile" and shear multilevel creep tests (See Figure VI.13).
- 2) Calculation of the stiffness: Two-thirds of the selected experimental data are randomly used to calculate the experimental stiffness of the adhesives by linear regression.
- 3) Filling the stiffness array: The previous step is repeated n -times. For each new randomly selected experimental data, the stiffness is stocked in a n -sized array.
- 4) Confidence interval: The average (\bar{x}) and the standard deviation (S_d) of the n -sized stiffness array are calculated:

$$\bar{x} = \frac{1}{n} \sum_{i=1}^n x_i$$

$$S_d = \sqrt{\frac{1}{n-1} \sum_{i=1}^n (x_i - \bar{x})^2}$$
Eq. VI.22

The stiffness of the adhesives for the n -loop is defined by a 95% confidence interval:

$$K_n = \bar{x} \pm 2 \times S_d$$
Eq. VI.23

- 5) *Convergence*: Step 3 and 4 are repeated with a bigger n number until stabilization of both average and standard deviation. Thus, the real value of the experimental stiffness is between the upper stiffness value (K_{exp}^+) and the lower stiffness value (K_{exp}^-) defined by the converged value of the confidence interval:

$$\begin{aligned} K_{exp}^+ &= \bar{x} + 2 * S_d \\ K_{exp}^- &= \bar{x} - 2 * S_d \end{aligned} \quad \text{Eq. VI.24}$$

The experimental stiffness of the adhesive is calculated for “tensile” and shear loadings. In consequence, two different stiffnesses are determined: one for “tensile” loadings and one for shear loadings. Figure VI.13 illustrates the technique used to identify the experimental stiffness of the adhesives. Table VI-2 presents the final value of the “tensile” and shear stiffness.

n	BM1822		SP498	
	Shear stiffness (kN/mm)	Tensile stiffness (kN/mm)	Shear stiffness (kN/mm)	Tensile stiffness (kN/mm)
100	K= 285.6 ± 12.1	K= 2071.8 ± 88.9	K= 450.3 ± 9.2	K= 2853.4 ± 200.2
1000	K= 285.6 ± 12.7	K= 2075.5 ± 77.3	K= 454.7 ± 8.6	K= 2867.3 ± 206.3
10000	K= 285.3 ± 12.8	K= 2074.9 ± 79.6	K= 455.0 ± 8.8	K= 2872.0 ± 206.9

Table VI-2: Confidence interval of the “tensile” and shear stiffness.

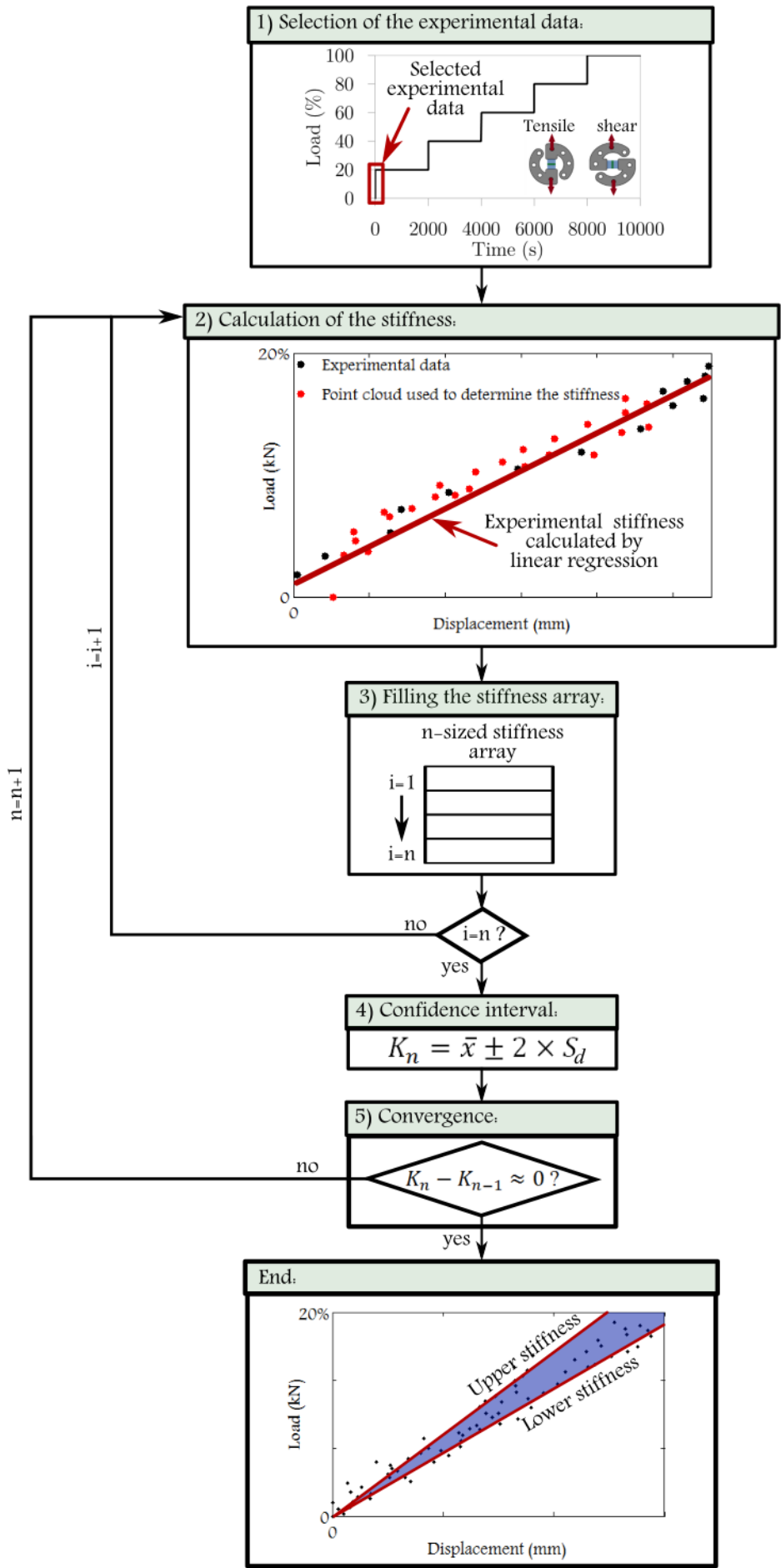


Figure VI.13: Identification procedure of the experimental stiffness of the adhesives.

VI.4.1.1. Determining the numerical elastic parameters

Once the experimental stiffness of the adhesives has been determined, elastic finite element simulations are performed with the 3D model presented in section VI.3.1. These simulations have the aim of selecting the best couple (E, ν) that represents simultaneously the experimental stiffness in “tensile” and shear loadings. Here, we have chosen a large number of possible couples between $E=[10:10000]$ MPa and $\nu=[0.2:0.49]$. For every possible couple (E, ν) , an error is calculated:

$$Error = \begin{cases} 0, & \text{if } K_{exp}^- < K_{FE} < K_{exp}^+ \\ \left(\frac{K_{average} - K_{FE}}{K_{average}} \right)^2, & \text{otherwise} \end{cases} \quad \text{Eq. VI.25}$$

With,

$$K_{average} = \frac{K_{exp}^+ + K_{exp}^-}{2}$$

Where (K_{FE}) is the numerical stiffness, (K_{exp}^-) is the lower experimental stiffness and (K_{exp}^+) is the upper experimental stiffness determined from the confidence interval (See Eq.VI.24). Figure VI.14 plots the function error for “tensile” and shear loadings. It is evident that the couple (E, ν) with a null function error for both types of load corresponds to the correct value of the elastic parameters. The selected couple (E, ν) has been validated by comparing the numerical predictions of monotonic tests as shown in Figure VI.15.

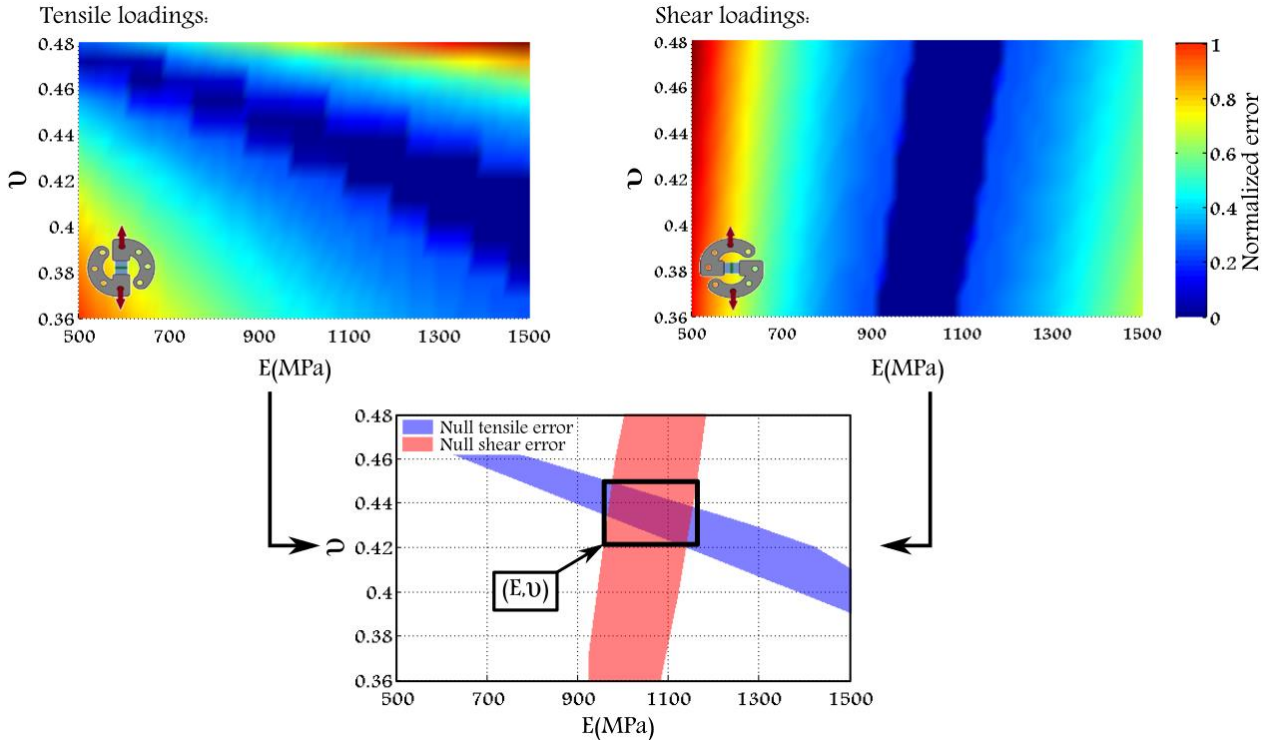


Figure VI.14: Identification of the elastic parameters of the adhesives of the study. The correct couple (E, ν) corresponds to the intersection of the null tensile error (blue region) and the null shear error (red region).

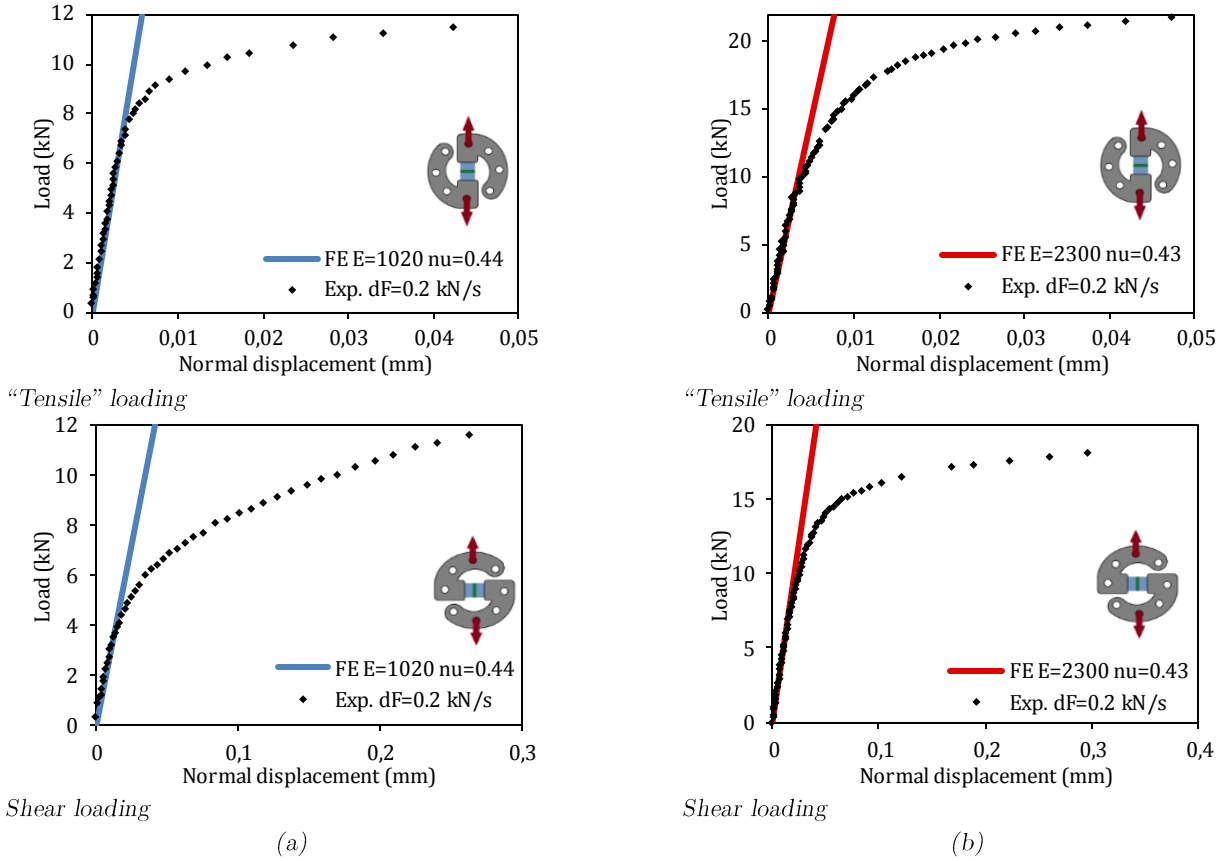


Figure VI.15: Validation of the elastic parameters of the Betamate-1822 (a) and Sikapower-498 (b) adhesive in monotonic tests.

VI.4.2. Viscous spectrum (n_o, n_c)

As stated in section VI.2, the viscosity is described by a summation of elementary viscous mechanisms (ξ_i). Each mechanism has a particular relaxation time (τ_i) and a weight (μ_i), which are supposed to describe a Gaussian form. Hence, the shape of the viscous spectrum (i.e. the value of all couples τ_i, μ_i) can be completely defined by two parameters: the “standard deviation” (n_o) and the mean (n_c). This hypothesis assumes that the isochronism principle⁸ is respected. That is, the “shape” of the creep displacement only depends on the time; all other variables such as the type of load ($\gamma=0^\circ, 45^\circ, 90^\circ$) or their magnitude have no influence.

In order to validate the isochronism principle, the shape of the displacement for every creep level needs to be compared. Thus, the normalized displacement (D_{norm}) is defined as follows:

$$D_{norm} = \frac{D(t) - D(t^{initial})}{D(t^{final}) - D(t^{initial})} \quad \text{Eq. VI.26}$$

⁸ Characteristic of having the same behavior at equal time intervals.

Where $(D(t))$ is the displacement at the time (t) , $(t^{initial})$ is the time at the beginning of the creep level and (t^{final}) is the time at the end of the creep level (See Figure VI.16).

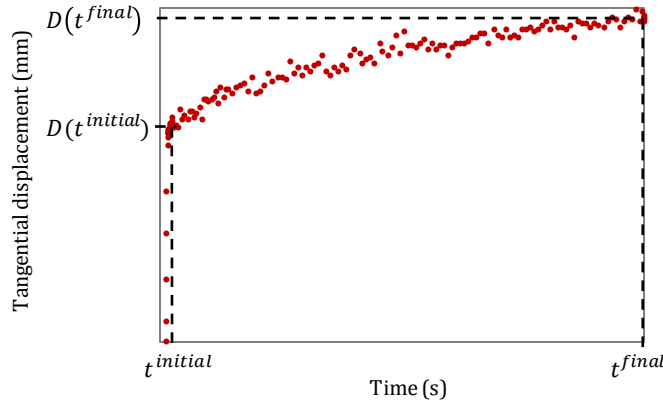


Figure VI.16: Representation of the variables used in the normalization of displacements.

Figure VI.17 shows the normalized displacements of all the creep levels of the “tensile”, tensile/shear and shear multilevel creep tests. It can be seen that most curves follow the same shape, which confirms the isochronous character of both adhesives (at least under static loading and without the influence of temperature). It is worth noting that the normalized displacement of the Betamate-1822 in “tensile” loadings (AR0) presents a different shape. This can be explained by the very slight creep displacement observed for “tensile” loadings, which is quite difficult to measure accurately and may lead to erroneous measurements.

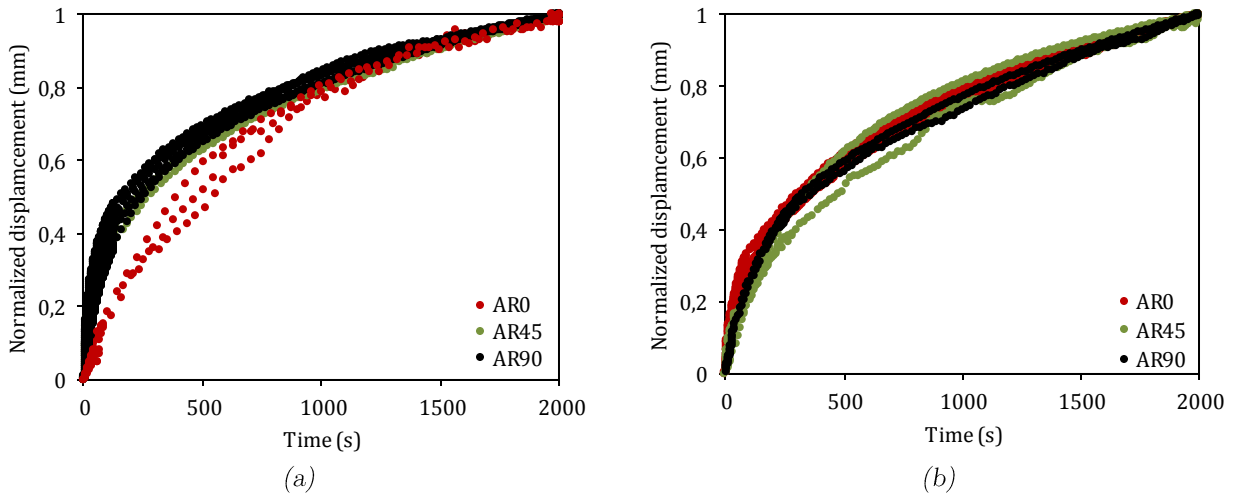


Figure VI.17: Normalized displacement of all creep levels of the “tensile” (AR0), tensile/shear (AR45) and shear (AR90) multilevel creep tests of the Betamate-1822 (a) and Sikapower-498 (b) adhesives.

The identification procedure of the viscous parameters requires numerical simulations of the creep response of the adhesive with different couples (n_0, n_c) . Here, we have considered all possible combinations comprised between:

$$\begin{aligned} n_0 &\in [1 : 20] \\ n_c &\in [1 : 20] \end{aligned} \quad \text{Eq. VI.27}$$

This range of possible combinations ensures a large number of relaxation times. Note that (n_0) and (n_c) are integer numbers.

As in the case of the elastic parameters, a function error is defined in order to determine the couple (n_0, n_c) that best represents the experimental results (See Eq. VI.28).

$$Error = \frac{1}{n} \sum_{i=1}^n \left(\frac{D_{norm}^{exp} - D_{norm}^{FE}}{D_{norm}^{exp}} \right)_i^2 \quad Eq. VI.28$$

Where (n) is the number of experimental data, (D_{norm}^{FE}) and (D_{norm}^{exp}) are, respectively, the numerical and the experimental normalized displacement.

The reduced 3D model presented in section VI.3.1 was used to perform the numerical simulations. It is worth noting that only the first creep level of one of the three types of load needs to be simulated. This is because the shape of the creep displacement is independent of the magnitude and the type of load. Therefore, we have modeled a single-level shear creep test to identify the best couple (n_0, n_c) . All other material parameters are fixed to remain under linear viscosity (i.e. $d^{H,D} = 0$).

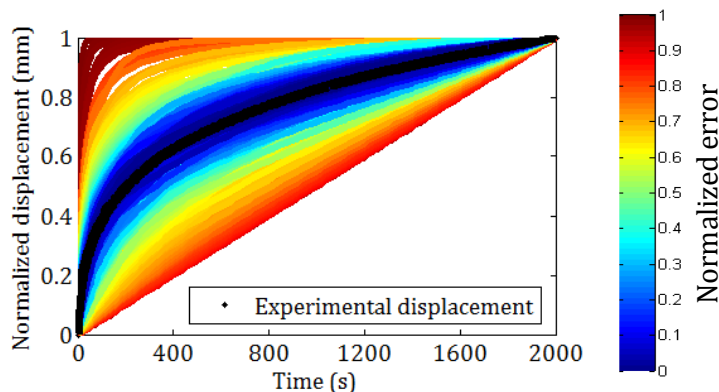


Figure VI.18: Numerical curves for different couples of the parameters (n_0) and (n_c) . The experimental displacements are plotted in black color. The FE curves closest to the experimental curve are plotted in blue color. Otherwise, the curves turn red.

The couple (n_0, n_c) is selected based on the error function defined by the Eq. VI.28 (See Figures VI.18 and VI.19). In this way, the couple with the lowest error has been chosen to define the viscous spectrum. Figure VI.20 compares the best numerical prediction and the experimental results for both adhesives.

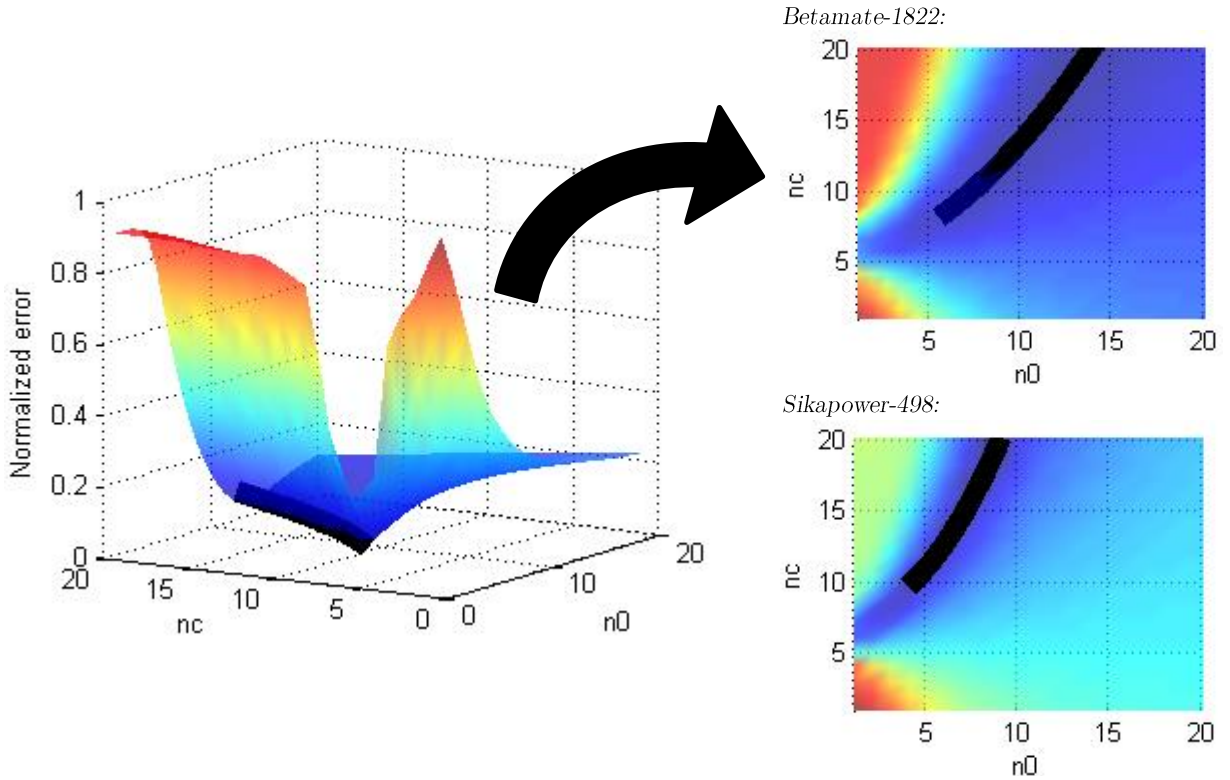


Figure VI.19: Evolution of the error as a function of the parameters (n_0) and (n_c). The couples (n_0, n_c) that minimize the error are plotted in black color.

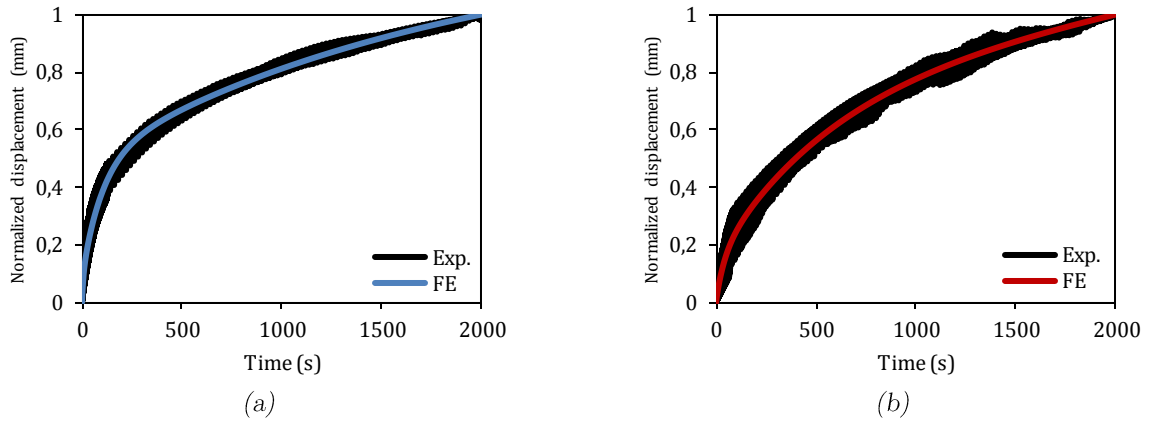


Figure VI.20: Validation of the selected viscous parameters (n_0) and (n_c): normalized FE displacements versus normalized experimental displacements of the BM1822 (a) and the SP498 (b) adhesives.

Once the spectrum has been identified, the number of elementary viscous mechanisms may be reduced in order to save computing time, as suggested by Rakotoarisoa (Rakotoarisoa, 2013). Thus, the viscous mechanisms with a negligible weight have been removed. Naturally, the limits (n_1) and (n_2) were modified. Figure VI.21 compares the spectrum distribution for ($n_t = 20$) and ($n_t = 12$). It can be seen that both distributions have the same shape. The numerical parameters used to describe the viscous spectrum are finally presented in Table VI-3.

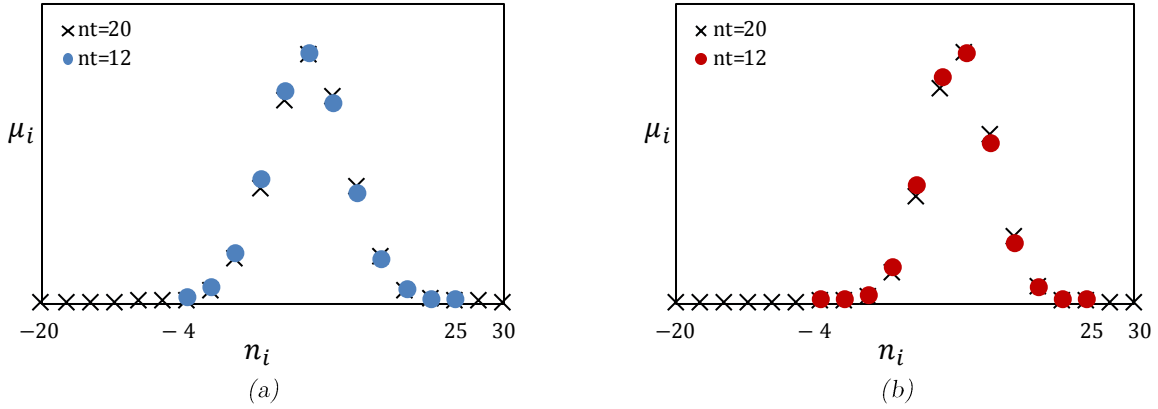


Figure VI.21: Viscous spectrum of the Betamate-1822 (a) and Sikapower-498 (b) adhesives. Comparison between a viscous spectrum with twenty mechanisms and a viscous spectrum without mechanisms with negligible weight.

	Betamate-1822	Sikapower-498
n_t	12	12
n_1	-4	-4
n_2	25	25
n_0	6	5
n_c	9	11

Table VI-3: Definition of the viscous spectrum parameters.

VI.4.3. Linear viscosity (a, b)

One of the conclusions of the experimental campaign was that both adhesives presented a dissimilar viscous regime depending on the type of load. Indeed, the behavior under shear loadings exhibits a very important viscous regime, whereas under “tensile” loadings this behavior is less noticeable. This aspect highlights the influence of hydrostatic pressure on the viscous behavior of the adhesives since the stress state of the adhesive joint in shear loadings ($\gamma=90^\circ$) is completely different from the stress state in “tensile” loadings ($\gamma=0^\circ$) (See Figure II.6).

Different solutions can be proposed in order to model the influence of the hydrostatic pressure; the one retained here is the separation of the linear viscoelastic compliance tensor ($\underline{\underline{\sigma}}_0^R$) into a hydrostatic part and a deviatoric part:

$$\underline{\underline{\sigma}}_0^R = \frac{1}{a} \underline{\underline{P}}^H + \frac{1}{b} \underline{\underline{P}}^D \quad \text{Eq. VI.29}$$

With,

$$\underline{\underline{P}}^H = \underline{\underline{H}}^H = \frac{1}{3} \underline{\underline{I}} \otimes \underline{\underline{I}} \quad \text{and} \quad \underline{\underline{P}}^D = \underline{\underline{H}}^D = \underline{\underline{I}} - \underline{\underline{H}}^H$$

Thus, two material parameters will define the linear evolution of the viscosity: one for hydrostatic loadings (a) and one for deviatoric loadings (b).

In order to not mix up the type of load effect with the non-linear evolution of the viscosity during the identification of the parameters (a) and (b) , it must be ensured that the viscous behavior of the adhesives remains linear. Therefore, the procedure presented in section V.3.1 was used in order to identify the linear creep levels. In this manner, for every multilevel creep test, the viscous displacement of the i creep level (D_v^i) is defined as the displacement at the end of the i creep level (D_{final}^i) minus the displacement at the beginning of the i creep level ($D_{initial}^i$) (See Figure VI.22-a). Plotting the viscous displacements of the adhesive at the end of every creep level (See Figure VI.22-b), the linear creep levels can clearly be separated from the non-linear creep levels (in many cases, only the first creep level has been considered as linear). The experimental displacements of the linear creep levels (non-normalized) can be now used to identify the set of parameters (a) and (b) .

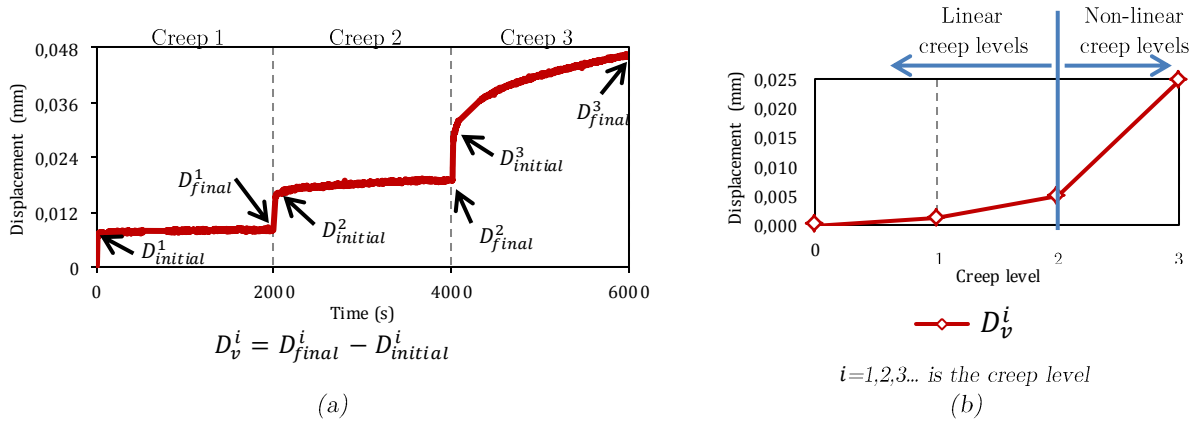


Figure VI.22: Identification of the linear viscous creep levels of the multilevel creep tests. Definition of the viscous displacement (D_v^i) (a) and linear creep levels (b).

The identification procedure of the linear viscous parameters (a) and (b) have been performed by running successive FE simulations in an iterative procedure with (a) and (b) varying from 10 to 5000 MPa. As explained before, the parameter (b) has been identified in the first place by using the shear multilevel creep test. This is because in shear Arcan loadings, a quasi-pure shear stress state is generated, which permits a correct identification of the deviatoric sensibility (See Figure II.6). Then, the parameter (a) was identified by using the “tensile” multilevel creep test. Figure VI.23 shows the role of the parameters (a) and (b) on the normal displacement (ND) and the tangential displacement (TD), respectively. It can be observed that the larger the magnitude of the parameters, the less compliance and in consequence, the less displacement is observed. Finally, the best numerical predictions for both adhesives are plotted in Figure VI.24.

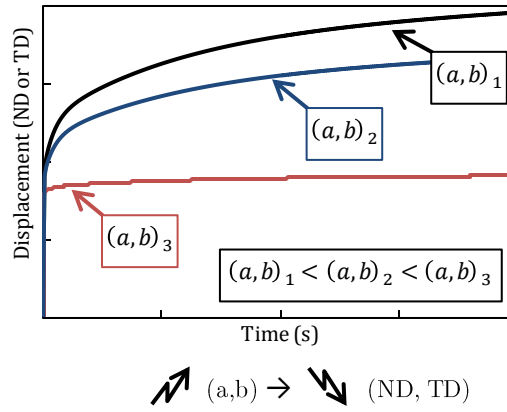


Figure VI.23: Role of the parameters (a) and (b) on the viscous response. FE simulations of a creep test under linear viscosity assumption.

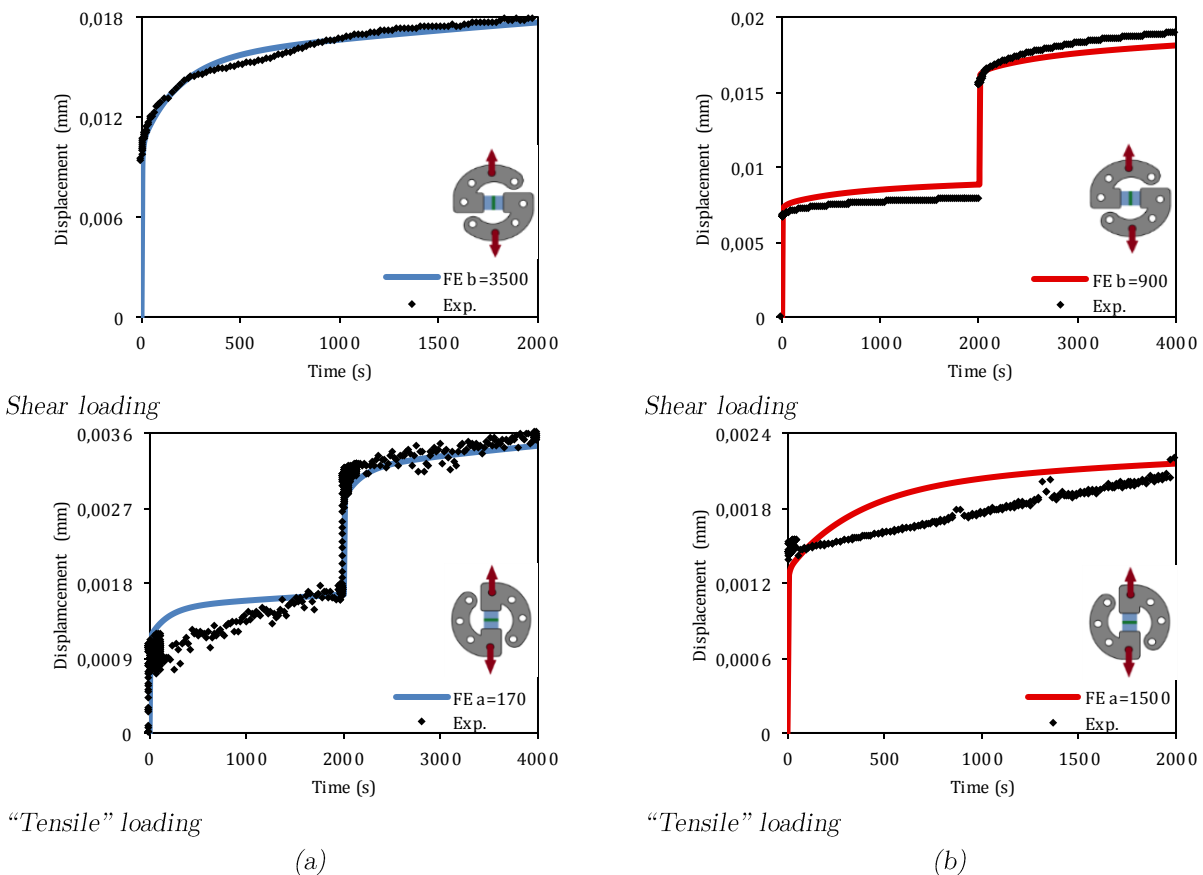


Figure VI.24: Identification of the parameters a and b of the Betamate-1822 (a) and Sikapower-498 (b) adhesives.

VI.4.4. Non-linear viscous parameters ($Y_o^H, Y_c^H, p^H, Y_o^D, Y_c^D, p^D$)

The non-linear character of the viscosity has been modeled by a softening of the viscoelastic compliance tensor ($\underline{\underline{S}}^R$) (See Eq. VI.17). This softening is characterized by two variables (d^H) and (d^D) that describe the hydrostatic and deviatoric non-linear evolution respectively:

$$\underline{\underline{S}}^R = \frac{1}{a(1 - \underline{\underline{d}}^H)} \underline{\underline{P}}^H + \frac{1}{b(1 - \underline{\underline{d}}^D)} \underline{\underline{P}}^D$$

An exponential form is used to define the evolution of the softening variables:

$$\underline{\underline{d}}^H = d_{max} \left(1 - e^{-\left(\frac{(Y - Y_0^H)^+}{Y_c^H}\right)^{p^H}} \right)$$

$$\underline{\underline{d}}^D = d_{max} \left(1 - e^{-\left(\frac{(Y - Y_0^D)^+}{Y_c^D}\right)^{p^D}} \right)$$

With,

$$\begin{aligned} \dot{\underline{\underline{d}}}^H &\geq 0 \\ \dot{\underline{\underline{d}}}^D &\geq 0 \end{aligned}$$

Where (Y) corresponds to a coupled thermomechanical potential defined in a hydrostatic and a deviatoric part:

$$Y = (\alpha(Y^H)^n + (Y^D)^n)^{1/n}$$

With,

$$\begin{aligned} Y^H &= \frac{1}{2a} (\underline{\underline{\sigma}} : \underline{\underline{H}}^H : \underline{\underline{\sigma}}) \\ Y^D &= \frac{1}{2b} (\underline{\underline{\sigma}} : \underline{\underline{H}}^D : \underline{\underline{\sigma}}) \end{aligned}$$

Leaving aside for a moment the parameters (α) and (n) which will be investigated in the next section, the kinetic of the non-linear evolution of the viscosity may be described by the parameters $(Y_0^H, Y_c^H, p^H, Y_0^D, Y_c^D, p^D)$. Figure VI.25 presents the role of each parameter on the evolution of the softening variables $(\underline{\underline{d}}^H, \underline{\underline{d}}^D)$. The onset of non-linearity of viscosity is defined by the parameters (Y_0^H, Y_0^D) . The parameters (Y_c^H, Y_c^D) and (p^H, p^D) describe the evolution of this non-linearity and represent, respectively, the speed and the shape of the softening variables.

The first step in the identification is determining the thresholds (Y_0^H, Y_0^D) . These parameters are quite easy to identify since we have considered that for all the “linear” creep levels the viscosity remains completely linear (See Figure VI.26-a). Therefore, the value of the thresholds corresponds to the current value of the thermomechanical potential (Y) at the end of the last linear creep level under “tensile” loadings (i.e. $Y_0^H = Y$) and under shear loadings (i.e. $Y_0^D = Y$) (See Figure VI.26).

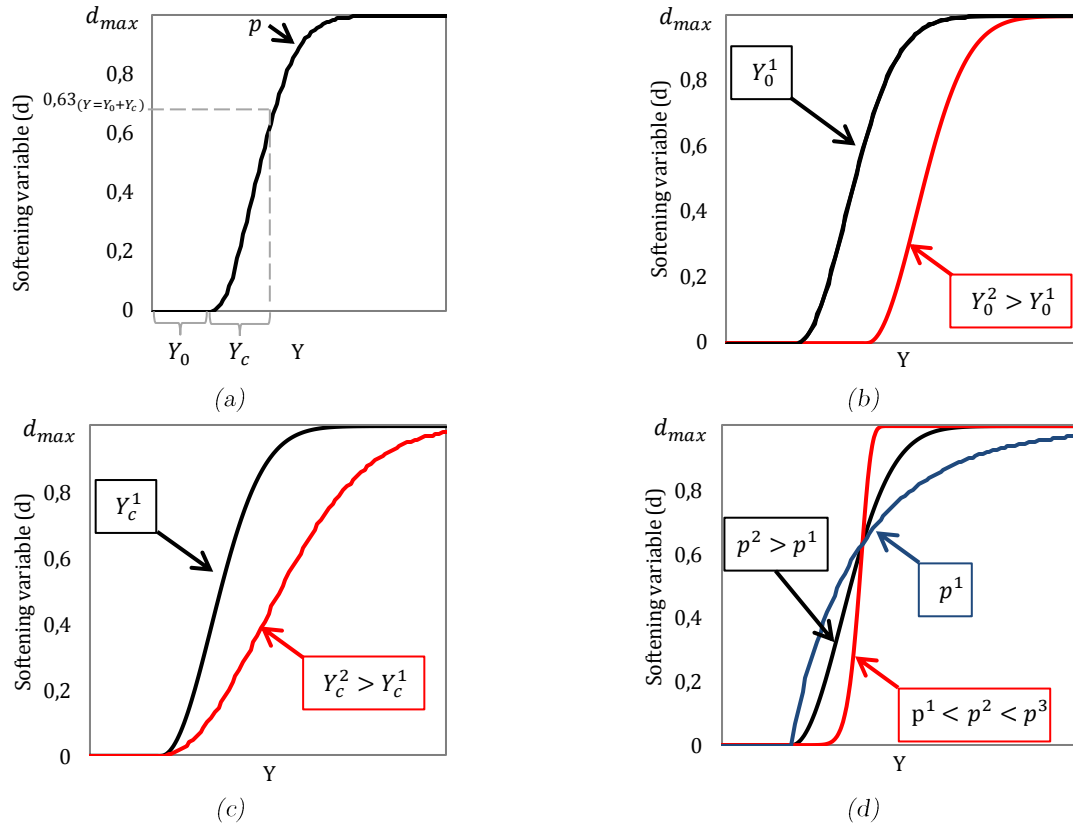


Figure VI.25: Role of the parameters Y_0, Y_c and p on the softening variable “d”. Shape of the softening variable (a), influence of the parameter Y_0 (b), the parameter Y_c (c) and the parameter p (d).

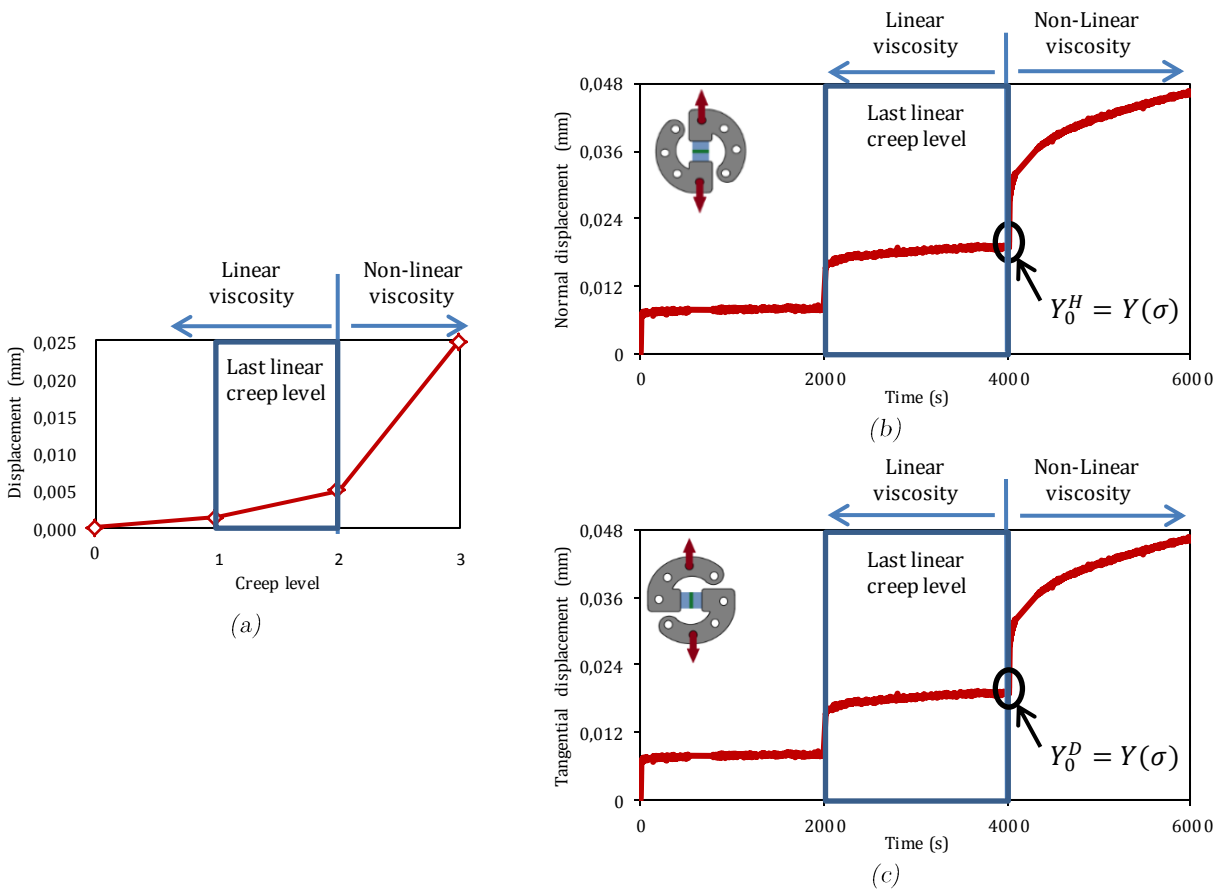


Figure VI.26: Linear and non-linear creep levels (a). Definition of the linear viscous thresholds Y_0^H (b) and Y_0^D (c).

In the case of the couples (Y_c^H, p^H) and (Y_c^D, p^D) , these parameters are intrinsically linked and the identification of them requires an optimization procedure (See Figure VI.6). Naturally, the couple (Y_c^D, p^D) is identified in the first place by comparing the experimental shear multilevel creep curve with the numerical curves. Then, the couple (Y_c^H, p^H) is identified using the “tensile” multilevel creep results. The best numerical prediction corresponding to each adhesive is presented in Figure VI.27.

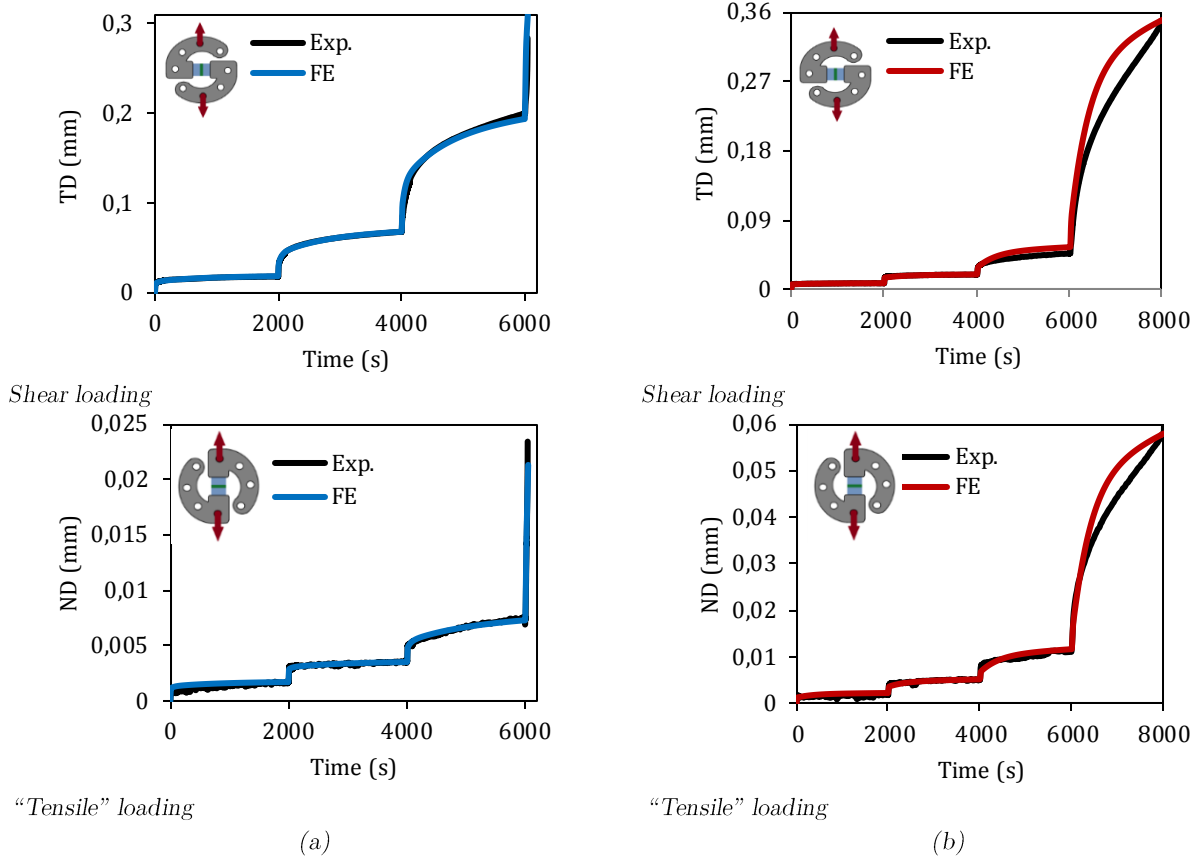


Figure VI.27: Numerical prediction versus experimental results of the multilevel creep tests of the Betamate-1822 (a) and Sikapower-498 (b) adhesives.

VI.4.5. Mixed mode (α, n)

The influence of the type of load on the response of the adhesive joint is defined by the parameters (α, β, n) in equation Eq. VI.19. For simplicity in the identification procedure, we have chosen $\beta = 1$; this, because under shear Arcan loadings the mode II is pure and independent of the mode I:

$$Y = (\alpha(Y^H)^n + (Y^D)^n)^{\frac{1}{n}} \quad \text{Eq. VI.30}$$

$$Y_{(\gamma=90^\circ)} \cong Y^D$$

Therefore, the behavior of the adhesives under shear loadings has already been identified. However, the behavior of the adhesives under “tensile” and tensile/shear loadings requires the identification of the parameters (α) and (n) . The role of these two parameters

in the mixed mode is explained in Figure VI.28. The parameter (α) represents the importance of the mode I on the softening. Indeed, the larger the parameter (α), the more important the mode I will be with respect to the mode II. On the other hand, the parameter (n) describes the mode coupling. The larger (n), the less coupling mixity will be.

The identification is based on an optimization procedure that compares the “tensile” and tensile/shear creep test with the numerical responses (See Figure VI.6). The best numerical results are presented in Figure VI.29.

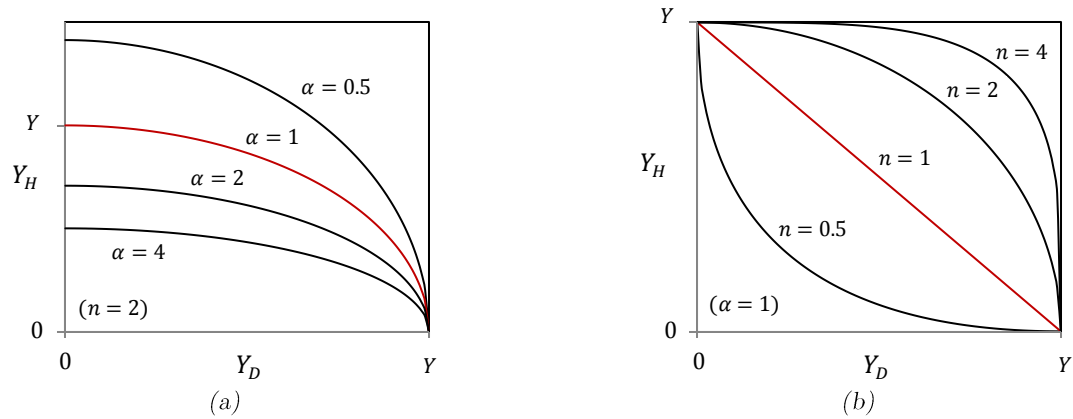


Figure VI.28: Role of the α (a) and n parameters (b) in the mixed mode.

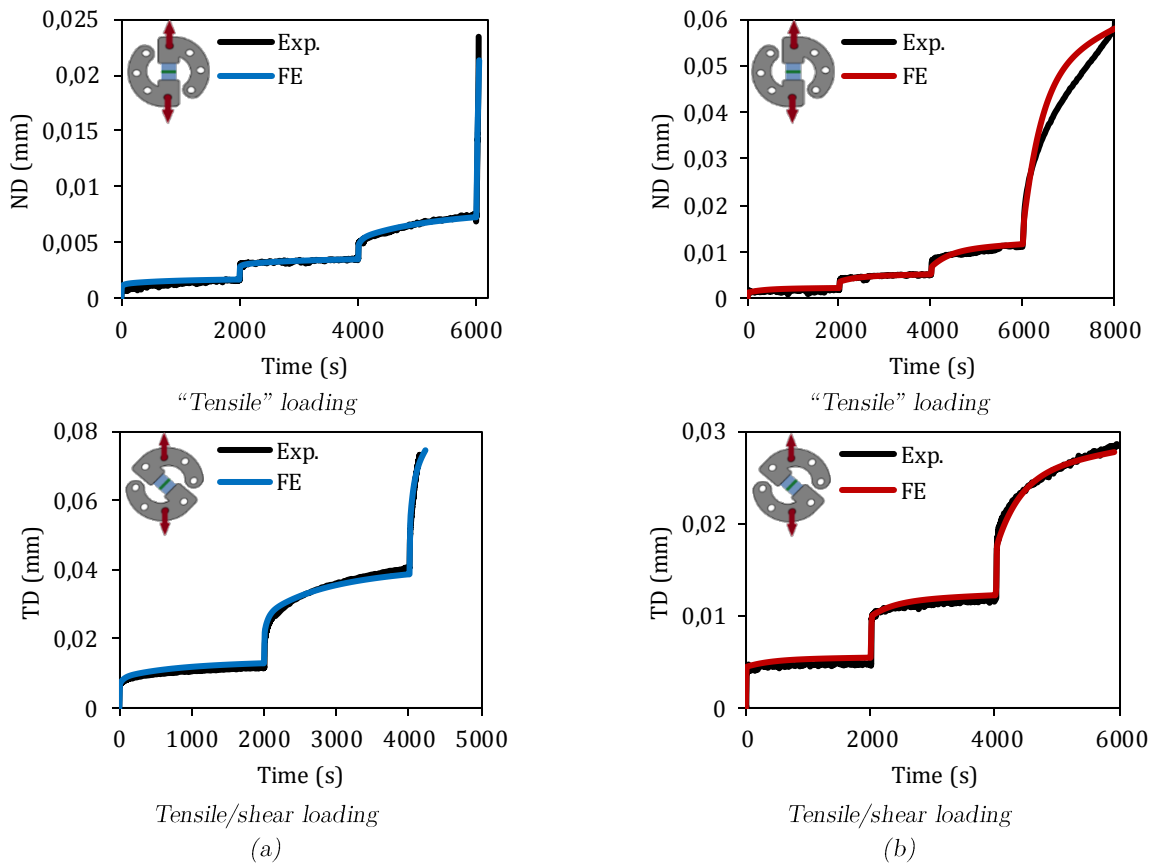


Figure VI.29: Numerical simulations versus experimental results of the multilevel creep tests under “tensile” and tensile/shear loadings of the Betamate-1822 (a) and Sikapower-498 (b) adhesives.

VI.4.6. Identified material parameters

Table VI-4 presents the complete set of identified material parameters of the behavior law of the Betamate-1822 and Sikapower-498 adhesives. The reader can observe that in the case of the Sikapower-498 adhesive, the parameters describing the softening in the hydrostatic space and in the deviatoric space ($Y_0^H, Y_c^H, p^H, Y_0^D, Y_c^D, p^D$) are the same. This is because for this particular adhesive, the non-linear evolution of the viscosity under “tensile” and shear loadings can be considered to be the same ($d^H = d^D$). In contrast, in the case of the BM1822 adhesive, the strong influence of the hydrostatic pressure has required the use of two different non-linear evolutions ($d^H \neq d^D$).

Material parameter	Modeling relevance	BM1822	SP498	Unit
E	Elasticity	1020	2300	MPa
ν		0.44	0.43	-
n_0	Viscous spectrum	6	5	-
n_c		9	11	-
a	Linear viscosity	3500	1300	MPa
b		170	900	MPa
Y_0^H	Linear viscoelastic threshold	0.1797	0	MPa
Y_0^D		0.2	0	MPa
Y_c^H	Non-linear viscosity under tensile loadings	0.021	0.4292	MPa
p^H		0.41	1.5448	-
Y_c^D	Non-linear viscosity under shear loadings	0.517	0.4292	MPa
p^D		0.619	1.5448	-
α	Mixed mode	1.33	0.5	-
n		0.629	0.41	-

Table VI-4: Identified material parameters.

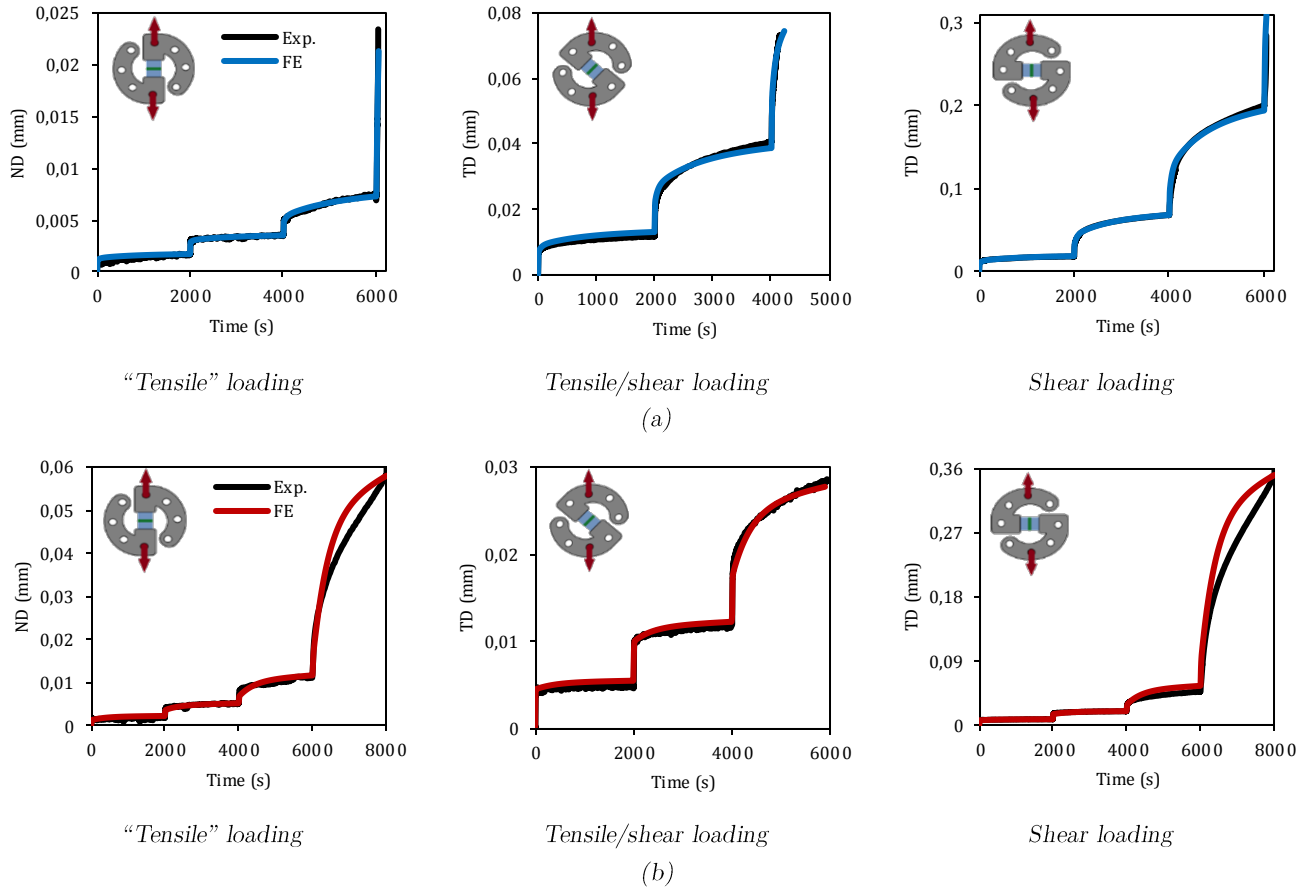


Figure VI.30: Numerical simulations versus experimental results of the tests used in the identification of the material parameters of the Betamate-1822 (a) and Sikapower-498 (b) adhesives.

VI.5. Validation of the behavior law

As shown in section VI.4, the identification of the parameters of the proposed behavior law was only based on three multilevel creep tests: one under “tensile” loadings, one under tensile/shear loadings and one under shear loadings. In order to validate the used behavior law, FE simulations have been performed and compared with the experimental curves obtained from other types of test.

VI.5.1. Validation using Arcan tests

During the characterization of the adhesives, monotonic tests with different loading rates (0.2kN/s and 2kN/s) and increasing cyclic tests were performed under “tensile”, tensile/shear and shear loadings (See Chapter V). Figures VI.31 and VI.32 compare the numerical predictions and the experimental curves of the BM1822 and the SP498 adhesives in monotonic Arcan tests and increasing cyclic Arcan tests. The results show a good correlation between the experimental and the numerical results.

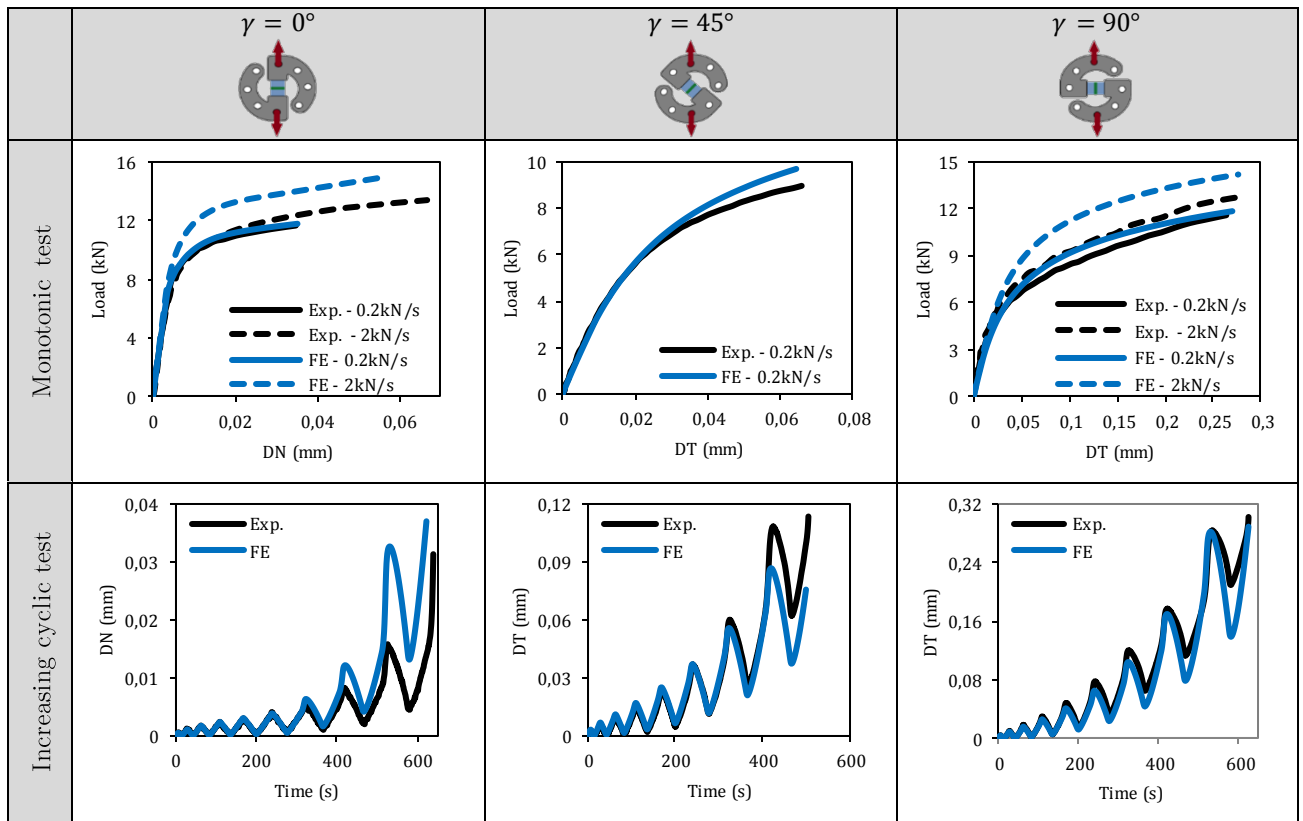


Figure VI.31: Comparison between FE predictions and experimental results of the Betamate-1822 adhesive.

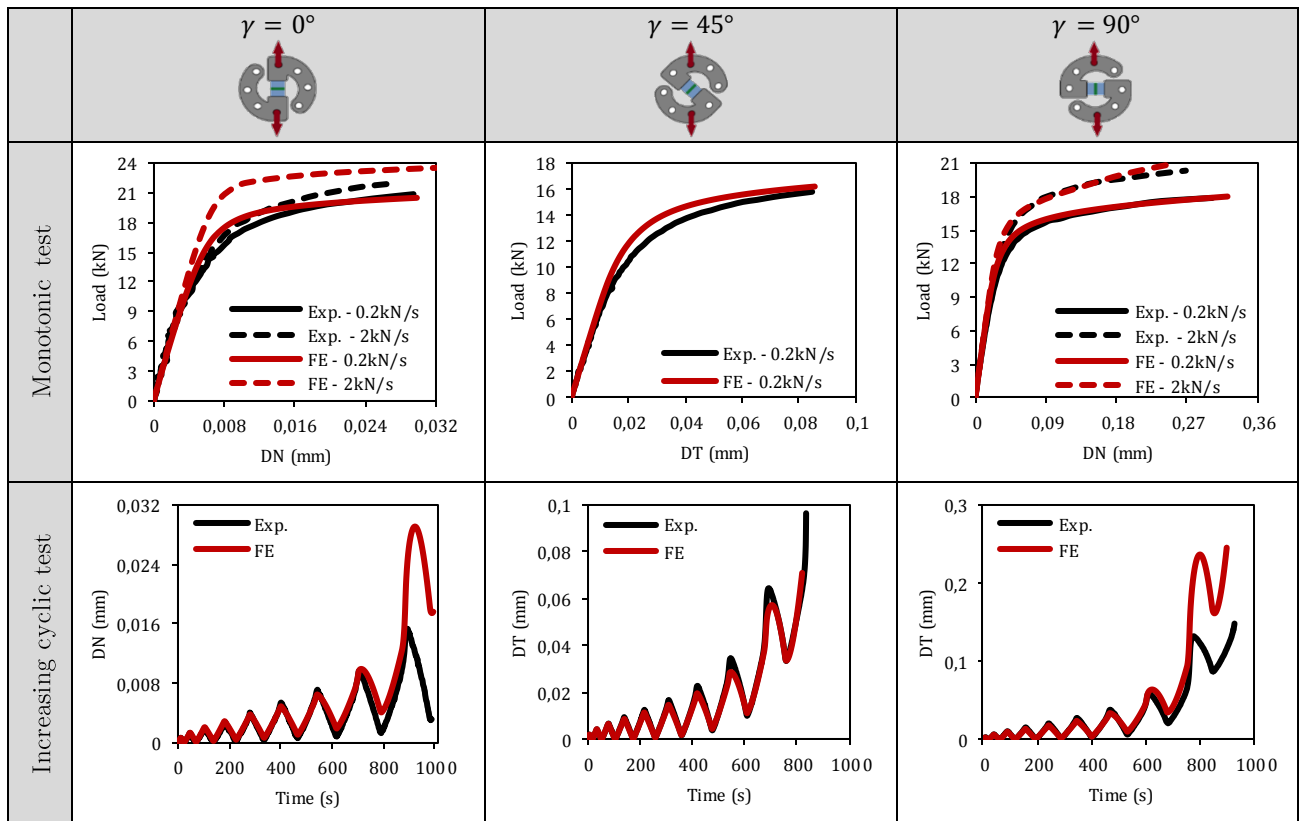


Figure VI.32: Comparison between FE predictions and experimental results of the Sikapower-498 adhesive.

VI.5.2. Comparison with Bulk test

Monotonic tests using Bulk specimens made of the adhesives of the study were performed by the partners of the FASTLITE project. The experimental results were then compared with the numerical predictions of the proposed behavior model. The specimens were manufactured by the Technical Centre for Mechanical Industries (CETIM, in its French acronym) following the French standard NF T 76-142. The curing cycle was the same used in the case of Arcan specimens and a high pressure was applied during polymerization (100 atm). The plates were then cut using the water-jet technique. The tests were performed at the “University of Valenciennes and Hainaut-Cambresis” (UVHC, in its French acronym) using a universal tensile machine under quasi-static loadings (1 mm/min). The tests were not conditioned under controlled temperature and humidity. Three specimens were tested and a low scattering was observed for each adhesive. The displacements of the useful area were obtained by means of a DIC system. The experimental displacement was then considered as the relative displacement of a line at the top and a line at the bottom of this area. The Bulk specimen geometry and the boundary conditions of the FEM are presented in Figure VI.33. The comparison of the numerical responses and the experimental curves is also presented.

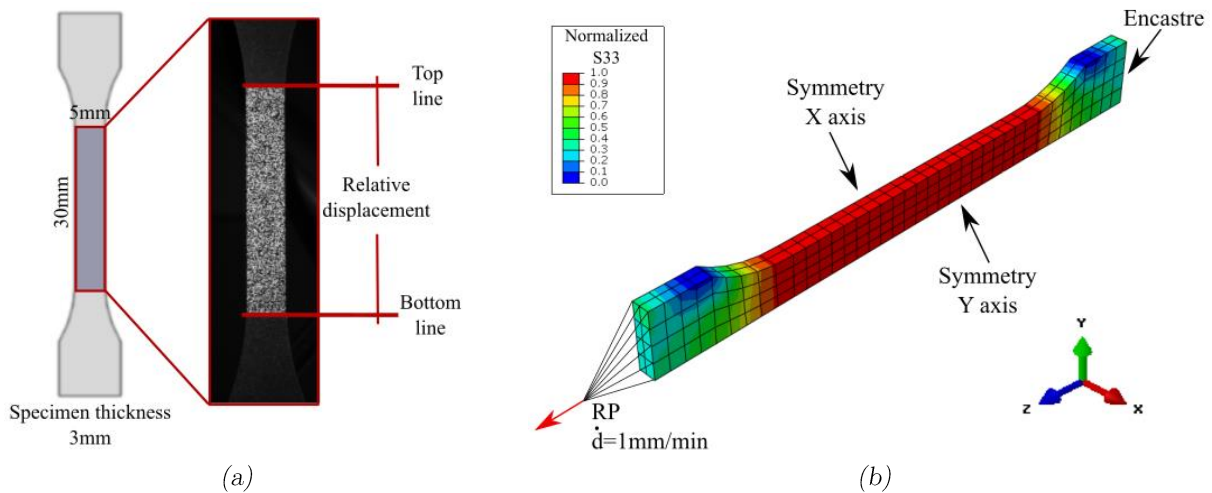


Figure VI.33: FE model (a) and geometry of the Bulk specimens (b).

As it can be seen in Figure VI.34, the numerical predictions follow a similar evolution of the experimental curves for both adhesives. This aspect suggests that the proposed behavior law is able to predict the behavior of the adhesives in pure tensile loadings even if no additional information was used during the identification procedure. Similarly, the results also validate the procedure used in the identification of the elastic parameters since a similar stiffness is observed on the numerical and experimental curves.

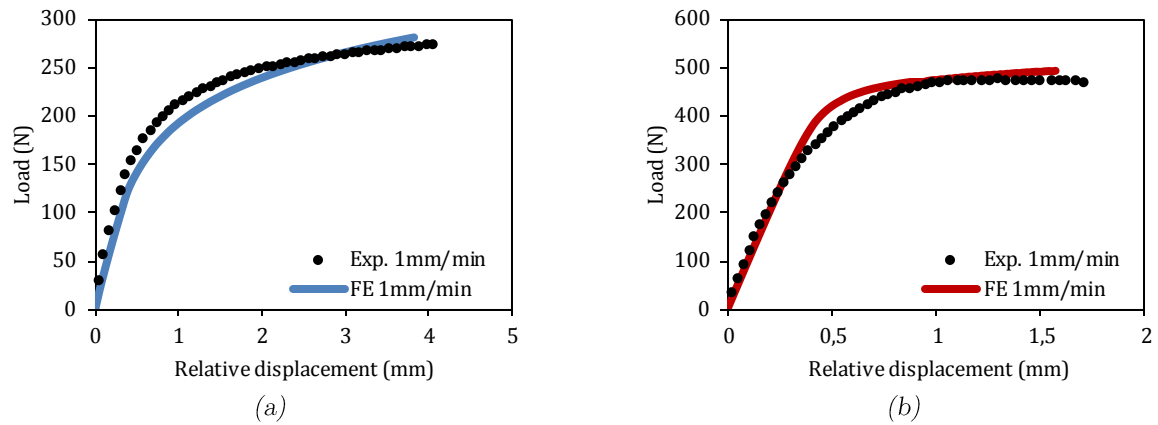


Figure VI.34: Comparison between FE predictions and experimental results of the Betamate-1822 (a) and Sikapower-498 (b) adhesives in Bulk tests.

VI.5.3. Comparison with Lap-shear test

Lap-shear tests were also performed with the adhesives of the study by the partners of the project at the UVHC University. The tests were performed by means of a universal tensile machine under controlling loading rate (1 mm/min). DIC measurements were used in order to obtain the relative displacement of the aluminum substrates at the top and bottom lines as shown in Figure VI.35.

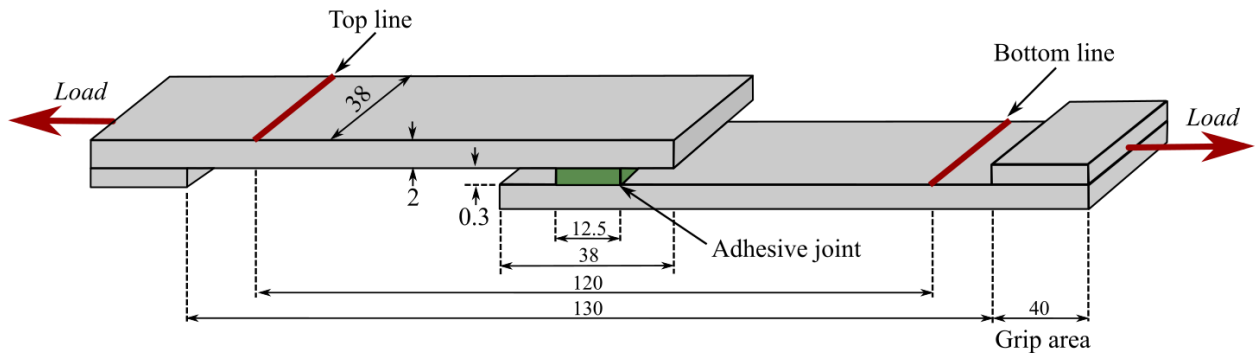


Figure VI.35: Geometry of the lap-shear specimens (mm) (not to scale).

A complete 3D finite element model was used in order to model the lap-shear test. Since the time calculus of this model was considerably high, a reduced 3D model considering one element of 0.1mm along the width of the specimen was proposed. The boundary conditions of these models are analogous to those of the Arcan models presented in section VI.3.1 (See Figure VI.36-a-b). Both models present a similar mesh, which has been adapted to ensure a convergence of the macroscopic response (relative displacement between the top and bottom lines). It is worth noting that the adhesive stress distribution continues to vary widely as a function of the mesh size near to the edges (presence of stress singularities). As shown in Figure VI.36, both models present an identical macroscopic response and a very similar Von Mises stress distribution under linear elasticity. It is worth noting that the use of the reduced 3D model decreases the computing time by about 70%.

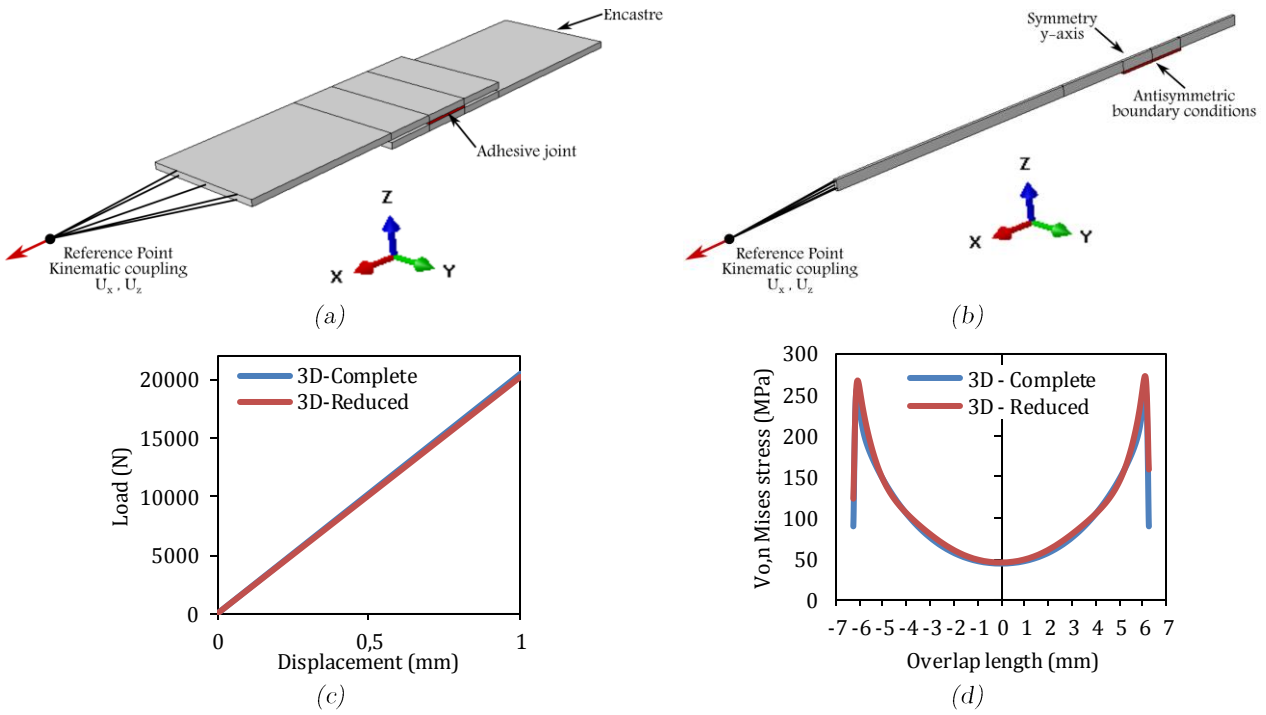


Figure VI.36: Complete 3D lap-shear model (a) and reduced 3D model (b). Comparison of the macroscopic response (c) and the Von Mises stress distribution of the models under linear elasticity.

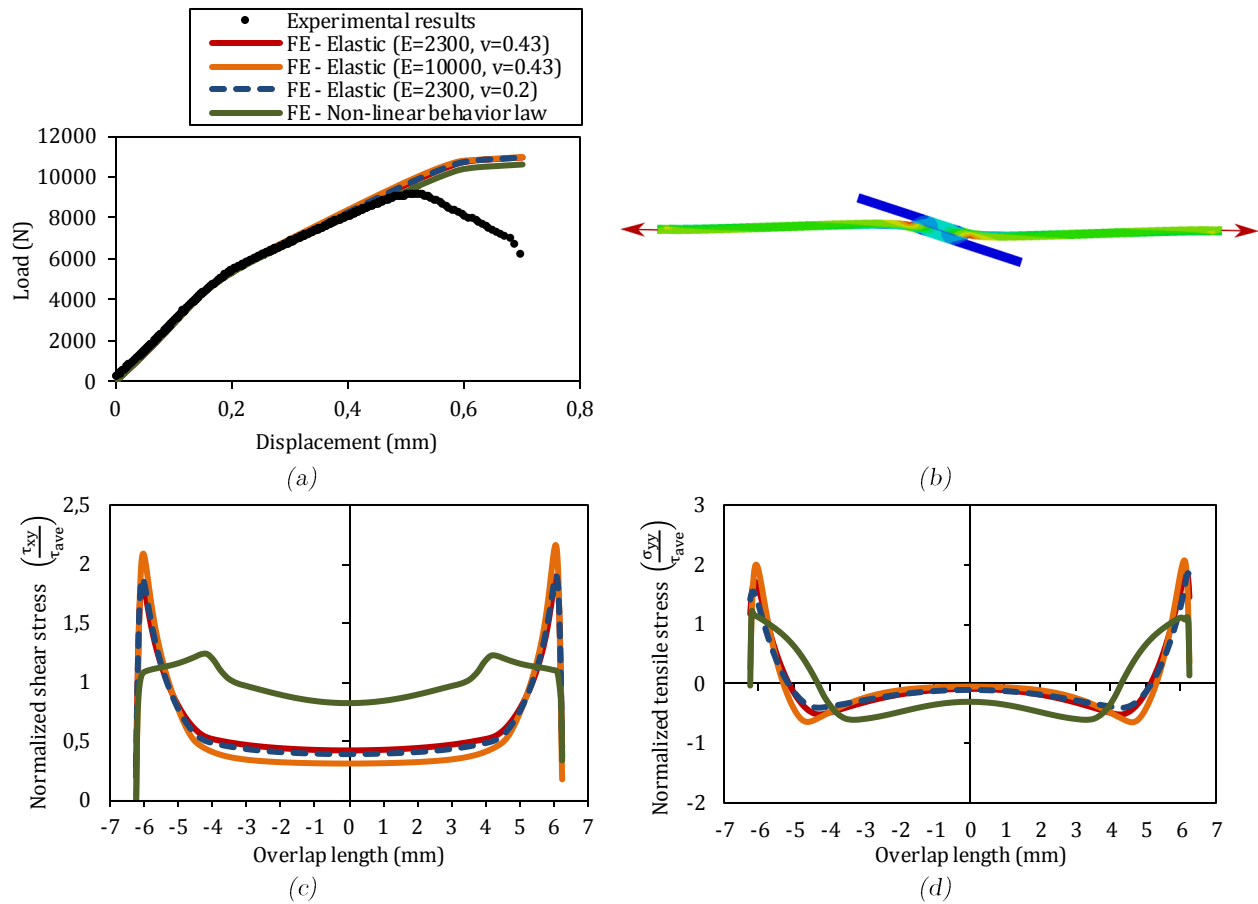


Figure VI.37: Comparison between numerical predictions and experimental results of the macroscopic response of Sikapower-498 lap-shear joints (a). Global deformation pattern of lap-shear specimens (b). Numerical distributions of the normalized shear stress (c) and the normalized tensile stress (d) along the overlap length.

The experimental lap-shear curves of both adhesives have been compared with numerical predictions using the reduced 3D model. A classical isotropic and a linear kinematic hardening law was then used to model the inelastic response of the substrates (AL5182); the material parameters were determined by means of a stress-strain curve. The adhesive behavior was modeled with: (i) an elastic law with the elastic parameters determined in section VI.4.1, (ii) an elastic law with higher Young modulus, (iii) an elastic law with lower Poisson's ratio and (iv) the complete non-linear behavior law identified in section VI.4.6. Figure VI.37 compares the experimental and numerical responses of Sikaposer498 lap-shear joints. The normalized shear stress distribution $\left(\frac{\tau_{xy}}{\tau_{ave}}\right)$ and the normalized tensile stress distribution $\left(\frac{\sigma_{yy}}{\tau_{ave}}\right)$ along the overlap length are also plotted. The numerical predictions showed that the behavior law used to model the adhesive behavior has a minor influence on the macroscopic response of lap-shear joints. This is because the bending deformation of the substrates modifies considerably the macroscopic displacement of the specimens (See Figure VI.37-b). In contrast, the stress distribution on the adhesive joint evolves as a function of the used behavior law. Figure VI.37-c-d compares the stress distributions obtained with different laws. We can observe that the use of a non-linear law reduces the stress values at the edges of the adhesive joint; this is because the non-linear behavior is progressively achieved from the edges to the center of the overlap length.

In conclusion, the lap-shear test does not constitute a representative test of the behavior of adhesives since the principal item in their modeling is the substrate behavior law. Nevertheless, this test may be used to model the failure criterion of adhesive joints. This is because the stress concentration at the edges of the adhesive joint constitutes a mixed stress state that may be modeled with relative simplicity.

VI.6. Discussions and limitations of the model

As shown in Figure VI.17, the shape of the normalized displacement in “tensile” loadings is slightly different from the shear and tensile/shear cases. This aspect gives the impression that the isochronism principle is not fulfilled and that the correct identification of the viscous parameters cannot be based on the multilevel creep test. However, it must not be forgotten that the displacements measured in Arcan “tensile” tests are very low, inducing an important observational error and measurement noise. Indeed, during a “tensile” creep level, the creep displacements measured are in the order of $5\mu\text{m}$, which is near the measurement accuracy of the DIC system used in this study.

As shown by several authors, the exposition to thermal cycles or long periods of high temperature reduces considerably the performance of materials. The influence of temperature on the behavior of adhesives has already been investigated in different works as in (Hicks *et al.*, 2015). However, the behavior law presented in this document has not taken into account this aspect. Therefore, a refined model should include the temperature dependence or even the “time-temperature superposition principle” in order to better describe the behavior of adhesives. As proposed in (Badulescu *et al.*, 2015), the thermal strain ($\underline{\epsilon}^{th}$) can also be considered in order to take into account the residual stress due to

the manufacturing process, which may have an important influence on the initial state of the adhesive. However, it is worth saying that the thermal degradation of the mechanical properties remains a complex field in adhesives science.

On the other hand, we have considered that the different viscous behavior of the adhesives in tensile or shear stresses can be modeled by an isotropic softening defined in a hydrostatic and a deviatoric part ($\underline{\underline{\mathcal{J}}}^R = \underline{\underline{\mathcal{J}}}^R(H^H) + \underline{\underline{\mathcal{J}}}^R(H^D)$). This assumption has been chosen mainly because, until now, no tests have been performed in order to clarify the nature of the observed softening. However, the hypothesis of an isotropic softening might be wrong and the compliance tensor should be described by some other directional tensors ($P^H \neq H^H$ and $P^D \neq H^D$). Indeed, it is well known that the presence of particles, reinforcements, voids and pollutants inside the adhesive joint (Soghrati and Liang, n.d.), may have a non-heterogeneous distribution with a preferential orientation due to the flow during the manufacturing process (Joannès *et al.*, 2010), which may induce an anisotropic behavior.

Similarly, it was assumed that the time dependence of the adhesives could be explained only by the influence of the loading rate on the viscous regime. Nevertheless, this time dependence may also have an important influence on the apparent Young's modulus. This aspect can be explored in detail by DMA tests, clarifying the nature of the viscoelastic behavior. Additionally, the softening has been considered as a function of the current stress state ($\underline{\underline{\mathcal{J}}}^R = \underline{\underline{\mathcal{J}}}^R(\sigma)$). However, the evolution of this softening may also be time-dependent and the addition of this may lead to better numerical predictions for higher loading rates.

Even if permanent strain has not been taken into account in the modeling of the adhesives, we have considered that the proposed model is sufficient to accomplish the objectives of the study. This hypothesis is based on the crash nature of the adhesives where a viscoelastic model seems to be adequate for their modeling. However, the absence of a permanent strain in the modeling is a strong assumption, which implies that the behavior of the adhesives might not be accurately predicted for high levels of stress. A more refined model may include a plastic or viscoplastic law as proposed in (Frank and Brockman, 2001). Finally, the model can also include damage effects of cracks on the elastic behavior. This damage can be described by a "damage" variable as a function of the stress or strain stresses. Therefore, a damage tensor must also be defined in order to determine the damage direction. It is worth mentioning once again that a refined model may significantly complicate the experimental campaign and the material parameters identification, which is opposed to the purpose of this study.

VI.7. Overview

Finite element models were developed in order to represent as close as possible the “real” state of an Arcan specimen during testing. The calculation time and the convergence of the mesh were studied in order to ensure a good performance.

The material model proposed in this chapter was developed in accordance with the phenomena observed in the experimental campaign. Thus, the influence of the hydrostatic pressure and the non-linear evolution of the viscosity have been taken into account. The identification methodology of the material parameters was only based on three multilevel creep tests: one under “tensile” loadings, one under tensile/shear loadings and one under shear loadings. This allows a rapid modeling of the adhesive behavior. Indeed, the characterization and modeling of a given adhesive are estimated in two working weeks.

The proposed model provides a good correlation between the numerical predictions and the experimental data obtained from other tests that were not used in the identification of the material parameters (monotonic Arcan tests, increasing cyclic tests and Bulk tests). This permits the model to be validated not only for creep loadings but also for monotonic and increasing cyclic loadings. It is important to say that because of the experimental data used in the identification procedure, the model is limited to quasi-static loadings.



Chapter VII. Conclusions and prospects

Introduction

This final chapter is devoted to the conclusions and the prospects of the study. A global overview of results is done in order to underline the most important aspects. First, the main conclusions of this work are discussed. Then, some aspects that should be taken into account during the characterization and the modeling of adhesives are discussed in the prospects section. Understanding how these aspects have an influence on the behavior of adhesive joints is important, both for the automotive industry and research activities. It is worth mentioning that it does not constitute an exhaustive investigation, but a preliminary study that should be continued in the future.

The adhesive aging and the influence of temperature have been analyzed through the Arcan test. Similarly, the behavior of the adhesive under cyclic loadings has been briefly explored and modeled. In this case, the experimental campaign was performed by using modified Scarf joints. Finally, hybrid rivet-bonded joints were tested under monotonic shear Arcan tests in order to study the good compatibility of both joining techniques.

VII.1. General conclusions

In order to respond to global warming and reduce the levels of air pollution caused by automobiles, new regulations limiting the levels of CO₂ emissions have been implemented. This target can be achieved by reducing the car weight by the use of lighter materials such as aluminum and composite materials. Nevertheless, this solution implies the research of joining techniques which are compatible with the car components and these new materials. Among the multiple possibilities, four joining techniques were preselected by the partners of the project: stud bonding, laser welding, self-pierce riveting and adhesive bonding. Therefore, the characterization and the modeling of these techniques under mixed quasi-static loadings is a crucial aspect that was studied in this Ph.D. thesis. Various aspects around multi-material assemblies have been treated; therefore, some conclusions are presented below as a guideline for further research.

The Arcan device as an adapted tool for the characterization of joining techniques under mixed loadings

The use of a modified Arcan device has been proposed as a new characterization test in order to load diverse types of specimen to different combinations of tensile-compression/shear loads. This device constitutes a suitable alternative as compared with traditional tests (Lap-shear and Cross-tension tests), which does not represent the mixed loadings presented in automotive structures. The modified Arcan test was originally proposed by Cognard to characterize the behavior of adhesives. Nevertheless, a minor change of the geometry of the specimen permitted an easy adaptation to self-pierce riveted assemblies (RivSet). It is worth noting that the characterization procedure based on the Arcan device can be now used to analyze the behavior of other joining techniques such as welding, threaded fasteners, snap fits, etc.

Characterization of adhesively bonded assemblies

The use of adhesively bonded assemblies in automotive applications requires that manufacturers ensure cohesive failures for every type of load presented in the automotive structure. Section III.2 established a bonding procedure leading to cohesive failures in almost all the assemblies of this study and under different types of load. However, adhesive failures were observed in PA66 assemblies. In order to overtake this problem, manual sanding was applied over the bonded surface of the composite. The results showed that manual sanding permits the adhesive to bond directly over the fibers of the composite, which improves the interface strength, leading to cohesive failures at higher failure loads. Nevertheless, this approach must be used carefully because it might lead to a decrease of the strength of the composite. This kind of technique should be investigated in further studies.

Similarly, it is crucial to analyze not only the optimal state of the assembly but also the influence of some crucial parameters that might lead to early failures and major safety

concerns. Therefore, the influence of fabric orientation, surface state and humidity, on the behavior of composite bonded assemblies has been investigated. The results showed a minor influence of the fabric orientation on the strength of the assembly. Different results may be found if UD laminates are used (Alexandre UGUEN, 2017). This may be explained by the orthotropic character of the composite. In contrast, surface state and humidity have a great influence on the strength, the failure mode and the behavior of the assembly.

In metal bonded assemblies, the presence of grease over the metal surface can play an important role in the strength of the joint. Therefore, monotonic Arcan tests were performed in order to compare the failure envelopes of greasy and non-greasy metal assemblies. Among the six different combinations of adhesive/adherend assemblies tested, only the SP498/22MnB5 assemblies were considerably affected by the presence of grease. In this particular case, the fracture occurred by mixed adhesive/cohesive failure at the substrate/adhesive interface at a lower failure load. Since no other assembly bonded with SP498 was affected by the presence of grease, we can conclude that the influence of grease not only depends on the grease absorption capability of the adhesive but also on the nature of the adherend, the nature of the substrate and the surface treatment. Indeed, the aluminum-silicon coating applied over the surface of the 22MnB5 steel can have a significant influence on the strength of the assembly. Therefore, Arcan tests with non-coated 22MnB5 plates should be performed in order to explore the interaction between the surface treatment and the presence of grease.

The use of the Arcan device has permitted the behavior of the adhesive of the study to be appropriately characterized. A large experimental database under quasi-static mixed loadings is now available to the partners of the project, including monotonic, multilevel creep and increasing cyclic tests. Since cohesive failures were observed without any significant influence of the interface, it is possible to assume that these experimental results are quite representative of the behavior of the adhesives. Finally, the respect of the bonding procedure proposed in this study drastically reduces the scattering of the experimental results. This bonding procedure takes into account the aging of the adhesive cartridge (which may have an important influence on the final result), the surface preparation of the substrates and the adhesive spreading procedure.

Modeling the behavior of adhesives

On the subject of the behavior of the adhesives of the study, three main phenomena were observed during the experimental campaign: *(i)* the hydrostatic pressure dependence, *(ii)* the influence of the loading rate and *(iii)* the non-linear evolution of viscosity during creep. A good modeling of these aspects ensures a good prediction of the mechanical behavior of bonded structures. Some other parameters such as temperature can also be considered in order to enrich the model. However, a refined model requires a greater number of experimental data and a more complex identification methodology. Consequently, the selected behavior law should have a good balance between accuracy of the model and application requirements. Here, we have considered a 3D spectral non-linear viscoelastic

model as an adequate model to describe the behavior of the adhesives of the study. This model supposes a Gaussian distribution of the relaxation times and weights (viscous spectrum), and a non-linear evolution of the viscosity in order to better predict the behavior for long or higher stresses. Additionally, the hydrostatic and the deviatoric part of the viscoelastic compliance tensor have been separated in order to consider the hydrostatic pressure dependence. The identification methodology of the material parameters was only based on the multilevel creep test in order to reduce the time spent during the experimental campaign. Then, the material parameters are determined by an inverse identification. This procedure requires the precise modeling of the Arcan specimen. Consequently, a 3D finite element model was developed in Abaqus/standard and adapted to iterative loops. The computing time and the convergence of the mesh were then studied in order to ensure a good performance. Finally, the numerical predictions of the proposed model have been compared with monotonic Arcan tests, increasing cyclic tests and Bulk tests. The good concordance between the numerical and experimental curves permitted the proposed model to be validated.

Is it really necessary to model the behavior of the adhesive?

In this study, the accurate description of the non-linear behavior of adhesives has been considered of vital importance for the modeling of adhesively bonded joints. This was assumed since the mechanical properties of the adhesives are quite lower than the adherends. However, this assumption loses all relevance in some particular cases such as thin lap-shear structures. Indeed, in these cases, the behavior of the adhesive has a negligible effect on the monotonic macroscopic response because of the bending deformation of adherends (See section VI.5.3). In contrast, when thick substrates are used or when tensile or cyclic loadings are involved; the non-linear behavior of the adhesive should be taken into account. In conclusion, the use or non-use of an accurate modeling of the adhesive behavior depends on the final application and the requirements of the user.

Finally, the last conclusion of this study is an invitation for further works in order to obtain better predictions of the behavior of multi-material assemblies. Many phenomena, problems and aspects were not investigated in detail during the current Ph.D. study. The next section will present some preliminary results that can be used as a basis for further studies.

VII.2. Prospects

VII.2.1. Evolution of the adhesive behavior

During their service life, cars are continuously exposed to changes in the work environment such as ambient temperature fluctuations, vibrations, humidity, impacts and corrosion. These changes generally induce a reduction of the mechanical properties of materials and joints, which might be the origin of premature failures of the body-car structure. Therefore, the influence of these changes should be taken into account during the design process of the car. Here, it has been proposed to study the influence of aging and temperature on the mechanical behavior of the adhesive of the study.

VII.2.1.1. Aging of the component of the adhesive cartridge

As explained in section IV.1.3, the same adhesive cartridge was re-used several times to bond different specimens at different dates. In order to reduce the possible discrepancy of results due to the aging of the component of the adhesive cartridge after opening, some considerations have been proposed and respected during the bonding procedure:

1. The adhesive cartridge used for an experimental campaign should be much sooner than the expiration date given by the manufacturer (at least 6 months before).
2. During the bonding procedure, the adequate quantity of adhesive needed is extracted from the adhesive cartridge; then, the cartridge is immediately stored in a vacuum bag at -18°C . The adhesive cartridge can be warmed up to room temperature to facilitate the extraction of adhesive.
3. After opening, an adhesive cartridge can be re-used for up to a maximum of 2 months.

Figure VII.1 presents the behavior of adhesive specimens bonded with Sikapower-498 and Betamate-1822 following the previous recommendations. Two unaged specimens (bonded just after the opening of the adhesive cartridge) are compared with two 2-month aged specimens (bonded two months after the opening of the adhesive cartridge). The results show a clear concordance of the mechanical properties of the two types of specimen. Additionally, a Betamate-1822 specimen bonded six months after the opening of the cartridge is also plotted. In this case, the specimen presents a different behavior with a lower “pseudo-elastic limit”. This discrepancy can be explained by divers aspects, for example, the air exposition influence as in the case of polyurethane adhesive (Bidaud, 2014) or the proximity to the expiration date of the cartridge (the 6-month aged specimen was bonded just 1 month before the expiration date). Since no conclusion can be made at this stage about the origin of the adhesive components aging observed, further studies should be performed on this matter.

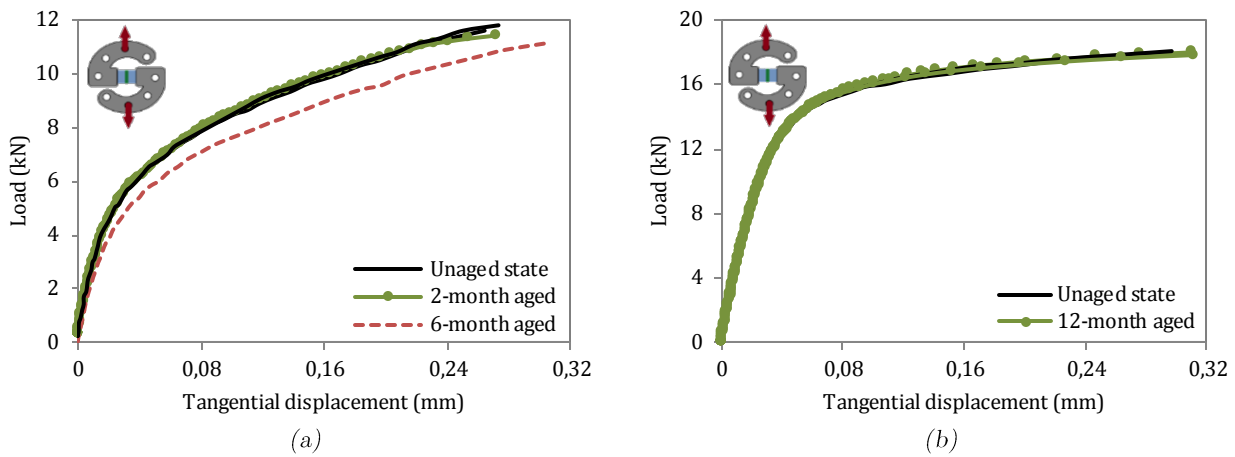


Figure VII.1: Adhesive components aging of the Betamate-1822 (a) and Sikapower-498 (b) adhesives. Load-displacement curves of shear Arcan tests.

VII.2.1.2. Aging of the adhesive after polymerization

A very important aspect of the design of adhesive joints is its durability over an extended period of time. Therefore, in order to study the evolution of the mechanical properties of the adhesives of the study after polymerization, an experimental campaign based on shear Arcan tests was performed. Two different aging states were tested:

- (i) Unaged state: the specimens were tested just after curing.
- (ii) Open-air: the specimens were tested twelve months after curing. They were stored under standard laboratory conditions (approximately 40% air humidity and $T=25^{\circ}\text{C}$).

Figure VII.2 compares the load-displacement curves of Sikapower-498 specimens for two types of aging. A similar rigidity at the beginning of the curve and a similar “pseudo-elastic” limit of both aging states can be observed. In contrast, the open-air specimens present a different non-linear regime and a lower failure load (about 12% lower). This aspect highlights an aging at room conditions of the adhesive that may be explained by the level of polymerization after curing. Indeed, no studies over the influence of the curing cycle were carried out in order to determine the optimal polymerization process. Therefore, it is possible that the used curing cycle does not ensure a 100% of polymerization and might be the cause of the aging observed. Further studies should be conducted in order to establish the adapted curing cycle and the cause of the aging.

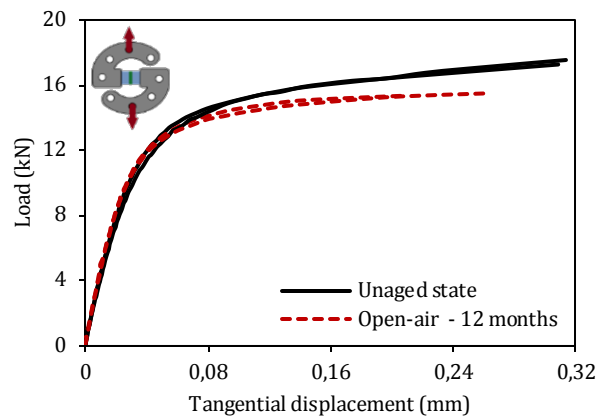


Figure VII.2: Aging of the Sikapower-498 adhesive after curing. Load-displacement curve of shear Arcan tests.

VII.2.1.3. Influence of temperature

It is well known that the temperature has a great influence on the behavior of polymeric materials; consequently, this should be taken into account during the dimensioning process of adhesive joints. A preliminary study on this matter was performed as a prospect of the current study. Adhesive specimens bonded with Sikaposer498 were tested under shear Arcan loadings at different temperatures.

As shown in Figure VII.3-a, the Arcan device was placed inside a thermal chamber for 2 hours at the desired temperature in order to ensure a stabilized temperature within the adhesive layer. This procedure was determined through a bonded specimen with a thermocouple at the center of the adhesive layer. It has been observed that the desired temperature was achieved inside the adhesive after 2 hours. Then, the tests were performed under controlling loading rate. The results show a great influence of temperature on the Sikapower-498 behavior, as presented in Figure VII.3-b. Indeed, high temperatures induce a prematurely non-linear regime, while low temperatures increase the “pseudo-elastic” limit. It is worth noting that a great non-linear regime and a similar rigidity are observed for all temperatures.

Figure VII.3-b also presents the time-temperature dependence of the Sikapower-498 adhesive. In general, the influence of temperature on the viscous behavior is the opposite of the loading rate effect. Thus, for example, a similar behavior can be observed at higher loading rates or at lower temperatures. In the particular case of the Sikapower-498 adhesive, the behavior observed in monotonic shear tests performed at **2kN/s** and room temperature (**T=25°C**) was quite similar to the behavior obtained at **0.2kN/s** and **T=6°C** (See dashed and green curves in Figure VII.3-b). This relation between temperature and loading rate can be used to investigate the behavior of the adhesive at different temperatures (that cannot be accessible due to experimental limitations) by means of different loading rates, and vice versa. Additionally, the time-temperature superposition principle may be used to determine the temperature and frequency dependence of the viscoelastic parameters of the adhesive.

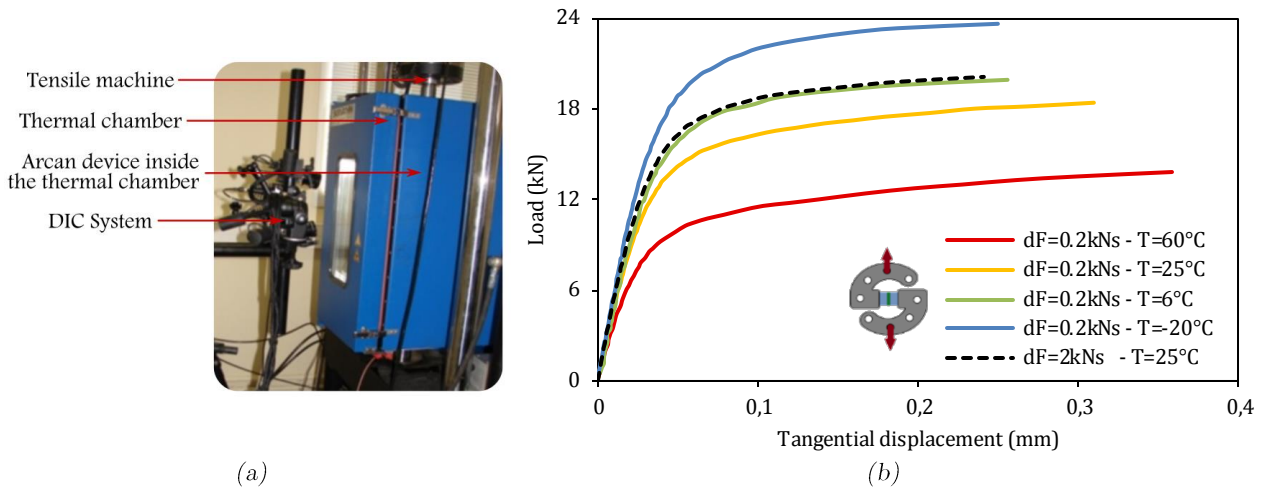


Figure VII.3: Influence of temperature on the behavior of the Sikapower-498 adhesive in monotonic shear loadings (b). Presentation of the experimental configuration of Arcan tests at different temperatures (a).

Multilevel creep tests were also performed in order to analyze the influence of temperature over the creep behavior. Three specimens were tested at different temperatures under consecutive creep levels of 2000 seconds at 20%, 40% and 60% of their respective failure load (see Figure VII.4-a). The results presented in Figure VII.4-b show a significant influence of temperature on the creep response. Indeed, the creep displacement seems to be an exponential function of temperature since a similar creep response is observed for $T=6^\circ\text{C}$ and $T=25^\circ\text{C}$, while for $T=60^\circ\text{C}$, the displacements are quite larger. As shown in Figure VII.5, this difference does not appear to depend on the viscous spectrum since the isochronism principle of the normalized displacements is respected for high and low temperatures. Therefore, for this particular adhesive, the only temperature-dependent material parameters seem to be the linear viscous parameters (a, b) and the non-linear viscous parameters (Y_0, Y_c, p).

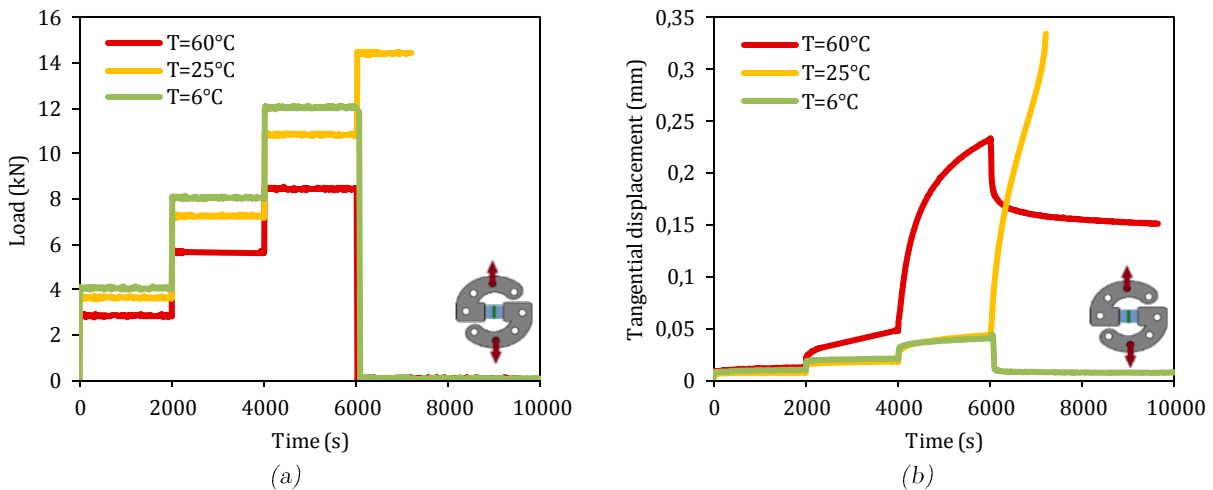


Figure VII.4: Influence of temperature on the behavior of the Sikapower-498 adhesive in multilevel creep shear test. Load-time curve (a) and displacement-time curve (b).

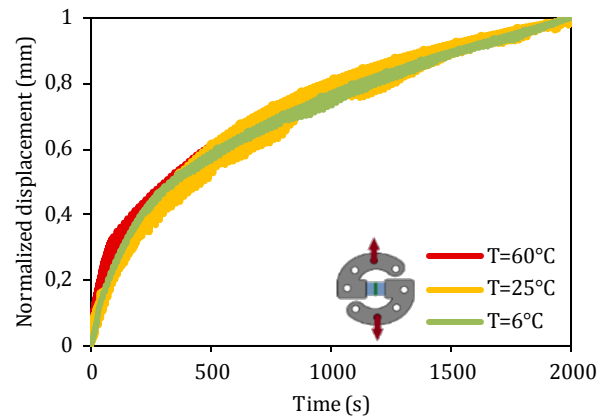


Figure VII.5: Normalized displacement of the Sikapower-498 creep levels at different temperatures.

The previously detailed results highlight the great influence of temperature on the behavior of the Sikapower-498 under monotonic and creep loadings. After being subjected to heat for long periods, creep displacements are more severe showing an important softening of the adhesive. This aspect can be explained because of the proximity to the glass transition temperature. Therefore, the behavior of the adhesive is not only dependent on the material properties or the applied load but also on the temperature and the exposure time. Additionally, since temperature also has an important influence during the production, storage and distribution process, it can also be interesting to study the behavior of the adhesive as a function of the temperature during these steps. In conclusion, further works need to be performed in order to take into account the temperature dependence upon the modeling of adhesive joints. DMA tests should be carried out in order to clarify and characterize the viscous behavior as a function of temperature.

VII.2.2. Cyclic behavior

As concluded in (Shenoy *et al.*, 2010) and (Thevenet *et al.*, 2013), the adhesive fatigue behavior can be strongly dependent on the material state (inclusions, defects, residual stresses), the type of load (tensile, shear, compression or mixed loadings) and the cyclic loading form (amplitude, mean load, and loading rate). Moreover, the mechanical response also depends on humidity and temperature levels. The influence of these parameters has traditionally been studied through lap-shear or bulk tests; however, a more suitable solution may be the use of “modified” scarf joints with an optimized geometry that limits the edge effects (Nicolas Carrere *et al.*, 2015) (See Figure VII.6). Indeed, this type of specimen localizes the maximum stress in the mid-plane of the adhesive to attain cohesive failures. Additionally, different combinations of tensile/shear loadings can be easily created by the definition of the angle (γ), as shown in Figure VII.6.

On the other hand, the modeling of the adhesive behavior can be implemented via FE models as proposed in section VI.3.1. For this purpose, the behavior law presented in this study can be used to describe the behavior of the adhesive under cyclic loadings. However, a particular attention should be paid since the loading rates presented in classic cyclic tests (1-5 Hz) are quite higher than the loading rates used in the identification procedure of the

material parameters. Therefore, it is recommended to identify the material parameters at higher loading rates representative of the fatigue load.

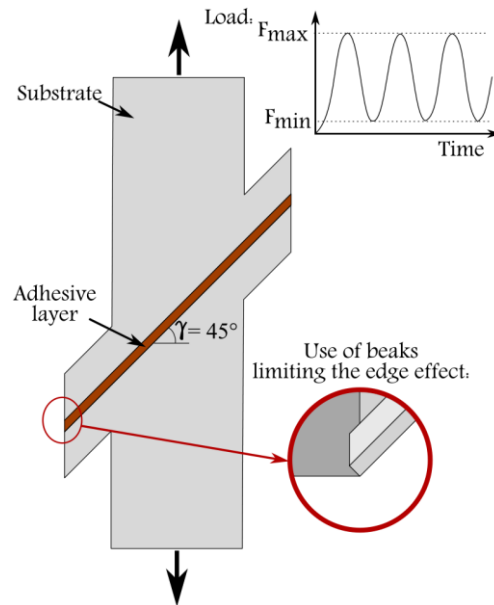


Figure VII.6: Scarf specimen geometry for tensile/shear loadings ($\gamma=45^\circ$).

VII.2.3. Hybrid RivSet/adhesive joints

Two or more joining techniques can be associated in order to produce joints with properties additional to those obtained from one single technique. The most common types of hybrid joints involve an adhesive in combination with a mechanical fastener. In the framework of the FASTLITE project, hybrid RivSet/adhesive joints have been selected as the most adapted solution due to the great compatibility of the two techniques and the possibility of fast joining. Indeed, strong joints can be obtained by using RivSet pieces that attach the assembly during the curing cycle of the adhesive without the need for additional supports or machining, which can increase the time and space required in the automotive production chain. Additionally, the use of RivSet fasteners may also increase the peel strength of adhesive joints.

In order to investigate the behavior and the strength of this hybrid technique, an exploratory campaign was performed with hybrid PA66/AL5182 specimens assembled by RivSet joints and bonded with Sikapower-498. The Arcan device proposed in section III.1.3 was used to characterize their mechanical responses. As shown in Figure VII.7-a, the adhesive thickness (0.3mm) and the bonded surface (around $50 \times 10 \text{mm}^2$) have been respected by using Teflon spacers; the RivSet piece is placed at the center of the assembly. The curing cycle presented in section I.7.4.1 has been followed in order to polymerize the Sikapower-498 layer. Then, the Arcan substrates were adhesively bonded to the hybrid assembly with Araldite 420 A/B adhesive (See Figure VII.7-b). Since this second adhesive has a curing cycle of 72h at room temperature followed by 5h at 70° Celsius, the behavior of the hybrid joint was slightly affected; in effect, the glass-transition temperature of the Sikapower-498 adhesive was never achieved (100°C).

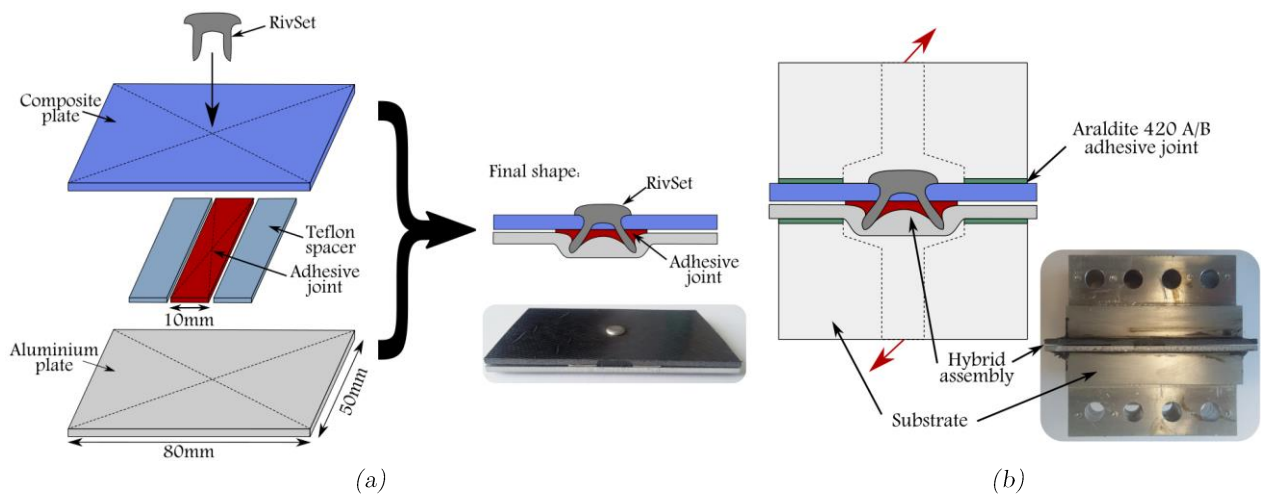


Figure VII.7: Hybrid RivSet/Adhesive assembly (a) and Arcan specimen (b).

As shown in Figure VII.8, the behavior of the tested specimen is characterized by an initial step where the macroscopic response is mainly controlled by the behavior of the adhesive layer. At the end of this step, the maximum load is achieved and the adhesive fails by cohesive mode. Then, in the second step, the assembly is held together by the RivSet piece. The final failure occurs when the RivSet fails. The results confirm the good compatibility of both techniques and the high mechanical performance under static shear loadings. Therefore, further studies may be performed in order to characterize hybrid assemblies under different combinations of tensile/shear loadings by means of the Arcan device. Additionally, the modeling of hybrid RivSet/adhesive joints should also be studied since the use of this type of joint seems to be an important improvement in the automotive design.

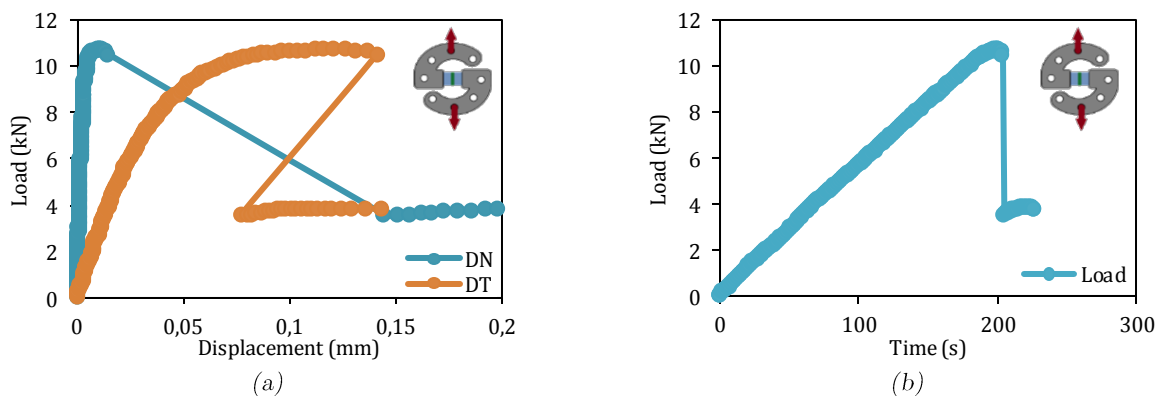


Figure VII.8: Experimental results of Hybrid PA66/AL5182 specimens in shear Arcan test. Load-displacement curve (a) and Load-time curve (b).

VII.2.4. “Cohesive” failures

Thanks to the experimental results obtained by means of the Arcan device, a set of bonded assemblies leading to cohesive failure have been determined. However, some lap-shear tests performed at the UVHC University have shown that some of these assemblies present adhesive failures: SP498/PA66 and SP498/Steel22MnB5. This aspect underlines that failure can be affected by some parameters that are inherent to the type of test.

Indeed, in a lap-shear test the presence of edge effects at the interface and the plasticity of the substrates may lead to a different failure mode. Consequently, in order to ensure cohesive failures, the analysis through the modified Arcan device with specimens reducing the edge effects is not enough. Nevertheless, the use of lap-shear test might not be a good solution either. This is because this type of test is not representative of the set of possible types of load presented in the automobile structure. Therefore, it is necessary to propose an alternative test permitting the interface to be subjected to a wide range of tri-axial loads and at the same time with stress concentrations observed in real assemblies. To this end, the use of the Arcan specimens without beaks, which allow the localization of the stress at the interface, can be considered as an adapted solution. Another interesting approach can also be the use of scarf joint specimens as proposed in (Wang and Xu, 2006).

VII.2.5. Some other parameters that should be taken into account

A great part of this study was focused on the behavior of adhesive joints in particular cases with low stress concentrations and assuming a homogeneous adhesive material. However, these cases are quite rare in real structures. Therefore, in order to better describe the mechanical response of adhesively bonded assemblies, it is necessary to take into account the effect of stress concentrations during their design phase. These concentrations may occur through a variety of mechanisms including (i) geometry singularities, (ii) material heterogeneities or (iii) residual stresses (mechanical or thermal).

- (i) Stress concentrations due to geometry singularities are strongly linked with the onset and propagation of cracks. Indeed, local stresses can induce premature cracks within the adhesive layer; their evolution and their influence on the behavior of the assembly are principally defined by the fracture toughness properties of the adhesive (G_{IC} and G_{IIC}). These properties can be obtained by traditional tests such as DCB and MMB tests or by some other experimental approaches based on the Arcan device as in (Stamoulis *et al.*, 2016). The fracture parameters of the Sikapower-498 have already been determined (See Table I-4); nevertheless, no experimental campaign has been performed on this topic for Betamate-1822. Therefore, the next step in the study of adhesive joints is the determination of the fracture toughness parameters of the Betamate-1822 adhesive. On the other hand, the modeling of the onset and propagation of cracks may be an interesting aspect to explore in the future. On that matter, a large number of 2D or 3D models can be found in the literature. The most typically used are the cohesive element models where a stress or strain criteria can be used to define the onset and the propagation of the crack (M. D. Banea and L. F. M. da Silva, 2008). This type of approach proposes a progressive damage function based on the traction-separation response between initially coincident nodes along a pre-defined crack zone (or path in the case of 2D models). Therefore, the FE model depends on the strength and the fracture toughness. Other approaches are based on analytical or semi-analytical methods, which present a considerably lower computation time as regards with cohesive models. A good example of that is the coupled stress and energy criterion proposed in (N. Carrere *et al.*, 2015).

Finally, in order to validate the numerical approach, lap-shear tests can be used since the stress concentration presented at the edges of the adhesive layer make them an adapted validation test. Indeed, edge effects can induce stress singularities that contribute to the onset and propagation of cracks in the overlap length.

- (ii) The mechanical properties of the adhesives of the study were assumed homogeneous. However, the presence of porosities or additives may have an important role on the stress distribution and the isotropy of the joint response. Therefore, further works should be consecrated to the analysis of the influence of 3D distributions of porosities, additives and/or defects on the mechanical behavior of adhesive joints. Figure VII.9 shows microscopic images of the adhesive layer of two Arcan specimens bonded with Betamate-1822 and Sikapower-498, respectively. A substantial number of additives with irregular shapes and sizes can be seen. On the contrary, no porosities can be observed.

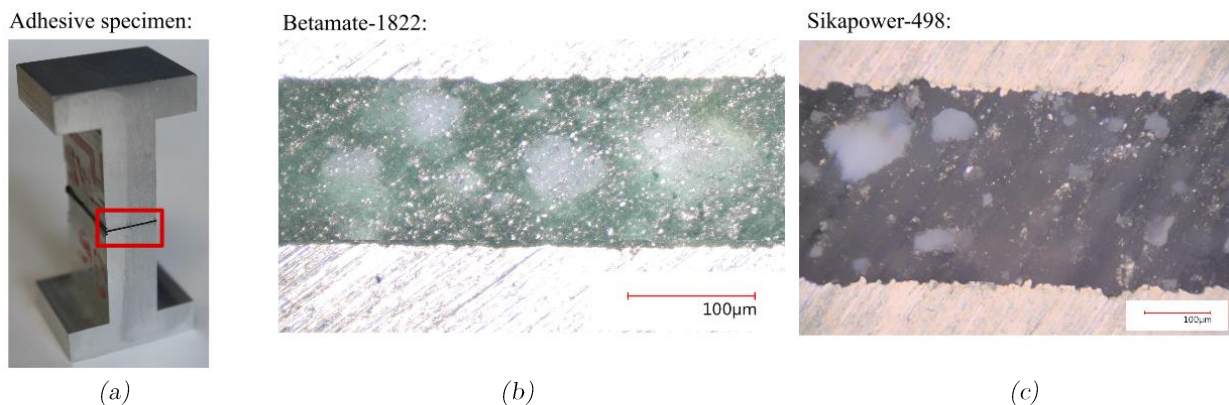


Figure VII.9: Presence of additives in the adhesive joint. Adhesive specimen cut at the transverse plane (a). Keyence digital microscopic images of the Betamate-1822 (b) and Sikapower-498 (c) adhesive layers in the region indicated by the red box.

- (iii) Residual stresses in adhesively bonded joints are principally linked to the polymerization procedure of the adhesive. Indeed, during hardening, mechanical loads (such as pressure) and/or thermal loads can induce local stresses within the adhesive layer, especially for stiff substrates. In thermal stresses, the residual stress is associated with a different volume change of the adhesive and the adherends due to their different thermal coefficients. Additionally, during the service life of the joint, the adhesive layer may be subjected to a wide range of temperatures, which implies the evolution of residual stresses. This stress evolution in combination with the temperature dependence might have a significant influence on the service life of the adhesive joint (Badulescu *et al.*, 2012). Therefore, in order to better understand the stress distribution within the adhesive layer before and during its service life, experimental measurements such as x-ray diffraction or neutron diffraction techniques should be carried out in the future.



References

- ADEME-Carlabelling, 2015. Consommations de carburant et émissions de CO₂.
- Alexandre UGUEN, 2017. Influence de l'endommagement plan sur le comportement hors plan des matériaux composites stratifiés et des assemblages collés. (Thèse financée par la DGA et la Région Bretagne). Université de Bretagne Occidentale, Brest.
- Alfonso, L., Uguen, A., Badulescu, C., Cognard, J.-Y., Bonnemains, T., Lolive, E., Carrere, N., 2015. Determination of the 3D failure envelope of a composite based on a modified Arcan test device. *Compos. Struct.* 131, 585–593. doi:10.1016/j.compstruct.2015.06.029
- ARaymond Network, © Raygroup SASU, n.d. Techbond®Pur process. Bonding Solutions. Document information.
- Arcan, M., Hashin, Z., Voloshin, A., 1978. A method to produce uniform plane-stress states with applications to fiber-reinforced materials. *Exp. Mech.* 18, 141–146. doi:10.1007/BF02324146
- Arnaud, N., Créac'hcadec, R., Cognard, J.Y., 2014. A tension/compression-torsion test suited to analyze the mechanical behaviour of adhesives under non-proportional loadings. *Int. J. Adhes. Adhes., Joint Design* 53, 3–14. doi:10.1016/j.ijadhadh.2014.01.013
- ASM International, 1990. *Engineered Materials Handbook: Adhesives and Sealants*.
- ASM International, Metals Park, 1994. *ASM Metals Handbook*, 8th edn. ed. Ohio.
- ASTM 5573, C.D.-14, 1999. Standard Practice for classifying failure modes in fiber-reinforced-plastic (FRP) joints. *Annu. Book ASTM Stand.*

- ASTM D5656-04, 2004. Standard Test Method for Thick-Adherend Metal Lap-Shear Joints for Determination of the Stress-Strain Behavior of Adhesives in Shear by Tension Loading.
- ASTM D5868, 2014. Standard Test Method for Lap Shear Adhesion for Fiber Reinforced Plastic (FRP) Bonding.
- Badulescu, C., Cognard, J.Y., Créac'hcadec, R., Vedrine, P., 2012. Analysis of the low temperature-dependent behaviour of a ductile adhesive under monotonic tensile/compression-shear loads. *Int. J. Adhes. Adhes.* 36, 56–64. doi:10.1016/j.ijadhadh.2012.03.009
- Badulescu, C., Germain, C., Cognard, J.-Y., Carrere, N., 2015. Characterization and modelling of the viscous behaviour of adhesives using the modified Arcan device. *J. Adhes. Sci. Technol.* 29, 443–461. doi:10.1080/01694243.2014.991483
- Balieu, R., Lauro, F., Bennani, B., Delille, R., Matsumoto, T., Mottola, E., 2013. A fully coupled elastoviscoplastic damage model at finite strains for mineral filled semi-crystalline polymer. *Int. J. Plast.* 51, 241–270. doi:10.1016/j.ijplas.2013.05.002
- Barnes, T.A., Pashby, I.R., 2000. Joining techniques for aluminium spaceframes used in automobiles: Part II — adhesive bonding and mechanical fasteners. *J. Mater. Process. Technol.* 99, 72–79. doi:10.1016/S0924-0136(99)00361-1
- Bidaud, P., 2014. Analysis of the cyclic behavior of an adhesive in an assembly for offshore windmills applications. Université de Bretagne Occidentale.
- Bollhoff, 2013. RivSet and RivTac technologies. Experimental report. Fastlite project.
- Böllhoff group, n.d. RivSet® Self-pierce riveting for perfect joints. Document information.
- Broudin, M., Le Gac, P.Y., Le Saux, V., Champy, C., Robert, G., Charrier, P., Marco, Y., 2015. Water diffusivity in PA66: Experimental characterization and modeling based on free volume theory. *Eur. Polym. J.* 67, 326–334. doi:10.1016/j.eurpolymj.2015.04.015
- Carrere, N., Badulescu, C., Cognard, J.-Y., Leguillon, D., 2015. 3D models of specimens with a scarf joint to test the adhesive and cohesive multi-axial behavior of adhesives. *Int. J. Adhes. Adhes.* 62, 154–164. doi:10.1016/j.ijadhadh.2015.07.005
- Carrere, N., Martin, E., Leguillon, D., 2015. Comparison between models based on a coupled criterion for the prediction of the failure of adhesively bonded joints. *Eng. Fract. Mech.* 138, 185–201. doi:10.1016/j.engfracmech.2015.03.004

-
- CETIM, 2013. Résultats pré-étude - Etats Initiaux.
- Chaichanawong, J., Thongchuea, C., Areerat, S., 2016. Effect of moisture on the mechanical properties of glass fiber reinforced polyamide composites. *Adv. Powder Technol.* doi:10.1016/j.apt.2016.02.006
- Chastel, Y., Passemard, L., 2014. Joining Technologies for Future Automobile Multi-material Modules. *Procedia Eng.*, 11th International Conference on Technology of Plasticity, ICTP 2014, 19-24 October 2014, Nagoya Congress Center, Nagoya, Japan 81, 2104–2110. doi:10.1016/j.proeng.2014.10.293
- Chiminelli, A., Breto, R., Jiménez, M.A., Velasco, F., Abenojar, J., Martínez, M.A., 2016. Experimental method for the determination of material parameters of plasticity models for toughened adhesives. *Int. J. Adhes. Adhes.* 68, 182–187. doi:10.1016/j.ijadhadh.2016.03.004
- Cognard, J.Y., 2008. Numerical analysis of edge effects in adhesively-bonded assemblies application to the determination of the adhesive behaviour. *Comput. Struct.* 86, 1704–1717. doi:10.1016/j.compstruc.2008.02.003
- Cognard, J.Y., Créac'hcadec, R., Sohier, L., Davies, P., 2008. Analysis of the nonlinear behavior of adhesives in bonded assemblies—Comparison of TAST and Arcan tests. *Int. J. Adhes. Adhes.*, Special Topic Issue on Structural Adhesive Joints 28, 393–404. doi:10.1016/j.ijadhadh.2008.04.006
- Cognard, J.Y., Créac'hcadec, R., Sohier, L., Leguillon, D., 2010. Influence of adhesive thickness on the behaviour of bonded assemblies under shear loadings using a modified TAST fixture. *Int. J. Adhes. Adhes.*, Special Issue on Joint Design 30, 257–266. doi:10.1016/j.ijadhadh.2009.11.003
- Cognard, J.Y., Davies, P., Gineste, B., Sohier, L., 2005. Development of an improved adhesive test method for composite assembly design. *Compos. Sci. Technol.*, JNC13-AMAC-Strasbourg 65, 359–368. doi:10.1016/j.compscitech.2004.09.008
- Cognard, J.Y., Davies, P., Sohier, L., Créac'hcadec, R., 2006. A study of the non-linear behaviour of adhesively-bonded composite assemblies. *Compos. Struct.*, Fifteenth International Conference on Composite Materials ICCM-15 Fifteenth International Conference on Composite Materials 76, 34–46. doi:10.1016/j.compstruct.2006.06.006
- Créac'hcadec, R., Cognard, J.Y., Heuzé, T., 2008. On Modelling the Non-linear Behaviour of Thin Adhesive Films in Bonded Assemblies With Interface Elements. *J. Adhes. Sci. Technol.* 22, 1541–1563. doi:10.1163/156856108X305741

Dassault Systèmes, n.d. Abaqus CAE.

Dassault Systèmes Simulia, 2012. Scripting User's Manual.

Davies, P., Sohier, L., Cognard, J.-Y., Bourmaud, A., Choqueuse, D., Rinnert, E., Créac'hcadec, R., 2009. Influence of adhesive bond line thickness on joint strength. *Int. J. Adhes. Adhes.* 29, 724–736. doi:10.1016/j.ijadhadh.2009.03.002

Devaux, O., 2015. Analyse et optimisation des assemblages ioniques collés sous chargements thermo-mécaniques [WWW Document]. <http://www.theses.fr>. URL <http://www.theses.fr/s139425> (accessed 10.4.16).

Duncan, B., 2010. 14 - Developments in testing adhesive joints A2 - Dillard, David A., in: *Advances in Structural Adhesive Bonding*, Woodhead Publishing Series in Welding and Other Joining Technologies. Woodhead Publishing, pp. 389–436.

EEA Technical report, 2014. Monitoring CO2 emissions from new passenger cars and vans in 2014 (No. 16/2015). Luxembourg.

Findley, W.N., Lai, J.S., Onaran, K., 1989. Creep and relaxation of nonlinear viscoelastic materials with an introduction to linear viscoelasticity. Dover Publications, New York.

Frank, G.J., Brockman, R.A., 2001. A viscoelastic–viscoplastic constitutive model for glassy polymers. *Int. J. Solids Struct.* 38, 5149–5164. doi:10.1016/S0020-7683(00)00339-5

Gallegos, C., 2010. Rheology, *Encyclopedia of life support systems-EOLSS*. ed.

Gay, A., Lefebvre, F., Bergamo, S., Valiorgue, F., Chalandon, P., Michel, P., Bertrand, P., 2016. Fatigue performance of a self-piercing rivet joint between aluminum and glass fiber reinforced thermoplastic composite. *Int. J. Fatigue* 83, Part 2, 127–134. doi:10.1016/j.ijfatigue.2015.10.004

GOM, 2011. Aramis® software version 6.3.1.

Groth, H.L., 1990. Viscoelastic and viscoplastic stress analysis of adhesive joints. *Int. J. Adhes. Adhes.* 10, 207–213. doi:10.1016/0143-7496(90)90105-7

Groupe Renault, 2014. EOLAB concept. Mondial de l'Automobile.

Han, L., Thornton, M., Shergold, M., 2010. A comparison of the mechanical behaviour of self-piercing riveted and resistance spot welded aluminium sheets for the automotive industry. *Mater. Des.* 31, 1457–1467. doi:10.1016/j.matdes.2009.08.031

-
- Handbook of industrial engineering: Technology and operations management, Third edition. ed, 2001. . Gavriel salvendy.
- He, X., Zhao, L., Deng, C., Xing, B., Gu, F., Ball, A., 2015. Self-piercing riveting of similar and dissimilar metal sheets of aluminum alloy and copper alloy. *Mater. Des.* 158-2015 65, 923–933. doi:10.1016/j.matdes.2014.10.002
- Hicks, C.R., Carlson, B.E., Mallick, P.K., 2015. Rheological study of automotive adhesives: Influence of storage time, temperature and shear rate on viscosity at dispensing. *Int. J. Adhes. Adhes.* 63, 108–116. doi:10.1016/j.ijadhadh.2015.08.011
- Iosipescu, N, 1967. New Accurate Procedure for Single Shear Testing of Metals. *J. Mater.* 3, 537–566.
- ISO 6922, 1987. Adhesives - Determination of tensile strength of butt joints.
- ISO 11003-2, 2001. Determination of shear behaviour of structural adhesives - Part 2: Tensile test method using thick adherends.
- Jean-Louis Batoz, 1995. Modélisation des structures par éléments finis, 1st ed. Hermès - Lavoisier.
- Jeffrey c. Lagarias, James A. Reeds, Margaret H. Wright, Paul E. Wrigh, 1998. Convergence properties of the nelder–mead simplex method in low dimensions. *Soc. Ind. Appl. Math.* 9, 112–147.
- Joannès, S., Renard, J., Gantchenko, V., 2010. The role of talc particles in a structural adhesive submitted to fatigue loadings. *Int. J. Fatigue*, Fourth International Conference on Fatigue of Composites (ICFC4) 32, 66–71. doi:10.1016/j.ijfatigue.2009.02.021
- LeBacq, C., Brechet, Y., Shercliff, H.R., Jeggy, T., Salvo, L., 2002. Selection of joining methods in mechanical design. *Mater. Des.* 23, 405–416. doi:10.1016/S0261-3069(01)00093-0
- Lemaitre, J., Chaboche, J.-L., 1994. *Mechanics of Solid Materials*. Cambridge University Press.
- Lévêque D., Maire J.-F., Mavel A., Petipas C., Schieffer A., 2000. Prédiction de la durée de vie et des performances résiduelles des composites carbone/résine. (No. n°RT 66/7086 DMSC/Y). Rapport technique ONERA.

- Lévêque D., Maire J.-F., Mavel A., Petipas C., Schieffer A., 2000. Prédiction de la durée de vie et des performances résiduelles des composites carbone/résine (contrat DPAC No. Rapport technique ONERA n°RT 66/7086 DMSC/Y).
- López-Guerra, E.A., Solares, S.D., 2014. Modeling viscoelasticity through spring-dashpot models in intermittent-contact atomic force microscopy. *Beilstein J. Nanotechnol.* 5, 2149–2163. doi:10.3762/bjnano.5.224
- Lovatt, A.M., Shercliff, H.R., 1998. Manufacturing process selection in engineering design. Part 1: the role of process selection. *Mater. Des.* 19, 205–215. doi:10.1016/S0261-3069(98)00038-7
- Lucas F. M. da Silva, Andreas Öchsner, Robert D. Adams, 2011. *Handbook of Adhesion Technology*. Springer Berlin Heidelberg.
- M. D. Banea, L. F. M. da Silva, 2008. Adhesively bonded joints in composite materials: an overview. *Proc IMechE Vol 223 Part J Mater. Des. Appl.*
- Mahnken, R., 2012. Simulation of strength difference coupled to softening in elasto-plasticity for adhesive materials. *Int. J. Adhes. Adhes.* 32, 1–14. doi:10.1016/j.ijadhadh.2011.08.006
- Mahnken, R., 2005. Simulation of strength difference for adhesive materials in finite deformation elasto-plasticity. *Comput. Methods Appl. Mech. Eng.* 194, 4097–4114. doi:10.1016/j.cma.2004.10.006
- Maire, J.-F., 1992. Etudes théorique et expérimentale du comportement de matériaux composites en contraintes planes. Thèse de doctorat de l'Université de Franche-Comté.
- Maire J.F., Lesne O., Pepitas C., 1996. Une nouvelle approche de la modélisation du comportement visqueux des composites organiques. (10èmes Journées nationales sur les composites. JNC 10). ONERA.
- Majda, P., Skrodzewicz, J., 2009. A modified creep model of epoxy adhesive at ambient temperature. *Int. J. Adhes. Adhes.* 29, 396–404. doi:10.1016/j.ijadhadh.2008.07.010
- Nikiforos Zacharof, Uwe Tietge, Peter Mock, 2015. CO2 emissions from new passenger cars in the EU: Car manufacturers' performance in 2014. International Council on Clean Transportation - ICCT.
- Oliveira, I., Teixeira, P., Ferreira, F., Reis, A., 2015. Inverse Characterization of Material Constitutive Parameters for Dynamic Applications. *Procedia Eng.*, ICSI 2015 The

-
- 1st International Conference on Structural Integrity Funchal, Madeira, Portugal 1st to 4th September, 2015 114, 784–791. doi:10.1016/j.proeng.2015.08.027
- P A Hilton, I A Jones, R Sallavanti, 2000. Laser Welding of Fabrics Using Infrared Absorbing Dyes. ASM - Int. Conf. Join. Adv. Spec. Mater. III.
- Porcaro, R., Hanssen, A.G., Aalberg, A., Langseth, M., 2004. Joining of aluminium using self-piercing riveting: Testing, modelling and analysis. *Int. J. Crashworthiness* 9, 141–154. doi:10.1533/ijcr.2004.0279
- Porcaro, R., Hanssen, A.G., Langseth, M., Aalberg, A., 2006. The behaviour of a self-piercing riveted connection under quasi-static loading conditions. *Int. J. Solids Struct.* 43, 5110–5131. doi:10.1016/j.ijsolstr.2005.10.006
- R. D. Adams, William C. Wake, J. Comyn, 1997. *Structural Adhesive Joints in Engineering*, 2nd ed. Springer Netherlands, London.
- Rakotoarisoa, C., 2013. *Prévision de la durée de vie en fatigue des composites à matrice organique tissés interlock*. Université de technologie de Compiègne-Onera.
- R.T. Cole, E.J. Ba Teh, J. Potter, 1982. Fasteners for composite structures. *Composites* 233–240.
- Sadowski, T., Golewski, P., Kniec, M., 2014. Experimental investigation and numerical modelling of spot welding-adhesive joints reponse. *Compos. Struct.*
- Schieffer, A., 2003. *Modélisation multiechelle du comportement mécanique des composites à matrice organique et effets du vieillissement thermique*. Université de technologie Troyes / Onera.
- Shenoy, V., Ashcroft, I.A., Critchlow, G.W., Crocombe, A.D., 2010. Fracture mechanics and damage mechanics based fatigue lifetime prediction of adhesively bonded joints subjected to variable amplitude fatigue. *Eng. Fract. Mech.* 77, 1073–1090. doi:10.1016/j.engfracmech.2010.03.008
- Soghrati, S., Liang, B., n.d. Automated analysis of microstructural effects on the failure response of heterogeneous adhesives. *Int. J. Solids Struct.* doi:10.1016/j.ijsolstr.2015.12.002
- Sohier, L., Cognard, J.Y., Davies, P., 2013. Analysis of the mechanical behaviour of adhesively bonded assemblies of composites under tensile–shear out-of-plane loads. *Compos. Part Appl. Sci. Manuf.* 53, 65–74. doi:10.1016/j.compositesa.2013.05.008

- Stamoulis, G., Carrere, N., Cognard, J.-Y., Davies, P., Badulescu, C., 2016. Investigating the fracture behavior of adhesively bonded metallic joints using the Arcan fixture. *Int. J. Adhes. Adhes.* 66, 147–159. doi:10.1016/j.ijadhadh.2016.01.001
- Stamoulis, G., Carrere, N., Cognard, J.Y., Davies, P., Badulescu, C., 2014. On the experimental mixed-mode failure of adhesively bonded metallic joints. *Int. J. Adhes. Adhes.* 51, 148–158. doi:10.1016/j.ijadhadh.2014.03.002
- Thevenet, D., Créac'hcadec, R., Sohier, L., Cognard, J.Y., 2013. Experimental analysis of the behavior of adhesively bonded joints under tensile/compression–shear cyclic loadings. *Int. J. Adhes. Adhes.* 44, 15–25. doi:10.1016/j.ijadhadh.2013.01.011
- T.L., A., 2005. *Fracture mechanics - Fundamentals and applications*, Third edition. ed.
- Yuh J. Chao, 2003. Ultimate Strength and Failure mechanism of resistnace spot weld subjected to tensile shear or combined tensile-shear loads. *J. Eng. Mater. Technol.*
- Zgoul, M., Crocombe, A.D., 2004. Numerical modelling of lap joints bonded with a rate-dependent adhesive. *Int. J. Adhes. Adhes.* 24, 355–366. doi:10.1016/j.ijadhadh.2003.11.006

Caractérisation et modélisation d'assemblages multi-matériaux sous sollicitations mixtes quasi-statiques pour la conception de structures automobiles

Résumé : Durant ces dernières années, les émissions de CO₂ liées à l'utilisation des voitures ont atteint des niveaux critiques contribuant au réchauffement climatique et causant des problèmes de santé. Afin de réduire ces émissions, l'industrie automobile française a décidé de réduire la masse des véhicules via l'utilisation de matériaux plus légers tels que les matériaux composites. Cependant, les techniques d'assemblage classiquement utilisées ne sont pas compatibles pour assembler ces nouveaux matériaux à la structure du véhicule (acier et aluminium). Le principal objectif de cette étude a donc été la caractérisation et la modélisation de nouvelles techniques d'assemblages multi-matériaux permettant une bonne résistance mécanique.

Quatre techniques d'assemblages multi-matériaux (métal/composite) ont été étudiées : (i) le collage par goujon, (ii) la soudure laser, (iii) le rivetage auto-perçant et (iv) le collage. Des essais traditionnels de simple recouvrement et de traction transverse ont été utilisés pour caractériser les deux premières techniques. Ensuite, un nouveau test de caractérisation basé sur un dispositif Arcan modifié a été proposé pour analyser le comportement des assemblages rivetés et le collage. Parmi les quatre techniques testées, le collage a été retenu comme la technique la plus adaptée aux exigences de l'industrie. Par conséquent, des essais Arcan ont été réalisés afin de déterminer le comportement quasi-statique des adhésifs de l'étude (Betamate1822 et Sikapower498). Ces essais ont ensuite été utilisés pour proposer et identifier une nouvelle loi de comportement 3D viscoélastique spectrale non-linéaire. La procédure d'identification des paramètres des adhésifs n'est basée que sur trois essais de fluage multiniveaux, permettant un dimensionnement rapide des structures collées. Enfin, la loi de comportement proposée a été validée grâce à la bonne corrélation entre les prédictions numériques et les courbes expérimentales des essais monotones à différentes vitesses de sollicitation et des essais de traction incrémentale.

La présente étude a été développée dans le cadre d'un projet automobile. Néanmoins, les conclusions et les perspectives de l'étude peuvent être extrapolées à d'autres domaines tout aussi intéressants.

Mots-clés : Réchauffement climatique, Industrie automobile, Matériaux composites, Assemblages multi-matériaux, techniques d'assemblage, Dispositif Arcan modifié, Adhésifs, Sollicitation mixte, Viscoélasticité spectrale, Essai de fluage multiniveaux, structures collées.

Characterization and modeling of multi-material assemblies under mixed quasi-static loadings for the design of automotive structures

Abstract : Nowadays, the emissions of CO₂ due to the use of automobiles have reached critical levels causing global warming and health problems. In order to reduce these emissions, the French automotive industry has decided to reduce the car weight by means of the use of lighter materials such as composite materials. However, the classical joining techniques are not adapted to assembly these new materials to the structure of the car (aluminum and steel alloys). Therefore, the characterization and modeling of new joining techniques of dissimilar materials is a problem that has been treated in the current study.

Four different joining techniques of dissimilar materials (metal/composite) have been studied: (i) stud bonding, (ii) laser welding, (iii) self-pierce riveting and (iv) adhesive bonding systems. Traditional lap-shear and cross-tension tests were used to characterize the first two joining techniques. Then, a new characterization test based on a modified Arcan device has been proposed to analyze the behavior of self-piercing rivet and adhesive bonding systems. Among all the four tested techniques, adhesive joints have been selected as the most adapted technique according to the requirements of the industry. Therefore, modified Arcan tests have been performed in order to determine the behavior of the adhesives of the study (Betamate1822 and Sikapower498). These tests were then used to propose and identify a new 3D non-linear viscoelastic spectral model. The identification procedure of the material parameters is only based on three multilevel creep tests, which permits the rapid dimensioning of adhesively bonded structures. Finally, the proposed behavior law was validated by the good concordance between the numerical predictions and the experimental curves of monotonic tests at different loading rates and increasing cyclic tests.

The current study was developed in the framework of an automotive project. Nevertheless, the conclusions and prospects of the study can be extrapolated to other interesting fields.

Keywords : Global warning, Automotive industry, Composite materials Multi-material assemblies, Joining techniques, Modified Arcan device, Adhesives, Mixed load, Spectral viscoelasticity, Multilevel creep test, Adhesively bonded structures.